Friedrich-Schiller-Universität Jena

Chemisch-Geowissenschaftliche Fakultät

Micro- and nanopatterning by local electrochemical lithography

Dissertation

zur Erlangung des akademischen Grades

doctor rerum naturalium (Dr. rer. nat.)

vorgelegt dem Rat der Chemisch-Geowissenschaftlichen Fakultät der Friedrich-Schiller-Universität Jena

vorgelegt von Master of Science He Liu

geboren am 07.12.1986 in Changchun

Gefördert durch Chinese Scholarship Council.

Gutachter:

1. Prof. Dr. Ulrich S. Schubert

Laboratory of Organic and Macromolecular Chemistry (IOMC), Friedrich Schiller University Jena, Humboldtstr. 10, 07743 Jena

2. Prof. Dr. Wolfgang Weigand

Institute for Inorganic and Analytical Chemistry, Friedrich Schiller University Jena, Humboldtstr. 8, 07743 Jena

Tag der öffentlichen Verteidigung: 09, 11, 2016

Table of contents

Documentation of authorship

This section contains a list of the individual authors contribution to the publications reprinted in this thesis.

P1) H. Liu,[1] S. Hoeppener,[2] U. S. Schubert[3] "Nanoscale materials patterning by local electrochemical lithography" *Adv. Eng. Mater.* **2016**, *18*, 890−902.			
Author	**1**	**2**	**3**
Conception of the manuscript	X		
Preparation of the manuscript	X		
Correction of the manuscript		X	X
Supervision of H. Liu		X	
Proposed publication	0.5		

P2) H. Liu,[1] R. Trautwein,[2] B. Schröter,[3] A. Ignaszak,[4] W. Weigand,[5] S. Hoeppener,[6] U. S. Schubert[7]

"Micropatterns of [Fe-Fe]-hydrogenase active-site model complexes fabricated by electro-oxidative lithography"

Langmuir **2015**, *31*, 11748−11753.

Author	**1**	**2**	**3**	**4**	**5**	**6**	**7**
Conception of the manuscript	X				X	X	
Lithography and immobilization of [Fe-Fe]	X						
Synthesis of [Fe-Fe] complexes		X					
AFM measurements	X						
IR measurements	X						
AES measurements			X				
CV measurements				X			
Preparation of the manuscript	X						
Correction of the manuscript				X	X	X	X
Supervision of H. Liu						X	
Supervision of R. Trautwein					X		
Proposed publication equivalent	1						

P3) H. Liu,[1] A. M. Schwenke,[2] F. Kretschmer,[3] S. Hoeppener,[4] U. S. Schubert[5]

"Au nanoparticle cluster arrays for high-performance SERS substrates fabricated by electro-oxidative lithography"

ChemNanoMat. **2016**, DOI: 10.1002/cnma.201600063.

Author	**1**	**2**	**3**	**4**	**5**
Conception of the manuscript	X				
Lithography and preparation of Au cluster	X				
Preparation of Au nanoparticles			X		
AFM measurements	X				
SEM measurements		X			
TEM measurements				X	
SERS measurements	X				
Preparation of the manuscript	X				
Correction of the manuscript		X	X	X	X
Supervision of H. Liu				X	
Proposed publication	1				

P4) D. Meroni,[1]* H. Liu,[2]* S. Ardizzone,[3] U. S. Schubert,[4] S. Hoeppener[5]
"Extending the range of possible substrates for the electro-oxidation of *n*-Octadecyltrichlorosilane (OTS) self-assembled monolayers" (*equal contribution)
Submitted to *Nanotechnology*.

Author	**1**	**2**	**3**	**4**	**5**
Conception of the manuscript	X	X			X
Preparation of OTS monolayers		X			
Lithgraphy		X			
IR measurements		X			
AFM measurements		X			
Preparation of the manuscript	X	X			
Correction of the manuscript	X		X	X	X
Supervision of H. Liu					X
Supervision of D. Meroni			X		
Proposed publication equivalent		1			

P5) H. Liu,[1] S. Hoeppener,[2] U. S. Schubert[3]
"Site-specific surface functionalization of graphene via electro-oxidative lithography for bio-sensing applications"
ChemPhysChem 2016, DOI: 10.1002/cphc.201600490.

Author	**1**	**2**	**3**
Conception of the manuscript	X		
Preparation of OTS	X		
Lithography	X		
AFM measurements	X		
Raman and IR measurements	X		
Preparation of glucose	X		
Preparation of the manuscript	X		
Correction of the manuscript		X	X
Supervision of H. Liu		X	
Proposed publication	1		

P6) H. Liu,[1] S. Hoeppener,[2] U. S. Schubert[3] "Reversible nanopatterning on polypyrrole films by atomic force microscope electrochemical lithography" *Adv. Funct. Mater.* **2016**, *26,* 614–619.			
Author	**1**	**2**	**3**
Conception of the manuscript	X		
Lithography	X		
AFM measurements	X		
SEM measurements	X		
Preparation of the manuscript	X		
Correction of the manuscript		X	X
Supervision of H. Liu		X	
Proposed publication	1		

Erklärung zu den Eigenanteilen des Promovenden/der Promovendin sowie der weiteren Doktoranden/Doktorandinnen als Koautoren an den Publikationen und Zweitpublikationsrechten bei einer kumulativen Dissertation.

Für alle in dieser kumulativen Dissertation verwendeten Manuskripte liegen die notwendigen Genehmigungen der Verlage („Reprint permissions“) für die Zweitpublikation vor.
Die KoAutoren der in dieser kumulativen Dissertation verwendeten Manuskripte sind sowohl über die Nutzung, als auch über die oben angegebenen Eigenanteile informiert und stimmen dem zu.

He Liu Jena, den _____

Ich bin mit der Abfassung der Dissertation als publikationsbasiert, d.h. kumulativ, einverstanden und bestätige die vorstehenden Angaben. Eine entsprechend begründete Befürwortung mit Angabe des wissenschaftlichen Anteils des Doktoranden/der Doktorandin an den verwendeten Publikationen werde ich parallel an den Rat der Fakultät der Chemisch-Geowissenschaftlichen Fakultät richten.

Prof. Dr. Ulrich S. Schubert Jena, den _____

1. Introduction

In recent years, more and more new functional materials have been used in daily life, such as in the fields of electronics, optics, medicine, and energy.[1–4] The successful application of these new materials with novel properties frequently depends on their effective integration into frameworks at the micrometer or even at the nanometer scale.[5,6] For instance, patterning graphene into desirable structures with micro- or nanoscale dimensions is important for tuning the transport properties of the graphene devices.[7] Colloidal quantum dots are usually utilized for the fabrication of electrical and optical devices. Consequently, micro- and nanopatterning processes are required to form necessary structures.[8] For conventional patterning approaches, i.e., optical and electron beam lithography, there are major disadvantages for the processing steps, including high costs, the utilization of multiple manufacturing steps and the requirement of harsh environmental conditions like vacuum, strong acid or base solutions and high temperatures. Thus, developing new patterning approaches with high accuracy, low cost, and mild fabrication conditions is desired to foster further progress of material science, in particular in the field of nanotechnology. Among many other techniques, scanning probe lithography (SPL) represents a promising method which offers precise control with high lateral resolution (below 10 nm),[9,10] and the potential for low cost fabrication processes that can be performed under ambient conditions. In addition, the utilization of scanning probe microscopy (SPM) enables a direct investigation of the created structures by SPM imaging. For typical SPL processes, a tip is utilized for tailoring surface properties based on electrical, mechanical, and thermal interactions. Among these SPL approaches, electrically induced local electrochemical lithography is regarded as an attractive tool because the electric field applied between the tip and the substrates can induce different electrochemical reactions (**Figure 1.1**). Compared with the classical semiconductor structuring approaches, not only surface patterns with a high resolution can be obtained utilizing this method, but also many functional groups or even new materials can be created, which largely expand the number of potential applications.

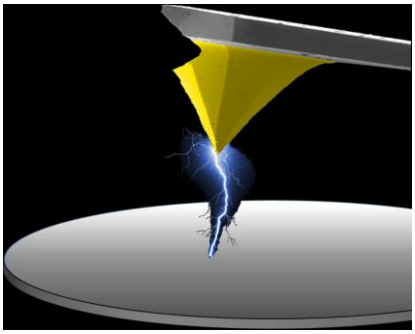

Figure 1.1 Schematic illustration of local electrochemical lithography based on a conductive tip.

The research field of electrically induced structuring of surfaces was introduced in 1990, when Dagata *et al*. first reported a local oxidative lithographic approach performed on a hydrogen-passivated silicon substrate by a scanning tunneling microscope (STM) tip. The obtained resolution of the written features reached 100 nm. Further measurements showed that oxygen was incorporated into the silicon surface during the lithographic process.[11] In 1993, Day and co-workers demonstrated the selective oxidation of silicon with a conductive atomic force microscopy (AFM) tip. Compared with STM lithography, a distinctive advantage of utilizing AFM is that the voltage applied between the tip and the substrate can be chosen independently of the feedback circuit, which enables to obtain an optimized voltage and a higher resolution lithography.[12] This improvement laid the foundation for the further development of local electrochemical lithography. To extend this technique from nanometer to micrometer or even millimeter dimensions, some parallel lithographic methods have been developed. For instance, Nishimura *et al*. prepared a AFM tip with a large contact area of 2.5 × 1.9 μm^2 and the resulting throughput is 10,000 times faster than that of conventional local electrochemical lithography based on a normal AFM tip.[13] Garcia and co-workers reported a simple way to upscale the local electrochemical lithography with an Au coated digital video disk (DVD) polymeric stamp. A nanostructured pattern with a millimeter scale was easily fabricated on silicon surfaces.[14] In the meanwhile, Sagiv and co-workers first demonstrated that a highly ordered 18-nonadecenyltrichlorosilane (NTS) monolayer can

be electrochemical oxidized by a conductive AFM tip. A line with functional carboxyl groups can be written on the NTS film.[15] The introduction of functional groups largely promoted the development of local electrochemical lithography, which provides more possibilities for the subsequent self-assembly processes or even chemical reactions.

The aim of this thesis is the preparation of functional micro- and nanopatterns by local electrochemical lithography. Different molecules and nanoparticles are self-assembled on the lithographic patterns to form functional systems and devices. In general, self-assembled monolayers (SAMs) are one of the most frequently used films for local electrochemical lithography. **Chapter 2** provides a detailed insight into the lithography performed on different SAMs, in particular, on OTS monolayers. The formed –COOH groups can be utilized as chemically active templates for the fabrication of various micro- and nanostructures after the lithographic process. **Chapter 3.1** demonstrates that [Fe-Fe]-hydrogenase active site model complexes ($[Fe(CO)_3]_2[(\mu\text{-}SCH_2)_2C(CH_2OH)_2]$) can be immobilized on micropatterned trichloro(octadecyl)silane (OTS) monolayers to form a microscale catalytic system. The complex molecules were selectively anchored in the patterned areas with good coverage. Moreover, the biomimetic metal centers of the hydrogenase model complex molecules still maintained their catalytic activity after the immobilization process, which was proven by cyclic voltammetry (CV) measurements. In **Chapter 3.2**, a highly efficient surface-enhanced Raman spectroscopy (SERS) substrate facilitating enhancement factors as high as $\sim 5\times10^6$ was fabricated by self-assembling Au nanoparticles onto dot pattern arrays of OTS monolayers. The electromagnetic field enhancement was obtained by both interparticle and intercluster plasmon coupling of the Au nanoparticles, which resulted in strong SERS signals. This effect was found to be strongly dependent on the intercluster spacing and a systematic study was conducted to elucidate this parameter. Silicon is the most common substrate for the local electrochemical lithography performed on OTS monolayers. **Chapter 4** is devoted to extending this lithographic process to other films. **Chapter 4.1** reports the functionalization of two technologically important substrates with OTS monolayers, i.e.,

titanium dioxide (TiO_2) and aluminum oxide (AlOx). Despite of the differences regarding the surface properties of these two substrates, good quality OTS monolayers were generated on both substrates by a careful adaptation of the deposition parameters. Afterwards, these OTS monolayer modified substrates could be further structured to create chemically active surface patterns. In **Chapter 4.2**, OTS monolayers were self-assembled on graphene layers. The mechanism of oxidation during the lithographic process was investigated. Not only the OTS was oxidized, but also the oxidation of graphene occurred, followed by the conversion of silicon to silicon oxide. As a consequence a system could be introduced that permits the chemical patterning as well as the possibility to locally modify the electronic properties of the underlying substrate. Additionally, a glucose sensor with a low detection limit was fabricated. **Chapter 4.3** describes the local electrochemical lithography performed on polypyrrole films doped with sodium dodecylbenzenesulfonate (PPy(DBS)) to obtain a memory nanodevice. Nanopatterns were formed by applying a bias voltage between a conductive AFM tip and the substrate. Afterwards, the generated nanopatterns could be erased completely, followed by rewriting at the same location of the polymer film. As such this thesis aims at the advancement of local electrochemical lithography with respect to the range of patternable substrates and targets the fabrication of functional devices, which are focused in the fields of energy, information storage, and sensors.

2. Local electrochemical lithography of self-assembled monolayers

Parts of this chapter have been published: P1) H. Liu, S. Hoeppener, U. S. Schubert, *Adv. Eng. Mater.* **2016**, *18*, 890−902.

Self-assembled monolayers (SAMs) have attracted strong attention since experimentally discovered in 1980.[16] The SAMs can be utilized in many fields of research and technology, such as, for the control of wetting and adhesion, biological engineering, sensors and micro- and nanofabrication.[17–20] The first SAMs which were utilized for local electrochemical lithography are NTS monolayers. As shown in **Figure 2.1**, the vinyl groups of NTS were oxidized to carboxyl groups during the lithographic process and could be further functionalized by self-assembly of other monolayers.[15] Afterwards, this lithographic technique was extended to a robust and chemically inert SAMs, i.e., OTS monolayers. The conductive tip induced the electrochemical conversion of the surface terminal $–CH_3$ groups of the OTS SAMs to –COOH groups.[21] The width of the generated patterns depends critically on the dimensions of the tip and the patterning conditions, including the applied voltage, the pulse duration, and the relative humidity, which defines the size of the formed water meniscus. In subsequent work, further investigations on the oxidative behavior of OTS monolayers on Si substrates were conducted. There are two main processes occurring during the electrochemical patterning: Firstly, the conversion of methyl groups of OTS to carboxyl groups, and secondly, the oxidation of the silicon substrate itself. The formation of carboxyl groups leads to a significant change in friction force, while the growth of silicon oxide can generate a distinct increase in height. Therefore, the time scales of these two competing oxidation processes could be determined through fiction force and height changes for different periods of oxidation times.[22,23]

In addition to NTS and OTS monolayers, other SAMs were utilized for a local electrochemical lithography as well. Yang and co-workers performed the local

electrochemical lithography on two different monolayers, i.e., a hexadecyl monolayer and an *N*-hydroxysuccinimide (NHS)-ester-functionalized undecyl (NHS-UA) monolayer. Compared with the oxidation conditions of OTS on silicon substrates, much milder conditions were required on both monolayers. Additionally, the generated carboxyl groups also provided the possibility for further pattern functionalization.[24] In addition to the commonly used SAMs, some more complicated monolayers can be used for this lithographic technique as well. For example, a mixed monolayer was prepared which consisted of propyltrichlorosilane and triethoxysilane derivatives featuring a redox-active trimethylbenzoquinone moiety. As shown in **Figure 2.2**, oxidative and reductive patterns can be fabricated on the same surface when a positive or a negative bias voltage was applied. Afterwards, pentathiophene dimethylchlorosilane and C_{60} molecules were assembled on the oxidized and reduced patterned areas, respectively. That means that both p-type and n-type materials can be assembled at the same time, which may enable the fabrication of complementary heterogeneous nanostructures.[25] When performing the lithography on SAMs which already contain functional head groups, both intrinsic and newly formed groups can be obtained using this approach, which may generate different functions simultaneously on the same substrate. For instance, Qin *et al*. prepared oligo(ethylene glycol) (OEG)-terminated alkyl monolayers on silicon substrates. In this case the conversion of ethylene glycol groups to carboxylic and aldehyde groups were induced by AFM oxidation lithography without substantial degradation of the OEG layer or oxidation of the silicon substrate. Highly protein-resistant surfaces and chemically active patterns can be obtained in this manner on the same Si substrate. Afterwards, biotinylated molecules and nanoparticles can be immobilized on the patterned areas.[26]

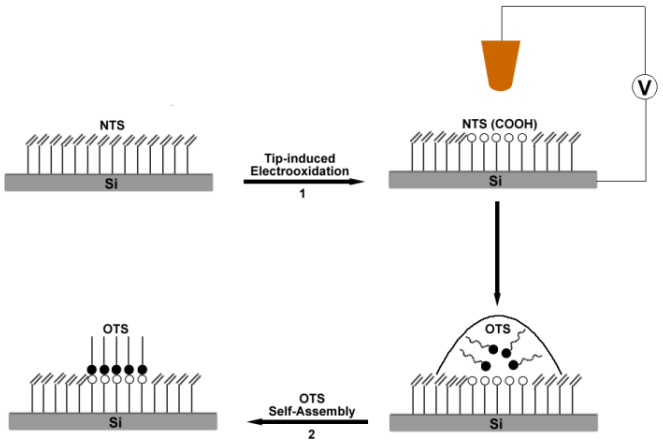

Figure 2.1 Schematic illustration of a two-step local electrochemical lithography and "development" process: 1) Tip-induced electro-oxidation of NTS monolayers and 2) site-selective self-assembly of OTS monolayers on the carboxyl groups. Reproduced with permission.[15] Copyright 1999, Wiley.

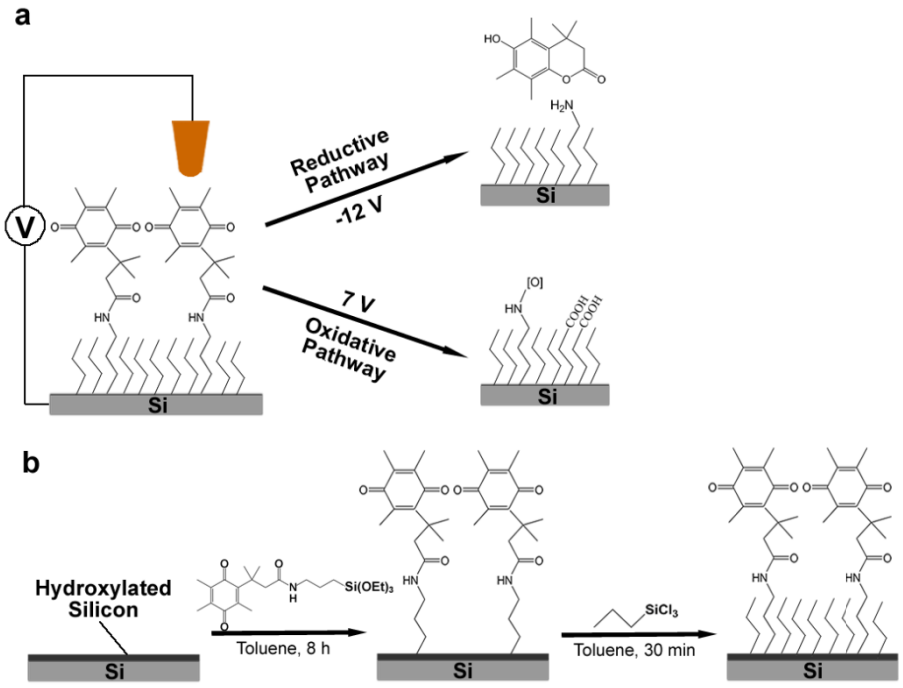

Figure 2.2 (a) Schematic view of local electrochemical lithography performed on a mixed monolayer with positive and negative bias voltage. (b) Route for synthesis of a mixed monolayer composed of benzoquinone and propyltrichlorosilane. Reproduced with permission.[25] Copyright 2010, American Chemical Society.

As mentioned above, after the lithographic process, the formed functional groups, i.e., –COOH groups or other hydrophilic groups on SAMs can be utilized as versatile chemically active patterns with micro- and nanometer dimentions. Many molecules, nanoparticles, and nano-objects can be self-assembled or even chemically grafted on the patterned areas. For instance, Chowdhury *et al*. demonstrated a new wetting driven self-assembly approach utilizing a patterned OTS monolayer as a template. First, some non-volatile low-melting organic materials were selectively immobilized onto the patterned areas due to the hydrophilic property of the carboxyl groups. Afterwards, silver or gold ions binding to these organic materials are able to form elemental metal nanoparticles in further chemical processing steps. This method can be extended to a variety of non-volatile materials with appropriate melting temperature and surface wetting characteristics to produce surface nanostructures.[27] Druzhinina and co-workers fabricated ring structures by local electrochemical lithography performed on OTS monolayers. Two different chemical pattern areas were obtained: The core area is composed by silicon oxide and a surrounding area forms an acid functionalized rim.[28] A bilayer structures can be obtained as well by assembly of a second OTS layer onto the –COOH groups. The tip induced lithography applied on the bilayer structure required significantly longer pulse durations to induce the formation of the desired –COOH groups. Applying this feature to the lithographic process, a gap with nanometer resolution was fabricated between the monolayer and the bilayer structures, where a nanoparticle was anchored by a self-assembled process. This combined approach may have broad applications for electrical sensors or single-electron transistors.[29] Functional molecules are also alternative choices for self-assembly processes on the patterned OTS films which may allow the utilization of a large variety of further chemical reactions. For example, bromo-undecyltrichlorosilane can be assembled to the carboxyl-terminated patterns, followed by the site-selective conversion into a generation of an azide terminated adlayer and subsequently performing the highly effective 1,3-dipolar cycloaddition reaction with acetylene functionalized molecules.[30] This bromine functionalized pattern can be used to prepare polymer brushes by atom transfer radical polymerization (ATRP) processes as

well.[31] As shown in **Figure 2.3**, it is worth pointing out that the approach to combine local electrochemical lithography and self-assembly of functional materials can be used in a wide range of fabrication processes to hierarchically prepare functional micro- and nano-devices.

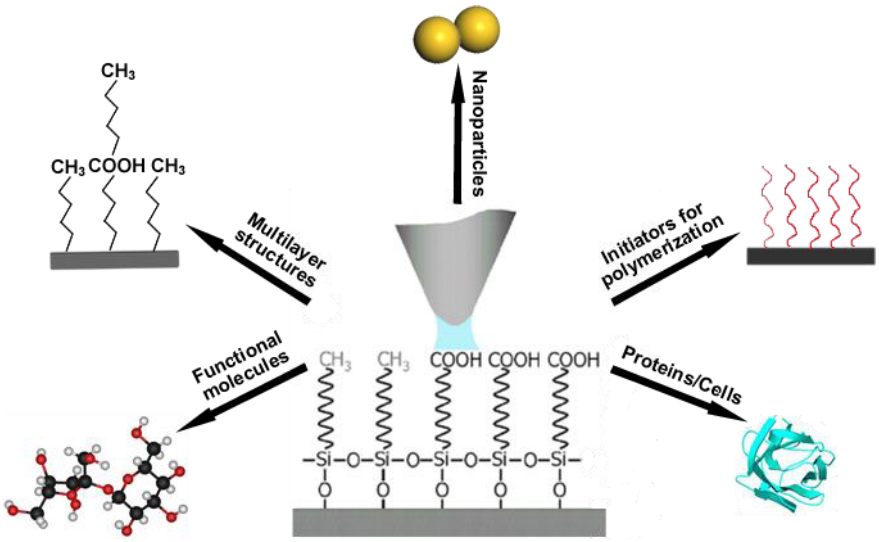

Figure 2.3 Overview of the possible functional materials which can be assembled on the patterned SAMs.

3. Self-assembly of functional materials on patterned OTS monolayers

Parts of this chapter have been published: P2) H. Liu, R. Trautwein, B. Schröter, A. Ignaszak, W. Weigand, S. Hoeppener, U. S. Schubert, *Langmuir* **2015**, *31*, 11748−11753. P3) H. Liu, A. M. Schwenke, F. Kretschmer, S. Hoeppener, U. S. Schubert, *ChemNanoMat*. **2016**, DOI: 10.1002/cnma.201600063.

As already introduced in Chapter 2, the methyl groups ($–CH_3$) of OTS monolayers can be oxidized to carboxyl groups (–COOH) by local electrochemical lithography, which enables further chemical modification steps. In this chapter, the self-assembly of functional molecules and nanoparticles on the patterned OTS films and potential applications of the formed structures will be summarized.

3.1 Micropatterns of [Fe-Fe]-hydrogenase active-site model complexes

Hydrogen is regarded as one of the best fuels for fuel cells.[32–34] In nature, hydrogen can be efficiently generated by hydrogenase enzymes, which catalyze the reversible redox reaction of dihydrogen ($H_2 \leftrightarrow 2H^+ + 2e^-$). The reversible catalytic reaction is accomplished by dithiolato-bridged [Fe-Fe]- or [Ni-Fe]-active sites of hydrogenase enzymes,[35] which also play a key role in the microbial energy metabolism.[36] In this chapter, [Fe-Fe]-hydrogenase active site model complexes ($[Fe(CO)_3]_2[(\mu\text{-}SCH_2)_2C(CH_2OH)_2]$) were grafted onto OTS micropatterns on a silicon substrate (OTS-Si). The two hydroxyl groups of the model complex are ideally suited to react with the carboxylic groups forming ester bonds, which enable a strong anchoring of the [Fe-Fe]-hydrogenase active-site model complexes ([Fe-Fe]) to the patterned areas.

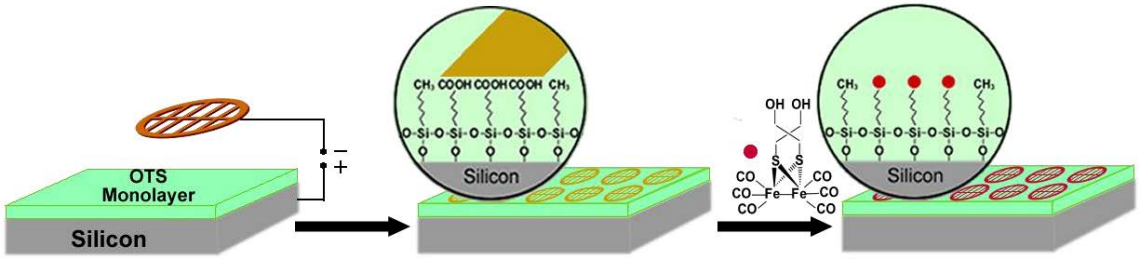

Scheme 3.1.1 Schematic representation of local electrochemical lithography based on a TEM grid and self-assembly of [Fe-Fe]-hydrogenase active site model complexes ([Fe-Fe]-Si).

The outline of the preparation sequence is schematically illustrated in **Scheme 3.1.1**. First, the micropatterns were prepared utilizing local electrochemical lithography based on a linear stripe TEM copper grid with a circle diameter of 3.05 mm. After the lithographic process, an optical micrograph of a water condensation micropattern of the grid structure could be observed (**Figure 3.1.1a**), indicating the successful oxidation of the monolayer. The water vapor is expected to condense in this case preferentially in the hydrophilic surface areas, i.e., the oxidized areas (corresponding to the dark regions in **Figure 3.1.1a**). Additionally, the friction force in the hydrophilic patterned regions is much stronger than that in the unmodified, hydrophobic OTS monolayer areas. Therefore, the grid patterns can be also directly observed by contact mode AFM investigations. **Figure 3.1.1b** shows a friction force picture of a stripe of the TEM grid pattern where the scanning direction was set from left to right. If the AFM tip was scanned from the opposite direction, a picture with inverse contrast was obtained (**Figure 3.1.1c**). This reversible friction change is a strong evidence that only negligible topographic alterations occurred during the lithographic process but a strong change of the surface properties, that is, a switch between hydrophobic and hydrophilic surface, is induced. That may suggest that –COOH groups were generated during the lithographic process. Afterwards, the microstructured substrate was utilized to selectively assemble [Fe-Fe] complex molecules via ester formation after the activation of the patterned substrate with dicyclohexylcarbodiimide/4-dimethylaminopyridine (DCC/DMAP). As shown in **Figure**

3.1.2a, after incubation the [Fe-Fe] complex molecules were selectively bound to the lithographic stripe areas. However, despite of a careful rinsing of the substrates after the reaction, some aggregates were formed on the surface as well. **Figure 3.1.2a** shows a higher magnification image of the patterned area. A large number of small particles was observed on the pattern areas with a good coverage.

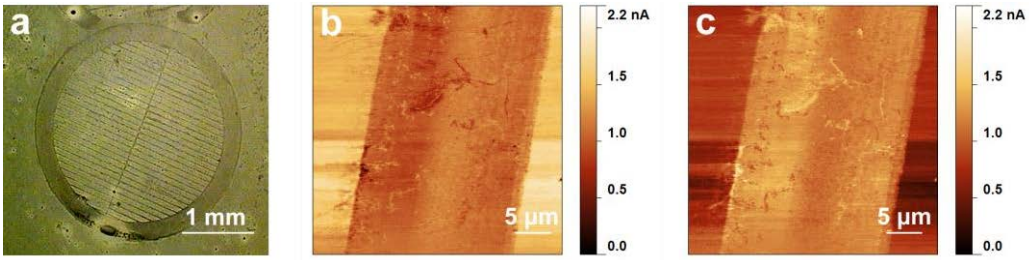

Figure 3.1.1 (a) An optical micrograph of a water condensation TEM grid pattern on an OTS monolayer. (b, c) Friction force images of a stripe of the printed TEM grid pattern. The scanning directions are set from left to right (b) and from right to left (c).

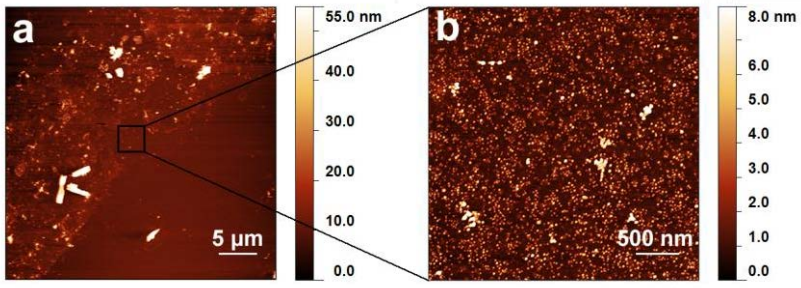

Figure 3.1.2 (a) Low and (b) high magnification tapping mode AFM images of [Fe-Fe] hydrogenase active site model complexes immobilized *in-situ* on the chemically active TEM grid pattern.

An additional evidence for the selective binding of the [Fe-Fe] model complexes on the patterned areas was obtained by means of Auger electron spectroscopy (AES). The locations of the micropatterns on the substrate were identified with a microscope and it was possible to perform measurements in the patterned areas as well as in the space between two stripes on the TEM grid pattern. As shown in **Figure 3.1.3a**, the signal

intensities of Fe and S in the strip area are much higher than those in the space area, which is a clear evidence for the successful binding of [Fe-Fe] model complex molecules on the micropatterned areas. In addition, a line scan approach was applied across the scan range which covered both a stripe and a space area. As shown in **Figure 3.1.3b**, in the beginning of the measurement (0 to 40 μm), the electron beam spot was focused on the space area and only low signal intensities were obtained for both Fe and S. As the electron beam spot reached the stripe area gradually, the signal intensities increased rapidly until the scanning position reached 70 μm. After the electron beam spot moved about 90 μm, the signal intensities decreased again, corresponding to the move of the electron beam back to the non-patterned area.

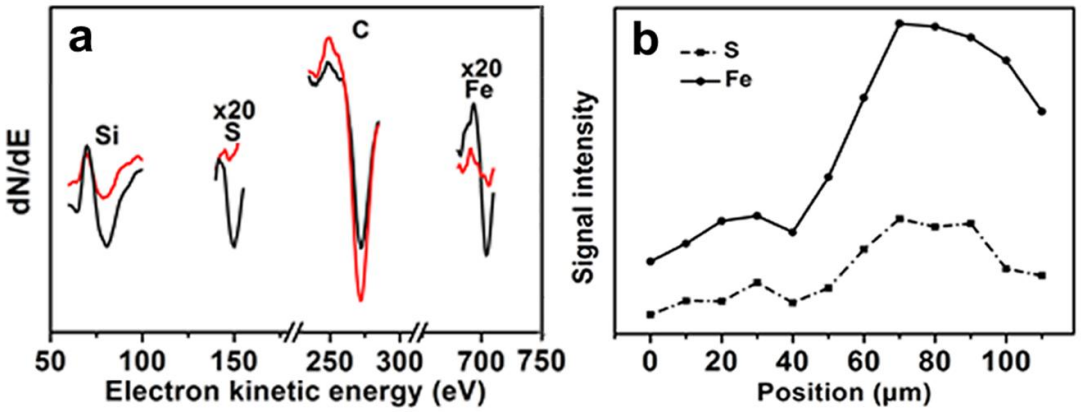

Figure 3.1.3 (a) AES spectra measured in a stripe area (black line) and the space between two stripes (red line) on a TEM grid micropattern. (b) Auger signal intensities of Fe and S at different locations of the micropattern obtained by a line scan approach.

Further evidence of the binding of the [Fe-Fe]-hydrogenase active site model complexes to the micropatterns is provided by FT-IR analysis. **Figure 3.1.4** shows the results obtained from investigations performed on the [Fe-Fe]-Si substrates and a control measurement performed on the pure powder of the complex. In both cases strong CO absorption peaks at 1050 to 1100 cm^{-1} are observed. The absorption at 1100 cm^{-1} in the spectrum of the patterned area is overlaid with the characteristic Si− O− C asymmetric

stretching vibration of the OTS molecules bound to the silicon wafer. The binding of the [Fe-Fe]-hydrogenase active site model molecules is furthermore confirmed by the appearance of a small absorption at 1760 cm^{-1}, which can be assigned to the ester bond formed between the carboxylic groups of the lithographic areas and the hydroxyl groups of the complexes. Because of the small absorption intensities, it is difficult to perform further investigations on the binding configuration. Moreover, a sharp absorption originating from the $-CH_2$ stretching vibrations was observed in the spectrum for the patterned substrate. These peaks belong to the well-packed functionalized OTS monolayer (and the monolayer on the backside of the silicon wafer), which indicate that the binding preparation process did not influence the quality of the monolayer. Moreover, an absorption belonging to the carboxylic acid is observed at 1790 cm^{-1}. This suggests that the [Fe-Fe]-hydrogenase active-site complexes do not form a dense coverage on the patterned areas. This is because not all the carboxylic acid groups can be bound by the complex molecules due to steric hindrances. This supports the AFM measurements, which also showed a noncomplete, granular functionalization of the patterned areas with complex molecules.

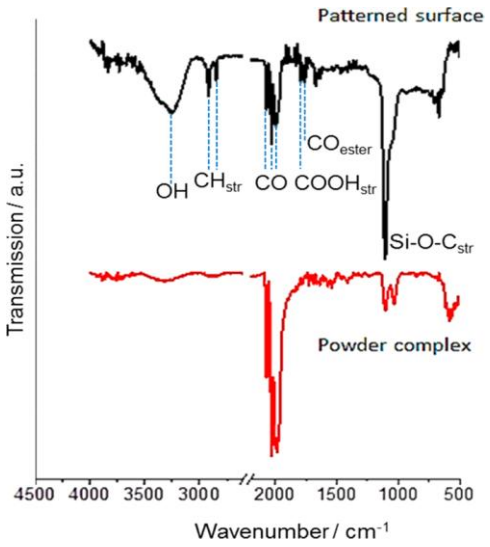

Figure 3.1.4 FT-IR spectra obtained from investigations on a micropatterned substrate (top) and on the powder of the complex (bottom). Spectra intensities are presented in arbitrary units and are not drawn to scale.

The catalytic activity of the [Fe-Fe] complex molecules on the micropatterns was further investigated by cyclic voltammetry (CV) measured in CH_3CN. As shown in **Figure 3.1.4a**, there are no obvious redox peaks for the micropatterned OTS-Si before the binding of the [Fe-Fe] complex molecules. However, in the case of [Fe-Fe]-Si, the CV curve displays one oxidation and two reduction processes. The irreversible anodic wave appears at +0.41 V measured against Fc/Fc^+. This wave represents the oxidation of Fe^IFe^I to $Fe^{II}Fe^{II}$. The observed value is slightly smaller compared to the value of the free complex (+0.67 V).[37] This is reasonable because in the present study the complex molecules are immobilized on a surface. The quasi-reversible and irreversible reduction waves are found at −1.51 V and −2.45 V, respectively. Compared with the observed CV curve, the reduction of the [Fe-Fe]-hydrogenase active site model complex in the solution phase showed the ability to take up two electrons at the same potential of −1.53 V (scan rate = 0.2 V/s) due to the phenomenon of potential inversion of the two one-electron reduction steps.[37] In addition, the CV measurement of the complex hmolecules in the solution phase showed another small reduction wave at −1.97 V (scan rate = 0.2 V/s), which was attributed to the reduction of products of follow-up reactions such as the loss of CO from the dianionic species of the complex.[37] In a similar process, for the [Fe-Fe] complex molecules which are bound on the OTS-Si, the first cathodic event observed at −1.51 V could arise from the two-electron reduction process, and the second reduction event (−2.45 V) occurs due to decomposition products. After adding acetic acid into the system, the current of the cathodic wave increases and the current intensity increases with increasing concentration of the acid (**Figure 3.1.4b**). These results are in agreement with the CV results obtained for the [Fe-Fe] complex molecules in solution, which indicates that an electrocatalytic proton reduction occurred during the measurement.[37,38] However, the current increase stopped after the acid concentration reached 0.6 mM, most probably because of a limited number of [Fe-Fe] complex molecules bound onto the micropatterns. According to the CV curve of [Fe-Fe]-Si, the coverage of immobilized [Fe-Fe] complex molecules can be estimated and the value is in the range of 0.002 mg cm^{-2}. On the basis of the CV results, it

can be concluded that the Fe-S active sites of the [Fe-Fe] complex molecules maintained their catalytic abilities after anchoring to the OTS-Si substrate.

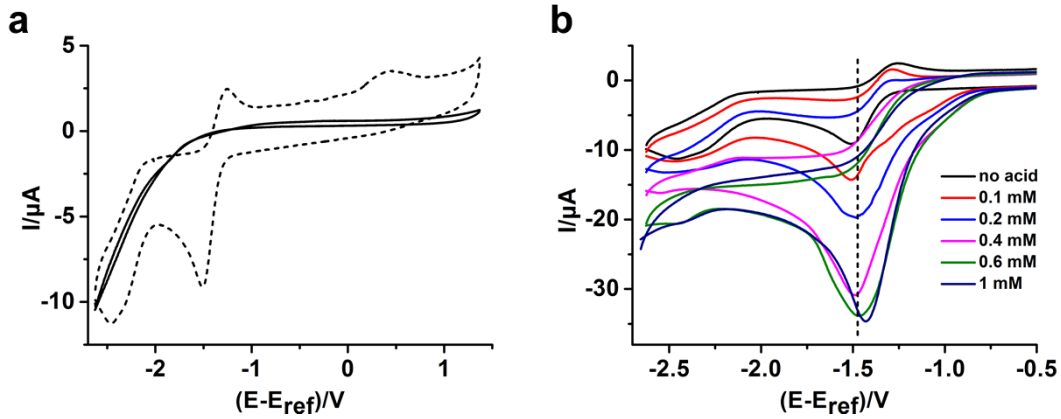

Figure 3.1.4 (a) CV curves of a micropatterned OTS-Si without [Fe-Fe] complexes (solid line) and a [Fe-Fe]-Si (dashed line). (b) CV results of a [Fe-Fe]-Si measured at various concentrations of AcOH.

In conclusion, a microscale catalytic system was fabricated by grafting the [Fe-Fe]-hydrogenase active site model complexes onto the OTS micropatterns. The CV results prove that the biomimetic Fe-S centers of [Fe-Fe] complex molecules still keep their catalytic activity and their redox behavior after the incubation processes. This post-attachment approach of micro-patterned Si substrates with [FeFe] complexes offers promising prospects for the preparation of micro H_2 fuel cells and biohybrid surface functionalizations.

3.2 Au nanoparticle cluster arrays

Besides functional molecules, nanoparticles can be assembled on the lithographic patterns as well. In this chapter, Au nanoparticles were self-assembled on the patterned OTS monolayers to form cluster arrays. Strong and reproducible surface-enhanced Raman spectroscopy (SERS) signals were obtained by both, interparticle and intercluster plasmon coupling of Au nanoparticles.

To obtain a positively charged surface structure, the patterned substrate was first immersed into a (3-aminopropyl)-trimethoxysilane (APTMS) solution. An APTMS film was site-selectively self-assembled on the lithographic areas by the formation of hydrogen bonds between the acid groups and the silanol groups of the APTMS.[29,39] Afterwards, sodium citrate stabilized Au nanoparticles were bound onto the positively charged dot sites based on an electrostatically guided self-assembly process. SEM images (**Figure 3.2.1a-g**) show the obtained Au nanoparticle cluster arrays with different gap distances. Two dimensional nanoparticle clusters which consist of many individual Au nanoparticles were spatially confined by the dot array templates. The gap distances between two neighboring clusters were changed from 30 to 400 nm by the lithographic process. It is difficult to decrease significantly the gap distance below 30 nm, because at very small distances the neighboring clusters tend to fuse and link together, which can be observed in **Figure 3.2.1a** (upper right corner). For each cluster, an aggregation of approximately 20 to 30 Au nanoparticles was observed. As shown in the TEM image (**Figure 3.2.1i**), the diameter of the individual Au nanoparticles is in the range of 10 to 15 nm and the distance between individual Au nanoparticles within each cluster is less than 5 nm (**Figure 3.2.1h**). These small distances are required for utilizing the plasmon coupling, which is beneficial for the formation of high signal intensities in the SERS measurements.[40,41]

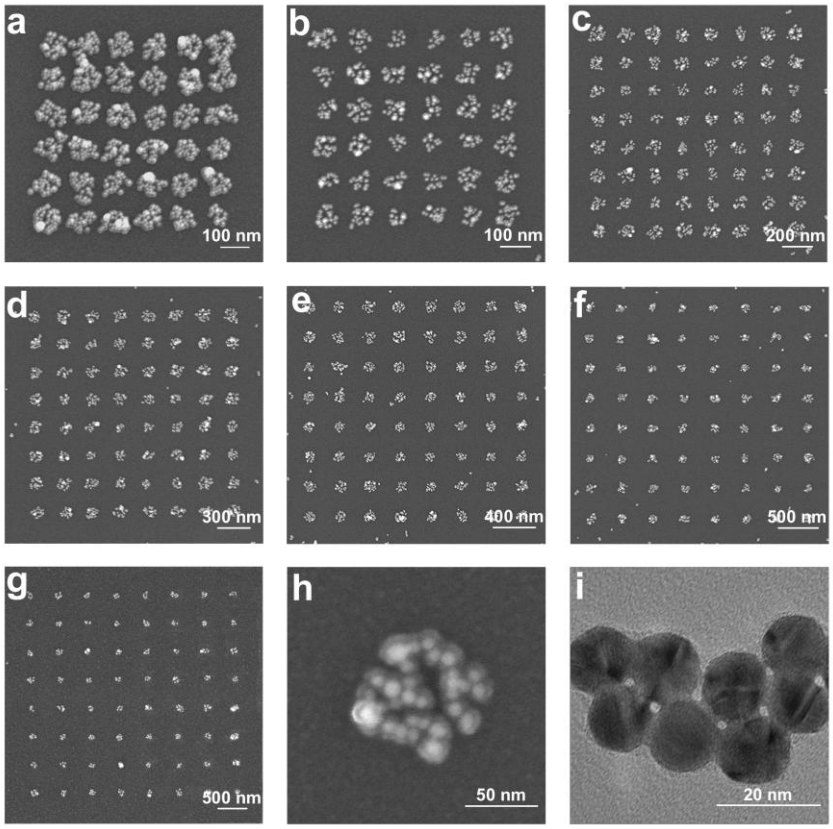

Figure 3.2.1 SEM images of Au nanoparticle cluster arrays with different gap distances: (a) 30 nm, (b) 50 nm, (c) 100 nm, (d) 150 nm, (e) 200 nm, (f) 300 nm, and (g) 400 nm. (h) A SEM picture of an individual cluster. (i) A HR-TEM image of Au nanoparticles.

The performance of the fabricated structures for the SERS measurements was investigated by benzenethiol (BT) molecules because of their efficient binding onto the Au nanoparticle surface by the formation of Au-S bonds.[42,43] **Figure 3.2.2a** shows the obtained SERS spectra of BT molecules on the patterned substrates with different lateral distances of the nanoparticle clusters. The most intense peak at 1565 cm^{-1} was chosen for comparison and to calculate the SERS enhancement factors (EF) of different samples. The EF is calculated as the formula of $\mathbf{EF} = (I_{substrate} / I_{reference}) \times (N_{reference} / N_{substrate})$, where $I_{substrate}$ and $I_{reference}$ are the peak intensities at 1565 cm^{-1} of the SERS substrate and the liquid neat benzenethiol (BT), respectively. $N_{reference}$ and $N_{substrate}$ are the numbers of BT molecules in the focal region of the laser illumination and on the SERS substrate within the laser spot, respectively. For the ease of calculation, we assume that the BT molecules

are uniformly adsorbed on the Au nanoparticle surface in a monolayer-like fashion.[44] As shown in the spectra, the SERS signals strongly increase with decreasing the gap distance between two neighboring clusters. **Figure 3.2.2b** shows that at a very small gap distance (30 nm), the enhancement factor reaches values as high as ~5×10^6. This values decrease quickly with the gap distance increasing and reach a constant level at a gap distance of ~200 nm. The obtained high EF values are attributed to be superposition of two types of the plasmon coupling: Firstly, within each individual cluster, the distance between the Au nanoparticles is less than 5 nm, which will induce a strong enhancement of the incident electromagnetic field by interparticle plasmon coupling. This contribution is present in all samples and its value is reflected by the plateau of the EF value of large cluster separations. Secondly, the enhanced electromagnetic field can be further amplified by the coupling between the neighboring clusters, i.e., by intercluster plasmon coupling.[45,46] In the present study, the intercluster plasmon coupling becomes very weak when the distance is larger than 200 nm, which induces a relatively low and constant EF value that is generated only by the interparticle plasmon coupling.

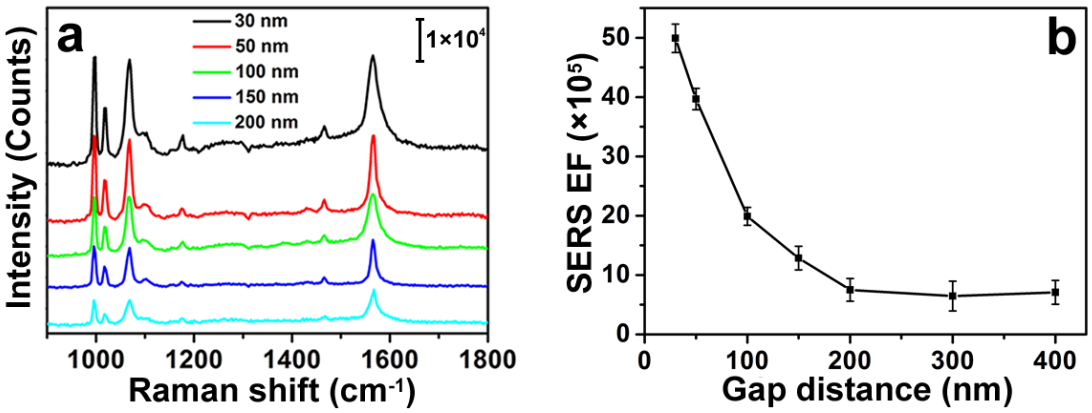

Figure 3.2.2 (a) SERS spectra of benzenethiol (BT) molecules and (b) the calculated enhancement factors (EF) measured the SERS substrates with different gap distances.

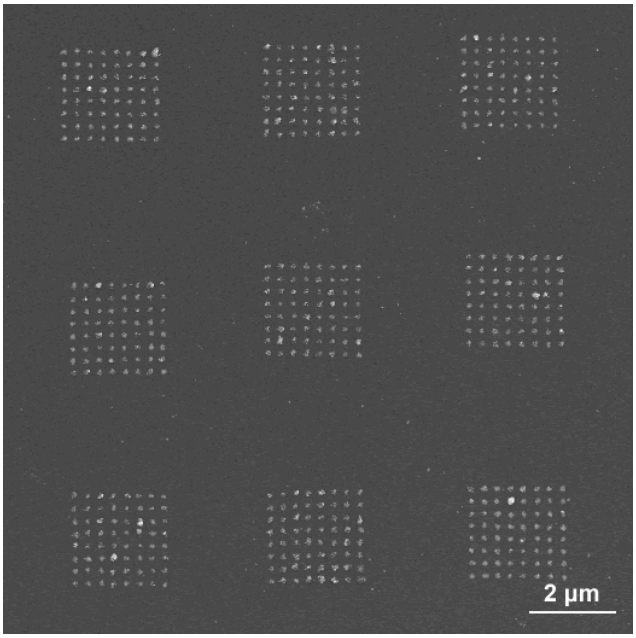

Figure 3.2.3 SEM image of a SERS substrate with nine individual cluster array patterns (gap distance: 150 nm). In this study similar arrays were fabricated for all gap distances to investigate the reproducibility of the SERS signals.

In addition to obtain a high EF value, another important SERS performance parameter is the reproducibility. Here, the EF reproducibility was tested by investigating the standard deviation of the EF values obtained from nine cluster array patterns with the same gap distance prepared on one substrate (an example is displayed in **Figure 3.2.3**). As shown in **Figure 3.2.4**, the SERS substrate with a gap distance of 30 nm shows a good reproducibility of the EF value and the standard deviation value is only 5%. In contrast, SERS measurements of a non-patterned substrate of the same Au nanoparticles were performed. In the case of the non-patterned substrate, only a relatively low EF value was observed, because the distance between neighboring Au nanoparticles is usually larger than 10 nm which is too large to create a strong interparticle coupling. Although some particle aggregates are formed (**Figure 3.2.5**) they are much smaller than the cluster structures formed on the patterned SERS substrates. Therefore, these particle aggregates are not suitable to induce a strong plasmon coupling for the SERS enhancement. In

addition, the standard deviation of the EF value for the non-patterned substrate is much larger (32%), which is a consequence of the random distribution of the Au nanoparticles.

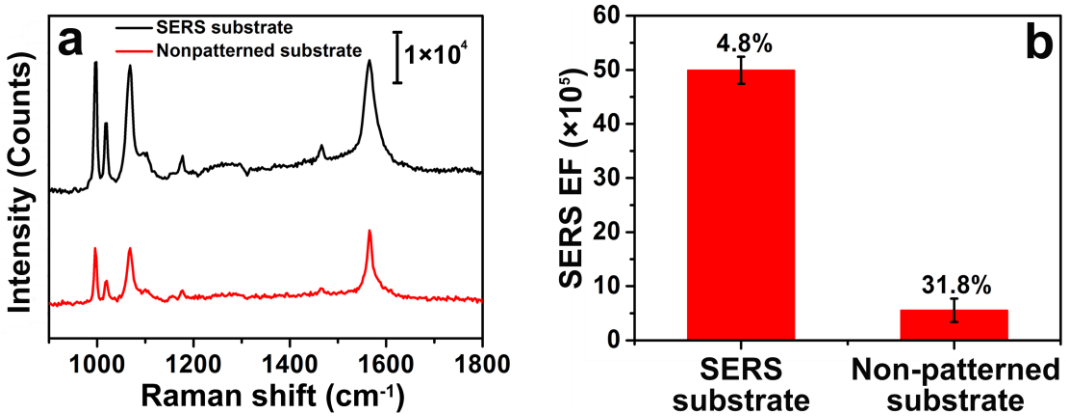

Figure 3.2.4 (a) SERS spectra and (b) corresponding enhancement factors (EF) of the SERS substrate with a gap distance of 30 nm and the non-patterned Au nanoparticle substrate. The error bars indicate the standard deviation as percentage of the mean EF value from nine cluster array patterns with the same gap distance.

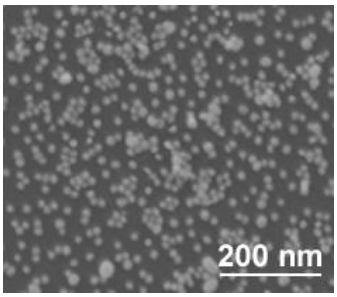

Figure 3.2.5 SEM picture of a non-patterned Au nanoparticle substrate.

The examples summarized in this chapter demonstrate the possibility to hierarchically fabricate functional surface structures based on local electrochemical lithography by utilizing molecules and nanoparticles. In the next chapter the applicability of the patterning process is extended to other substrates beside the Si substrates used in this chapter.

4. Extending of the range of substrates suitable for local electrochemical lithography

Parts of this chapter have been and will be published: P4) D. Meroni, H. Liu, S. Ardizzone, U. S. Schubert, S. Hoeppener, submitted to *Nanotechnology*. P5) H. Liu, S. Hoeppener, U. S. Schubert, *ChemPhysChem* **2016**, DOI: 10.1002/cphc.201600490. P6) H. Liu, S. Hoeppener, U. S. Schubert, *Adv. Funct. Mater.* **2016**, *26,* 614–619.

Silicon is the most frequently used substrate for local electrochemical lithography. However, other substrates can be utilized for this technique as well. In this chapter, several technologically important materials are investigated for the lithographic process, including AlOx, TiO_2, graphene, and polypyrrole doped with sodium dodecylbenzenesulfonate (PPy(DBS)). The extention of the range of substrates can enlarge the scope of applications of local electrochemical lithography.

4.1 TiO_2 and AlOx

Local electrochemical lithography represents a powerful tool for the patterning of SAMs, in particular of OTS monolayers. Commonly used substrates are SiOx and ITO. Here, two additional important substrates, i.e., titanium dioxide (TiO_2) and aluminum oxide (AlOx) substrates were investigated for their abilities to be structured by local electrochemical lithography. Moreover, a comparative study was conducted which indicated the differences in the preparation of OTS monolayers on SiOx, ITO, TiOx, and AlOx substrates as well as in their utilization and electrochemical characterization as substrates for the lithographic process.

For local electrochemical lithography based on a conductive AFM tip, one of the essential factors is the availability of smooth substrates. Si wafers and ITO substrates are commercially available in a good quality. TiO_2 and AlOx substrates have to be

custom-made. TiO_2 layers were prepared on either glass or commercial ITO substrates by calcination of spin coated titanium sol films, which form homogeneous surfaces with a relatively small surface roughness. AlOx substrates were prepared by coating of an evaporated Al film deposited onto a mica substrate. The native oxide layer can be formed by additionally O_2 plasma treatment. To handle the flexible films conveniently, a silicon support was used to stabilize them. OTS monolayers were prepared for all substrates by a dip coating process in a bicyclohexyl (BCH) solution. The immersion time was found to be rather different for the individual substrate materials. The typical required immersion times are listed in **Figure 4.1.1** as well as the characteristic properties of the formed monolayers. Silicon substrates required the shortest preparation time, whereas ITO, AlOx and TiO_2 required relatively long assembly times to obtain reasonable OTS monolayers. Only based on water contact angle measurements the quality of the monolayers is difficult to assess, because even slight differences in the surface roughness might have a considerable influence as well. Hence, the monolayers were additionally evaluated by the application of AFM and FT-IR investigations. If an orderly packed OTS monolayer was formed on the surface, the wavenumber of the $^{-}CH_2$ stretching vibrations should be 2918 cm^{-1} or even less.[47] As shown in figure AlOx displays the best monolayer quality. The degree of order the OTS molecules of TiO_2 and ITO is slightly lower compared to AlOx and SiOx, which is indicated by their higher wavenumbers of the $^{-}CH_2$ stretching vibrations.

	Silicon / Silicon oxide	ITO	TiO_2	AlO_x
Immersion time	< 1 min	5 to 10 min	10 to 15 min up to 1 h	5 min
Water contact angle	107° ± 1°	108° ± 1°	105° ± 2°	104° ± 2°
FT-IR CH_2 positions / cm^{-1}	2918 / 2850	2922 / 2852	2919 / 2850	2916 / 2849
Tapping mode topography	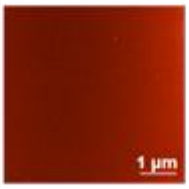	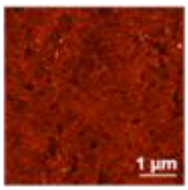	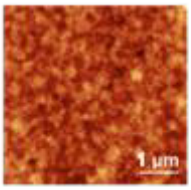	

Figure 4.1.1 Summary of the parameters and characteristic properties of OTS monolayers prepared on different substrates.

For the lithographic processes on these OTS functionalized silicon/silicon oxide, ITO, TiO_2 and AlOx substrates, negative bias voltage pulses were applied to the tip in vector or spectroscopy mode. Detailed studies of the lithographic behavior have up to now only be reported for OTS monolayer on SiOx and ITO substrates.[29,48] Hence, a comparative study was performed to investigate the differences of the oxidation characteristics also on the other substrates. The required oxidation conditions to obtain patterned surfaces are summarized in **Figure 4.1.2**. A range of oxidation times is reported for each substrate, which defines a plateau region where the patterning results stay more or less constant, as previously reported in the literature for OTS-Si systems.[29] It can be clearly seen that different oxidation conditions are required for different OTS functionalized substrates. In particular the oxidation time and bias voltages show strong variations. The oxidation times of OTS-Si are very short (5 to 10 ms), while ITO and AlOx substrates require longer oxidation times (10 to 60 ms). For OTS-TiO_2, oxidation times as long as 90 ms are necessary to obtain lithographic features. In general, high electrical currents will result in the decomposition of the water meniscus between the tip and the substrate. Therefore, for the highly conductive substrates ITO and AlOx a Si spacer was inserted in the setup acting as a resistor to decrease the electron transport between the tip and the substrate.[49]

On the other hand, lithography on SiOx and TiO_2, were performed without additional resistors. The relative humidity is another parameter to be considered during the lithographic process. In the case of ITO, lithography could be successfully performed by working at a high relative humidity. The situation is different for the OTS-TiO_2 and OTS-AlOx samples since the lithography could be performed at relative low humidity conditions (45 to 55%). That suggests the relative humidity represents a less crucial parameter for these two substrates.

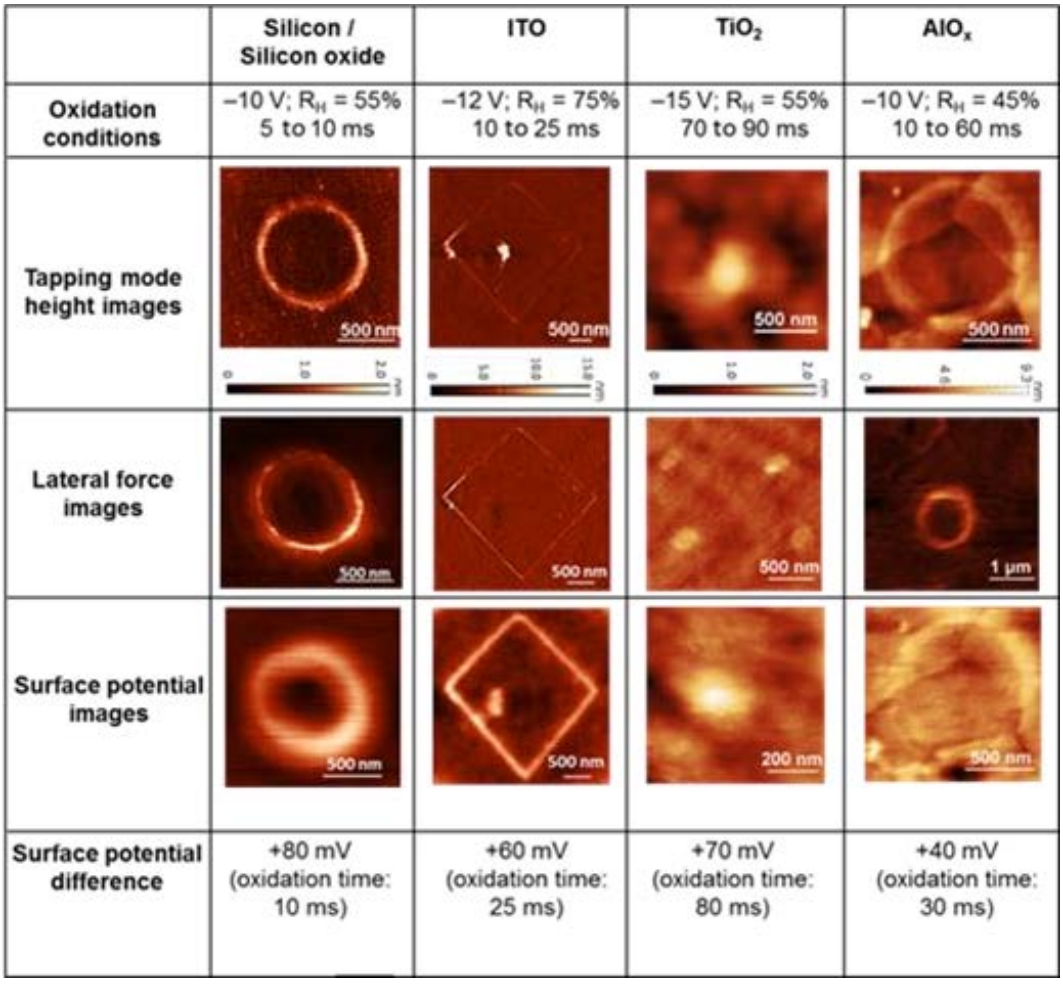

Figure 4.1.2 Comparison of the lithographic processes on different OTS modified substrates.

To make sure that the formed structures are caused by the functionalization of the OTS monolayer and are not resulting from the degradation of the monolayer and/or an

associated phase transition of the underlying substrates, oxidative lithography was also performed on the bare substrates. Scanning Kelvin probe microscopy (SKPM) was utilized for measuring the surface potential during the lithographic process, which is mainly influenced by the chemical changes on the surface. As previously reported, for silicon/silicon oxide substrates elevated structures of oxide were formed after the lithographic process. No obvious differences in the surface potential were observed on the bare substrates of ITO, AlOx and SiOx, which is due to the fact that the anodized features and the substrates consist of the same material (**Figure 4.1.3a, c**).[49] In the case of TiO_2, no significant change of the surface potential could be obtained. However, elevated topographical structures could not to be observed in tapping mode AFM as well for this substrate (**Figure 4.1.3b, d**). This can be explained by the fact that the TiO_2 was prepared by a sol-gel process, which means a bulk oxide phase has already formed on the surface. Conversely, the other substrates are just covered by a thin native oxide layer. As another evidence for the successful functionalization of OTS monolayers, the growth of silver nanoparticles on the patterned structures was tested. The chemical active patterns which contain carboxyl groups can be loaded with Au ions, followed by the reduction with hydrazine or hydrogen peroxide vapor. The formed small nanoparticles can be increased in size by means of a silver enhancer solution to enlarge the particle size. As shown in **Figure 4.1.4**, the silver nanoparticles are selectively immobilized on the patterned areas of ITO, TiO_2, and AlOx substrates, which represent an additional proof for the successful patterning of all OTS modified substrates.

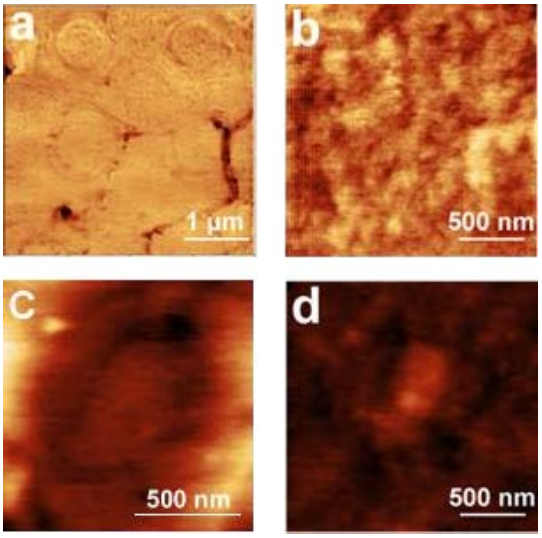

Figure 4.1.3 (a, b) Lateral force and (c, d) surface potential images of AlOx and TiO_2 after the lithographic processes.

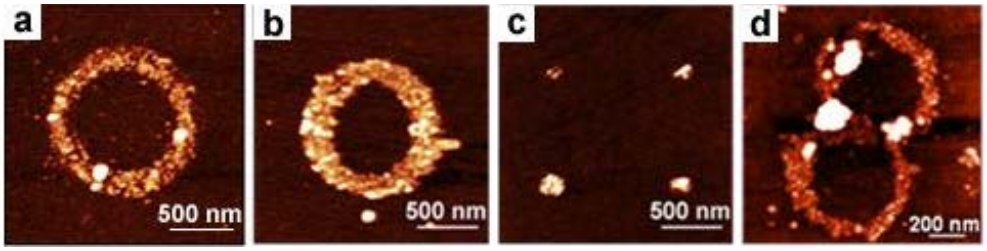

Figure 4.1.4 AFM images of silver nanoparticle patterns on a) SiOx, b) AlOx, c) TiO_2, and d) ITO substrates.

In this study, two new technologically important substrates, i.e., AlOx and TiO_2, were tested for local electrochemical lithography. Similar to SiOx and ITO, AlOx and TiO_2 substrates are suitable for this lithographic technique. Chemically active patterns functionalized with carboxyl groups can be obtained during the lithographic process, which can be used for further processing.

4.2 Graphene

In addition to conventional metal and semiconducting materials, another highly interesting substrate is graphene, which was also investigated for local electrochemical lithography approach. This two-dimensional sp^2 carbon network material has been actively investigated as a building block for the applications of various electronic devices, due to its exceptionally high conductivity and carrier mobility.[50–52] Similar to silicon-based materials in microelectronic processing, lithographic patterning represents an essential step for the fabrication of graphene devices.[53] In this chapter, a new direct-write method by local electrochemical lithography performed on graphene layers is reported. A chemically active pattern was obtained on the OTS modified graphene oxide (GO) surface and, additionally, the electronic property of the underlying graphene layers can be manipulated.

The outline of the performed modification steps is schematically illustrated in **Scheme 4.2.1**. GO can be dispersed well in aqueous solutions due to the polar oxygenous groups on the surface. Moreover, these groups can be further utilized for the modification of the GO by chemical reactions, such as the self-assembly of long alkyl silane chains.[54,55] To test the presented functionalization sequence, a silicon substrate is cleaned by Ar plasma treatment, followed by coating with a layer of APTMS molecules. The amine groups of the APTMS can act as an efficient adhesion promotor for the assembly of graphene oxide onto the wafer. Afterwards, OTS is self-assembled (OTS-GO) on top of the GO, utilizing the oxygenous groups of the GO as binding sites for the OTS network.

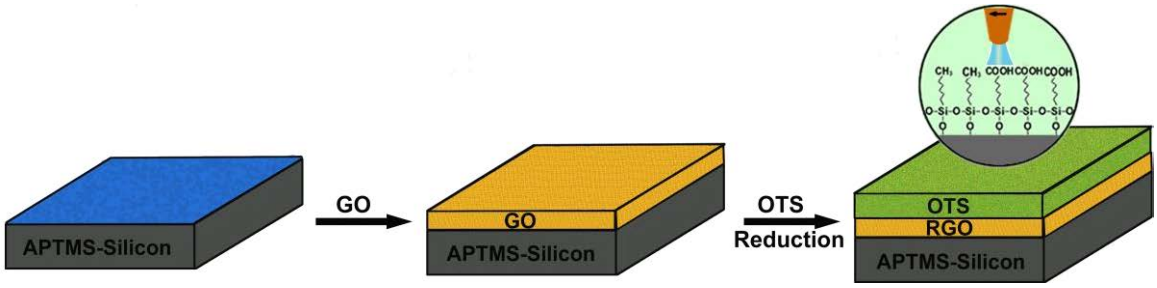

Scheme 4.2.1 Schematic illustration of the preparation of the OTS-GO films and the local electrochemical lithographic process on OTS-RGO films.

Each functionalization step can be investigated by means of water contact angle (WCA) measurements, FT-IR investigations and morphological studies performed by AFM. While the silicon wafer after the plasma cleaning treatment shows a typical water contact angle of <5°, after grafting the APTMS layer the water contact angle increases to 58 ± 3°. The value slightly decreases to 45 ± 4° after the immobilization of GO (GO-APTMS), due to the presence of the oxygeneous groups on the GO surface. As displayed in **Figure 4.2.1b**, a discontinuous film of individual GO sheets with a thickness of ~1 nm was attached onto the APTMS modified surface. After the assembly of OTS molecules (OTS-GO), the contact angle of the substrate increased significantly to approximately 98 ± 3°. This value is much higher than that of GO-APTMS, but still lower than that of a compact OTS monolayer (110 ± 3°).[56] This can be explained by the fact that only a discontinuous film of GO was assembled on the substrate surface. All these observations were further proven by FT-IR spectroscopy, i.e., by the analysis of the $^{-}CH_2$ stretching vibrations. The peaks are not observable for the APTMS-GO substrates, since the signal intensities which belong to the propyl groups of the APTMS molecules are too weak. However, after the self-assembly of the OTS monolayer, the $^{-}CH_2$ vibrations are observable and the corresponding peaks are located at 2918 and 2850 cm^{-1}, respectively (**Figure 4.2.2a**). The positions of these peaks reveal that a well-organized OTS monolayer was formed on the GO sheets. Additionally, as depicted in **Figure 4.2.2c**, the AFM measurements show the formation of a smooth OTS monolayer morphology with a root mean square (RMS) roughness of 0.77 nm.

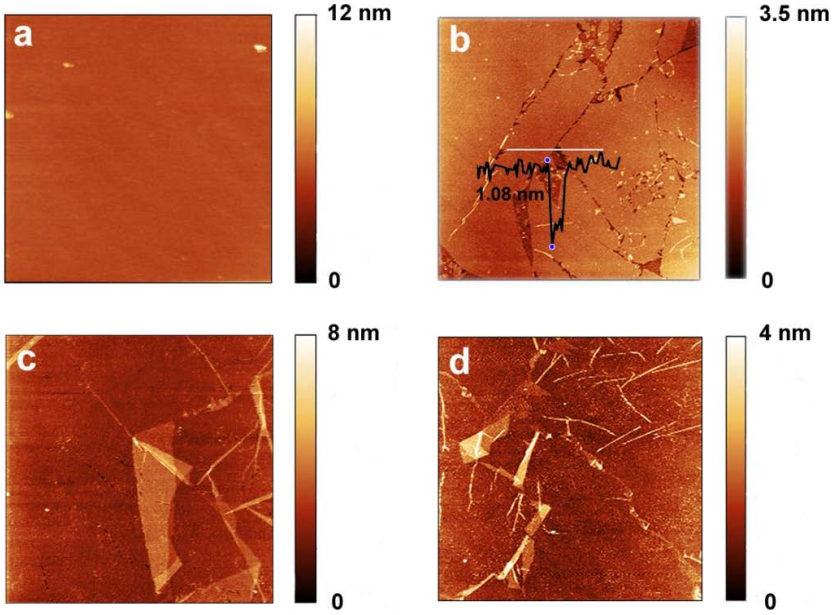

Figure 4.2.1 AFM topography images of (a) APTMS, (b) GO-APTMS, (c) OTS-GO, and (d) OTS-RGO films. The area for the image is always 5 µm × 5 µm.

The graphene oxide can be reduced by an additional heating step. The OTS-GO substrate was heating to 200 °C under a protective N_2 atmosphere for 2 h.[57,58] Despite the elevated temperatures, the contact angle of the obtained substrate (OTS-RGO) did not significantly decrease after the reduction step (97 ± 3°). As depicted in the FT-IR spectra, the peaks of the $^{-}CH_2$ stretching vibrations only shifted slightly towards higher wavenumbers. Although the AFM investigations show a more disordered OTS film structure formed in the surface, only a small increase in the surface roughness (RMS roughness: 1.02 nm) was observed (**Figure 4.2.1d**). That means that a reasonably homogeneous film with a low surface roughness was preserved after the thermal annealing step. The advantage of this reduction step is that the relatively low heat-treatment temperatures of 200 °C can avoid the destruction of the OTS monolayer and, moreover, will prevent the splitting of the GO sheets into smaller domains.[58] Raman spectra of OTS-GO and OTS-RGO are displayed in **Figure 4.2.2b**. The curves show two prominent peaks at 1346 and 1600 cm^{-1} relating to the D and G modes of the graphene, respectively. The G mode is corresponding to the vibration of sp^2-hybridized carbon and the D mode relates to

sp^3-hybridized carbon.[57,58] The ratio of I_d/I_g is corresponding to the electronic structure of GO/RGO. This value decreased from 1.50 to 1.16 after the heating process, which means that a large part of the GO was reduced to RGO. Another evidence for the successful reduction of GO was obtained by sheet resistance measurements. The resistance value decreased from 9740 ± 25 to 67 ± 3 Ω/sq after heat treatment. These experiments prove that conductive RGO layers can be generated which are still covered by a reasonably well ordered OTS monolayer (**Figure 4.2.1a**).

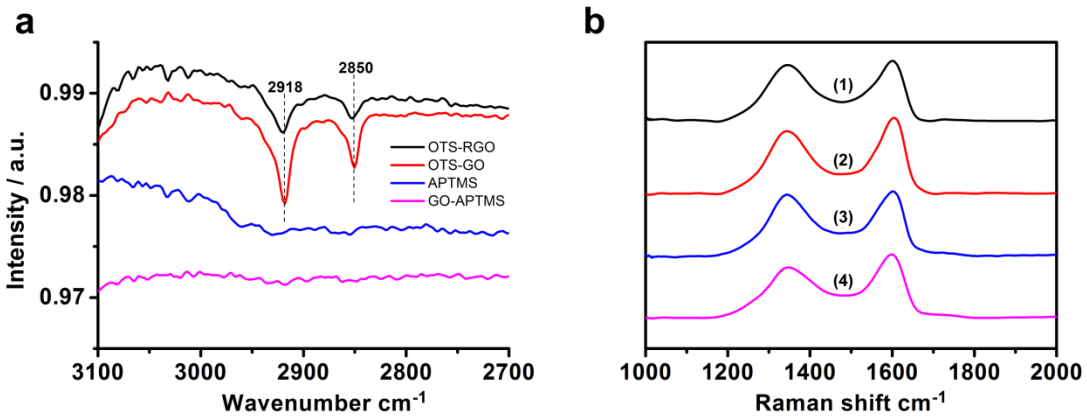

Figure 4.2.2 (a) FTIR spectra of different substrates; (b) Raman spectra of OTS-GO (1), OTS-RGO (2), lithographic square areas before (3) and after heating reduction (4).

After the preparation of the OTS-RGO films, the lithographic process was performed utilizing a conductive AFM tip. As shown in **Figure 4.2.3a**, a ring structure was obtained after the lithography. An associated height increase of ~1.5 nm in the patterned areas was observed by tapping mode AFM investigations. The height increase is caused by the fact that the oxidation of the RGO or even the oxidation of the silicon substrate itself occurred during the lithographic process. To investigate this issue in more detail, micro-Raman investigations (**Figure 4.2.2b**) of a lithographic square area (**Figure 4.2.3b**) were performed. The characteristic ratio of intensities of the D and G bands (I_d/I_g) was 1.46, which is close to the value of the GO before the thermal reduction. These findings indicate that both OTS monolayers and the underling RGO were oxidized after the lithography. Afterwards the substrate can be thermally reduced again utilizing the same

heating process as mentioned above. The reduction was confirmed by micro-Raman investigations. The ratio of I_d/I_g decreased to 1.19 again which was close to the value of OTS-RGO before the lithography (**Figure 4.2.2b**).

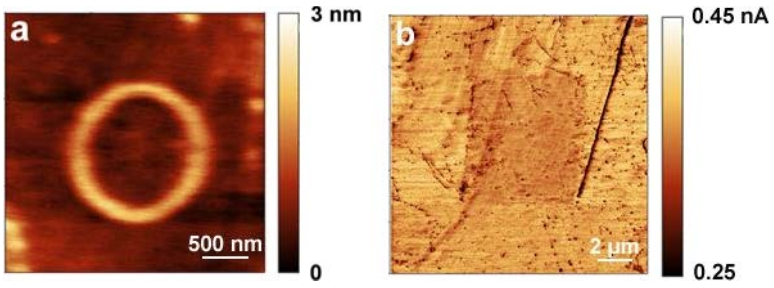

Figure 4.2.3 (a) **A** height image of a ring structure on the OTS-RGO substrate. (b) A lateral force image of a square pattern.

To obtain more insights of the lithographic process, scanning Kelvin probe microscopy (SKPM) was utilized for investigating the details of the lithographic process. The surface potential is mainly influenced by the chemical changes on the surface. **Figure 4.2.4a** shows the surface potential map of an oxidized circle structure and the value increased by ~25 mV in the patterned area (**Figure 4.2.4b**). This increase is in agreement with the lithography performed on OTS-Si substrates.[59] In addition to the chemical modification, a strong change of conductivity is observed in the lithographic areas as well due to the oxidation of the RGO. As shown in the current image (**Figure 4.2.4c**), the current decreases in the oxidized areas indicated the re-oxidation of the RGO, which can also be observed in the previously discussed micro-Raman investigations. However, it has to be mentioned that the drop in conductivity could be also related to the growth of the silicon oxide at the monolayer-Si interface. To further investigate this issue, detailed measurements of the lithographic oxidative process were performed by inscribing a set of dot patterns with different oxidation times. The same tip was used for the lithography and the analysis of all structures. The changes in the height and the conductivity were analyzed for the individual structures. The lithographic processes were carried out on bare silicon wafers, RGO assembled on an APTMS modified silicon wafer and on the

OTS-RGO substrates for comparison (**Figure 4.2.5**). **Figure 4.2.5a** summarizes the height increase of each substrate during the oxidative process. For the bare silicon reference a self-limiting growth of the oxide patterns is observed.[60] In the case of RGO-APTMS and OTS-RGO a different height increasing profile is obtained. In the beginning of the oxidative process a relatively slow height increase is observed until a feature height of ~0.5 nm is reached. After that the height increase accelerates until the value reaches 2.5 nm. After 8 ms the height increase stops after the structure height reaches 3 nm. No significant differences could be observed between the RGO and the OTS-RGO substrates. This leads to the conclusion that the oxidation of the OTS monolayer has little effect on the observed height increases. We suggest that in the first stage the height increase was mainly caused by the oxidation of graphene and then the oxidation of the Si substrates occurred during the second and third stage. This conclusion is in agreement with that of Chuang and co-workers.[61] Moreover, for the first stage of the OTS-RGO oxidation, the value of height increase is approximately 0.5 nm, which is consistent with that of the height change expected from the transition of graphene to grahene oxide.[62] Additionally, the current decrease of the oxidized dot patterns was characterized as well (**Figure 4.2.5b**). The current differences between the patterned areas and the surrounding unmodified substrates are decreasing gradually for all curves. In analogy with the contribution of the height increase, the influence of the current decrease caused by the OTS monolayer is also insignificant. Obviously, the final difference between the OTS-RGO and the bare silicon wafer (−4 pA) reflects the conductivity change of the RGO.

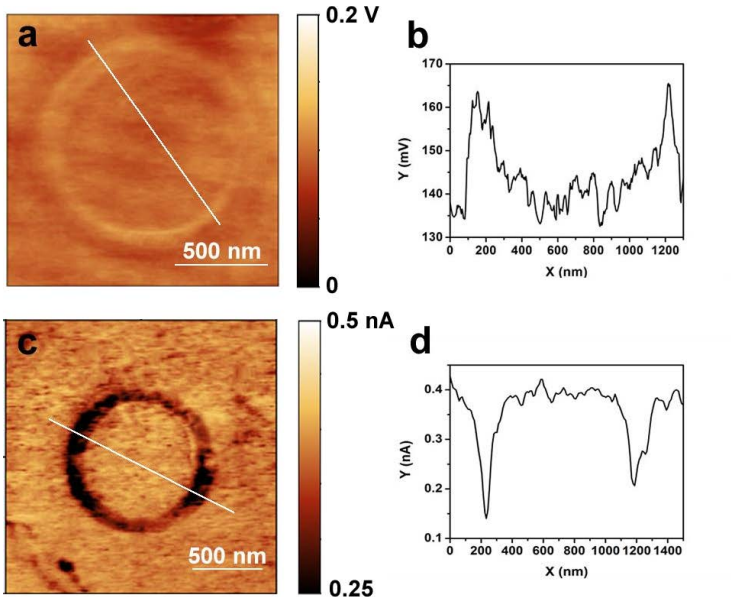

Figure 4.2.4 Surface potential and current images (a, c) and their corresponding section analyses (b, d) for the local electrochemical lithography performed on the OTS-RGO substrate.

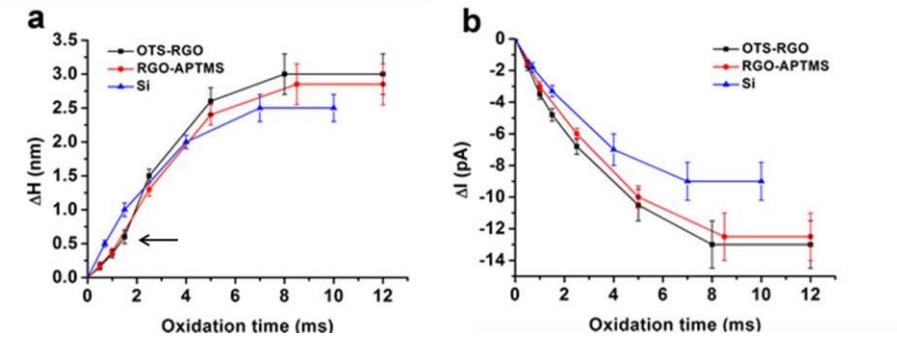

Figure 4.2.5 Analysis of (a) the height increase and (b) the current decrease of dot patterns at different lithographic times.

As mentioned in the previous chapter, the chemical active patterns which contain the carboxyl groups can be selectively loaded with Au ions, followed by reduction with H_2O_2 vapor. The formed small nanoparticles can grow to larger nanoparticles by means of an electroless silver plating method (**Figure 4.2.6a**). After the binding of Ag nanoparticles, the substrate can be reduced again using the same heating method. It can be clearly seen that the particles remain on the patterned area after the thermal reduction process (**Figure 4.2.6b**).

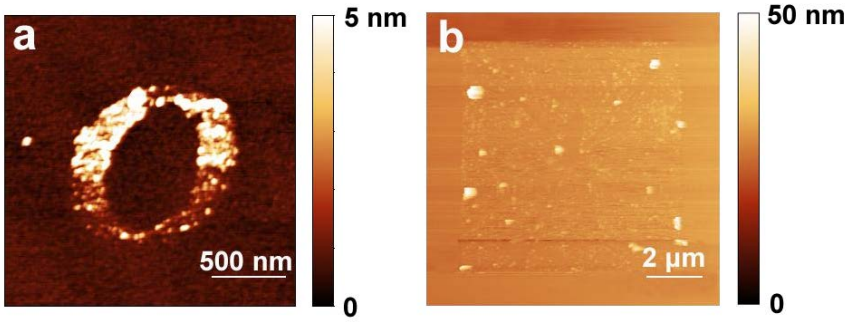

Figure 4.2.6 Tapping mode AFM images of Ag nanoparticles grown on different pattern areas (a circle and a square).

Graphene offers potential applications for the fabrication of biosensors due to its unique properties, including fast electron transportation and large detection area. Here, a glucose sensor was fabricated based on an OTS-RGO micropattern. The micropattern was prepared by the application of a copper TEM grid as a replacement for the conductive tip to obtain large chemically active patterns in one oxidative step. **Figure 4.2.7a** displays an optical micrograph of a water condensation TEM grid micropattern obtained in the lithographic step. Water vapor tends to condense in the hydrophilic patterned areas (dark regions). After thermal reduction, the patterned substrate was used to bind glucose oxidase (GOD) by the formation of amide bonds after an activation process with *N*-hydroxysuccinimide/1-(3-dimethylaminopropyl)-3-ethylcarbodiimide (NHS/EDC). As depicted in **Figure 4.2.7b and 7c**, the enzymes were selectively immobilized on the lithographic stripe areas with good coverage. In general, GOD catalyzes the oxidation of glucose in the following reaction: D-glucose + O_2 + H_2O → D-gluconic Acid + H_2O_2. The reaction product hydrogen peroxide can increase the conductance of graphene.[63] In case a device with microscale dimensions is used, even a small amount of H_2O_2 enables a significant increase of the current. That means that a very low detection limit of glucose can be obtained by this method. **Figure 4.2.7b** illustrates the change of the current values related to different concentrations of glucose. For low concentrations of glucose, the current shows a fast linear increase. The current increase slows down when the concentration of glucose is higher than 0.1 mM and the final saturated detection concentration is 1 mM. This can be explained by the fact that a limited number of active

sites of GOD are bound on the substrate. In a control experiment, an unmodified stripe micropattern without GOD was prepared. However, the current did not change significantly with increasing the concentration of glucose (**Figure 4.2.7d**), which proves that the oxidation caused by GOD has the main effect in this sensing process.

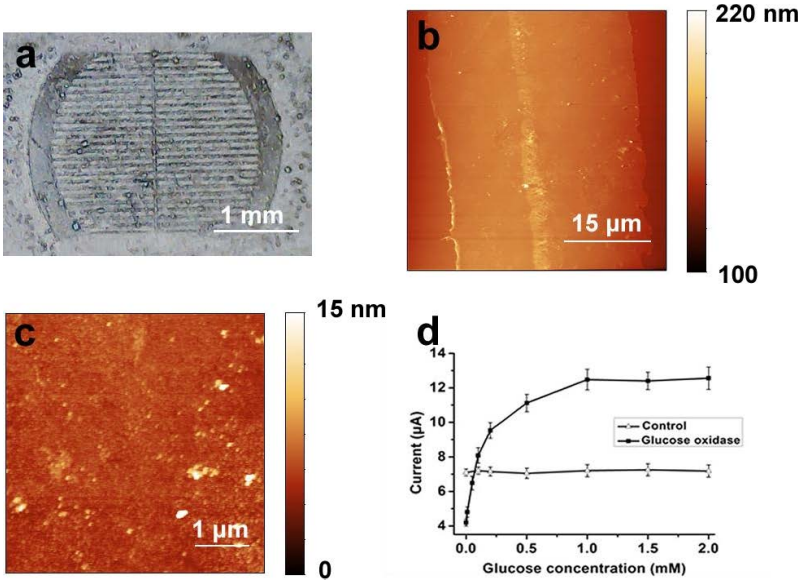

Figure 4.2.7 (a) An optical micrograph of a TEM grid pattern on OTS-RGO. (b, c) AFM images of GOD on the lithographic areas and (d) current response of glucose at different concentrations.

In conclusion, graphene was successfully utilized for local electrochemical lithography. During the patterning process, not only the oxidation of the OTS occurred, but also the graphene was oxidized, followed by the conversion of silicon to silicon oxide. In analogy to the OTS-Si substrate, a chemically active pattern was formed on the graphene layers. Moreover, a functional device, i.e., a glucose sensor, was fabricated by the application of OTS-RGO micropatterns. The method offers an effective way to manipulate the electronic as well as the chemical properties of graphene, providing attractive possibilities for the fabrication of complex device structures.

4.3 Polypyrrole

Besides self-assembled monolayers, polymer films are suitable for local electrochemical lithography as well. In this chapter, a reversible memory nanodevice was fabricated based on polypyrrole (PPy) doped with NaDBS (PPy(DBS)) films. A bias voltage, which is applied between the tip and the substrate, induces the reversible redox reaction of PPy(DBS). The resolution of the generated nanopatterns can reach approximately 80 nm. These patterns can be erased completely by applying the opposite voltage. Additionally, the write-erase process can be repeated on the same position of the polymer film. With this approach reversible volume changes and resistance switching effects can be realized on the PPy(DBS) film.

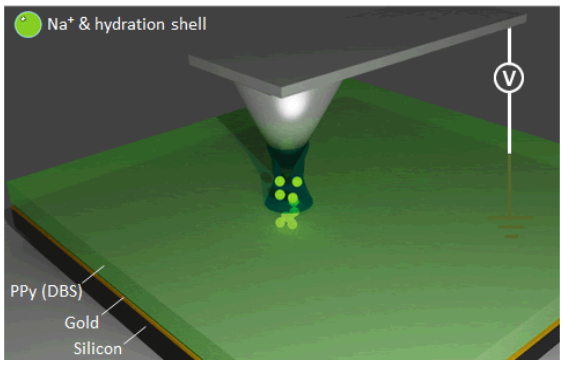

Scheme 4.3.1 Schematic illustration of the write-erase process on PPy(DBS) films.

The eletropolymerization time of PPy(DBS) was set to be 1 min to obtain a smooth surface. As depicted in **Figure 4.3.1a and 1b**, a smooth polymer film with a thickness of ~60 nm was generated on the Au substrate. The root mean square roughness is in the range of 1.5 nm, as measured by AFM tapping mode investigations. **Figure 4.3.1c** shows that some small protrusions appeared on the PPy(DBS) surface, which increased in size at longer polymerization times.[64] In general, if the conductive polymer is doped with large anions, such as dodecylbenzenesulfonate (DBS), these anions will be trapped within the polymer matrix when the polymer is reduced. In the meanwhile, the Na^+ cations and their associated solvation shells will move into the matrix to maintain the charge neutrality, and

thus, an expansion of the PPy occurs. For the present lithographic process, a negative bias voltage (−5 V) was applied to the Au substrate. The conductive AFM tip was scanned along a defined pathway (e.g., a circle) while keeping the contact force constant (**Scheme 4.3.1**). Afterwards, the resulting pattern was imaged using AFM tapping mode. As shown in **Figure 4.3.2a**, a circle grew at the position where the tip was scanned with an applied bias voltage as result of the volume expansion. This process also alters the conductivity of the substrate. The current intensity was measured between the tip and each point of the surface. As depicted in the current map (**Figure 4.3.2b**), the conductivity in the lithographic area (−6 nA) was lower than that in the other areas (−11 nA), which indicates that reduced, more insulating PPy(DBS) was formed during the lithographic process in the tip contact area. It is worth mentioning that a relatively small bias voltage (1 V) was used to avoid inducing additional changes of the PPy(DBS) films during the current intensity measurements. A constant force was utilized for the patterning of the PPy films. Higher contact forces had no significant influence on the width of the patterned structures, but will decrease the lifetime of the tip, due to the loss of the conductive coating or the contamination of the tip with traces of polymer. On the other hand, if a very small contact force is applied the formation of the required water meniscus between the tip and the polymer film will be unreliable. Therefore the patterning process would be incomplete. In general, by optimizing the applied force to the tip it is possible to perform ~100 writing and erasing cycles without significant degradation of the patterning quality. Additionally, the effect of the applied bias voltage was investigated as well. Normally, lowering the applied voltages requires longer lithographic times to obtain comparable results, however, below a voltage of −3 V at a relative humidity of 50% no pattern was formed, even at very long contact times. This is due to the fact that the redox reaction of PPy(DBS) is unable to initiate under this condition. The stability of the patterns was tested after three weeks and no differences in the patterned areas were found. Moreover, repeated scanning by the AFM tip on the pattern surface did not degrade or affect the topographic features.

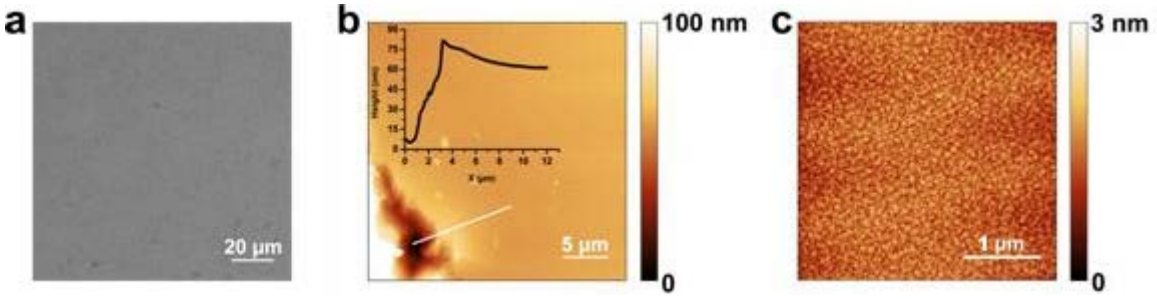

Figure 4.3.1 (a) SEM and (b) AFM topography images of the PPy(DBS) films and cross section of the topography measured along the white line. (c) Zoomed view of (b).

After demonstrating the successful electrochemical modification of the substrates their potential utilization as storage devices was investigated. The ability of erasing the created structures was tested. **Figure 4.3.2c** shows that the generated circle in the first writing step can be erased completely when the tip is scanned with an opposite voltage (5 V) and with the same inscription time (5 ms). In addition, the lithographic pattern was also removed in the current image (**Figure 4.3.2d**), which indicates that the reduced PPy(DBS) was oxidized again during the erasing process and returned to the conducting state. In the case of testing the rewriting ability, it is essential to ensure that the lithographic process was performed in the same area where the pattern was written the first time. For this purpose, a dot mark was additionally placed as a traceable label in the upper left corner of each image during the first writing step (see arrows in **Figure 4.3.2**). As shown in **Figure 4.3.2e**, another circle was written at the same location of the PPy(DBS) film utilizing the same lithographic procedure. Afterwards, the structure could be erased again by applying the opposite voltage. Write-erase cycles could be performed at the same position for 17 times with no observable memory effect of the previous cyclic process.

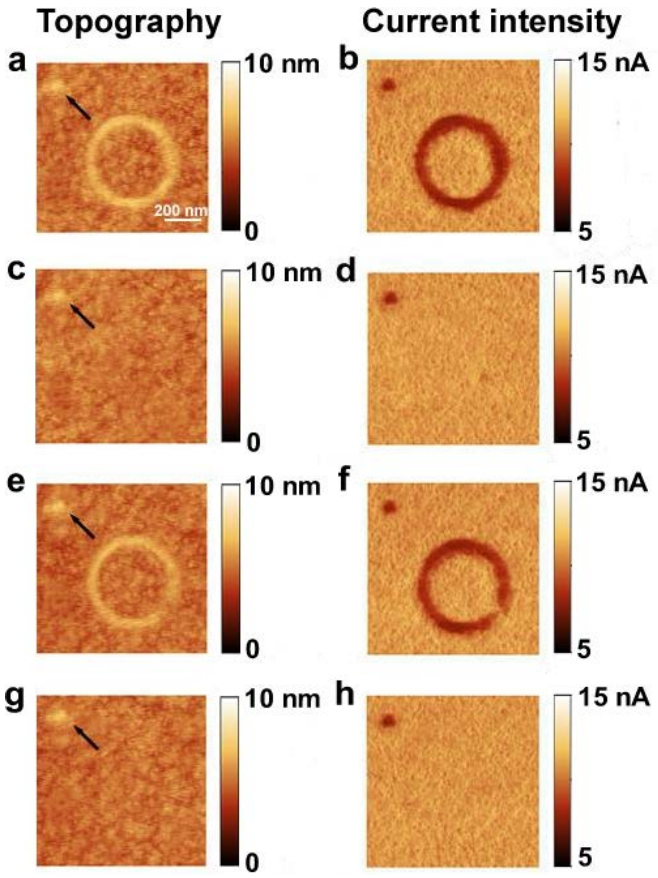

Figure 4.3.2 (a) Topography and (b) current images of a circle pattern (writing time: 5 ms); (c, d) after erasing the circle (erasing time: 5 ms); (e, f) rewriting a circle at the same location (writing time: 5 ms); (g, h) after re-erasing the circle (erasing time: 5 ms). For orientation a marker was inscribed in the upper-left corner of the images (indicated by an arrow). The size of each image is 1 μm × 1 μm.

Additionally, scanning Kelvin probe microscopy (SKPM) was utilized to analyze the mechanism of the electrochemical lithographic process. **Figure 4.3.3** shows a surface potential image of a writing circle on the PPy(DBS) film. For the patterned area, the surface potential decreased from ~70 to ~40 mV, followed by returning to the original value after the erasing process (**Figure 4.3.3c**). The reversible changes also indicate that PPy(DBS) underwent reduction and re-oxidation processes which are related to the writing and erasing processes, respectively. As reported in literature, in addition to the reversible expansion, irreversible processes may also occur during the redox reaction of PPy(DBS), due to the irreversible insertion of ions and solvent shells.[65] In order to

obtain a better understanding of the PPy(DBS) changes occurring during the reversible expansion, lithographic processes at different writing times were performed. As depicted in **Figure 4.3.3d** and **3e**, the surface potential decreased significantly at longer writing times (8 ms), i.e., from ~70 to ~25 mV. After the erasing process, the potential of the pattered area did not recover completely as a result of the irreversible insertion of Na^+ ions (**Figure 4.3.3f**). For this reason, a detailed study of the limitations of the write-erase process was conducted. **Figure 4.3.4** summarizes the topography and current images of the generated circles at different lithographic times. In the case of the writing processes, the expansion of the polymer volume increased with writing time. The height of circles increased from ~2 to ~8 nm and the line width increased from ~80 to ~200 nm when the lithographic times changed from 2 to 10 ms. The current change of structures showed a similar trend and decreased from ~2 to ~9 mA. These results demonstrate that more PPy(DBS) was reduced during the redox reaction if longer lithographic times were applied. Thus, stronger expansion of the volume and a decrement of the conductivity took place. As shown in **Figure 4.3.4**, the pattern can be erased completely if the writing time is in the range of 2 to 5 ms. However, if the writing time increased to 8 ms, only a part of the structure could be erased. When utilizing longer writing times, i.e., 10 ms, the inerasable parts became larger. Moreover, the inerasable parts were nearly the same even when increasing the erasing time to 15 ms. Thus, it was concluded that the reversible redox reaction can be accomplished only when short lithographic times were used, while longer times will cause an irreversible write-erase process. The reason is that the reversible expansion of PPy(DBS) occurs quickly, while the irreversible reaction takes much longer.[65] Additionally, it is worth pointing out that short writing times are also beneficial to obtain structures with high lateral resolution. It was also observed that lithographic voltages below −9 V cause non-erasable structures. This can be explained by the fact that an irreversible reaction of the PPy occurred and/or excessive Joule heating might result in an irreversible mass transport in this case.

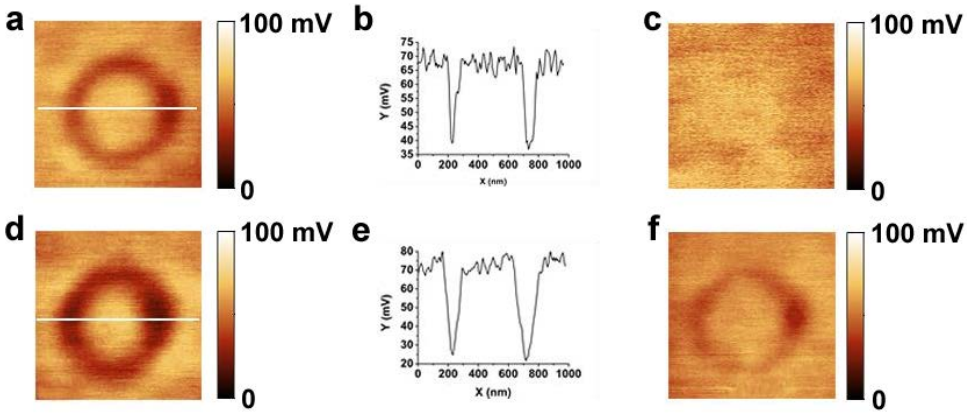

Figure 4.3.3 (a, c) Surface potential images after writing and erasing a circle (writing time: 5 ms and erasing time: 5 ms). (b) Cross section of the white line in (a). (d, f) Surface potential images after writing and erasing a circle using longer times (writing time: 8 ms and erasing time: 8 ms). (e) Cross section of the white line in (d). The size of each image is 1 μm × 1 μm.

Writing/erasing time	2 ms	5 ms	8 ms	10 ms
Writing (topography)	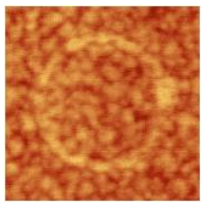	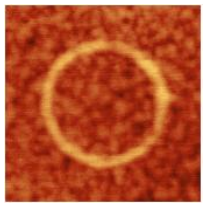	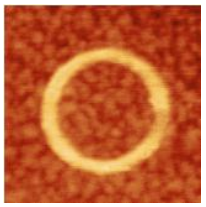	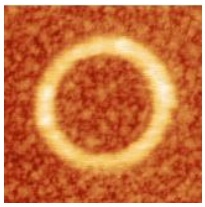
Writing (current)			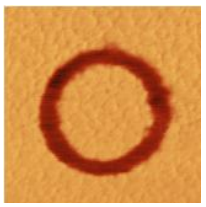	
Erasing (topography)	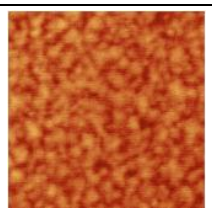	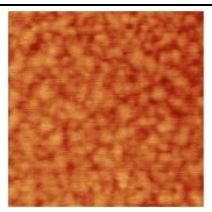	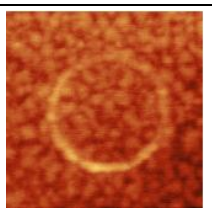	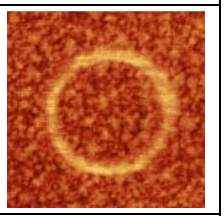
Erasing (current)			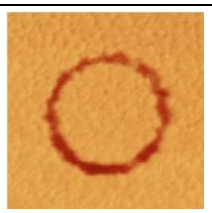	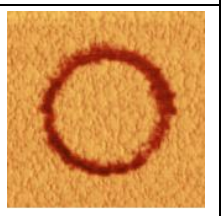

Figure 4.3.4 Comparison on topography and current intensity of the writing and erasing processes at different operation times. The size of each image is 1 μm × 1 μm.

In summary, PPy(DBS) films were investigated for the local electrochemical lithographic process. A reversible nanopattern with a resolution limit of ~80 nm was fabricated on the polymer film. The changes of current intensity and surface potential indicate that PPy(DBS) underwent reduction and re-oxidation processes, which were corresponding to writing and erasing processes, respectively. These reversible volume changes and resistance switching effects provide a possibility for the fabrication of memory nanodevices on the basis of conductive polymers.

5. Summary

The present thesis addressed the preparation of functional micro- and nanopatterns by local electrochemical lithography (**Figure 5.1**). Different molecules and nanoparticles could be self-assembled on the lithographic patterns to form functional systems and devices. Several technologically important materials were investigated to extend the range of substrates for the lithographic approach.

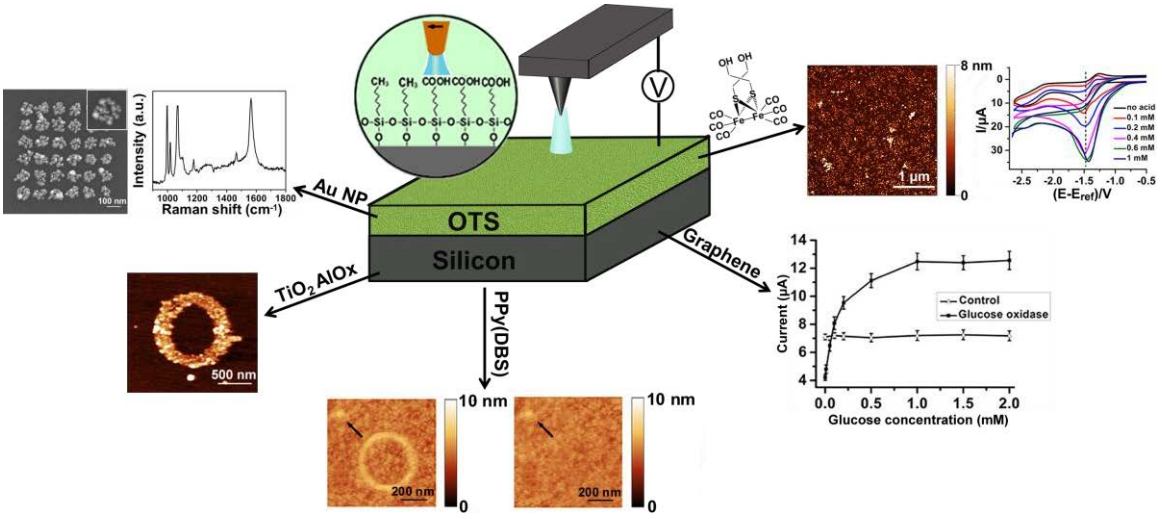

Figure 5.1 Overview of the content of the chapters presented in this thesis.

In general, self-assembled monolayers (SAMs), in particular OTS monolayers are one of the most frequently used films for local electrochemical lithography. The methyl groups ($–CH_3$) groups of OTS can be oxidized to carboxyl groups (–COOH) during the lithographic process, which enables further chemical functionalization procedures. As such, the first application of patterned OTS monolayers was to create a microscale catalytic system. [Fe-Fe]-hydrogenase active-site model complexes were immobilized onto a micropattern surface by ester bond formation. The catalytic activity of the [Fe-Fe] complex molecules was investigated by cyclic voltammetry (CV) measurement. One oxidation and two reduction peaks were observed in the CV curves, which relate to the different redox processes of the di-iron complex. Moreover, the current of the cathodic

waves was increasing when adding acetic acid to the catalytic system, due to the electrocatalytic proton reduction in the solution. According to the CV results it could be demonstrated that the biomimetic metal centers of [Fe-Fe]-hydrogenase active-site complex molecules still kept their catalytic activity after the immobilization on the patterned OTS monolayers. Besides functional molecules, also nanoparticles could be assembled on the patterned OTS monolayers as well. Au nanoparticles were utilized and can be immobilized on a dot pattern substrate to form cluster arrays. Strong SERS signals were generated due to the interparticle and intercluster plasmon coupling of the nanoparticles. In particular, an enhancement factor (EF) value of $\sim 5\times10^6$ was achieved when the interparticle separation was less than 5 nm and the intercluster seperation was 30 nm. Moreover, a good reproducibility of the EF was obtained for the prepared samples, because of the regular periodic structures.

In general, silicon is the most frequently used substrate for local electrochemical lithography performed on OTS monolayers. In this thesis, three additional technologically important substrates, i.e., TiO_2, AlOx, and graphene, were also tested to extend the possibilities to utilize this patterning approach. Despite of the relevant differences concerning the surface properties, in terms of film thickness and conductivity of the tested substrates, good quality OTS monolayers were obtained in all case by a careful adaptation of the deposition parameters. In analogy to OTS-Si, –COOH groups were formed on these OTS modified substrates after the lithographic process using special oxidation parameters. In particular, for the graphene layers, the mechanism of oxidation was analyzed by investigating the height increase and the current decrease of the written dots at different oxidation times. Not only the OTS was oxidized, but also the oxidation of graphene occurred, followed by the conversion of silicon to silicon oxide. The formed GO can be reduced again by means of a thermal reduction method. The demonstrated process provides an approach to manipulate the electronic and the chemical properties simultaneously for the graphene substrates, which is difficult to achieve by other methods. Moreover, a glucose sensor with a low detection limit was fabricated on the patterned

graphene substrate. In addition to OTS monolayers, polymer films are suitable for local electrochemical lithography as well. Here, polypyrrole doped with sodium dodecylbenzenesulfonate (PPy(DBS)) was investigated for the introduction of a reversible lithographic process that allows reversible nanopatterning with a lateral resolution limit of approximately 80 nm. A distinct height increase was observed during the patterning process because of the incorporation of Na^+ ions and their solvation shells into the PPy matrix. Afterwards, the generated pattern can be erased and rewritten again at the same location of the film. The changes of current transport and surface potential indicate that PPy(DBS) underwent reduction and re-oxidation processes, which are corresponding to writing and erasing processes, respectively. This patterning method could open up possibilities for the fabrication of memory devices on the nanoscale by utilization of PPy.

In summary, this thesis addressed the fabrication of functional systems and devices at micro- and nanoscale by local electrochemical lithography, including a microcatalytic [Fe-Fe] model complex molecules system, highly active SERS substrates and a glucose sensor device. For extending the application scope of this lithographic technique, different technologically important substrates, i.e., AlOx, TiO_2, graphene, and PPy, were tested and selected potential applications were investigated as well. Next to the fabrication of functional devices the characterization of the patterning processes was a focus of the thesis. Advanced characterization tools, i.e., SKPM, micro-Raman, AES, SEM and TEM, were utilized to carefully investigate the patterning processes. As such, this thesis could contribute to the field of local electrochemical lithography and opening new possibilities for device fabrication.

6. Zusammenfassung

Die vorliegende Arbeit befasst sich mit der Herstellung funktioneller Mikro- und Nanostrukturen durch Anwendung der elektrochemischen Lithographie (**Abbildung 6.1**). Dabei konnten lithographische Strukturen hergestellt werden, die durch Selbstorganisationsprozesse mit verschiedenen Molekülen und Nanopartikeln funktionalisiert wurden. Auf diese Weise konnten funktionelle Mikro- und Nanosysteme aufgebaut werden. Neben der Herstellung dieser Strukturen lag ein weiterer Schwerpunkt der Arbeiten auf der Übertragung des verwendeten Lithographieverfahrens auf andere, technologisch relevante Substratmaterialien.

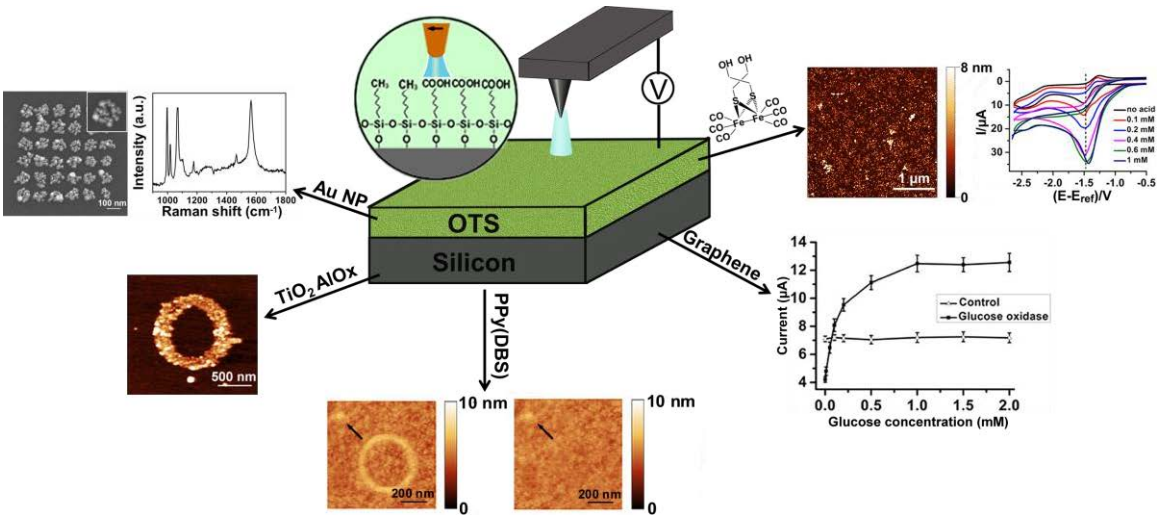

Abbildung 6.1 Übersicht über den Inhalt der Kapitel dieser Doktorarbeit.

Bislang wurden insbesondere selbstorganisierte Monolagen aus *n*-Octadecyltrichlorosilan (OTS) als Substrate für die lokale elektrochemische Lithographie eingesetzt. Hierbei werden die oberflächenterminalen Methyl Gruppen ($-CH_3$) der Alkylketten während des Lithographieprozesses zu Säure Gruppen (–COOH) oxidiert, was eine nachfolgende, weitere Funktionalisierung dieser Gruppen erlaubt. In dieser Arbeit wurde zunächst ein mikrostrukturiertes katalytisches System auf den strukturierten OTS Monolagen aufgebaut. Dabei wurden [Fe-Fe]-Hydrogenase-Modellkomplexe auf den

mikrostrukturierten Oberflächen mittels einer Esterbindung verankert. Die katalytische Aktivität der Komplex wurde mit Hilfe der Cyclovoltammetrie (CV) untersucht. Dabei konnten ein Oxidations- und zwei Reduktionsschritte nachgewiesen werden, die zu verschiedenen Redoxprozessen der Di-Eisen-Komplexe gehören. Es konnte weiterhin gezeigt werden, dass der Strom im Bereich des kathodischen Potentialbereichs durch die Zugabe von Essigsäure aufgrund der elektrokatalytischen Reduktion von Protonen in der Lösung zunahm. Aus diesen CV-Daten kann geschlossen werden, dass die auf der strukturierten OTS Monolage verankerten biomimetischen Metallzentren der [Fe-Fe]-Hydrogenase-Modellkomplexe trotz der Anbindung zum Substrat ihre katalytische Aktivität behalten.

Neben funktionellen Molekülen können auch Nanopartikel auf den strukturierten OTS Monolagen angebunden werden. In der vorliegenden Arbeit wurden Goldnanopartikel verwendet, die in der Form eines Punktrasters auf der Oberfläche angeordnet werden können. Dabei bilden sich auf jedem der Punktbereiche Cluster, die aus 20 bis 30 einzelnen Nanopartikeln bestehen. Diese Punktraster zeigen aufgrund von interpartikulären Plasmonenkopplungen der Einzelpartikel sowie Kopplungen zwischen den Clustern sehr stark oberflächenverstärkte Ramansignale. Im Falle eines Clusterabstandes von 30 nm und einem mittleren Abstand der individuellen Nanopartikel innerhalb des Clusters von <5 nm konnte eine Verstärkung der Ramansignale um einen Faktor von $\sim 5 \times 10^6$ erreicht werden. Darüber hinaus zeigten die so hergestellten Substrate auf Grund ihrer hochgeordneten periodischen Strukturen eine gute Reproduzierbarkeit der erreichbaren Verstärkungsfaktoren.

Bislang war Silizium das meistverwendete Substratmaterial, um die elektrochemische Lithographie an OTS-Monolagen durchzuführen. In dieser Arbeit konnten drei weitere technologisch relevante Substratmaterialien etabliert werden: Titandioxid (TiO_2), Aluminiumoxid (AlOx) und Graphen. Damit konnte der Einsatzbereich der elektro-oxidativen Lithographie maßgeblich erweitert werden. Unabhängig von den sehr unterschiedlichen Eigenschaften der verwendeten Substrate bezüglich ihrer Schichtdicken und ihrer Leitfähigkeiten, konnten auf allen Substraten durch eine Anpassung der

Beschichtungsparameter qualitativ gute OTS Monolagen erhalten werden. Analog zur elektro-oxidativen Lithographie, die auf Siliziumsubstraten (OTS-Si) durchgeführt wurden, konnten auch bei den anderen Substraten durch die Strukturierung –COOH Gruppen erhalten werden, die mit Hilfe verschiedener analytischer Methoden, wie z.B. durch Scanning Kelvin Probe Messungen, nachgewiesen wurden. Allerdings waren jeweils optimierte Oxidationsparameter notwendig. Insbesondere für Graphenschichten wurde der Oxidationsprozess im Detail untersucht. Dabei wurden sowohl die Höhenzunahme der oxidierten Strukturen als auch der Abfall der lokalen Leitfähigkeit in Abhängigkeit von der angewendeten Oxidationszeit betrachtet. In diesem Fall fand nicht nur eine Oxidation der OTS Monolage statt, sondern auch das Graphen selbst wurde durch den Lithographieprozess oxidiert, was schlussendlich bei sehr langen Oxiadationszeiten auch zu einer Oxidation des Siliziumsubstrates führt. Das in diesem Prozess gebildete Graphenoxid kann mit Hilfe einer thermischen Reduktion wieder in sogenanntes reduziertes Graphenoxid umgewandelt werden. Damit ist im Falle von Graphen nicht nur eine chemische Strukturierung mit Hilfe der oxidativen Lithographie möglich, sondern es lassen sich gleichzeitig auch die elektronischen Eigenschaften des Graphensubstrates kontrollieren. Diese Möglichkeit kann nur schwer mit Hilfe anderer Strukturierungsmethoden erzielt werden. Mikrostrukturierte Graphenschichten wurden darüber hinaus erfolgreich genutzt um einen Glukosesensor mit einer sehr geringen Detektionsgrenze aufzubauen.

Neben den OTS-Monolagen können auch Polymerfilme für die elektrochemische Lithographie verwendet werden. In der vorliegenden Arbeit wurde Polypyrrol dotiert mit Natriumdodecylbenzolsulfonat (PPy(DBS)) verwendet, um ein Substrat zu erhalten, mit dem eine reversible Nanostrukturierung mit einer Lateralauflösung von circa 80 nm etabliert werden kann. Während der Strukturierung des Substrates wurde eine Zunahme der Topographie im Bereich der Nanostruktur nachgewiesen, die auf die Einlagerung von Na^+ Ionen und ihrer zugehörigen Lösungsmittelhüllen in die PPy Matrix zurückzuführen ist. Nach diesem Strukturierungsschritt kann die entstandene topographische Struktur reversibel wieder gelöscht, bzw. neu geschrieben werden. Die entstandenen

topographischen Strukturen unterscheiden sich darüber hinaus in ihrer Leitfähigkeit und dem Oberflächenpotenzial. Diese Beobachtungen legen nahe, dass das PPy(DBS) reversible Reduktions- und Re-Oxidationsprozesse durchlaufen kann, die den Schreib- bzw. Löschzyklen entsprechen. Die hier eingeführte Strukturierungsmethode bietet neue Möglichkeiten zur Herstellung von Speichermedien auf der Nanometerskala.

Zusammenfassend konnten in der vorliegenden Arbeit mikro- und nanostrukturierte funktionelle Systeme mit Hilfe der elektro-chemische Lithographie hergestellt werden. Deren Bandbreite reicht von mikrokatalytischen [Fe-Fe]-Modellkomplexsystemen, über hocheffiziente SERS-Substrate bis hin zu einem Glukosesensor. Im Hinblick auf die Anwendbarkeit der verwendeten Strukturierungsmethode konnten wichtige Beiträge geleistet werden, indem AlOx, TiO_2, Graphen und PPy als neue potentielle Substrate für die elektrochemische Strukturierung eingeführt wurden. Neben der Herstellung funktioneller Strukturen stand die Untersuchung des Oxidationsverhaltens dieser Substrate im Fokus dieser Arbeit und lieferte Einblicke in die ablaufenden Prozesse. Die Ergebnisse dieser Studien wurden mit Hilfe von hochentwickelten und spezialisierten Analysemethoden, wie SPKM, micro-Raman, AES, SEM und TEM untermauert. Damit konnte diese Arbeit dazu beitragen, Verbesserungen im Bereich der elektrochemischen Lithographie einzuführen und neue Möglichkeiten für die Herstellung funktioneller Strukturen aufzuzeigen.

7. References

[1] Y.-Z. Long, M. Yu, B. Sun, C.-Z. Gu, Z. Fan, *Chem. Soc. Rev.* **2012**, *41*, 4560–4580.

[2] S. Lal, S. Link, N. J. Halas, *Nat. Photonics* **2007**, *1*, 641–648.

[3] F. Canal, J. Sanchis, M. J. Vicent, *Curr. Opin. Biotechnol.* **2011**, *22*, 894–900.

[4] H. Wang, H. Dai, *Chem. Soc. Rev.* **2013**, *42*, 3088–3113.

[5] M. Junkin, J. Watson, J. P. Vande Geest, P. K. Wong, *Adv. Mater.* **2009**, *21*, 1247–1251.

[6] J. Y. Cheng, D. P. Sanders, H. D. Truong, S. Harrer, A. Friz, S. Holmes, M. Colburn, W. D. Hinsberg, *ACS Nano* **2010**, *4*, 4815–4823.

[7] J. Feng, W. Li, X. Qian, J. Qi, L. Qi, J. Li, *Nanoscale* **2012**, *4*, 4883–4899.

[8] W. Xie, R. Gomes, T. Aubert, S. Bisschop, Y. Zhu, Z. Hens, E. Brainis, D. Van Thourhout, *Nano Lett.* **2015**, *15*, 7481–7487.

[9] H. Dai, N. Franklin, J. Han, *Appl. Phys. Lett.* **1998**, *73*, 1508–1510.

[10] E. B. Cooper, S. R. Manalis, H. Fang, H. Dai, K. Matsumoto, S. C. Minne, T. Hunt, C. F. Quate, *Appl. Phys. Lett.* **1999**, *75*, 3566–3568.

[11] J. A. Dagata, J. Schneir, H. H. Harary, C. J. Evans, M. T. Postek, J. Bennett, *Appl. Phys. Lett.* **1990**, *56*, 2001–2003.

[12] H. C. Day, D. R. Allee, *Appl. Phys. Lett.* **1993**, *62*, 2691–2693.

[13] S. Nishimura, T. Ogino, J. Shirakashi, *Jpn. J. Appl. Phys.* **2008**, *47*, 715–717.

[14] . avallini, . ei, . iscarini, . a rc a, *Appl. Phys. Lett.* **2003**, *83*, 5286–5288.

[15] R. Maoz, S. R. Cohen, J. Sagiv, *Adv. Mater.* **1999**, *11*, 55–61.

[16] J. Sagiv, *J. Am. Chem. Soc.* **1980**, *399*, 92–98.

[17] S. Schilp, A. Kueller, A. Rosenhahn, M. Grunze, M. E. Pettitt, M. E. Callow, J. A. Callow, *Biointerphases* **2007**, *2*, 143–150.

[18] S. Sun, M. Montague, K. Critchley, M.-S. Chen, W. J. Dressick, S. D. Evans, G. J. Leggett, *Nano Lett.* **2006**, *6*, 29–33.

[19] K. Motesharei, D. Myles, *J. Am. Chem. Soc.* **1998**, *7863*, 7328–7336.

[20] X.-M. Li, J. Huskens, D. N. Reinhoudt, *J. Mater. Chem.* **2004**, *14*, 2954–2971.

[21] R. Maoz, E. Frydman, S. R. Cohen, J. Sagiv, *Adv. Mater.* **2000**, *12*, 725–731.

[22] D. Wouters, R. Willems, S. Hoeppener, C. F. J. Flipse, U. S. Schubert, *Adv. Funct. Mater.* **2005**, *15*, 938–944.

[23] J. H. Hoh, A. Engel, *Langmuir* **1993**, *9*, 3310–3312.

[24] M. Yang, D. Wouters, M. Giesbers, U. S. Schubert, H. Zuilhof, *ACS Nano* **2009**, *3*, 2887–2900.

[25] D. A. Unruh, C. Mauldin, S. J. Pastine, M. Rolandi, J. M. J. Fréchet, *J. Am. Chem. Soc.* **2010**, *132*, 6890–6891.

[26] G. Qin, J. Gu, K. Liu, Z. Xiao, C. M. Yam, C. Cai, *Langmuir* **2011**, *27*, 6987–6994.

[27] D. Chowdhury, R. Maoz, J. Sagiv, *Nano Lett.* **2007**, *7*, 1770–1778.

[28] T. Druzhinina, S. Hoeppener, N. Herzer, U. S. Schubert, *J. Mater. Chem.* **2011**, *21*, 8532–8536.

[29] T. S. Druzhinina, S. Hoeppener, U. S. Schubert, *Small* **2012**, *8*, 852–857.

[30] C. Haensch, S. Hoeppener, U. S. Schubert, *Nanotechnology* **2009**, *20*, 135302.

[31] C. R. Becer, C. Haensch, S. Hoeppener, U. S. Schubert, *Small* **2007**, *3*, 220–225.

[32] S. M. Mitrovski, L. C. C. Elliott, R. G. Nuzzo, *Langmuir* **2004**, *20*, 6974–6976.

[33] B. Loges, A. Boddien, H. Junge, M. Beller, *Angew. Chem. Int. Ed.* **2008**, *47*, 3962–3965.

[34] M. Motoyama, C.-C. Chao, J. An, H. J. Jung, T. M. Gür, F. B. Prinz, *ACS Nano* **2014**, *8*, 340–351.

[35] D. M. Heinekey, *J. Organomet. Chem.* **2009**, *694*, 2671–2680.

[36] P. M. Vignals, A. Colbeau, *Curr. Issues Mol. Biol* **2004**, *6*, 159–188.

[37] R. Trautwein, L. R. Almazahreh, H. Görls, W. Weigand, *Z. Anorg. Allg. Chem.* **2013**, *639*, 1512–1519.

[38] T. Liu, M. Wang, Z. Shi, H. Cui, W. Dong, J. Chen, B. Akermark, L. Sun, *Chem. Eur. J.* **2004**, *10*, 4474–4479.

[39] S. Liu, R. Maoz, J. Sagiv, V. Reho, *Nano Lett.* **2004**, *4*, 845–851.

[40] A. A. Tseng, *Small* **2005**, *1*, 924–939.

[41] E. Altewischer, M. P. van Exter, J. P. Woerdman, *Nature* **2002**, *418*, 304–306.

[42] S. Li, D. Wu, X. Xu, R. Gu, *J. Raman Spectrosc.* **2007**, *38*, 1436–1443.

[43] J. D. Caldwell, O. Glembocki, F. J. Bezares, N. D. Bassim, R. W. Rendell, M. Feygelson, M. Ukaegbu, R. Kasica, L. Shirey, C. Hosten, *ACS Nano* **2011**, *5*, 4046–4055.

[44] W. J. Cho, Y. Kim, J. K. Kim, *ACS Nano* **2012**, *6*, 249–255.

[45] B. Yan, A. Thubagere, W. R. Premasiri, L. D. Ziegler, L. Dal Negro, B. M. Reinhard, *ACS Nano* **2009**, *3*, 1190–1202.

[46] J. Li, A. Salandrino, N. Engheta, *Phys. Rev. B* **2007**, *76*, 245403.

[47] R. Maoz, J. Sagiv, D. Degenhardt, H. Möhwald, P. Quint, *Supramol. Sci.* **1995**, *2*, 9–24.

[48] D. Wouters, S. Hoeppener, U. S. Schubert, *Angew. Chem. Int. Ed.* **2009**, *48*, 1732–1739.

[49] D. Meroni, S. Ardizzone, U. S. Schubert, S. Hoeppener, *Adv. Funct. Mater.* **2012**, *22*, 4376–4382.

[50] F. Schedin, A. K. Geim, S. V Morozov, E. W. Hill, P. Blake, M. I. Katsnelson, K. S. Novoselov, *Nat. Mater.* **2007**, *6*, 652–655.

[51] Y. Zhang, T.-T. Tang, C. Girit, Z. Hao, M. C. Martin, A. Zettl, M. F. Crommie, Y. R. Shen, F. Wang, *Nature* **2009**, *459*, 820–823.

[52] A. W. Cummings, D. L. Duong, V. L. Nguyen, D. Van Tuan, J. Kotakoski, J. E. Barrios Vargas, Y. H. Lee, S. Roche, *Adv. Mater.* **2014**, *26*, 5079–5094.

[53] Y. Zhou, Q. Bao, B. Varghese, L. A. L. Tang, C. K. Tan, C.-H. Sow, K. P. Loh, *Adv. Mater.* **2010**, *22*, 67–71.

[54] A. B. Bourlinos, D. Gournis, D. Petridis, T. Szabó, A. Szeri, I. Dékány, *Langmuir* **2003**, *19*, 6050–6055.

[55] B. Lee, Y. Chen, F. Duerr, D. Mastrogiovanni, E. Garfunkel, E. Y. Andrei, V. Podzorov, *Nano Lett.* **2010**, *10*, 2427–2432.

[56] D. L. Angst, G. W. Simmons, *Langmuir* **1991**, *7*, 2236–2242.

[57] H. Kang, A. Kulkarni, S. Stankovich, R. S. Ruoff, S. Baik, *Carbon* **2009**, *47*, 1520–1525.

[58] J. Ou, J. Wang, S. Liu, B. Mu, J. Ren, H. Wang, S. Yang, *Langmuir* **2010**, *26*, 15830–15836.

[59] D. Meroni, S. Ardizzone, U. S. Schubert, S. Hoeppener, *Adv. Funct. Mater.* **2012**, *22*, 4376–4382.

[60] P. Avouris, T. Hertel, R. Martel, *Appl. Phys. Lett.* **1997**, *71*, 285–287.

[61] M.-C. Chuang, H.-M. Chien, Y.-H. Chain, G.-C. Chi, S.-W. Lee, W. Y. Woon, *Carbon* **2013**, *54*, 336–342.

[62] H. C. Schniepp, J.-L. Li, M. J. McAllister, H. Sai, M. Herrera-Alonso, D. H. Adamson, . K. rud'homme, . ar, D. A. Saville, I. A. Aksay, *J. Phys. Chem. B* **2006**, *110*, 8535–8539.

[63] Y. Huang, X. Dong, Y. Shi, C. M. Li, L.-J. Li, P. Chen, *Nanoscale* **2010**, *2*, 1485–1488.

[64] T. Silk, Q. Hong, J. Tamm, R. G. Compton, *Synth. Met.* **2000**, *93*, 59–64.

[65] D. Melling, S. Wilson, E. W. H. Jager, *Smart Mater. Struct.* **2013**, *22*, 104021.

List of abbreviations

AES	Auger electron spectroscopy
AFM	Atomic force microscopy
APTMS	(3-Aminopropyl)-trimethoxysilane
ATRP	Atom transfer radical polymerization
CV	Cyclic voltammetry
DCC	Dicyclohexylcarbodiimide
DMAP	4-Dimethylaminopyridine
EDC	1-(3-Dimethylaminopropyl)-3-ethylcarbodiimide
EF	Enhancement factor
[Fe-Fe]	$[Fe(CO)_3]_2[(\mu\text{-}SCH_2)_2C(CH_2OH)_2]$
NHS	*N*-hydroxysuccinimide
NTS	18-Nonadecenyltrichlorosilane
OTS	Trichloro(octadecyl)silane
OTS-Si	OTS on Si substrate
PPy(DBS)	Polypyrrole doped with sodium dodecylbenzenesulfonate
SAMs	Self-assembled monolayers
SERS	Surface-enhanced Raman spectroscopy
SKPM	Scanning Kelvin probe microscopy
SPL	Scanning probe lithography
SPM	Scanning probe microscopy
STM	Scanning tunneling microscope
TEM	Transmission electron microscope

Curriculum vitae

07.12.1986	Born in Siping, China
1993-2002	Compulsory education in Siping, China
09/2002-06/2005	High school education in Siping, China
09/2005-06/2009	Studies of Chemistry at the Jilin University, China Degree: Bachelor
09/2009-06/2012	Studies of Polymer Chemistry at the Jilin University, China Degree: Master Topic: Functional inorganics/polyelectrolyte layer-by-layer assembled films
Since 10/2012	PhD student at the Friedrich Schiller University Jena in the group of Prof. Dr. U. S. Schubert, Germany Topic: Micro- and nanopatterning by local electrochemical lithography

Jena, den

_____

He Liu

Publication list

Peer-reviewed publications:

1.

H. Liu, S. Hoeppener, U. S. Schubert
"Nanoscale materials patterning by local electrochemical lithography"
Adv. Eng. Mater. **2016**, *18*, 890−902.

2.

H. Liu, R. Trautwein, B. Schröter, A. Ignaszak, W. Weigand, S. Hoeppener, U. S. Schubert
"Micropatterns of [Fe-Fe]-hydrogenase active-site model complexes fabricated by electro-oxidative lithography"
Langmuir **2015**, *31*, 11748−11753.

3.

H. Liu, A. M. Schwenke, F. Kretschmer, S. Hoeppener, U. S. Schubert
"Au nanoparticle cluster arrays for high-performance SERS substrates fabricated by electro-oxidative lithography"
ChemNanoMat. **2016**, DOI: 10.1002/cnma.201600063.

4.

H. Liu, S. Hoeppener, U. S. Schubert
"Reversible nanopatterning on polypyrrole films by atomic force microscope electrochemical lithography"
Adv. Funct. Mater. **2016***, 26,* 614–619.

5.

H. Liu, S. Hoeppener, U. S. Schubert
"Site-specific surface functionalization of graphene via electro-oxidative lithography for bio-sensing applications"
ChemPhysChem **2016**, DOI: 10.1002/cphc.201600490.

Submitted publications:

1.

D. Meroni,* H. Liu,* S. Ardizzone, U. S. Schubert, S. Hoeppener
"Extending the range of possible substrates for the electro-oxidation of *n*-Octadecyltrichlorosilane (OTS) self-assembled monolayers" (*equal contribution)
Submitted to *Nanotechnology*.

Acknowledgements / Danksagung

Finally, I would like to express my gratitude to all the people who supported me during my PhD studies.

At first, I want to thank Prof. Dr. Ulrich S. Schubert who gave me the opportunity to work on this topic. I enjoyed working in such an international and really well equipped group. I would also thank CSC scholarship for financial support.

Second, I would like to thank PD Dr. Stephanie Höppener for the great supervision as well as for the correction of my thesis and the manuscripts, also for help of writing the German summary part. I am also grateful to Stephanie for the TEM measurements, the introduction to AFM, and so many times for the adjustment of the IR spectroscopy.

My gratitude goes to Steffi Stumpf for the SEM teaching and measurements. Also, you provide me a lot of help during my daily life. I remember you tried to teach me German words after lunch, although I am not a good student. Without you, the life will be much more difficult for me to stay here. I would like to thank Almut Schwenke for the SEM measurements and lots of discussions and suggestions to my work. Thank you for your patience to answer so many questions every day. I feel amazing and really appreciate you can learn so many Chinese good words. I also want to thank Dr. Florian Kretschmer for helping me with experiments in particular preparing the gold nanoparticles. It has been a pleasure cooperating and talking with you. Martin Reifarth, if I have questions about organic chemistry, I always ask you. Thanks for your help with distilling the solvents. Many thanks to Pelin Sungur for your delicious Turkish food.

I would like to thank Prof. Wolfgang Weigand for providing the [Fe-Fe] molecules, PD Dr. Stephanie Höppener for figures modification, Dr. Anna Ignaszak and Kun Cong for

the cyclic voltammetry measurements, Dr. Bernd Schröter for AES testing, Di Yan for the Raman measurements and Renzo Paulus for the help with hard- and software related problems.

Special gratitude goes to my friends (Lan, Zhenglong, Qingfu, Yanze, Xuekai…). It is difficult to say everybody's names, but thank you for bring the happiness. I am also grateful to the office E003/ZAF for a nice working and living atmosphere.

Last but not least I would like to thank my family for their great support. This thesis would not be possible without you.

Declaration of authorship / Selbstständigkeitserklärung

Ich erkläre, dass ich die vorliegende Arbeit selbständig und unter Verwendung der angegebenen Hilfsmittel, persönlichen Mitteilungen und Quellen angefertigt habe.

I certify that the work presented here is, to the best of my knowledge and belief, original and the result of my own investigations, except as acknowledged, and has not been submitted, either in part or whole, for a degree at this or any other university.

Jena, den

_____

He Liu

Publications P1 – P6

Publication P1

Nanoscale materials patterning by local electrochemical lithography

H. Liu, S. Hoeppener, U. S. Schubert

Adv. Eng. Mater. **2016**, *18*, 890−902.

ADVANCED ENGINEERING MATERIALS

REVIEW

DOI: 10.1002/adem.201500486

Nanoscale Materials Patterning by Local Electrochemical Lithography**

By *He Liu, Stephanie Hoeppener** and *Ulrich S. Schubert*

Scanning probe lithography (SPL) techniques are mainly based on electrical, mechanical, and thermal interactions between a tip and substrates. By comparison, the electrical field-induced SPL is highly attractive because a variety of chemical changes can be induced on the surface based on electrochemical reactions taking place during the lithography processes. In this review, we provide an overview of recent advances in the field of electrical field-induced SPL processes, i.e., the local electrochemical lithography. Different substrate materials are discussed, and new concepts, applications and technological improvements are presented.

1. Introduction

Nanomaterials have been used in many fields, such as electronics, optics, medicine, and energy.[1–4] The successful application of these materials with novel properties depends in many cases on their effective integration into frameworks at the nanometer scale.[5,6] For conventional nanolithography, i.e., optical and electron beam lithography, there are major disadvantages, including high costs, the need for multiple processing steps, and the utilization of harsh environments, like, vacuum, strong acid or base solutions, and high temperatures. Thus, finding alternative nanopatterning approaches with high accuracy, low cost, working at mild fabrication conditions is appreciated for a further progress of nanoscience. Among many other techniques, scanning probe lithography (SPL) represents a promising method, which offers precise control with high lateral resolution (below 10 nm),[7,8] the potential for low cost, and fabrication processes that can be carried out under ambient conditions. In addition, the utilization of scanning probe microscopy (SPM) enables a direct investigation of the created nanostructures by SPM imaging. For typical SPL processes, a tip will be used for tailoring surface properties on the substrates based on electrical, mechanical, and thermal interactions. Among these SPL approaches, electrical-induced local lithography is regarded as an attractive tool because the electrical field between the tip and the substrates can induce different electrochemical reactions, that means, functional groups or even new materials on the substrate surface can be obtained based, e.g., on electrochemical reactions, which largely expands the number of potential applications. In 1990, Dagata et al. first reported the local oxidation of hydrogen-passivated silicon by a scanning tunneling microscope (STM). The obtained resolution of the written features reached 100 nm. Further tests showed the oxygen incorporation into the silicon surface during the lithography process.[9] In 1993, Day et al. succeeded in the selective area oxidation of silicon with a conductive atomic force microscopy (AFM) tip. Compared with STM lithography, a distinctive advantage of AFM is that the voltage applied between the tip and the substrate can be chosen independently of the feedback circuit, which enables selecting an optimum voltage for and high-resolution lithography.[10] This improvement laid the foundation for further developments of local electrochemical lithography and ignited a new area of research that has relevance to a large number of applications that utilize nanostructured surfaces.

Here, we provide an overview of recent developments of the local electrochemical lithography technique. The review is organized as follows: in Section 2, the nanolithography of semiconducting and metal substrates is introduced. In a

[*] *Dr. S. Hoeppener, H. Liu, Prof. U. S. Schubert*
Laboratory of Organic and Macromolecular Chemistry (IOMC), Friedrich Schiller University Jena, Humboldtstr. 10, 07743 Jena, Germany
E-mail: s.hoeppener@uni-jena.de
Dr. S. Hoeppener, H. Liu, Prof. U. S. Schubert
Jena Center for Soft Matter (JCSM), Friedrich Schiller University Jena, Philosophenweg 7, 07743 Jena, Germany

[**] *He Liu is grateful to the China Scholarship Council (CSC) for a fellowship grant. The work was conducted in the framework of the "Photonic Nanostructures" (PhoNa) project funded by the German Ministry of Education and Research (BMBF) in the program "Spitzenforschung und Innovation in den Neuen Ländern."*

ADVANCED ENGINEERING MATERIALS

He Liu studied Chemistry at Jilin University (China) from 2005 to 2012. After receiving his MSc, he joined Prof. U. S. Schubert's group at the Friedrich Schiller University Jena (Germany). He is currently working at local electro-oxidative lithography.

Stephanie Höppener studied Physics at the University of Münster, Germany. After obtaining her PhD she moved as a Minerva Postdoc fellow to the Weizmann Institute of Science, Israel, and is since 2004 group leader in the research group of Prof. Schubert at the TU Eindhoven, Netherlands, and since 2009 at the Friedrich Schiller University Jena, Germany. Her research interests focus on scanning probe and electron microscopy techniques for the investigation of self-organized polymer systems.

Ulrich S. Schubert studied chemistry in Frankfurt and Bayreuth, Germany, as well as in Richmond, USA. After his PhD studies and a postdoc in Strasbourg, France, he moved to Munich, Germany, for his habilitation (1999). He was Professor at the Center for NanoScience, Munich, Germany, in Eindhoven, Netherlands, and holds now a chair in Jena, Germany, with research interest in polymers for life sciences, supramolecular chemistry, inkjet printing, energy storage, and self-healing materials.

previous review, the electrochemical lithography of self-assembly monolayers was highlighted.[11] Therefore, only a short description and some new advances in this field will be presented in Section 3. Nanolithography of polymer coatings and some technological changes will be summarized in Sections 4 and 5, respectively. Finally, the development of this field of research will be summarized and an outlook on SPL lithography will be provided.

2. Nanolithography of Semiconducting and Metal Substrates

2.1. Semiconducting Substrates

The first local electrochemical lithography was performed on silicon substrates.[9] After that, the research was followed rapidly by other studies. In 1995, Sugimura and Nakagiri discussed the mechanism of STM-induced electrochemical lithography in detail on hydrogen-terminated silicon surfaces.[12] As shown in Figure 1, the adsorbed water is regarded to form an electrochemical cell and electrochemical reactions will proceed between the tip and the substrate by applying an appropriate bias voltage. The net electrochemical reactions are show in Equation 1 and 2.[13]

$$\text{Sample reaction}: \ M + n\,H_2O \rightarrow MO_n + 2n\,H^+ + 2n\,e^- \quad (1)$$

$$\text{Tip reaction}: \ 2n\,H_2O + 2n\,e^- \rightarrow n\,H_2 + 2n\,OH^- \quad (2)$$

During the electrochemical lithography process one important factor which determines the resolution of the pattern is the lateral diffusion of OH^- ions. In the general ionic-diffusion mechanism, OH^- ions migrate through the water meniscus between the tip and the substrate. Xie et al. developed a new shock-wave (SW) assisted spreading mechanism for OH^- ion diffusion under a high bias voltage at high humidity conditions. The authors suggested that transient SW propagation could largely extend the characteristics of the lateral distribution of OH^- ions. Some unique oxide patterns were obtained by single- and multiple-shock pulses during the oxidation process.[14] Hwang and co-workers demonstrated a simple method to improve the AFM local oxidative rate and height of oxides by coating a thin layer of gold on Si and InP substrates. The authors proved that the gold layer can increase the conductance and can inhibit the decline in growth rate caused by the increasing resistance of the growing oxide.[15] Based on a similar principle, Vijaykumar et al. produced silicon oxide patterns with a height of 13 and 40 nm on Si surfaces which were decorated with Au nanoislands and nanocrystals, respectively.[16] Losilla et al. used silicon oxide patterns fabricated by local oxidation nanolithography as a template for the positioning of charged tetrathiafulvalene derivative semiconductors utilizing electrostatic interactions.[17] Martinez et al. fabricated a complex single-crystalline silicon nanowire field-effect transistor with a channel width of 4 nm by a combination of local oxidation lithography and additional etching steps. The authors proved that the AFM lithography process was compatible with many integrated circuit processes, such as the Si-CMOS technology.[18] Mo et al. prepared biomimetic nanotextures on a H-passivated Si

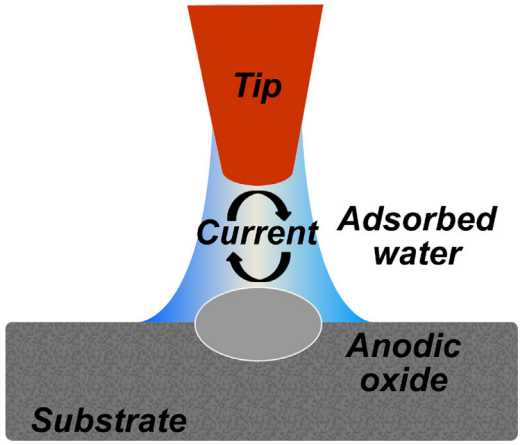

Fig. 1. Schematic illustration of local electrochemical lithography on silicon. Reproduced with permission.[13] Copyright 2006, RSC Publishing.

surface. The desired dimension with a height of the nanotexture of about 1 nm could be accomplished by controlling the lithography parameters, such as the bias voltage, the oxidation time, and the humidity. The silicon substrate with the biomimetic nanotextures exhibited an improved adhesive resistance compared with untreated silicon. These surfaces with special nanotextures may be used for applications in microhydromechanics, wettability control, biosensors, and biochips.[19] Silicon carbide (SiC) represents a well-known band gap semiconductor material, but it is difficult to be employed for local electrochemical lithography because of its physical hardness and chemical inactivity. Jo et al. succeeded in obtaining electrochemical oxide growth on 4H-SiC. The authors increased the tip loading force (>100 nN), hence, a high electric field ($\approx 8 \times 10^6$ V cm^{-1}) was produced on a highly doped SiC surface.[20] Ahn and co-workers investigated the effect of crystalline plane orientations of SiC (*a*-, *m*-, and *c*-planes) on the local oxidation of 4H-SiC wafers by AFM. The authors found that the oxidative rate and height of the *a*-plane and the *m*-plane were lower compared to those of the *c*-plane, mainly due to the difference of the surface planar density.[21] In addition to silicon materials, other semiconducting substrates are also suitable for local electrochemical lithography. Tan et al. achieved band gap variation by selective thinning of CdTe nanowires with a conductive tip.[22] The bias voltage applied to the AFM tip was higher than the threshold of electric field-assisted evaporation of CdTe. Thus, the authors were able to precisely control the thickness of the nanowire by the real-time monitoring of the etching process. Resonance tunneling diodes with double barrier quantum well structures were prepared by varying the nanowire thickness from 3.5 to 8.5 nm. Ahn et al. investigated the oxidation SPL on different doping types (p- and n-types) and plane orientations (100, 711) of GaAs. The local oxidation rates of p-type and GaAs (100) were higher compared with those of n-type and GaAs (711), respectively.[23] Spinney and co-workers fabricated carbon lines with a width of 40 nm. Thereby, the carbon can be collected onto a positively biased AFM tip from a glassy carbon substrate and was deposited onto thin gold films when a negative voltage was applied to the tip. The mechanism may be based on high-field discharge, electromigration, or surface migration processes, but is up to now not completely understood.[24] Kumar et al. systematically studied the etching of carbon nanotubes by oxidation SPL. Features with various sizes were obtained and small structures of down to 58 nm were generated by optimizing the process parameters.[25] Recently, graphene has become one of the most exciting materials because of its highly interesting properties. Masubuchi et al. demonstrated the local oxidation of graphene with a conducting AFM tip. The graphene/graphene oxide/graphene junction showed a nonlinear *I–V* characteristic due to the presence of a Schottky barrier at the junction (Figure 2).[26] Mativetsky et al. found that graphene oxide (GO) could be reduced to graphene by a local electrochemical reduction process. The obtained micropatterned reduced GO-transistor revealed an eight

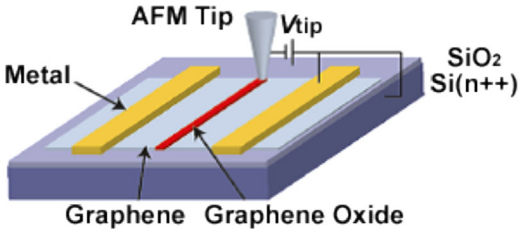

Fig. 2. Schematic setup for oxidation SPL on a graphene flake. Reproduced with permission.[26] Copyright 2011, American Chemical Society.

order of magnitude increase in current density compared to an unreduced GO-transistor.[27] Yong et al. fabricated a graphene cellular array on SiO_2 layers. The graphene layer can be oxidized by an electric field applied between the AFM tip and the substrate. Charges were accumulated on an isolated cell of patterned graphene with a decay time constant of about 70 min.[28]

2.2. Metal Substrates

Besides semiconducting materials, a great number of metal substrates have been used for the local electrochemical lithography as well, such as aluminum, gallium, germanium, molybdenum, niobium, titanium, etc.[29–38] Boisen et al. prepared an aluminum oxide pattern with a line width of ≈100 nm by oxidation SPL. By combining reactive ion etching, aluminum and aluminum oxide were both suitable as etch masks to fabricate a variety of structures.[29] Davis and co-workers also fabricated an Al oxide pattern using non-contact AFM local anodic oxidation. Compared with contact mode AFM, the non-contact mode can reduce the tip/sample interaction forces, i.e., reduce the tip wear greatly. The authors obtained a surface pattern with a line width of 10 nm by adjusting the oxidation parameters. Afterwards, this writing process was also applied on a CMOS chip, which may be used as a first step for producing nanomechanical devices.[30] Tsai et al. prepared gallium oxide nanodots on an indium tin oxide glass substrate to fabricate resistive random access memories. The structure consisted of a top layer (an AFM tip), the insulator layer (GaO_x), and the bottom layer (Ga films). The device can be switched from a high-resistance state to a low-resistance state and can be reset again by applying a suitable a bias voltage.[31] Oliveira et al. reported an AFM lithography approach on germanium thin films. The generated Ge oxide can be used as a mask and can be easily removed by water.[32] In a similar approach, Kawai et al. developed MoO_3 masks by oxidation SPL on Mo films. Afterwards, a pattern of epitaxial $(Fe,Mn)_3O_4$ thin films was obtained by chemical etching with the MoO_3 mask. The authors demonstrated that Mo-assisted AFM lithography was characterized by low contamination and high patterning flexibility, therefore, being convenient for patterning Fe-based oxide nanostructures.[33,34] Espinosa et al. fabricated a nanoscale transistor on a single-layer MoS_2 flake. The insulating MoO_3 barriers with a width of 200 nm were patterned by a conductive AFM tip being moved across the

ADVANCED ENGINEERING MATERIALS

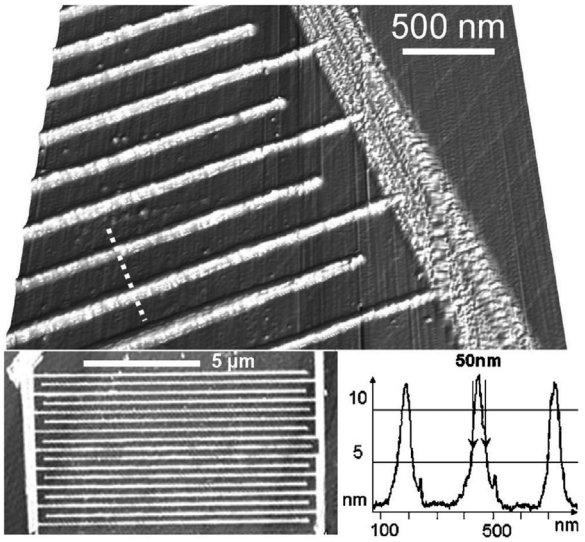

Fig. 3. AFM pictures of NbN meander-lines. The bright regions are the patterned oxide lines. Reproduced with permission.[37] Copyright 2007, AIP Publishing.

source and the drain electrodes.[35] Bouchiat et al. prepared niobium oxide protrusions by AFM-controlled anodization. This pattern could be utilized for forming Josephson junctions and superconducting quantum interference devices (SQUIDs).[36] Delacour patterned narrow niobium oxynitride lines with 30 nm resolution on niobium nitride ultrathin films. Superconducting single-photon detectors with "meander-lines" structures were fabricated and single photon response was achieved under blue and red illumination (Figure 3).[37] An early example of tip-induced electrochemical lithography on titanium surfaces was demonstrated by Suginura et al.[38] Afterwards, Siles and co-workers fabricated Ti-oxide-Ti junctions on thin Ti films by applying the local probe lithography process. The TiO_2 junctions at the nanoscale show *I–V* characteristics similar to a switchable rectifier and a memristive behavior owing to ionic motion through the metal-semiconductor interfaces.[39] Sagunova et al. studied the kinetics of local probe oxidation on different metal films, such as, V, Nb, Ta, Ti, TiN, and W. The oxidation rate depends on different parameters of the metals, like the resistivity, the presence and the thickness of a natural surface oxide film, the relationship between the densities of metals and oxides, and the electrochemical constant of the oxidation process. Moreover, the authors suggested that local insulator nano-regions were formed much easier on vanadium compared with other metals, because of the high rate of anodic probe oxidation.[40]

3. Nanolithography of Self-Assembly Monolayers

3.1. Different Self-Assembled Monolayers

Self-assembled monolayers (SAMs) have attracted much attention since experimentally discovered in 1980.[41] The applications of SAMs are numerous, such as, control of wetting and adhesion, biological engineering, molecular recognition for sensors and nanofabrication, etc.[42–45] In 1999, Sagiv and co-workers first reported that a highly ordered 18-nonadecenyltrichlorosilane (NTS) monolayer on silicon can be electrochemically oxidized by applying a bias voltage to a conductive AFM tip. A line of approximately 10 nm in width could be written on the NTS surface. As shown in Figure 4, the vinyl groups of NTS converted into carboxyl groups after electrical oxidation lithography, followed by the self-assembly of additional *n*-octadecyltrichlorosilane (OTS) films.[46] In subsequent work, the authors extended this lithography to the robust and methyl-terminated OTS monolayers. The tip induced an electrochemical conversion from $-CH_3$ to $-COOH$ groups which enabled other chemical derivatization steps.[47] Moreover, Wouters et al. conducted further research on the lithography process of OTS monolayers on Si substrates. There are two essential processes for this electrochemical lithography: Firstly, the conversion of methyl groups of OTS to carboxyl groups, and secondly, the formation of silicon oxide at the silicon substrate. The formation of carboxyl groups will lead to a significant change in friction force, while the growth of silicon oxide features a distinct increase in height. Therefore, the authors could determine the time scales of these two oxidized processes through fiction and height measurements after different periods of the oxidation process.[48] Hoeppener et al. extended this local oxidation lithography method to other OTS monolayers modified substrates besides Si, such as $AlOx$, TiO_2, ITO, and even graphene. Yang et al. performed this patterning method on two other monolayers, i.e., a hexadecyl monolayer and an *N*-hydroxysuccinimide (NHS)-ester-functionalized undecyl (NHS-UA) monolayer. Compared with the oxidation conditions applied for OTS on Si, milder conditions were required on these two monolayers: the bias voltage thresholds were reduced by approximately 2 V for the hexadecyl monolayers and ≈3.5 V for the NHS-UA monolayers. In addition, the

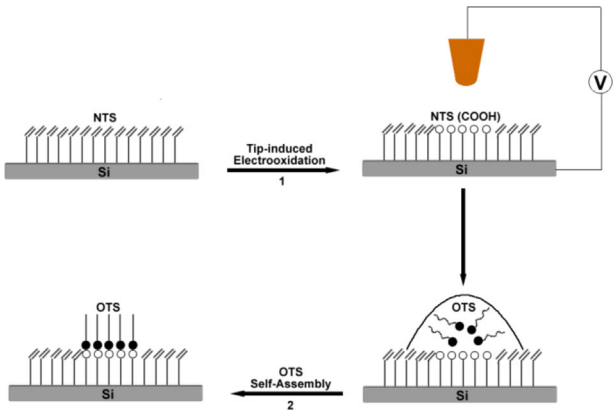

Fig. 4. Schematic view of a two-step electrochemical patterning and development process: 1) tip-induced electro-oxidation of NTS self-assembled monolayer on the silicon substrate and 2) site-selective self-assembly of OTS on the polar surface groups. Reproduced with permission.[46] Copyright 1999, Wiley.

REVIEW

generated carboxyl groups also provided possibilities for a further pattern fabrication.[49] Unruh et al. utilized a mixed monolayer which consisted of propyltrichlorosilane and triethoxysilane derivatives featuring a redox-active trimethylbenzoquinone moiety. As shown in Figure 5, oxidative and reductive patterns were formed on the same surface when a positive and a negative bias voltage were applied to the AFM tip. Afterwards, the authors assembled pentathiophene dimethylchlorosilane and C_{60} molecules on the oxidized and reduced patterns, respectively. This suggested that both, p-type and n-type materials, can be assembled on the same substrate, which may enable in the future the fabrication of heterogeneous nanostructures.[50] Qin et al. fabricated oligo(ethylene glycol) (OEG)-terminated alkyl monolayers on silicon substrates. The conversion of the ethylene glycol groups to carboxylic and aldehyde groups was achieved by oxidation SPL without substantial degradation of the OEG layer or oxidation of the silicon substrate. Subsequently, the authors attached avidin molecules to the oxidized pattern, followed by immobilization of biotinylated molecules and nanoparticles. According to the avidin–biotin binding interactions, a wide range of biotinylated biomolecules could be patterned on these modified silicon substrates.[51]

3.2. Applications of Chemically Active Patterns

As mentioned above, the local electrochemical lithography of surfaces offers a promising method to introduce chemical functionalities at the nanometer scale. Commonly used films for this technique are OTS monolayers. The formed −COOH groups generated during the lithographic process were utilized as templates for the fabrication of chemically active patterns. Checco et al. proved that ethanol vapor could be condensed onto the hydrophilic −COOH stripes and the topology of the ethanol nanostripes was well described by the density functional theory with dispersive, non-retarded potentials.[52] Berson et al. fabricated an ion-conducting surface pattern based on the top −COOH groups. The length scales of the patterns ranged from nanometers to centimeters. The transport of a single layer of different metal ions could be confined to a predefined surface path by utilizing this approach.[53] Druzhinina and co-workers fabricated ring structures by electrochemical oxidation lithography on OTS monolayers. Two different chemical areas were obtained: the core, consisting of silicon oxide, and the surrounding, an acid-functionalized rim feature.[54] Afterwards, the authors fabricated a bilayer structure, i.e., the −COOH groups generated by lithography can link to a

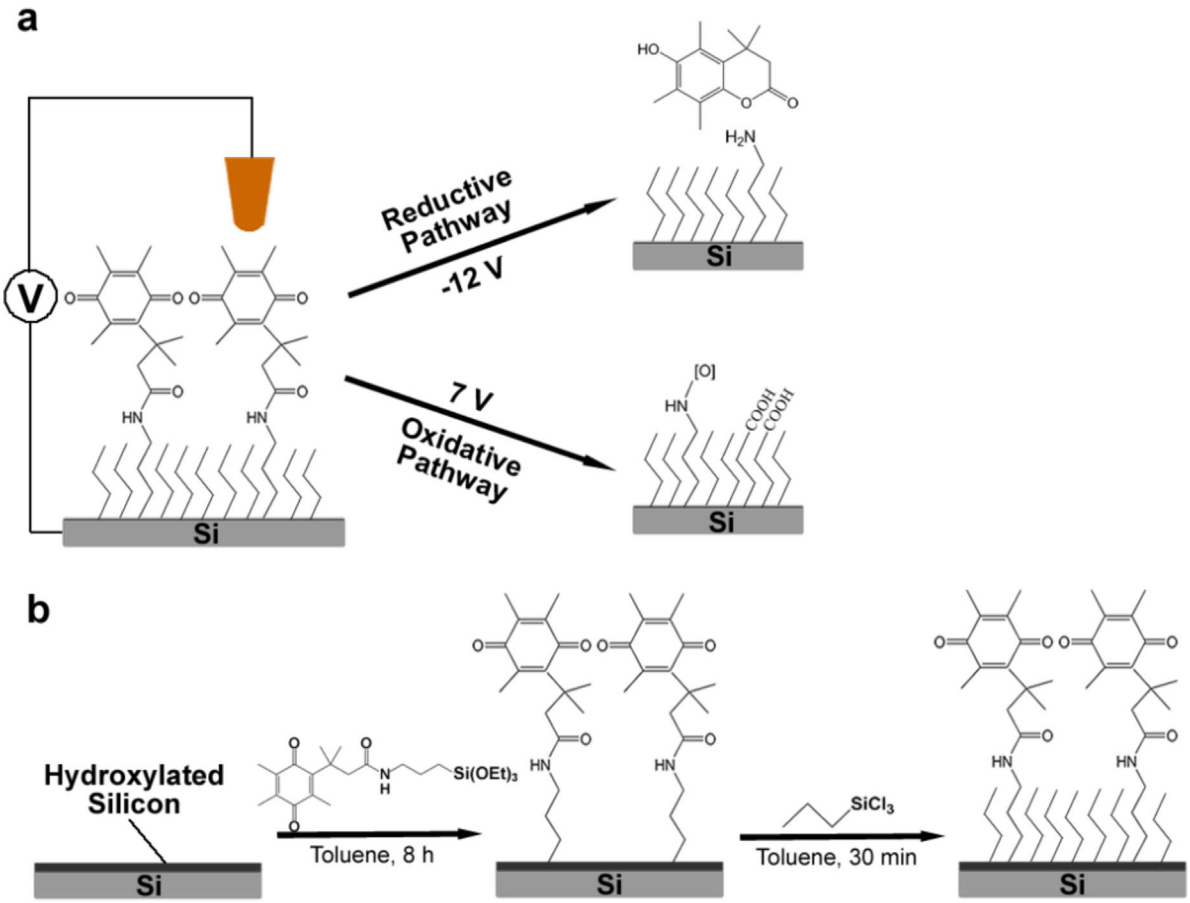

Fig. 5. (a) Schematic illustration of AFM patterning on the mixed monolayer with positive and negative bias voltage. (b) The route for synthesis of mixed monolayer composed of benzoquinone and propyltrichlorosilane. Reproduced with permission.[50] Copyright 2010, American Chemical Society.

ADVANCED ENGINEERING MATERIALS

second OTS layer based on the formation of hydrogen bonds. The tip-induced oxidation applied on the bilayer required significantly longer pulse durations. Utilizing this feature of the oxidation process, the authors fabricated a nanometric gap between the monolayer and bilayer structures, where a self-assembly nanoparticle was anchored. This combined approach may have broad applications for sensors or single-electron transistors.[55] In subsequent research, the authors performed the site-selective assembly of individual, preselected nanotubes onto the pattern area terminated by −COOH groups. As shown in Figure 6, a cross-shaped configuration of two carbon nanotubes was obtained. Moreover, the construction material is not only limited to carbon nanotubes but might be suitable for other nanowires as well.[56] Haensch et al. assembled bromo-undecyltrichlorosilane to this COOH-terminated patterns, followed by the site-selective generation of an azide-terminated adlayer and performing the highly effective 1,3-dipolar cycloaddition reaction with acetylene-functionalized molecules.[57] Becer et al. also used this bromine-functionalized pattern to prepare polymer brushes by atom transfer radical polymerization (ATRP).[58] Chowdhury et al. developed a new wetting driven self-assembly approach based on a local electrochemically oxidized OTS monolayer used as a template. First, some non-volatile low-melting organic materials were selectively immobilized onto the pattern due to the hydrophilic property of the −COOH groups. Subsequently, the silver or gold ions binding to the organic materials could form elemental metal nanoparticles by further chemical processing. This method can be extended to a variety of non-volatile materials with appropriate melting temperature and surface wetting characteristics to produce surface nanostructures.[59]

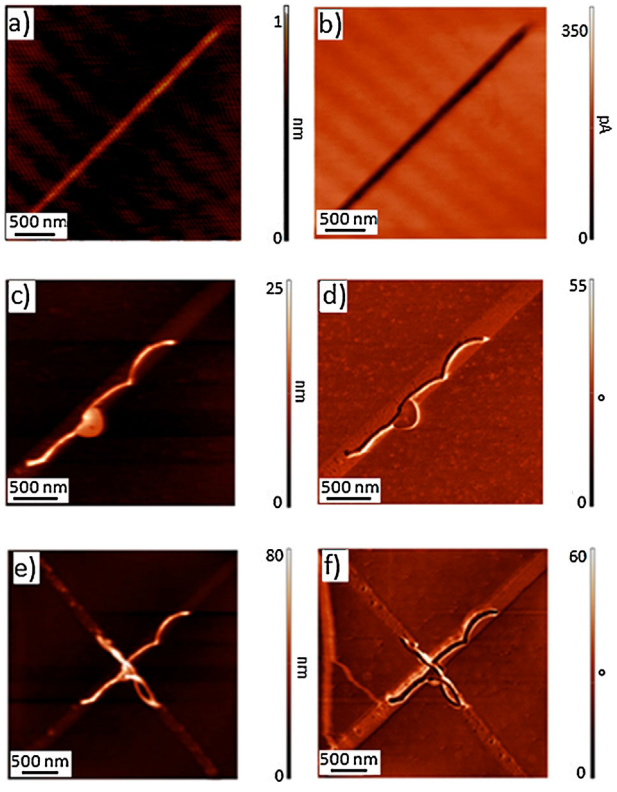

Fig. 6. (a) Height and (b) lateral force images of an oxidized line on OTS monolayers. (c) Height and (d) phase images of an individual carbon nanotube assembled on the same line. (e) Height and (f) phase images of a second carbon nanotube assembled on the vertical line. Reproduced with permission.[56] Copyright 2013, American Chemical Society.

4. Nanolithography of Polymer Coatings

Scanning probe-induced electropolymerization represents another important member of the local electrochemical lithography process family. Jang et al. developed the rapid direct writing of conductive polymer nanostructures by electrochemical cross-linking. As shown in Figure 7, a conductive AFM tip acted as the working electrode and precursor polymer **1** could be converted into the conducting polymer **2** by applying an appropriate voltage between the tip and the substrates. The structure sizes can be controlled by the writing speed, the writing mode, and the applied voltage.[60] According to a similar approach, Nam et al. fabricated polypyrrole nanowires by electropolymerization of pyrrole monomers on gold surfaces.[61] Xie et al. created nanoscale heterogeneous structures from the insulating matrix poly(*N*-vinyl carbazole) (PVK). The conductive structure formation was based on the cross-linking of the carbazole groups by bridge oxygen, which was induced by an AFM nano-discharge process.[62] Mandal et al. observed that the substrate-specific molecule geometry and mobility represented two important rate-determining factors for the tip-induced chain polymerization of diacetylene compounds.[63] Afterwards, Okawa et al. fabricated polydiacetylene nanowires by chain polymerization initiated by an STM tip. A resonant tunneling diode was produced by connecting these two conductive polydiacetylene nanowires to a single phthalocyanine molecule.[64]

In addition to electropolymerization, local electrochemical lithography can also be employed directly on

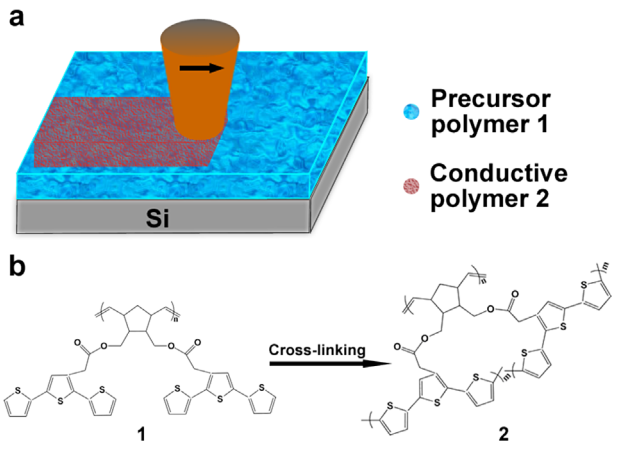

Fig. 7. (a) Electropolymerization nanolithography process. (b) Conversion of insulating precursor polymer to conductive polymer by electrochemical cross-linking. Reproduced with permission.[60] Copyright 2004, American Chemical Society.

polymer films to obtain nanostructures. Advincula et al. investigated the performance of different layer-by-layer-assembled polymer films with AFM electrical lithography. For films of quinquethiophene/phthalocyanine, the conductivity can be controlled reversibly between the conducting state and the insulating state, due to an electrochemical charging–discharging effect (Figure 8).[65] For poly(3,4-ethylenedioxythiophene)-poly(styrenesulfonate)/poly(diallyldimethylammonium chloride) (PDDA) multilayers, a write–read–erasable memory device was fabricated. A large height increase was observed after the lithography process based on mass transport by Joule heating. Afterwards, the pattern could be erased by applying a low voltage (from −1 to 1 V).[66] In the case of poly{1-4[4-(3-carboxy-4-hydroxyphenylazo)–benzene–sulfonamido]-1,2-ethanediyl, sodium salt} (PAZO)/PDDA) films, a similar phenomenon of mass transport and alignment of azobenzene was observed due to the local electric field-induced Joule heating.[67] Choi et al. obtained nano-/micro-sized patterns on a methoxy-poly(ethylene glycol) (PEG) modified Si substrate. The protrusive silicon oxide pattern created by electrical oxidation lithography shows a higher chemical activity compared to the original PEG area. As a consequence, streptavidin labeled with Au-colloidal particles and non-labeled streptavidin could be selectively immobilized on the silicon oxide-patterned areas.[68] Rankin et al. guided the orientation of ferroelectric domains in a poly(vinylidene fluoride) (PVDF) film by a surface pattern. Depended on a surface photoreduction reaction, metal nanoparticles were deposited onto the pattern area.[69] Ma and co-workers reported for the first time the utilization of poly(methyl methacrylate) (PMMA) brushes as electrets to store electrostatic charges. Both positively and negatively charged patterns could be formed by controlling the voltage applied to the tip. In addition, the authors found that the trapped charges in the PMMA brushes were stable even in organic solvents, such as, hexane and toluene. These results may open new ways for polymer brushes to be part of applications in electronic devices.[70]

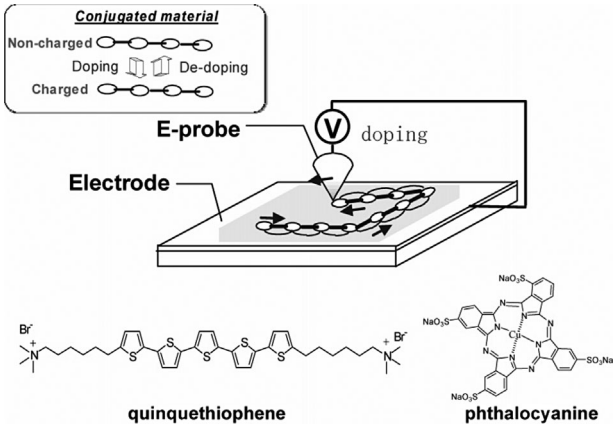

Fig. 8. Schematic illustration of the fabrication process of a write–read memory device. Reproduced with permission.[65] Copyright 2006, American Chemical Society.

5. Technological Changes

As a nanotechnology tool, local electrochemical lithography is utilized so far only in the laboratory rather than in an industrial production. Technological changes or improvements are the key factors for the future development of this patterning method. In short, the whole lithography process is controlled by three parts, i.e., the tip, the lithography mediums, and the substrate. Any optimization of these three parts will have significant impact on the improvement of the lithography process.

5.1. Changes of the Electrochemical Lithography Medium

For the typical local electrochemical lithography experiment, water vapor is adsorbed and forms a water bridge between the tip and the substrates which is regarded as an electrochemical cell. Sometimes it is desired to exchange the aqueous environment by other gas or liquids. In 1997, Pyle reported AFM lithography under an anhydrous ammonia atmosphere. Si_3N_4 lines were grown on the silicon surface with a negatively biased tip. The electrochemical process occurred as described by equation 3.[71]

$$3\,Si + 4\,NH_3 \rightarrow Si_3N_4 + 6\,H_2 \quad (3)$$

Garcia et al. achieved SiC*x* nanostructures based on a dynamic AFM operating in ethyl alcohol vapor.[72] The lithography process is illustrated in Figure 9. The liquid bridge, acting as the electrochemical cell, was induced by the bias voltage. When the bias voltage was switched off, the tip would be retracted and the bridge would break. Afterwards, the authors performed the polymerization and cross-linking of the octane molecules on the silicon surface and prepared a pattern of 2 nm structures with 6 nm periodicities.[73] Zhang et al. demonstrated the reduction of graphene oxide at the nanoscale with a Pt-coated tip under hydrogen atmosphere. The conductive tip used here played a key role in the catalytic reduction of the graphene. Conductive-crossed nanoribbons and field effect transistors (FET) with good functionalities were fabricated by this method.[74] In order to avoid oxidizing the substrates below, in some cases, inert atmosphere was used for the local electrochemical lithography. Fréchet and co-workers reported organic monolayers containing 3,5-dimethoxy-R,R-dimethylbenzyloxycarbonyl (DDZ)-protected amino and thiol groups. After the electrical cleavage of the

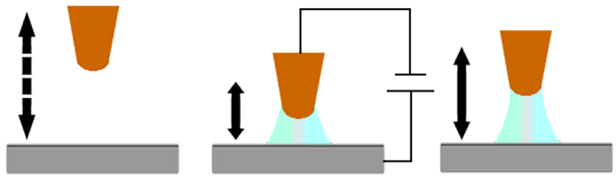

Fig. 9. Schematic illustration of the dynamic lithography process. Reproduced with permission.[72] Copyright 2005, Wiley.

ADVANCED ENGINEERING MATERIALS

DDZ groups, amine and thiol patterns were produced on the surface, followed by self-assembly of dendritic macromolecules and Au nanoparticles, respectively.[75,76]

An early study of utilizing liquid as lithographic medium was reported by Nagahara et al. The patterning of Si and GaAs surfaces was performed in (0.05%) HF solution. The oxide generated by the electrochemical reactions could be etched directly by HF and patterns with a line width of 20 nm were accomplished.[77] Hilton et al. performed lithography on silicon surfaces in a water environment. The oxide structures showed a full order of magnitude increase in both structure height and growth rate compared to lithographic process performed in air, due to the electrolytically generated bubbles in water which promoted the oxide growth.[78] Mirkin et al. investigated the effect of different monolayers on the electrochemical lithography process. The authors suggested that both the hydroxide anion and the bias voltage were essential factors for the pattern generation. As such, high hydroxide ion concentrations and shorter chain lengths of molecules of the monolayers, which are easily accessible for the hydroxide anions, favor the oxidation of the silicon. Conversely, negatively charged groups, like −COOH-terminated monolayers, will create an electrostatic barrier for OH^- penetration, which suppresses the silicon oxide formation.[79] Kinser and co-workers proved that even an inert nonpolar organic solvent (i.e., hexadecane) could be utilized as a medium to induce oxidation on hydrogen-passivated silicon substrates. The authors suggested that the organic solvent may have only little effect on the lithography process when the organic solvent was in contact with air or even at low relative humidity. The chemical and kinetic behavior was consistent with lithography processes performed in air environment as well.[80,81] Fréchet et al. investigated the role of surface hydrophobicity for electrochemical lithography in hexadecane. As shown in Figure 10, there are two possible chemical pathways for this patterning process. For a hydrophilic surface, a stable water meniscus is generated on the surface. Thus, the oxide growth after the lithography process is in analogy with the oxidation process in air environment. In the case of a hydrophobic hexamethyldisilizane (HMDS) modified surface, the wafer cannot form a stable meniscus. As a consequence, the solvent will decompose by the bias voltage and generates an sp^2-hybridized carbon structure on the surface.[82] Obermair et al. developed an interesting approach for the reversible writing of Cu nanostructures with an AFM tip. When polycrystalline gold films were immersed into copper sulfate and H_2SO_4 solution, a thin copper oxide film will automatically form on the gold surface, which can be used as a passivating coating to inhibit the electrochemical deposition of Cu. The authors utilized an AFM tip to scan on the gold surface at force loads of 10 nN, resulting in the destruction of the passivating layers. Subsequently, Cu could be electrochemically deposited on the scanning position. Afterwards, this Cu nanostructures could be dissolved again by applying an electrochemical dissolution potential.[83]

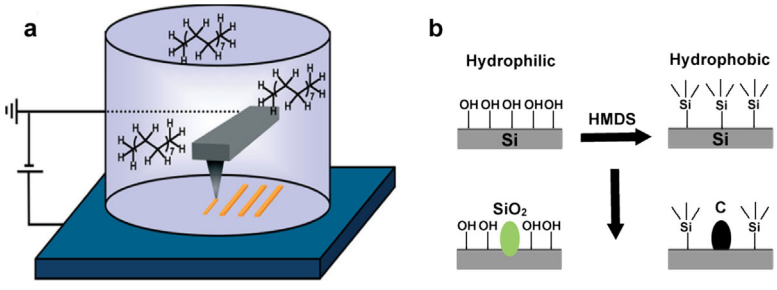

Fig. 10. (a) Representation of the set-up for local electrochemical lithography in hexadecane. (b) Schematic representation of the two chemical pathways according to surface hydrophilicity. Reproduced with permission.[82] Copyright 2007, Wiley.

5.2. Electrochemical "Dip-Pen" Nanolithography

The dip-pen nanolithography (DPN) method has attracted great attention since it was developed by Mirkin and co-workers in 1999.[84] This technique relies on an AFM tip to transfer molecular inks to the substrate through a water meniscus. In 2000, Liu and co-workers introduced an additional development step to DPN. The authors suggested that the tiny water meniscus could be not only a transfer medium, but also an electrochemical cell in which the dissolved salts could be reduced into metals and deposited on the substrate surface. They called this new technique electrochemical dip-pen nanolithography (E-DPN).[85] Two examples of Pt and Au metal reduction and deposition on a Si surface were demonstrated. During the scanning process, H_2PtCl_6 and $HAuCl_4$ adsorbed on AFM tips, dissolve in the water meniscus, and were electrochemically reduced to Pt(0) and Au(0), respectively, by applying a positive bias voltage to the tip.[85,86] Afterwards, the authors electrochemically polymerized 3,4-ethylenedioxythiophene (EDOT) on both semiconducting and insulating surfaces, and poly-EDOT lines with a width of less than 100 nm were obtained.[87] Gallium nitride/gallium oxide nanowire heterostructures were prepared as well. In this study, a KOH solution was used as ink and was adsorbed on the tip. The electrochemical reaction between the GaN and KOH occurred when applying a suitable bias voltage to the tip and gallium oxide was generated on an GaN nanowire. The authors demonstrated that this heterostructures revealed rather different electronic properties due to the electronic transport barriers of gallium oxide.[88] Similar to the work of Liu et al., Chu deposited gold nanoparticles on a single-walled carbon nanotube with E-DPN. This method may have potential applications for the fabrication of nanodevices, like single-electron transistors, etc.[89] Cai et al. developed another approach which was also derived from DPN but was different from the approach introduced by Liu et al. First, a COOH-terminated pattern was fabricated by AFM-based local oxidation lithography on an OTS monolayer. Meanwhile, the ink molecules (mercaptopropyltrimethoxysilane)

adsorbed on the AFM tip were delivered onto the just generated –COOH structures according to a hydrolysis reaction (Figure 11). Multilayers can even be accomplished by repeating this oxidation lithography accompanied with the delivery process.[90] Tanabe and co-workers employed a new approach which is different from the conventional E-DPN. First, Ag^+ ions were absorbed onto TiO_2 substrates before the lithography process was performed. Voltage was applied between the tip and the substrates, and the Ag ions could be reduced to Ag nanoparticles on the surface. By a different scanning method, it was possible to obtain Ag nanoparticles and nanorods with various size and morphology.[91]

5.3. Scanning Electrochemical Microscopy

Scanning electrochemical microscopy (SECM) is a kind of scanning probe microscopy which is used to measure the local electrochemical behavior of gases, liquids, and solid interfaces. SECM records the current flowing through an ultramicroelectrode (UME), which results from the oxidation or reduction reactions on the surface of the samples. In addition to mapping the reactivity of chemical species on the interface, this technology can be used for surface patterning as well. An early work was reported by Mandler and co-workers who applied the SECM for the high-resolution etching of n- and p-GaAs.[92] Afterwards, the group reported gold and palladium electrodeposition onto polyvinylpyridine films. First, $Ru(NH_3)_6^{3+}$ was reduced to $Ru(NH_3)^{2+}$ by an UME. The reduced mediator could be used not only for monitoring the distance between the UME and the surface, but can also diffuse to the polymer films. Subsequently the $AuCl_4-$ or $PdCl_4^{2-}$, which were incorporated in the polymeric matrix, could be reduced on the surface.[93] Wittstock et al. applied an Au microelectrode to induce the local desorption of self-assembled dodecylthiolate monolayers on gold surfaces. After that, another functionalized thiol was re-adsorption on the desorbed pattern.[94] Combined with the microcontact printing method, Wilhelm developed a patterned enzyme layer composed of glucose oxidase and horseradish peroxidase.[95] Hazimeh et al. discussed the principle of SECM to study the surface etching kinetics, which showed that the pattern evolution followed the expansion of the etchant on the substrate surface. The model that was presented is based on the formation of a reductive etching of perfluorinated monolayers which were immobilized on insulating (Si/SiO_2 or glass) or conductive (ITO) surfaces.[96] Marck et al. reported that the local polymerization of polythiophene was achieved by SECM. The monomer in the solution was electropolymerized onto an oxidized manganese dioxide surface. In addition, the authors used a "chemical lens" that can react with the UME-induced protons to focus the protons' diffusion field. Thus, the resolution of the pattern could be scaled down to 8 μm with a 10 μm Pt microelectrode.[97] Grisotto accomplished the local electrografting of vinylic monomers in aqueous solution by SECM. The reaction process is shown in Figure 12. The substrate acted as the cathodic working electrode and the UME as the anodic counter electrode. The localized grafting reactions occurred on the substrate (reduction of protons), on the tip (oxidation of water), and in the medium (radical reactions).[98] Compared with conventional AFM electrochemical lithography process, SECM lithography is an effective tool for the rapid fabrication of micrometer-size patterns, but is limited in the obtainable resolution.

5.4. Parallel Lithography

The structures generated by a tip-induced electrochemical lithography are fabricated in a serial patterning processes and the scan speed is limited by the piezo system. To overcome these problems, some parallel lithography methods have been developed. Nishimura et al. prepared an SPM tip with a contact area of $2.5 \times 1.9\ \mu m^2$ and the resulting throughput reached $125\ \mu m^2\ s^{-1}$, which of 10,000 times faster than that of conventional SPM oxidation lithography.[99] Wouters and co-workers created large-scale oxidation patterns on OTS monolayers by a modified automated AFM. The automated equipment was facilitated with a programmable θ-y stage with ≈1 μm precision. The tip can be landed and withdrawn automatically and a software was implemented to control the lithography process. Based on this development, a pattern composed of 1,000 identical circles was obtained with a

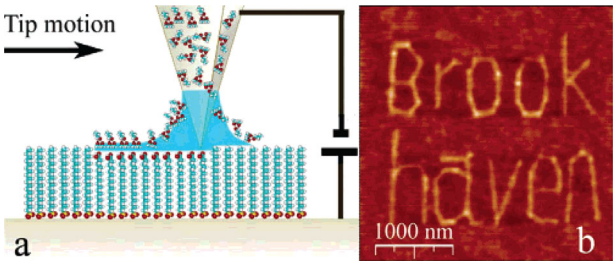

Fig. 11. (a) Schematic representation of the lithographic process and (b) a typical pattern prepared on OTS monolayers. Reproduced with permission.[90] Copyright 2005, American Chemical Society.

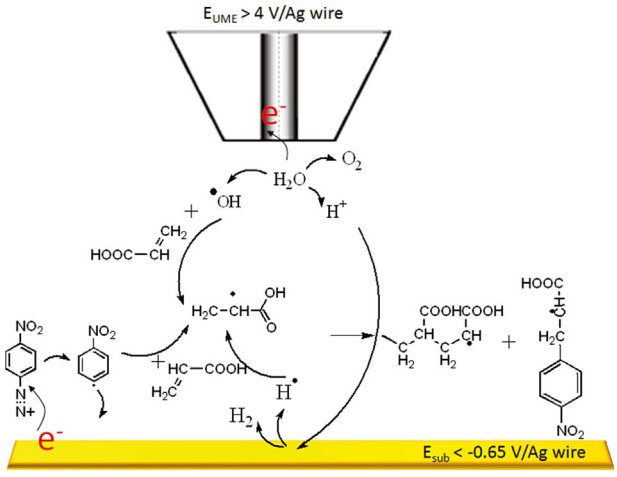

Fig. 12. Schematic view of chemical reactions during the electrografting process. Reproduced with permission.[98] Copyright 2011, American Chemical Society.

ADVANCED ENGINEERING MATERIALS

single tip. Afterwards, a four-cantilever array was also used as the first attempt for demonstrating the parallel probe oxidation of OTS monolayers.[100] Li et al. created nanoscale devices on the $LaAlO_3/SrTiO_3$ interface with a 1-D array of conductive tips. The authors were able to control each tip independently by holding the tip array at a fixed potential and changing the voltage applied to the individual electrode.[101] Deiss and co-workers prepared a multiscaled electrochemical probe with 6,000 nanotips by wet chemical etching followed by sputter-coating of an ordered optical fiber bundle, which was used to pattern a Teflon surface. This SECM lithography method is expected to generate structures in a short time in a parallelized and high-throughput manner.[102] García and co-workers demonstrated a simple way to upscale the local oxidation nanolithography with an Au-coated digital video disk (DVD) polymeric stamp. A 5×6 mm^2 pattern with variable length and 100 nm in width was generated on silicon substrates.[103] In subsequent effort, the group developed an instrument to control the lithography process precisely which consisted of a stamp holder, a sample base, and a supporting frame (Figure 13). The instrument enabled to control the applied pressure to the sample and the position of the stamp. Arrays of parallel lines with a separation of 100 nm were achieved over 1 cm^2 within 1 min.[104] Then, the authors introduced a thin film of polymethylmethacrylate (PMMA) between the stamp and silicon substrates which was easily removed by acetone after the lithography step. The flexibility of the PMMA films enabled the stamp to form a more homogenous contact with the surface of silicon.[105] Similar to the previous work, Albonetti developed Au-coated polydimethylsiloxane (PDMS) as a soft stamp to perform the local oxidation lithography on silicon surfaces.[106] Hoeppener and co-workers used a transmission electron microscope (TEM) copper grid as a stamp to accomplish a local electrochemical oxidation on OTS monolayers. The grid should be exposed to a saturated water vapor atmosphere first, and is subsequently pressed against the OTS films on silicon immediately while applying a suitable bias voltage. The authors proved the conversion of $-CH_3$ groups of the OTS to $-COOH$ groups after lithography, which was in analogy with the AFM tip-induced local oxidation on OTS monolayers.[107] The stamp-induced pattern on one OTS film could be transferred again to another new OTS monolayer. When exposed to a wet environment, water will adsorb onto the oxidized area due to the hydrophilic property of $-COOH$ groups. Then, the electrochemical oxidation reactions occurred again when applied a suitable bias voltage between two OTS films and the pattern information on one surface can be replicated to the other one.[108]

5.5. Other Innovations

The improvements of the lithography processes and equipments offer promising prospects for a practical application of the nanofabrication approach. Normally, a water meniscus between the tip and the substrate represents an essential factor in the majority of the local electrochemical processes which is regarded as a cell for electrochemical reactions. Su et al. developed an effective method to enhance the local relative humidity by approaching a capillary tube to the lithographic area (Figure 14). Water is evaporated from the capillary tube, followed by diffusion to the surrounding area, and then condenses between the tip and the substrate. The advantage of this approach is a fast response in relative humidity that can be accomplished in the prospective area instead of affecting the whole system.[109] Vicary and co-workers designed a high-speed scan stage using a quartz crystal resonator (Figure 15). Single silicon oxide nanostructures with a lateral dimension of 15 nm were generated on timescales as low as 500 ns by tapping mode AFM. High-speed oxidation lithography of 2 cm s^{-1} was realized with a quartz crystal resonator operating at 20 kHz.[110] A sharp and wear-resistant tip is essential for AFM lithography application. Smirnov et al. developed diamond nanowire-based AFM tips with 300 nm thick nanocrystalline diamond layers. The apex radius of the integrated diamond nanowire is as small as 5 nm and the resonance frequencies of the modified tips increase with increasing diamond coating thickness (from 160 to 260 kHz). Moreover, a significant enhancement of the quality factor was generated ($Q = 120$ to 710). These diamond-modified probes showed a high imaging resolution and good wear-resistance properties compared with commercially available Si, diamond, or metal-coated tips. In later investigation, the authors doped boron into the diamond-modified tips to increase the conductivity by focused ion beam technology. These conductive tips can be used e.g. in bifunctional AFM–SECM measurements.[111]

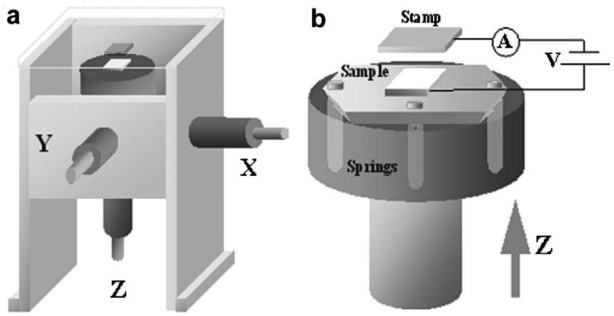

Fig. 13. Schematic illustration of the parallel oxidation lithography instrument. Reproduced with permission.[104] Copyright 2006, AIP publishing.

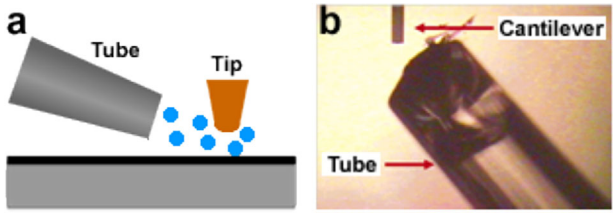

Fig. 14. (a) Scheme of enhancing the local relative humidity with a tube. (b) An optical photograph of a capillary tube approaching an AFM cantilever. Reproduced with permission.[109] Copyright 2005, American Chemical Society.

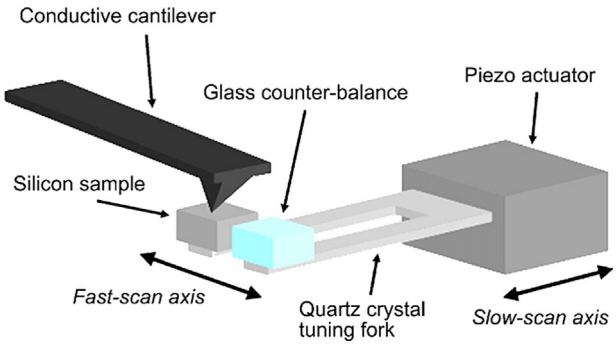

Fig. 15. The structure of the high-speed scan stage. A silicon sample is mounted on one leg of the quartz crystal resonator and a glass counter-balance is fixed on the other leg. Reproduced with permission.[110] Copyright 2008, Elsevier.

6. Conclusions and Outlook

Photolithography is currently the most widely used technique in the semiconductor industry. The small features of a pattern are limited by the wavelength of the light, therefore, traditional UV lithographic processes are inherently limited. Many alternative techniques have been developed, such as, extreme ultraviolet lithography, X-ray lithography, electron beam lithography, etc. These techniques allow minimum feature sizes down to 50 nm. But they require complex facilities which lead to excessive costs.

Scanning probe lithography represents a promising approach which also offers precise control with high lateral resolution. More importantly, it is a low-cost technique and can be utilized under ambient conditions. Up to now, the SPL technique is mainly based on electrical, mechanical, and thermal interactions between the tip and the substrate. In this feature article, we focused on the electrical field-induced local probe lithography process. By comparison, this lithography method is able to form patterns and at the same time induce a variety of chemical changes on the surface based on electrochemical reactions. So far, this technique has been used on both semiconducting and metallic substrates. Many chemical active patterns are also achieved on different self-assembly monolayer surfaces. Moreover, combined with electrochemical deposition and electropolymerization methods, different nanostructures with a broad range of materials can be obtained.

Although there have been some technological innovations developed recently, local electrochemical lithography is still a research method for the laboratory scale rather than for industrial application. In general, the resolution of patterns depends largely on the size of the tip. Therefore, a very sharp tip is required if a pattern with a small size is desired. Moreover, problems arise due to the low durability of tips applied during the lithographic process. This may be partly solved by producing tips with durable materials like diamond or scanning in a noncontact mode which can largely reduce the damage of the tip. Another challenge is the low-throughput production that is also inherent to other scanning probe lithographic techniques. The use of stamps is a solution to increase the lithography rate, but the patterning resolution is up to now decreased compared to the utilization of the tip. Tip arrays may be a good choice to solve this problem and they are widely used in the dip-pen nanolithography techniques, however, the control of multiple tips to perform electrochemical lithography is also not a simple procedure. The large number of possibilities emerging from the local electrochemical lithography motivates the further improvement of capabilities of the instruments and suggests that this patterning method will contribute to the future development of nanofabrication.

Article first published online: January 22, 2016
Manuscript Revised: October 19, 2015
Manuscript Received: September 26, 2015

[1] Y.-Z. Long, M. Yu, B. Sun, C.-Z. Gu, Z. Fan, *Chem. Soc. Rev.* **2012**, *41*, 4560.
[2] S. Lal, S. Link, N. J. Halas, *Nat. Photonics* **2007**, *1*, 641.
[3] F. Canal, J. Sanchis, M. J. Vicent, *Curr. Opin. Biotechnol*. **2011**, *22*, 894.
[4] H. Wang, H. Dai, *Chem. Soc. Rev.* **2013**, *42*, 3088.
[5] M. Junkin, J. Watson, J. P. Vande Geest, P. K. Wong, *Adv. Mater.* **2009**, *21*, 1247.
[6] J. Y. Cheng, D. P. Sanders, H. D. Truong, S. Harrer, A. Friz, S. Holmes, M. Colburn, W. D. Hinsberg, *ACS Nano* **2010**, *4*, 4815.
[7] H. Dai, N. Franklin, J. Han, *Appl. Phys. Lett*. **1998**, *73*, 1508.
[8] E. B. Cooper, S. R. Manalis, H. Fang, H. Dai, K. Matsumoto, S. C. Minne, T. Hunt, C. F. Quate, *Appl. Phys. Lett*. **1999**, *75*, 3566.
[9] J. A. Dagata, J. Schneir, H. H. Harary, C. J. Evans, M. T. Postek, J. Bennett, *Appl. Phys. Lett*. **1990**, *56*, 2001.
[10] H. C. Day, D. R. Allee, *Appl. Phys. Lett*. **1993**, *62*, 2691.
[11] D. Wouters, S. Hoeppener, U. S. Schubert, *Angew. Chem. Int. Ed*. **2009**, *48*, 1732.
[12] H. Sugimura, N. Nakagiri, *Jpn. J. Appl. Phys*. **1995**, *34*, 3406.
[13] R. Garcia, R. V Martinez, J. Martinez, *Chem. Soc. Rev.* **2006**, *35*, 29.
[14] X. N. Xie, H. J. Chung, Z. J. Liu, S.-W. Yang, C. H. Sow, A. T. S. Wee, *Adv. Mater.* **2007**, *19*, 2618.
[15] J. S. Hwang, Z. Y. You, S. Y. Lin, Z. S. Hu, C. T. Wu, C. W. Chen, K. H. Chen, *Appl. Phys. Lett*. **2005**, *86*, 161901.
[16] T. Vijaykumar, G. Raina, S. Heun, G. U. Kulkarni, *J. Phys. Chem. C* **2008**, *112*, 13311.
[17] N. S. Losilla, N. S. Oxtoby, J. Martinez, F. Garcia, R. Garcia, M. Mas-Torrent, J. Veciana, C. Rovira, *Nanotechnology* **2008**, *19*, 455308.
[18] J. Martinez, R. V. Martínez, R. Garcia, *Nano Lett*. **2008**, *8*, 3636.
[19] Y. Mo, M. Bai, *J. Colloid Interface Sci.* **2009**, *333*, 304.

[20] Y.-D. Jo, S.-H. Seo, W. Bahng, S.-C. Kim, N.-K. Kim, S.-S. Kim, S.-M. Koo, *Appl. Phys. Lett*. **2010**, *96*, 082105.
[21] J.-J. Ahn, Y.-D. Jo, S.-C. Kim, J.-H. Lee, S.-M. Koo, *Nanoscale Res. Lett*. **2011**, *6*, 235.
[22] S. Tan, Z. Tang, X. Liang, N. A. Kotov, *Nano Lett*. **2004**, *4*, 1637.
[23] J.-J. Ahn, K.-S. Moon, S.-M. Koo, *Nanoscale Res. Lett*. **2011**, *6*, 550.
[24] P. S. Spinney, S. D. Collins, R. L. Smith, *Nano Lett*. **2007**, *7*, 1512.
[25] K. Kumar, O. Sul, S. Strauf, D. S. Choi, F. Fisher, M. G. Prasad, E.-H. Yang, *IEEE Trans. Nanotechnol*. **2011**, *10*, 849.
[26] S. Masubuchi, M. Arai, T. Machida, *Nano Lett*. **2011**, *11*, 4542.
[27] J. M. Mativetsky, E. Treossi, E. Orgiu, M. Melucci, G. P. Veronese, P. Samorì, V. Palermo, *J. Am. Chem. Soc*. **2010**, *132*, 14130.
[28] H. Yong, K. Kim, W. Choi, J. Park, M. Ahmad, Y. Seo, *Carbon* **2012**, *50*, 4640.
[29] A. Boisen, K. Birkelund, O. Hansen, F. Grey, *J. Vac. Sci. Technol. B* **1998**, *16*, 2977.
[30] Z. J. Davis, G. Abadal, O. Hansen, X. Borisé, N. Barniol, F. Pérez-Murano, A. Boisen, *Ultramicroscopy* **2003**, *97*, 467.
[31] J. T. H. Tsai, C.-H. Hsu, C.-Y. Hsu, C.-S. Yang, *Electron. Lett*. **2013**, *49*, 554.
[32] A. B. Oliveira, G. Medeiros-Ribeiro, A. Azevedo, *Nanotechnology* **2009**, *20*, 345301.
[33] L. Pellegrino, Y. Yanagisawa, M. Ishikawa, T. Matsumoto, H. Tanaka, T. Kawai, *Adv. Mater*. **2006**, *18*, 3099.
[34] N. Suzuki, H. Tanaka, T. Kawai, *Adv. Mater*. **2008**, *20*, 909.
[35] F. M. Espinosa, Y. K. Ryu, K. Marinov, D. Dumcenco, A. Kis, R. Garcia, *Appl. Phys. Lett*. **2015**, *106*, 103503.
[36] V. Bouchiat, M. Faucher, C. Thirion, W. Wernsdorfer, T. Fournier, B. Pannetier, *Appl. Phys. Lett*. **2001**, *79*, 123.
[37] C. Delacour, J. Claudon, J.-P. Poizat, B. Pannetier, V. Bouchiat, R. Espiau de Lamaestre, J.-C. Villegier, M. Tarkhov, A. Korneev, B. Voronov, G. Gol'tsman, *Appl. Phys. Lett*. **2007**, *90*, 191116.
[38] H. Sugimura, T. Uchida, N. Kitamura, H. Masuhara, *Appl. Phys. Lett*. **1993**, *63*, 1288.
[39] P. F. Siles, B. S. Archanjo, D. L. Baptista, V. L. Pimentel, J. Joshua, B. R. A. Neves, G. Medeiros-Ribeiro, *J. Appl. Phys*. **2011**, *110*, 024511.
[40] I. V. Sagunova, V. I. Shevyakov, S. A. Gavrilov, A. N. Belov, *Semiconductors* **2010**, *44*, 1709.
[41] J. Sagiv, *J. Am. Chem. Soc*. **1980**, *399*, 92.
[42] S. Schilp, A. Kueller, A. Rosenhahn, M. Grunze, M. E. Pettitt, M. E. Callow, J. A. Callow, *Biointerphases* **2007**, *2*, 143.
[43] S. Sun, M. Montague, K. Critchley, M.-S. Chen, W. J. Dressick, S. D. Evans, G. J. Leggett, *Nano Lett*. **2006**, *6*, 29.
[44] K. Motesharei, D. Myles, *J. Am. Chem. Soc*. **1998**, *7863*, 7328.
[45] X.-M. Li, J. Huskens, D. N. Reinhoudt, *J. Mater. Chem*. **2004**, *14*, 2954.
[46] R. Maoz, S. R. Cohen, J. Sagiv, *Adv. Mater*. **1999**, *11*, 55.
[47] R. Maoz, E. Frydman, S. R. Cohen, J. Sagiv, *Adv. Mater*. **2000**, *12*, 725.
[48] D. Wouters, R. Willems, S. Hoeppener, C. F. J. Flipse, U. S. Schubert, *Adv. Funct. Mater*. **2005**, *15*, 938.
[49] M. Yang, D. Wouters, M. Giesbers, U. S. Schubert, H. Zuilhof, *ACS Nano* **2009**, *3*, 2887.
[50] D. A. Unruh, C. Mauldin, S. J. Pastine, M. Rolandi, J. M. J. Fréchet, *J. Am. Chem. Soc*. **2010**, *132*, 6890.
[51] G. Qin, J. Gu, K. Liu, Z. Xiao, C. M. Yam, C. Cai, *Langmuir* **2011**, *27*, 6987.
[52] A. Checco, O. Gang, B. Ocko, *Phys. Rev. Lett*. **2006**, *96*, 056104.
[53] J. Berson, D. Burshtain, A. Zeira, A. Yoffe, R. Maoz, J. Sagiv, *Nat. Mater*. **2015**, *14*, 613.
[54] T. Druzhinina, S. Hoeppener, N. Herzer, U. S. Schubert, *J. Mater. Chem*. **2011**, *21*, 8532.
[55] T. S. Druzhinina, S. Hoeppener, U. S. Schubert, *Small* **2012**, *8*, 852.
[56] T. S. Druzhinina, C. Höppener, S. Hoeppener, U. S. Schubert, *Langmuir* **2013**, *29*, 7515.
[57] C. Haensch, S. Hoeppener, U. S. Schubert, *Nanotechnology* **2009**, *20*, 135302.
[58] C. R. Becer, C. Haensch, S. Hoeppener, U. S. Schubert, *Small* **2007**, *3*, 220.
[59] D. Chowdhury, R. Maoz, J. Sagiv, *Nano Lett*. **2007**, *7*, 1770.
[60] S.-Y. Jang, M. Marquez, G. A. Sotzing, *J. Am. Chem. Soc*. **2004**, *126*, 9476.
[61] K. Nam, G. Lee, H. Jung, J. Park, C. H. Kim, J. Seo, D. S. Yoon, S. W. Lee, T. Kwon, *Nanotechnology* **2011**, *22*, 225303.
[62] X. N. Xie, M. Deng, H. Xu, S. W. Yang, D. C. Qi, X. Y. Gao, H. J. Chung, C. H. Sow, V. B. C. Tan, A. T. S. Wee, *J. Am. Chem. Soc*. **2006**, *128*, 2738.
[63] S. K. Mandal, Y. Okawa, T. Hasegawa, M. Aono, *ACS Nano* **2011**, *5*, 2779.
[64] Y. Okawa, S. K. Mandal, C. Hu, Y. Tateyama, S. Goedecker, S. Tsukamoto, T. Hasegawa, J. K. Gimzewski, M. Aono, *J. Am. Chem. Soc*. **2011**, *133*, 8227.
[65] A. Baba, J. Locklin, R. Xu, R. Advincula, *J. Phys. Chem. B* **2006**, *110*, 42.
[66] G. Jiang, A. Baba, R. Advincula, *Langmuir* **2007**, *23*, 817.
[67] A. Baba, G. Jiang, K.-M. Park, J.-Y. Park, H.-K. Shin, R. Advincula, *J. Phys. Chem. B* **2006**, *110*, 17309.
[68] I. Choi, S. K. Kang, J. Lee, Y. Kim, J. Yi, *Biomaterials* **2006**, *27*, 4655.
[69] C. Rankin, C. Chou, D. Conklin, D. A. Bonnell, *ACS Nano* **2007**, *1*, 234.
[70] X. Ma, Z. Xie, Z. Liu, X. Liu, T. Cao, Z. Zheng, *Adv. Funct. Mater*. **2013**, *23*, 3239.

[71] J. L. Pyle, T. G. Ruskell, R. K. Workman, X. Yao, D. Sarid, *J. Vac. Sci. Technol. B* **1997**, *15*, 38.
[72] M. Tello, R. Garcia, J. A. Martín-Gago, N. F. Martínez, M. S. Martín-González, L. Aballe, A. Baranov, L. Gregoratti, *Adv. Mater.* **2005**, *17*, 1480.
[73] R. V. Martínez, N. S. Losilla, J. Martinez, Y. Huttel, R. Garcia, *Nano Lett.* **2007**, *7*, 1846.
[74] K. Zhang, Q. Fu, N. Pan, X. Yu, J. Liu, Y. Luo, X. Wang, J. Yang, J. Hou, *Nat. Commun.* **2012**, *3*, 1194.
[75] Z. M. Fresco, I. Suez, S. A. Backer, J. M. J. Fréchet, *J. Am. Chem. Soc.* **2004**, *126*, 8374.
[76] Z. M. Fresco, J. M. J. Fréchet, *J. Am. Chem. Soc.* **2005**, *127*, 8302.
[77] L. A. Nagahara, T. Thundat, S. M. Lindsay, *Appl. Phys. Lett.* **1990**, *57*, 270.
[78] A. M. Hilton, K. W. Jacobson, B. P. Lynch, G. J. Simpson, *J. Vac. Sci. Technol. B* **2008**, *26*, 47.
[79] J. Jang, R. G. Sanedrin, D. Maspoch, S. Hwang, T. Fujigaya, Y. Jeon, R. A. Vega, X. Chen, C. A. Mirkin, *Nano Lett.* **2008**, *2*, 1451.
[80] C. R. Kinser, M. J. Schmitz, M. C. Hersam, *Nano Lett.* **2005**, *5*, 91.
[81] C. R. Kinser, M. J. Schmitz, M. C. Hersam, *Adv. Mater.* **2006**, *18*, 1377.
[82] I. Suez, M. Rolandi, S. A. Backer, A. Scholl, A. Doran, D. Okawa, A. Zettl, J. M. J. Fréchet, *Adv. Mater.* **2007**, *19*, 3570.
[83] C. Obermair, M. Kress, A. Wagner, T. Schimmel, *Beilstein J. Nanotechnol.* **2012**, *3*, 824.
[84] R. D. Piner, J. Zhu, F. Xu, S. Hong, C. A. Mirkin, *Science* **1999**, *283*, 661.
[85] Y. Li, B. W. Maynor, J. Liu, *J. Am. Chem. Soc.* **2001**, *123*, 2105.
[86] B. W. Maynor, Y. Li, J. Liu, *Langmuir* **2001**, *17*, 2575.
[87] B. W. Maynor, S. F. Filocamo, M. W. Grinstaff, J. Liu, *J. Am. Chem. Soc.* **2002**, *124*, 522.
[88] B. W. Maynor, J. Li, C. Lu, J. Liu, *J. Am. Chem. Soc.* **2004**, *126*, 6409.
[89] H. Chu, Z. Jin, Y. Zhang, W. Zhou, L. Ding, Y. Li, *J. Phys. Chem. C* **2008**, *112*, 13437.
[90] Y. Cai, B. M. Ocko, *J. Am. Chem. Soc.* **2005**, *127*, 16287.
[91] I. Tanabe, T. Tatsuma, *J. Phys. Chem. C* **2012**, *116*, 3995.
[92] D. Mandler, A. J. Bard, *Langmuir* **1990**, *6*, 1489.
[93] D. Mandler, A. J. Bard, *J. Electrochem. Soc.* **1990**, *137*, 1079.
[94] G. Wittstock, R. Hesse, W. Schuhmann, *Electroanalysis* **1997**, *9*, 746.
[95] T. Wilhelm, G. Wittstock, *Angew. Chem. Int. Ed.* **2003**, *42*, 2248.
[96] H. Hazimeh, S. Nunige, R. Cornut, C. Lefrou, C. Combellas, F. Kanoufi, *Anal. Chem.* **2011**, *83*, 6106.
[97] C. Marck, K. Borgwarth, J. Heinze, *Chem. Mater.* **2001**, *13*, 747.
[98] F. Grisotto, A. Ghorbal, C. Goyer, J. Charlier, S. Palacin, *Chem. Mater.* **2011**, *23*, 1396.
[99] S. Nishimura, T. Ogino, J. Shirakashi, *Jpn. J. Appl. Phys.* **2008**, *47*, 715.
[100] D. Wouters, U. S. Schubert, *Nanotechnology* **2007**, *18*, 485306.
[101] S. Li, M. Huang, F. Bi, H. Rubin-falcone, S. Ryu, C. Eom, P. Irvin, J. Levy, *IEEE Trans. Nanotechnol.* **2013**, *12*, 518.
[102] F. Deiss, C. Combellas, C. Fretigny, N. Sojic, F. Kanoufi, *Anal. Chem.* **2010**, *82*, 5169.
[103] M. Cavallini, P. Mei, F. Biscarini, R. García, *Appl. Phys. Lett.* **2003**, *83*, 5286.
[104] J. Martinez, N. S. Losilla, F. Biscarini, G. Schmidt, T. Borzenko, L. W. Molenkamp, R. Garcia, *Rev. Sci. Instrum.* **2006**, *77*, 086106.
[105] N. S. Losilla, J. Martínez, R. García, *Nanotechnology* **2009**, *20*, 475304.
[106] C. Albonetti, J. Martinez, N. S. Losilla, P. Greco, M. Cavallini, F. Borgatti, M. Montecchi, L. Pasquali, R. Garcia, F. Biscarini, *Nanotechnology* **2008**, *19*, 435303.
[107] S. Hoeppener, R. Maoz, J. Sagiv, *Nano Lett.* **2003**, *3*, 761.
[108] S. Hoeppener, R. Maoz, J. Sagiv, *Adv. Mater.* **2006**, *18*, 1286.
[109] M. Su, Z. Pan, V. P. Dravid, T. Thundat, *Langmuir* **2005**, *21*, 10902.
[110] J. A. Vicary, M. J. Miles, *Ultramicroscopy* **2008**, *108*, 1120.
[111] W. Smirnov, A. Kriele, E. Sillero, J. Hees, O. A. Williams, N. Yang, C. Kranz, C. E. Nebel, *Anal. Chem.* **2011**, *83*, 4936.

Publication P2

Micropatterns of [Fe-Fe]-hydrogenase active-site model complexes fabricated by electro-oxidative lithography

H. Liu, R. Trautwein, B. Schröter, A. Ignaszak, W. Weigand, S. Hoeppener, U. S. Schubert

Langmuir **2015**, *31*, 11748−11753.

Langmuir

Article

pubs.acs.org/Langmuir

Micropatterns of [Fe-Fe]-Hydrogenase Active-Site Model Complexes Fabricated by Electro-Oxidative Lithography

He Liu,[†,‡] Ralf Trautwein,[∥] Bernd Schröter,[⊥] Anna Ignaszak,[†,§] Wolfgang Weigand,[‡,∥] Stephanie Hoeppener,*[,†,‡] and Ulrich S. Schubert[†,‡]

[†]Laboratory of Organic and Macromolecular Chemistry (IOMC), Friedrich Schiller University Jena, Humboldtstr. 10, 07743 Jena, Germany

[‡]Jena Center for Soft Matter (JCSM), Friedrich Schiller University Jena, Philosophenweg 3, 07743 Jena, Germany

[§]Department of Chemistry, University of New Brunswick, 30 Dineen Drive, Fredericton, New Brunswick, E3B 5A3, Canada

[∥]Institute for Inorganic and Analytical Chemistry, Friedrich Schiller University Jena, Humboldtstr. 8, 07743 Jena, Germany

[⊥]Institute of Solid State Physics, Institute of Applied Physics, Friedrich Schiller University Jena, Helmholtzweg 5, 07743 Jena, Germany

ABSTRACT: [Fe-Fe]-hydrogenase active site model complexes ($[Fe(CO)_3]_2[(\mu\text{-}SCH_2)_2C(CH_2OH)_2]$) were immobilized on micropatterned *n*-octadecyltrichlorosilane (OTS) monolayers deposited on a Si substrate to form a microscale catalytic system. The micropatterns were generated by electro-oxidative lithography performed with a conductive TEM grid. The [Fe-Fe]-hydrogenase active-site complex molecules were selectively anchored in lithographic line areas with good coverage. Additionally, the biomimetic metal centers of the hydrogenase active-site complex molecules still maintained their catalytic activity and their redox-active properties after the immobilization process, which was proven by cyclic voltammetry.

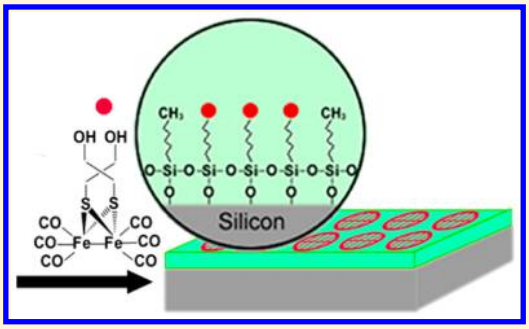

INTRODUCTION

Hydrogen is regarded as one of the best fuels for fuel cells.[1−4] Several fundamental problems remain to be solved to utilize hydrogen as an alternative clean energy source. One challenge is to develop new approaches to generate hydrogen. In nature, hydrogen can be efficiently generated by hydrogenase enzymes, which catalyze the reversible redox reaction of dihydrogen ($H_2 \leftrightarrow 2H^+ + 2e^-$), a process that plays a key role in the microbial energy metabolism.[5] This reversible catalytic reaction is accomplished by the [Fe-Fe]- or [Ni-Fe]-active sites of hydrogenase enzymes.[6,7] For many applications the immobilization of the hydrogenase active-site enzymes is a fundamental step for their utilization. Ibrahim et al. reported that it is possible to incorporate diiron units of [Fe-Fe]-hydrogenase active sites into a poly(pyrrole) framework grown on platinum or carbon.[8] Model complexes of [Fe-Fe]-hydrogenase active sites bearing suitable functionalities can be attached, for example, onto amino-functionalized electrode surfaces[9,10] or negatively charged self-assembled monolayers,[11] or even by binding a redox mediator to the surface and immobilization of the [Fe-Fe]-hydrogenase active sites.[12] Also, the *N*-hydroxysuccinimide ester formation was utilized to attach [Fe-Fe]-hydrogenase active site models.[13] On the basis of such systems also bioinspired and biohybrid surfaces can be created.[14−16] In these approaches the immobilization of hydrogenase active-site model complexes poses special requirements, as the molecular binding and orientation play an important role in the efficiency of the catalytic process.[17] Another critical point of the immobilization is the functionalization efficiency of the binding process itself to form dense monolayers of hydrogenase active-site complexes on the surface. Therefore, a careful selection of the applied preparation protocols is required. For some applications it is desirable to arrange, for example, enzyme biomimetic molecules in small, spatially defined regions of a substrate. These include, for example, the fabrication of sensor devices, where the local confinement is used to improve their sensitivity or the immobilization of active molecules in micro- or even nanometer areas for the study of enzyme reactions or enzyme cascades. In the latter application different enzymes are located in close vicinity on a surface, and the products generated from the first enzyme can be further processed by a second enzyme. For these cascade reactions diffusion plays an important role and small distances between the enzymes improve the efficiency of the cascade reactions.[18] For these tasks a versatile lithographic structuring technique is required, which potentially allows the covalent immobilization and combination of different enzyme model molecules on surfaces. A suitable technique to achieve these goals is chemical lithography, which allows the fabrication of hierarchical structures with micro- and even nanometer precision providing tailor-made chemical binding sites. Here we utilize electro-oxidative lithography to create such chemically active surface

Received: July 24, 2015
Revised: September 30, 2015
Published: October 14, 2015

DOI: 10.1021/acs.langmuir.5b02730
Langmuir 2015, 31, 11748−11753

Scheme 1. Schematic Representation of Electro-Oxidative Lithography Based on a TEM Grid and Assembly of [Fe-Fe]-Hydrogenase Active Site Model Complexes

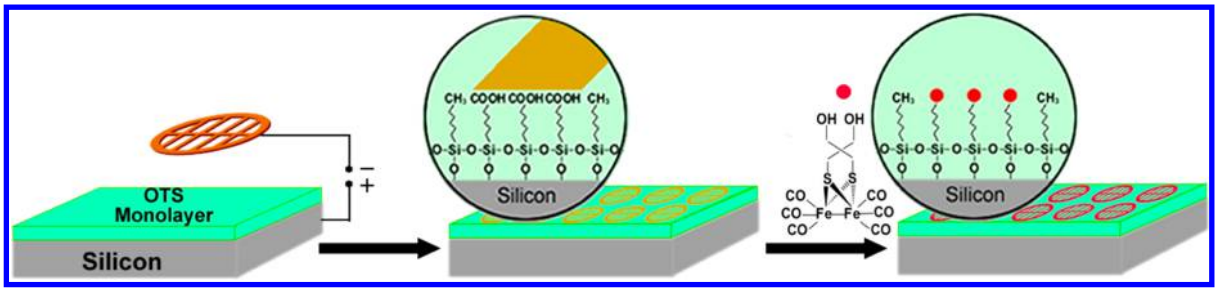

patterns on a *n*-octadecyltrichlorosilane monolayer.[19,20] This electrochemical−oxidation process creates carboxylic acid functionalities in the patterned areas, which can be subsequently used to bind active molecules onto the pattern. This approach is moreover compatible with the existing advanced integrated circuit processes, which may open up other possibilities for the preparation of micro H_2 fuel cells.[21] In this study we utilize [Fe-Fe]-hydrogenase active site model complexes ($[Fe(CO)_3]_2[(\mu\text{-}SCH_2)_2C(CH_2OH)_2]$) to functionalize the created surface patterns. The catalytically active complex ($[Fe(CO)_3]_2[(\mu\text{-}SCH_2)_2C(CH_2OH)_2]$)[22] has been prepared by reaction of $Fe_3(CO)_{12}$ with 1,2-dithiolane-4,4-dimethanol in toluene at 100 °C for 1 h, followed by column chromatography in 45% yield. The two hydroxy groups are ideally suited to react with the carboxylic groups achieving ester bonds, which enable a strong anchoring of the [Fe-Fe]-hydrogenase active-site model complexes to the lithographic line pattern (Scheme 1). After the assembly process, the [Fe-Fe]-hydrogenase active-site model complexes still maintained their catalytic activity.

EXPERIMENTAL DETAILS

Materials. Toluene, *n*-octadecyltrichlorosilane (OTS), biscyclohexane (BCH), *N*,*N*-dimethylformamide (DMF), *N*,*N*′-dicyclohexylcarbodiimide (DCC), and 4-(dimethylamino)pyridine (DMAP) were obtained from Sigma-Aldrich. BCH was distilled over sodium before use. All other reagents were used without further purification. Double-sided polished p-type silicon wafers (100) were obtained from Siegert Wafer (resistivity: 5 to 10 Ω cm). The Si substrates were treated with Ar plasma for 2 min before use.

Preparation of [Fe-Fe]-Hydrogenase Active-Site Functionalized Microstructured Silicon Substrates. OTS monolayers were prepared by immersing the cleaned silicon wafers in a solution of OTS (10 μL) in BCH (2 mL) for 1 min, followed by sonication in toluene and blow drying in N_2. Subsequently, the electro-oxidative lithography was performed with a TEM grid (Agar Grids 300 Parallel Bar, Copper, 3.05 mm). The applied voltage was −25 V and the pulse time was set to 3 s. Nine individual circle patterns were fabricated on each OTS-Si substrate (1.5 cm × 1 cm) to increase the area of complex functionalization for CV measurements. [Fe-Fe]-hydrogenase active-site model complex molecules were synthesized as previously described.[22] Afterward, the micropatterned OTS-Si substrate was incubated in a reaction mixture of [Fe-Fe]-hydrogenase active site complexes (2 mg), DCC (50 mg), DMAP (10 mg), and DMF (2 mL) for 24 h, followed by sonication in DMF and drying in N_2. The substrates were stored under a protective atmosphere in a desiccator. Only AFM and FT-IR studies were performed under ambient conditions after the [Fe-Fe]-hydrogenase active-site complexes were immobilized on the surface patterns.

Thin-Film Characterization. The films were analyzed by atomic force microscopy (AFM, NT-MDT, NTegra Aura) using commercial AFM tips (NT-MDT, NCS35/AIBS) in tapping and contact mode.

Auger electron spectroscopy (AES) measurements were performed at room temperature using a scanning Auger electron spectrometer with a Varian cylindrical mirror analyzer. AES spectra were acquired with a primary beam energy of 3 keV. The diameter of the electron beam is in the range of 20 μm.

FT-IR investigations were conducted on a Bruker Hyperion system in the rim area of the TEM grid patterns to maximize the functionalized area. Measurements were performed in transmission mode using a MLCT liquid-nitrogen-cooled detector and a polarizer to improve the signal-to-noise ratio. Spectra were recorded using a spectra averaging of 128 measurements at a resolution of 4 cm^{-1}.

Electrochemical Characterization. Cyclic voltammetric measurements were performed by utilizing a three-electrode technique utilizing an electrochemical analyzer (Princeton Applied Research, VersaSTAT MC). The working electrode and the counter electrode were formed by the [Fe-Fe]-hydrogenase active site functionalized Si substrate and a platinum wire, respectively. Ag/Ag^+ in CH_3CN was used as the reference electrode. All experiments were performed in CH_3CN (Aldrich, anhydrous, 99.8%) solutions containing 0.1 M Bu_4NPF_6 (Fluka, electrochem. grade) at room temperature. The solutions were purged with N_2 for 5 min and measurements were conducted under a constant N_2 flow. All cyclic voltammograms were recorded at a scan rate of 100 mV s^{-1}. All potential values reported in this study are referenced to the potential of the Fc/Fc^+ couple.

RESULTS AND DISCUSSION

Preparation and Characterization of [Fe-Fe]-Si Films. The aim of the present study is the assembly of [Fe-Fe]-hydrogenase active-site complexes ([Fe-Fe]) on a micropatterned OTS-Si substrate ([Fe-Fe]-Si) to form a microscale catalytic system. The outline of the performed preparation sequence is schematically illustrated in Scheme 1.

First, the micropatterns were prepared utilizing electro-oxidative lithography, which has been previously reported.[19] Briefly summarized, electro-oxidative lithography is a tip or stamp based approach that allows the structuring of OTS monolayers with chemically active functional groups. A negative bias voltage is applied between the conductive stamp and the substrate, resulting in the local oxidation of the OTS monolayers. Thereby, the water meniscus, formed by the water layer on the stamp and the monolayer-coated substrate, creates an electrochemical cell. By applying the voltage to this cell, a water mediated electrochemical oxidation of the monolayer takes place and polar functional groups, presumably, carboxylic acids, are formed. The width of the generated patterns depends on the dimension of stamp and the patterning conditions, including the applied voltage, the pulse duration, and the relative humidity, which defines the size of the formed water meniscus. In this study, a TEM copper grid with a diameter of 3.05 mm consisting of parallel line features was utilized as a stamp. The successful pattern formation can be

DOI: 10.1021/acs.langmuir.5b02730
Langmuir 2015, 31, 11748−11753

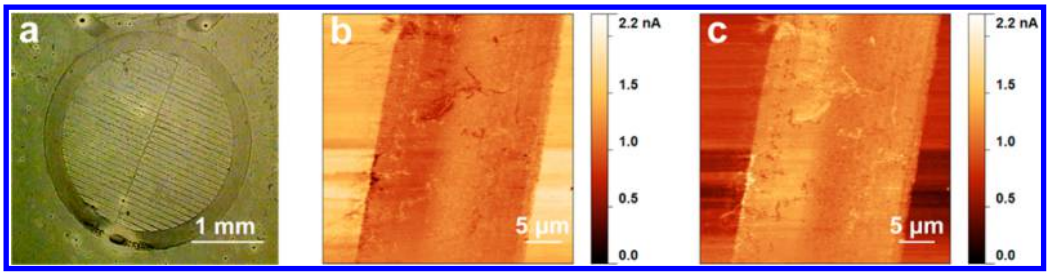

Figure 1. (a) Optical micrograph of a water condensation TEM grid pattern on OTS-Si. (b,c) Friction force contact mode AFM images of a stripe of the printed TEM grid pattern. The scanning directions are set from left to right (b) and from right to left (c).

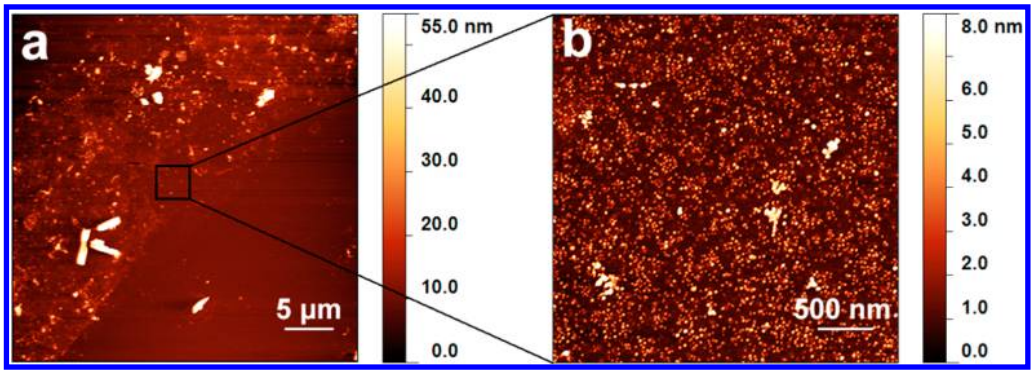

Figure 2. (a) Low- and (b) high-magnification tapping mode AFM images of [Fe-Fe]-hydrogenase active-site model complexes generated on the chemically active TEM grid pattern.

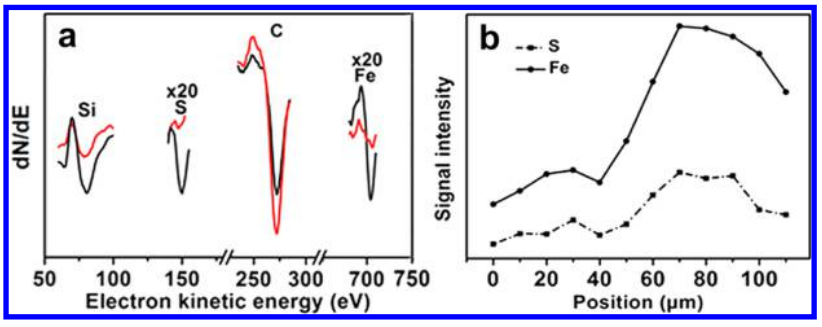

Figure 3. (a) AES spectra acquired in a stripe area (black line) and the space between two stripes (red line) on a micropattern of [Fe-Fe]-Si. (b) Auger signal intensities of Fe and S at different positions of the micropattern obtained by a line scan.

easily evaluated by applying water vapor onto the structured OTS monolayer (Figure 1a).

The water vapor preferentially condenses on the grid structures due to the hydrophilic properties of the −COOH functions (corresponding to the dark regions in Figure 1a), whereas the nonoxidized OTS monolayer retains its hydrophobicity. Additionally, this effect can be visualized by friction force AFM studies. Figure 1b shows a friction force image of a line of the oxidized TEM grid pattern. It is clearly seen that the line feature appears with a dark contrast. If the scan direction is reversed, also the contrast of the line changes (Figure 1c). This observation reflects the large spot-to-spot force variations associated with the different hydration and adhesion properties of the $-CH_3$ and −COOH regions.[20] The reversed friction contrast is regarded as a strong indication for a change of the surface properties and can be seen as a hint that only negligible topographic alterations occur during the oxidation process.

These microstructured substrates were utilized to selectively bind [Fe-Fe]-hydrogenase active-site complexes via ester formation. Therefore, the micropatterns were activated with DCC/DMAP. Figure 2a,b depicts tapping mode AFM images of the micropattern after incubation and immobilization of the [Fe-Fe]-hydrogenase active-site molecules. It can be seen that the molecules selectively attach to the lithographic line pattern and a large number of small particles is attached on the patterned area (Figure 2b). Despite a careful rinsing of the substrates after functionalization it is observed that also larger aggregates are formed on the patterns (Figure 2a).

The chemical composition of the bound molecules cannot be determined by means of AFM investigations. Therefore, additional Auger electron spectroscopy (AES) investigations were conducted. By utilization of a microscope, the positions of the micropatterns on the substrate were located and it was possible to perform accurate measurements in the line area as well as in the nonpatterned areas. As shown in Figure 3a, the signal intensities of Fe and S are much higher in the line area than in the space area, which is an additional evidence of the binding of [Fe-Fe]-hydrogenase active site complexes in the micropatterned areas. Figure 3b depicts a line scan measured across of an individual line feature focusing on the Fe and S signals. In the nonfunctionalized space area (from 0 to 40 μm), only low signal intensities were obtained for both Fe and S,

DOI: 10.1021/acs.langmuir.5b02730
Langmuir 2015, 31, 11748−11753

whereas a gradual increase in both signals is observed in the region from 40 to ~70 μm of the scanning position. The signal intensities of Fe and S decrease after the electron beam reached a scanner position of 90 μm, coinciding with the return of the electron beam to the nonpatterned area. Despite the limited resolution provided by this method, a clear evidence of the presence of the [Fe-Fe]-hydrogenase active-site complexes on the patterned template is provided.

Further insight into the binding of the [Fe-Fe]-hydrogenase active site model complexes to the micropatterns is provided by FT-IR analysis. Because of the fact that the sensitivity for the investigation of monolayers and submonolayers of molecules by FT-IR is low, investigations on the patterned substrates were performed in the rime region of the pattern (Figure 1a). Figure 4 depicts the results obtained from investigations performed on

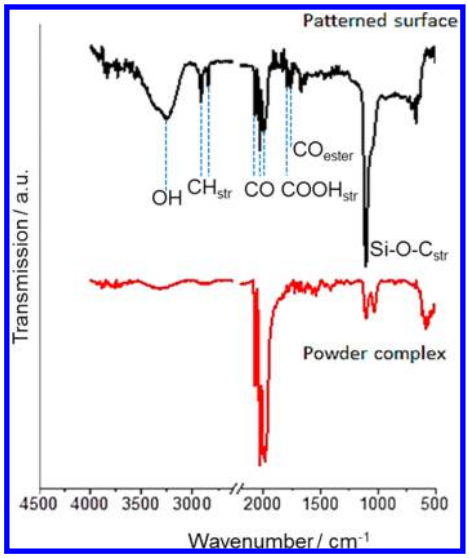

Figure 4. FT-IR investigations on a patterned substrate (top) and on the complex (bottom). Spectra intensities are presented in arbitrary units and are not drawn to scale. Both spectra show essential characteristics of the [Fe-Fe]-hydrogenase active site model complexes as well as they reveal characteristic peaks of the monolayer.

the patterned substrates, which are compared with a control measurement performed on the pure complex. Therefore, the complex was dissolved and deposited on a silicon wafer, and the solvent was allowed to dry.

There is a good agreement with the absorption found for the [Fe-Fe]-hydrogenase active-site complex and the spectra obtained on the pattern. In both cases strong CO absorption are observed as well as the characteristic absorption at 1050 to 1100 cm^{-1}, which were found in the pure complex. The absorption at 1100 cm^{-1} in the spectrum of the patterned area is overlaid with the characteristic Si−O−C asymmetric stretching vibration of the OTS molecules bound to the silicon wafer. The binding of the [Fe-Fe]-hydrogenase active site molecules is reflected by the appearance of a small absorption at 1760 cm^{-1}, which can be assigned to the ester formation between the carboxylic groups of the pattern and the OH groups of the complexes. Because of the small absorption intensities a further investigation of the binding configuration, however, is difficult. Additionally, it is observed that sharp absorption originating from the CH stretching vibrations arise in the spectrum obtained on the patterned substrate. These belong to the well-ordered functionalized OTS monolayer (and the monolayer on the backside of the silicon wafer) and indicate that the binding process did not influence the quality of the monolayer. Moreover, an absorption that can be assigned to the carboxylic acid is observed at 1790 cm^{-1}, indicating, that the [Fe-Fe]-hydrogenase active-site complexes do not form a dense coverage on the patterned area. This is conceivable if the bulky structure of the [Fe-Fe]-complex is taken into account. Because of steric hindrances it is unlikely that every carboxylic acid functionality, available in the patterned monolayer, will bind to a complex molecule. This is in agreement with the AFM images, which confirmed a noncomplete, granular functionalization of the patterned areas with complex molecules.

Electrochemical Characterization. Finally, the catalytic activity of the [Fe-Fe]-hydrogenase active-site complex molecules on the micropatterns was investigated by cyclic voltammetry (CV) performed in CH_3CN solution. As shown in Figure 5a, there are no obvious redox peaks for the micropatterned OTS-Si before the functionalization with the [Fe-Fe]-hydrogenase active-site complexes; however, in the case of [Fe-Fe]-Si, the cyclic voltammetry curve displays one oxidation and two reduction processes. The irreversible anodic wave in the absence of acid appears at +0.41 V versus F_c/F_c^+. This wave marks the oxidation of Fe^IFe^I to $Fe^{II}Fe^{II}$. The observed values differ slightly from reference curves of the free complex (+0.67 V),[22] which is reasonable as in the present case an immobilized molecule attached to a surface is investigated. The CV of [Fe-Fe]-Si displays a quasi-reversible and an irreversible reduction events at −1.51 and −2.45 V, respectively. In comparison, the reduction of the [Fe-Fe]-hydrogenase active site complex in the solution phase showed the ability to uptake two electrons at the same potential of −1.53 V (scan rate = 0.2 V/s) due to the phenomenon of potential inversion of the two one-electron reduction steps.[22] In

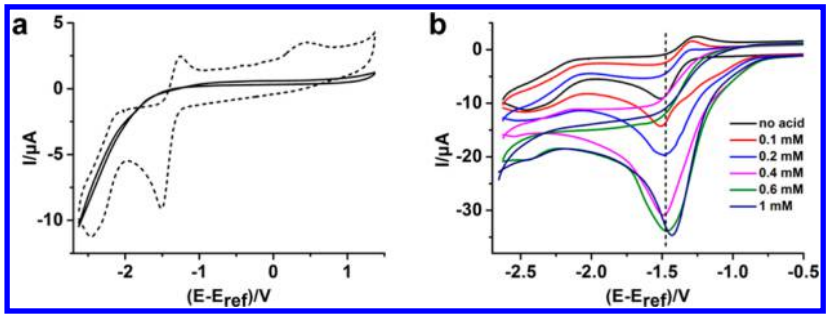

Figure 5. (a) CV results of micropatterned OTS-Si without [Fe-Fe]-hydrogenase active site complexes (solid line) and [Fe-Fe]-Si (dashed line). (b) CV results of a [Fe-Fe]-Si at various concentrations of AcOH.

DOI: 10.1021/acs.langmuir.5b02730
Langmuir 2015, 31, 11748−11753

addition, the cyclic voltammogram of this complex in the solution phase displayed another small reduction event at −1.97 V (scan rate = 0.2 V/s), which was attributed to the reduction of products of follow-up reactions such as loss of CO from the dianionic species of the complex.[22] In a similar manner, the first cathodic event observed at −1.51 V for the [Fe-Fe]-Si complex could arise from the two-electron reduction process, whereas the second reduction event (−2.45 V) is due to decomposition products. Indeed, the reversibility of the first reduction wave of the complex in the solution phase is higher than in the case of the [Fe-Fe]-Si complex.[22] Moreover, the addition of acetic acid induced an increase in the current of the cathodic waves and the current intensity increased with increasing concentration of the acid (Figure 5b). These results are in agreement with the CV results of [Fe-Fe]-hydrogenase active-site complex molecules in solution, which can prove that an electrocatalytic proton reduction occurred in the CH_3CN solution (catalytic proton reduction wave at −1.8 V);[22,23] however, the increase in the current intensity stopped after the concentration of the acid reached 0.6 mM, most probably due to a limited number of [Fe-Fe]-hydrogenase active site complex molecules grafted onto the micropatterns. On the basis of the CV curves of [Fe-Fe]-Si, the coverage of immobilized [Fe-Fe]-hydrogenase active-site complex molecules can be approximated and the value is on the order of 0.002 mg cm^{-2}. According to the CV results, we conclude that the Fe−S active sites of the [Fe-Fe]-hydrogenase active-site complex molecules are still active after binding to the OTS-Si substrate.

CONCLUSIONS

In this study, we demonstrated the successful functionalization of microstructured chemically active surface templates by the assembly of [Fe-Fe]-hydrogenase active-site model complexes. Carboxyl groups generated by electro-oxidative lithography with a conductive TEM grid were used to bind the [Fe-Fe]-hydrogenase active site complex molecules by ester bond formation. The [Fe-Fe]-hydrogenase active site complex molecules were selectively immobilized on the lithographic line areas with good, but not complete, coverage. One oxidation and two reduction peaks were observed in the CV curves, which are corresponding to the different redox processes of the diiron complex. Moreover, by the addition of acetic acid, the current of the cathodic waves increased, which is caused by the electrocatalytic proton reduction in the solution. These CV results indicate that the biomimetic metal centers of [Fe-Fe]-hydrogenase active-site complex molecules still keep their catalytic activity and redox behavior after the immobilization processes. We suggest that this postattachment approach of micropatterned Si substrates with [Fe-Fe]-hydrogenase active site complexes could be extended to other catalytic model molecules to form microscale catalytic systems and hence offers promising prospects for the preparation of, for example, micro H_2 fuel cells and biohybrid surfaces.

AUTHOR INFORMATION

Corresponding Author

*Fax: +49 3641 948202. E-mail: s.hoeppener@uni-jena.de.

Notes

The authors declare no competing financial interest.

ACKNOWLEDGMENTS

H.L. is grateful to the China Scholarship Council (CSC) for a fellowship grant. The work was conducted in the framework of the "Photonic Nanostructures" (PhoNa) project funded by the German Ministry of Education and Research (BMBF) in the program "Spitzenforschung und Innovation in den Neuen Ländern". We thank Mr. Kun Cong for his support with the cyclic voltammetric measurements.

REFERENCES

(1) Mitrovski, S. M.; Elliott, L. C. C.; Nuzzo, R. G. Microfluidic Devices for Energy Conversion: Planar Integration and Performance of a Passive, Fully Immersed H2-O2 Fuel Cell. *Langmuir* **2004**, *20*, 6974−6976.

(2) Loges, B.; Boddien, A.; Junge, H.; Beller, M. Controlled Generation of Hydrogen from Formic Acid Amine Adducts at Room Temperature and Application in H2/O2 Fuel Cells. *Angew. Chem., Int. Ed.* **2008**, *47*, 3962−3965.

(3) Motoyama, M.; Chao, C.-C.; An, J.; Jung, H. J.; Gür, T. M.; Prinz, F. B. Nanotubular Array Solid Oxide Fuel Cell. *ACS Nano* **2014**, *8*, 340−351.

(4) Liu, S.; Zhou, L.; Wang, P.; Zhang, F.; Yu, S.; Shao, Z.; Yi, B. Ionic-Liquid-Based Proton Conducting Membranes for Anhydrous H2/Cl2 Fuel-Cell Applications. *ACS Appl. Mater. Interfaces* **2014**, *6*, 3195−3200.

(5) Vignals, P. M.; Colbeau, A. Molecular Biology of Microbial Hydrogenases. *Curr. Issues Mol. Biol.* **2004**, *6*, 159−188.

(6) Heinekey, D. M. Hydrogenase Enzymes: Recent Structural Studies and Active Site Models. *J. Organomet. Chem.* **2009**, *694*, 2671−2680. (7) Lubitz, W.; Ogata, H.; Rüdiger, O.; Reijerse, E. Hydrogenases. *Chem. Rev.* **2014**, *114*, 4081−4148.

(7) Apfel, U.-P.; Halpin, Y.; Görls, H.; Vos, J. G.; Schweizer, B.; Linti, G.; Weigand, W. Synthesis and Characterization of Hydroxy-Functionalized Models for the Active Site in Fe-Only-Hydrogenases. *Chem. Biodiversity* **2007**, *4*, 2138−2148.

(8) Ibrahim, S. K.; Liu, X.; Tard, C.; Pickett, C. J. Electropolymeric Materials Incorporating Subsite Structures Related to Iron-Only Hydrogenase: Active Ester Functionalised Poly(pyrroles) for Covalent Binding of {2Fe3S}-Carbonyl/cyanide Assemblies. *Chem. Commun.* **2007**, 1535−1537.

(9) Thomas, C. M.; Rüdiger, O.; Liu, T.; Carson, C. E.; Hall, M. B.; Darensbourg, M. Y. Synthesis of Carboxylic Acid-Modified [Fe-Fe]-Hydrogenase Model Complexes Amenable to Surface Immobilization. *Organometallics* **2007**, *26*, 3976−3984.

(10) Krassen, H.; Stripp, S.; von Abendroth, G.; Ataka, K.; Happe, T.; Heberle, J. Immobilization of the [FeFe]-Hydrogenase CrHydA1 on a Gold Electrode: Design of a Catalytic Surface for the Production of Molecular Hydrogen. *J. Biotechnol.* **2009**, *142*, 3−9.

(11) Madden, C.; Vaughn, M. D.; Diez-Perez, I.; Brown, K. A.; King, P. W.; Gust, D.; Moore, A. L.; Moore, T. A. Catalytic Turnover of [FeFe]-Hydrogenase Based on Single-Molecule Imaging. *J. Am. Chem. Soc.* **2012**, *134*, 1577−1582.

(12) Krassen, H.; Stripp, S. T.; Boehm, N.; Berkessel, a.; Happe, T.; Ataka, K.; Heberle, J. Talor-Made Modification of a Gold Surface for the Chemical Binding of a High-Activity [FeFe] Hydrogenase. *Eur. J. Inorg. Chem.* **2011**, *2011*, 1138−1146.

(13) Le Goff, A.; Artero, V.; Metaye, R.; Moggia, F.; Jousselme, B.; Razavet, M.; Tran, P. D.; Palacin, S.; Fontecave, M. Immobilization of FeFe Hydrogenase Mimics onto Carbon and Gold Electrodes by Controlled Aryldiazonium Salt Reduction: An Electrochemical, XPS and ATR-IR Study. *Int. J. Hydrogen Energy* **2010**, *35*, 10790−10796.

(14) Karyakin, A. A.; Morozov, S. V.; Karyakina, E. E.; Zorin, N. A.; Perelygin, V. V.; Cosnier, S. Hydrogenase Electrodes for Fuel Cells. *Biochem. Soc. Trans.* **2005**, *33*, 73−75.

(15) Tye, J. W.; Hall, M. B.; Darensbourg, M. Y. Better than Platinum? Fuel Cells Energized by Enzymes. *Proc. Natl. Acad. Sci. U. S. A.* **2005**, *102*, 16911−16912.

DOI: 10.1021/acs.langmuir.5b02730
Langmuir 2015, 31, 11748−11753

(16) Kaur-Ghumaan, S.; Stein, M. [NiFe] Hydrogenases: How Close Do Structural and Functional Mimics Approach the Active Site? *Dalton Trans.* **2014**, *43*, 9392−9405.
(17) King, P. W. Designing Interfaces of Hydrogenase-Nanomaterial Hybrids for Efficient Solar Conversion. *Biochim. Biophys. Acta, Bioenerg.* **2013**, *1827*, 949−952.
(18) Rocha-Martín, J.; de las Rivas, B.; Muñoz, R.; Guisán, J. M.; López-Gallego, F. Rational Co-Immobilization of Bi-Enzyme Cascades on Porous Supports and Their Applications in Bio-Redox Reactions with In Situ Recycling of Soluble Cofactors. *ChemCatChem* **2012**, *4*, 1279−1288.
(19) Hoeppener, S.; Maoz, R.; Sagiv, J. Constructive Microlithography: Electrochemical Printing of Monolayer Template Patterns Extends Constructive Nanolithography to the Micrometer-Millimeter Dimension Range. *Nano Lett.* **2003**, *3*, 761−767.
(20) Druzhinina, T. S.; Höppener, C.; Hoeppener, S.; Schubert, U. S. Hierarchical, Guided Self-Assembly of Preselected Carbon Nanotubes for the Controlled Fabrication of CNT Structures by Electrooxidative Nanolithography. *Langmuir* **2013**, *29*, 7515−7520.
(21) Hahn, R.; Wagner, S.; Schmitz, A.; Reichl, H. Development of a Planar Micro Fuel Cell with Thin Film and Micro Patterning Technologies. *J. Power Sources* **2004**, *131*, 73−78.
(22) Trautwein, R.; Almazahreh, L. R.; Görls, H.; Weigand, W. The Influence of OH Groups in $[Fe(CO)_3]_2[(\mu\text{-}ECH_2)_2C(CH_2OH)_2]$ (E = S, Se) Complexes toward the Cathodic Process. *Z. Anorg. Allg. Chem.* **2013**, *639*, 1512−1519.
(23) Liu, T.; Wang, M.; Shi, Z.; Cui, H.; Dong, W.; Chen, J.; Akermark, B.; Sun, L. Synthesis, Structures and Electrochemical Properties of Nitro- and Amino-Functionalized Diiron Azadithiolates as Active Site Models of Fe-Only Hydrogenases. *Chem. - Eur. J.* **2004**, *10*, 4474−4479.

DOI: 10.1021/acs.langmuir.5b02730
Langmuir 2015, 31, 11748−11753

Publication P3

Au nanoparticle cluster arrays for high-performance SERS substrates fabricated by electro-oxidative lithography

H. Liu, A. M. Schwenke, F. Kretschmer, S. Hoeppener, U. S. Schubert

ChemNanoMat. **2016**, DOI: 10.1002/cnma.201600063.

ACES Asian Chemical Editorial Society

DOI: 10.1002/cnma.201600063

CHEMNANOMAT
Communication

SERS Substrates

Gold Nanoparticle Cluster Arrays for High-Performance SERS Substrates Fabricated by Electro-oxidative Lithography

He Liu,[a, b] Almut M. Schwenke,[a, b] Florian Kretschmer,[a, b] Stephanie Hoeppener,*[a, b] and Ulrich S. Schubert[a, b]

Abstract: The availability of high-performance substrates for surface enhanced Raman spectroscopy (SERS) in a reproducible fashion is of tremendous importance for transferring the technology into a routine analysis tool. We describe the fabrication of highly efficient SERS substrates facilitating enhancement factors as high as $\sim 5 \times 10^6$ by combining self-assembly strategies with electro-oxidative nanolithography, which allows the fabrication of cluster arrays consisting of individual gold nanoparticles at ambient conditions and at low costs. Different aspects on the fabrication process, that is, the optimization of the cluster distances, the contribution of intra- and interparticle plasmon coupling, as well as the determination of the signal enhancement and substrate reproducibility, are discussed.

Surface-enhanced Raman scattering (SERS) has attracted increasing attention due to its remarkable enhancement and excellent selectivity for investigating specific vibrational transitions of various analytes, providing a chemical fingerprint to identify and detect a large variety of chemical substances. In the 1970s the SERS effect was first observed by the detection of trace amounts of pyridine adsorbed onto roughened silver electrodes.[1] Since then, the SERS technique has been successfully utilized in various fields of research, e.g., for the trace detection of chemical and biological molecules[2] and for applications outside the laboratory environment, e.g., for the effective detection of food additives and explosives.[3] In general, there are two primary mechanisms for the SERS enhancement.[4] One is the chemical enhancement effect, which applies only for species that have formed chemical interactions with the surface. The other is the electromagnetic field enhancement effect, which is dominant in most SERS applications. The electromagnetic field effect arises from the coupling of surface plasmons at nanoscale junctions of noble metal nanoparticles (so-called hot spots).[5] Thus, the surface structure of the utilized substrate represents a critical aspect for the generation of the electromagnetic field enhancement. The substrates should support the propagation of the surface plasmon coupling, resulting in a strong enhancement of the Raman signals. Normally, there are two kinds of SERS substrates: random and engineered substrates.[6] For random substrates, such as fractal nanoparticle aggregates, localized dipole modes can be induced, which lead to the enhancement of the SERS signals. However, the reproducibility of the enhancement is difficult to control because of the random distribution of the nanoparticles.[7] In the case of engineered substrates, high SERS enhancements and a good reproducibility can be obtained at the same time, due to the high precision of the customized fabrication of the periodical structures at spatially defined locations.[8] Among other techniques, focused-ion-beam[9] and electron-beam[10] lithography are the most frequently used methods for the preparation of engineered SERS substrates. The main limitations for these approaches are their relatively high cost and the time-consuming fabrication of the devices. Block copolymers represent another alternative for the fabrication of SERS substrates, which can easily form periodic and high-density features to guide, e.g., nanoparticle cluster formation. For instance, Wang et al. demonstrated the fabrication of dense arrays of mushroom-shaped gold nanopillars with a periodicity of 50 nm by utilization of poly(styrene-*b*-2-vinylpyridine) (PS-*b*-P2VP) templates.[11] Osinkina and co-workers reported a two-step approach for the fabrication of gold nanostar arrays, applied as SERS substrates, by a combination of block copolymer micelle lithography and electroless deposition.[12] Nevertheless, there are also limitations for the utilization of the block copolymer template-based methods. For example, the removal of the polymer templates could result in the partial destruction of the periodic structures. In addition, to obtain structures with different shape and separation, copolymers with different block lengths and block ratios are required and have to be synthesized.[13] In general these examples highlight the two conceptually different approaches to obtain SERS active substrates: top-down approaches, which allow a good control of the obtained structures, and bottom-up strategies, which utilize self-assembly steps. Both approaches feature advantages and disadvantages and their utilization strongly depends on the focus of the research. While expensive and complex nanofabrication

[a] H. Liu, A. M. Schwenke, Dr. F. Kretschmer, Dr. S. Hoeppener, Prof. U. S. Schubert
Friedrich-Schiller-University Jena
Fürstengraben 1, 07743 Jena (Germany)
E-mail: S.Hoeppener@uni-jena.de

[b] H. Liu, A. M. Schwenke, Dr. F. Kretschmer, Dr. S. Hoeppener, Prof. U. S. Schubert
Laboratory for Organic and Macromolecular Chemistry
Jena Center for Soft Matter Friedrich Schiller University Jena
07743 Jena (Germany)

Supporting information for this article can be found under http://dx.doi.org/10.1002/cnma.201600063.

schemes are well suited to gain a deeper understanding of the SERS effect (e.g., by investigating the properties of well-defined SERS building blocks, that is, dimer- and multimer structures), self-assembly strategies promise advantages in terms of fabrication speed and cost effectiveness on the expense of working with less-well-defined structures. Here, we report the development of a new method for the fabrication of SERS substrates by electro-oxidative lithography, clearly aiming for the second approach of integrating self-assembly schemes into the fabrication process. As such, the fabricated structures are seen as individual nanoparticle clusters, which might differ in their respective SERS properties. Nevertheless, it is possible to fabricate such SERS active substrates with a high reproducibility and they allow study of cooperative effects between the individual particles as well as between different clusters. By fabricating a larger number of them the standard deviation for a whole pattern can be minimized. This lithographic method represents a cost-effective technique and can be applied under ambient processing conditions. In the present work, *n*-octadecyltrichlorosilane (OTS) monolayers were used as support that can be chemically structured by means of electro-oxidative lithography, thus, providing localized binding sites to immobilize nanoparticles. The local oxidation of the OTS monolayers with a conductive AFM tip represents a promising method for the fabrication of structures with chemical functionalities at the nanometer scale.[14] After the lithographic process, Au nanoparticles can be self-assembled on the patterned areas to form cluster arrays. Patterns with different gap distances varying from 30 to 400 nm between two neighboring Au clusters were tested regarding their SERS activities. In particular, the substrate with the highest density array of Au clusters revealed very high SERS intensities with an enhancement factor (EF) of $\sim 5 \times 10^6$ and a good reproducibility of the signal.

Au nanoparticle cluster arrays were fabricated utilizing the steps illustrated in Figure 1. In the first step, a dot array pattern was created by the electro-oxidative lithographic process using the vector mode, implemented into the AFM software. Electro-oxidative lithography is a tip- or stamp-based approach that enables the structuring of an OTS monolayer with chemically active functional groups.[15] For this purpose, a negative bias voltage was applied between a conductive, Pt-coated AFM tip and the OTS-Si substrate, resulting in the local oxidation of the surface. The size of the generated dot patterns depends on the tip dimension and the patterning conditions, including the applied voltage, pulse duration and relative humidity. During the lithographic process an electro-chemical oxidation reaction occurs in the formed water meniscus between the AFM tip and the substrate, i.e., the $-CH_3$ groups of OTS are converted into polar functional $-COOH$ groups, in the region of the tip contact.[16] The friction force in the electro-oxidized, hydrophilic regions is much stronger than that in the unmodified, hydrophobic OTS monolayer areas. Therefore, the lithographic patterns can be directly observed by contact mode friction force AFM investigations.

Figure 2a displays a friction force image of a dot array pattern and the scan direction was set from left to right. If the AFM tip is scanned from the opposite direction, a picture with inverse contrast is obtained (Figure 2b).

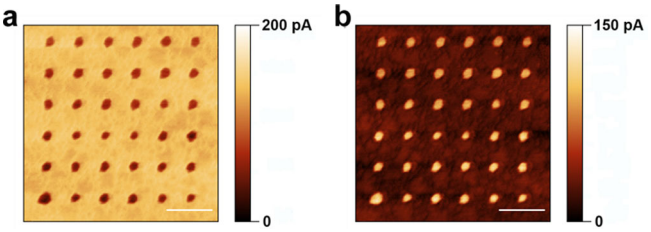

Figure 2. Friction force contact mode AFM images of a dot array pattern. The scanning directions are set from left to right (a) and from right to left (b). The scale bar in each image is 500 nm.

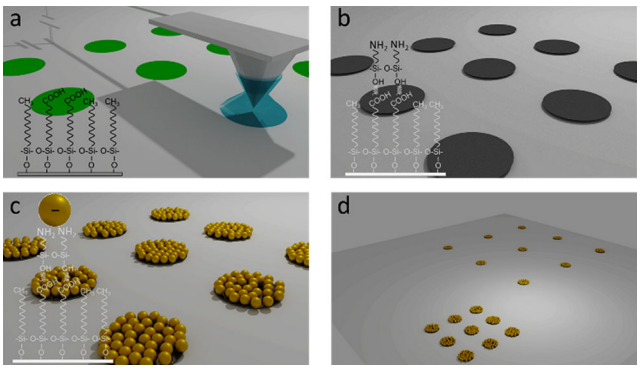

Figure 1. Schematic representation of the fabrication of the Au nanoparticle cluster array substrates. (a) Tip-mediated electrochemical oxidation of a self-assembled OTS monolayer on silicon. (b) Site-selective self-assembly of an APTMS monolayer on the structured areas. (c) Site-selective binding of negatively charged Au nanoparticles exclusively on the patterned areas to form nanoparticle clusters. (d) Patterns of clusters with different lattice spacing of the clusters. The chemical modifications are highlighted by the insets.

This reversible friction strongly indicates that an obvious change of the surface properties, i.e., a switch between hydrophobic and hydrophilic, was induced. This change reflects the large spot-to-spot force variations associated with the different hydration and adhesion properties of the $-CH_3$ and the formed $-COOH$ groups.[17] After the lithographic process, the nanostructured substrate was immersed into the APTMS solution and an additional layer of APTMS molecules was site-selectively self-assembled on the patterned areas and the substrates were carefully rinsed with toluene to remove non-specifically adsorbed APTMS molecules.[18] Finally, Au nanoparticles, which were stabilized by sodium citrate, were bound on the positively charged dot sites of the substrate based on an electrostatically guided self-assembly process.

Figure 3a–g shows SEM images of Au nanoparticle cluster arrays with different gap distances. Two dimensional nanoparticle clusters consisting of several individually immobilized Au nanoparticles were spatially confined by the dot templates. The gap distances between two clusters could be changed from 30 to 400 nm by the electro-oxidative lithography process. It is difficult to decrease the gap distance significantly below 30 nm, because at very small distances individual clus-

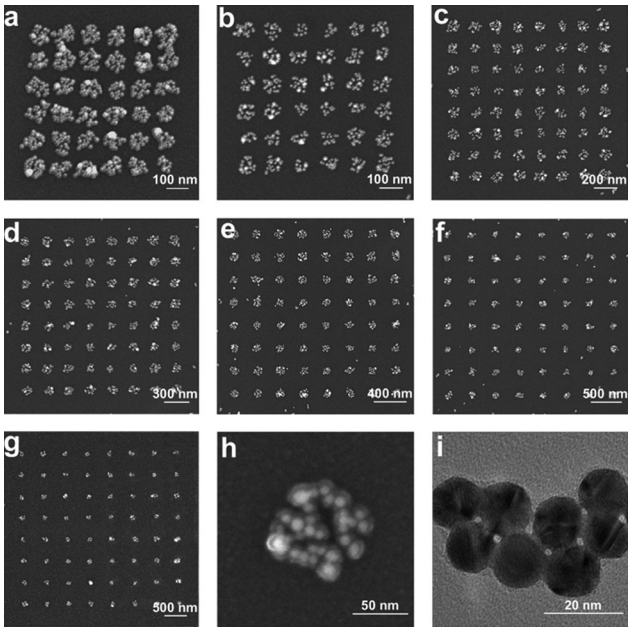

Figure 3. SEM images of Au nanoparticle cluster arrays prepared with different gap distances: (a) 30 nm, (b) 50 nm, (c) 100 nm, (d) 150 nm, (e) 200 nm, (f) 300 nm and (g) 400 nm. (h) A SEM image of an individual cluster. (i) HR-TEM image of Au nanoparticles.

ters tend to fuse and link together, which can be seen, e.g., in Figure 3a (upper right corner). For all clusters a good coverage of the dot area with nanoparticles was observed. Each cluster consists of approximately 20 to 30 individual nanoparticles. As shown in the TEM image (Figure 3i), the diameter of the individual Au nanoparticles is in the range of 10 to 15 nm and for each cluster the distance between individual Au nanoparticles within the cluster is less than 5 nm (Figure 3h). These small distances are beneficial for the plasmon coupling, which is required for obtaining high signal intensities in the SERS measurements.[9,10] The small distances of the individual Au nanoparticles within the cluster are a direct result of the differences in the wetting behavior of the patterned areas and the surrounding OTS monolayer. While the water contact angle on the OTS substrate is $>110^{\circ}$ the APTMS functionalized oxidized areas in the spot regions are rendered more hydrophilic. This allows for the preferential deposition of nanoparticles in these areas since dewetting effects result in a higher particle concentration and thus a more dense packing of the nanoparticles on the patterned areas. In order to test the reproducibility of the SERS signals, nine individual nanoparticle array patterns were fabricated for each gap distance (example shown in Figure S1 in the Supporting Information).

For the SERS measurements, benzenethiol (BT) was used as a test molecule due to its efficient assembly on the Au nanoparticle cluster surface by the formation of Au–S bonds.[19] After application of the BT solution and incubation the substrates were thoroughly rinsed with plenty of water to remove non-specifically absorbed BT molecules.

Figure 4a shows the SERS spectra of BT on Au nanoparticle cluster arrays with different lateral distances of the clusters. The most intense peak at 1565 cm^{-1} was chosen for comparison of the different substrates and to calculate the SERS enhancement factors (EF) (details are provided in the Supporting Information). It is worth noting that the numbers of clusters for the patterns with gap distances of 30 and 50 nm are lower than others, which means that less BT molecules in the focal region areas for these two patterns were adsorbed. Moreover, since the size of the laser spot is about 2.5 μm, for the patterns with gap distances of 300 and 400 nm, the laser only covered a part of the patterned areas. For the ease of calculation, we assume that the BT molecules are uniformly assembled on the Au nanoparticles in a monolayer-like fashion.[20] The SERS signals strongly increase with decreasing distance between the Au nanoparticle clusters.

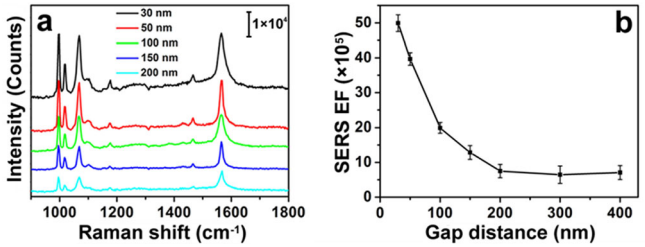

Figure 4. (a) SERS spectra of benzenethiol (BT) and (b) the calculated enhancement factors (EF) measured on Au nanoparticle cluster array substrates with different gap distances.

As shown in Figure 4b, at very short gap distances between the Au clusters (30 nm), the enhancement factor reaches values as high as $\sim 5\times10^{6}$. As the gap distance increases, the EF values decrease significantly and reach a constant level at a gap distance of ~200 nm. The obtained high EF values are attributed to the fact that, firstly, for each individual cluster, the distance between the Au nanoparticles is less than 5 nm within each cluster spot, which will cause a strong enhancement of the incident electromagnetic field by interparticle plasmon coupling. Secondly, this enhanced electromagnetic field can be further increased by coupling between the individual cluster, i.e., by intercluster plasmon coupling.[6a,21] In the present study, the intercluster plasmon coupling becomes very weak when the distance between the clusters is larger than 200 nm, which causes a relatively low and constant EF value that is dominated by the interparticle plasmon coupling.

In addition to the EF increase, another important SERS performance parameter is the reproducibility of the EF. The EF reproducibility was tested by analyzing the standard deviation of the EF values measured from nine cluster arrays with the same gap distance prepared on one substrate.

As shown in Figure 5, the SERS substrate (gap distance: 30 nm) displays a good reproducibility and the standard deviation value of the mean EF value is 4.8%. For comparison, a non-patterned substrate of the Au nanoparticles was investigated as well, revealing only a relatively low EF ($\sim 6.2\times10^{4}$), since the distance between individual nanoparticles is usually larger than 10 nm which decreases the interparticle coupling. Moreover, some particle aggregates are formed (Figure S2) and these aggregates are much smaller compared to the cluster structures on the SERS substrate. Thus, it can be concluded

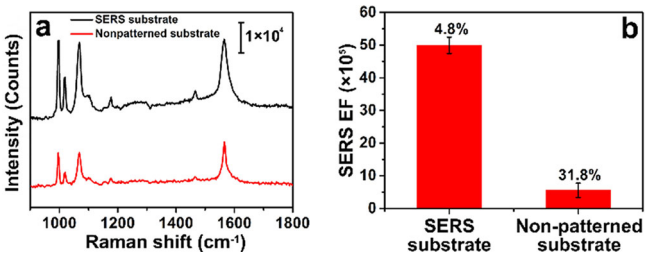

Figure 5. (a) SERS spectra and (b) corresponding enhancement factors (EF) of the SERS substrate (gap distance: 30 nm) and the non-patterned Au nanoparticle substrate. The error bars indicate the standard deviation as percentage of the mean EF value from nine independent measurements on nine similarly structured areas.

that these particle aggregates are not suitable to induce a strong electromagnetic field coupling for the SERS enhancement. Additionally, the standard deviation value of the mean EF value for the non-patterned substrate is much larger (31.8%), which is caused by the random distribution of the Au nanoparticles.

Au nanoparticle cluster arrays were fabricated by combining a fast and cost-efficient top-down electro-oxidative lithography approach with bottom-up self-assembly procedures. The intercluster separations can be systematically controlled from 30 nm to $>$400 nm. A significant electromagnetic field enhancement was obtained by both interparticle and intercluster plasmon coupling of Au nanoparticles, which resulted in strong SERS signals. In particular, high-performance SERS substrates were obtained with an interparticle separation of less than 5 nm within the cluster and an intercluster separation down to 30 nm in between the individual cluster spots and an EF value as high as $\sim 5\times10^6$ was achieved. In addition, we found that a gap distance between two clusters of more than 200 nm did not result in an increase of the EF and the values remained constant even for larger cluster separations. This is due to the fact that the intercluster coupling is too weak. Moreover, a good reproducibility of the EF was achieved for the fabricated samples, resulting from the regular periodic structures. This approach combined electro-oxidative lithography and self-assembly procedures to fabricate highly sensitive SERS substrates with improved reproducibility. It can be pointed out that the reported method to combine electro-oxidative lithography and self-assembly of functional materials can be used in a large variety of other applications to hierarchically structure nanomaterials. These include, among others, the utilization of molecules, nanoparticles, or nano-objects, offering attractive possibilities to fabricate functional nano-devices.

Experimental Section

Materials: Bicyclohexane (BCH), toluene, *n*-octadecyltrichlorosilane (OTS), (3-aminopropyl)-trimethoxysilane (APTMS), sodium citrate dihydrate, and benzenethiol (BT) were obtained from Sigma Aldrich. Hydrogen tetrachloroaurate(III) trihydrate ($HAuCl_4\times3H_2O$) was purchased from Alfa Aesar. BCH was distilled over sodium before use. All other reagents were used without further purification. Double side polished p-type silicon wafers (100) were obtained from Siegert Wafer (resistivity: 10 to 20 Ω cm).

Electro-oxidative lithography: Si substrates were treated with Ar plasma for 2 min before use. OTS monolayers were prepared by immersing a cleaned Si substrate in a solution of OTS (10 μL) in BCH (2 mL) for 1 min, followed by sonication in toluene and blow drying with N_2 (OTS-Si). Subsequently, the nanolithographic process was performed using an AFM (NT-MDT, NTegra Aura) placed in a home-built humidity chamber. Oxidation experiments were carried out at room temperature and at controlled humidity (RH) using a Pt coated AFM tip (μ-Masch, NCS36 Ti-Pt). Lithographic patterns were fabricated in contact mode.

Fabrication of Au nanoparticle cluster arrays: Au nanoparticles were prepared as follows:[22] 200 mL of a $HAuCl_4\times3H_2O$ (1 mM) solution was heated to 100 °C while stirring at 700 rpm. 1 mL of a sodium citrate solution (0.78 M) was added to the refluxing solution immediately. The color of the solution turned red after approximately 30 s. Heating was continued for 30 min, afterwards the solution was cooled down and stored in the dark at 4 °C. For the removal of the free sodium citrate, 2 mL of the Au nanoparticles solution was centrifuged (5000 rpm, 90 min) and the supernatant was exchanged by 0.9 mL of fresh water. The unmodified Si substrate (non-patterned substrate) and the Si substrate with lithographic patterns (SERS substrate) were first immersed in a solution of APTMS (10 μL) in BCH (2 mL) for 30 min, followed by sonication in toluene and blow drying in N_2. Afterwards, these substrates were immersed in the centrifuged Au nanoparticle solutions for 3 h, followed by rinsing with plenty of distilled water. Lateral force atomic force microscopy (AFM, NT-MDT, NTegra Aura) was performed using commercial AFM tips (μ-Masch NCS35/AIBS) in contact mode. Scanning electron microscopy imaging was conducted with a Zeiss LEO 1530 Gemini, utilizing the Inlense detector. All samples were coated with a thin layer of carbon prior to SEM imaging. TEM measurements were performed on a FEI Technai G^2 20.

SERS measurements: SERS measurements were performed on an inverted microscope with a ×100 objective (NA = 0.9, Olympus), utilizing 632.8 nm laser excitation with a laser spot size of ~2.5 μm. A notch filter was placed in front of the entrance of the spectrometer (SP2750i, Princeton Instruments). Benzene thiol (BT) was utilized as a test molecule for SERS investigations and the substrates were immersed into the ethanol solution of BT (1×10^{-6} M) for 30 min before each measurement. Substrates were subsequently carefully cleaned by excessive washing steps to remove non-specifically adsorbed molecules. Raman spectra were recorded using a CCD detector (PIXIS400, Princeton Instruments) with an acquisition time of 10 s.

Acknowledgements

He Liu is grateful to the China Scholarship Council (CSC) for a fellowship grant. The work was conducted in the framework of the "Photonic Nanomaterials" (PhoNa) project funded by the German Ministry of Education and Research (BMBF) in the program "Spitzenforschung und Innovation in den Neuen Ländern".

Keywords: atomic force microscopy (AFM) · gold nanoparticle cluster arrays · electro-oxidative lithography · self-assembly · surface enhanced Raman spectroscopy (SERS)

[1] a) M. Fleischmann, P. J. Hendra, A. J. Mcquillan, *Chem. Phys. Lett.* **1974**, *26*, 163 – 166; b) D. L. Jeanmaire, R. P. Van Duyne, *J. Electroanal. Chem.* **1977**, *84*, 1 – 20; c) M. G. Albrecht, J. A. Creighton, *J. Am. Chem. Soc.* **1977**, *99*, 5215 – 5217.
[2] a) S. Nie, S. R. Emory, *Science* **1997**, *275*, 1102 – 1106; b) D. R. Ward, N. K. Grady, C. S. Levin, N. J. Halas, Y. Wu, P. Nordlander, D. Natelson, *Nano Lett.* **2007**, *7*, 1396 – 1400; c) Y. C. Cao, R. Jin, C. A. Mirkin, *Science* **2002**, *297*, 1536 – 1541.
[3] a) J. Zheng, L. He, *Compr. Rev. Food Sci. Food Saf.* **2014**, *13*, 317 – 328; b) A. Chou, E. Jaatinen, R. Buividas, G. Seniutinas, S. Juodkazis, E. L. Izake, P. M. Fredericks, *Nanoscale* **2012**, *4*, 7419 – 7424.
[4] B. Sharma, R. R. Frontiera, A.-I. Henry, E. Ringe, R. P. Van Duyne, *Mater. Today* **2012**, *15*, 16 – 25.
[5] a) M. Moskovits, *J. Raman Spectrosc.* **2005**, *36*, 485 – 496; b) J. P. Camden, J. A. Dieringer, Y. Wang, D. J. Masiello, L. D. Marks, G. C. Schatz, R. P. Van Duyne, *J. Am. Chem. Soc.* **2008**, *130*, 12616 – 12617; c) F. Le, D. W. Brandl, Y. A. Urzhumov, H. Wang, J. Kundu, N. J. Halas, J. Aizpurua, P. Nordlander, *ACS Nano* **2008**, *2*, 707 – 718; d) Z. Zhang, P. Yang, H. Xu, H. Zheng, *J. Appl. Phys.* **2013**, *113*, 033102.
[6] a) B. Yan, A. Thubagere, W. Premasiri, L. D. Ziegler, L. Dal Negro, B. M. Reinhard, *ACS Nano* **2009**, *3*, 1190 – 1202; b) A. Gopinath, S. V. Boriskina, B. M. Reinhard, L. Dal Negro, *Opt. Express* **2009**, *17*, 3741 – 3753.
[7] M. I. Stockman, V. M. Shalaev, M. Moskovits, R. Botet, T. F. George, *Phys. Rev. B* **1992**, *46*, 2821 – 2831.
[8] A. Gopinath, S. V. Boriskina, N.-N. Feng, B. M. Reinhard, L. Dal Negro, *Nano Lett.* **2008**, *8*, 2423 – 2431.
[9] A. A. Tseng, *Small* **2005**, *1*, 924 – 939.
[10] E. Altewischer, M. P. van Exter, J. P. Woerdman, *Nature* **2002**, *418*, 304 – 306.
[11] Y. Wang, M. Becker, L. Wang, J. Liu, R. Scholz, J. Peng, U. Gösele, S. Christiansen, D. H. Kim, M. Steinhart, *Nano Lett.* **2009**, *9*, 2384 – 2389.
[12] L. Osinkina, T. Lohmüller, F. Jäckel, J. Feldmann, *J. Phys. Chem. C* **2013**, *117*, 22198 – 22202.
[13] F. L. Yap, P. Thoniyot, S. Krishnan, S. Krishnamoorthy, *ACS Nano* **2012**, *6*, 2056 – 2070.
[14] a) S. Hoeppener, U. S. Schubert, *Small* **2005**, *1*, 628 – 632; b) T. Druzhinina, S. Hoeppener, N. Herzer, U. S. Schubert, *J. Mater. Chem.* **2011**, *21*, 8532 – 8536.
[15] D. Wouters, R. Willems, S. Hoeppener, C. F. J. Flipse, U. S. Schubert, *Adv. Funct. Mater.* **2005**, *15*, 938 – 944.
[16] R. Maoz, S. R. Cohen, J. Sagiv, *Adv. Mater.* **1999**, *11*, 55 – 61.
[17] S. Hoeppener, R. Maoz, J. Sagiv, *Nano Lett.* **2003**, *3*, 761 – 767.
[18] a) T. S. Druzhinina, S. Hoeppener, U. S. Schubert, *Small* **2012**, *8*, 852 – 857; b) S. Liu, R. Maoz, J. Sagiv, *Nano Lett.* **2004**, *4*, 845 – 851.
[19] a) S. Li, D. Wu, X. Xu, R. Gu, *J. Raman Spectrosc.* **2007**, *38*, 1436 – 1443; b) J. D. Caldwell, O. Glembocki, F. J. Bezares, N. D. Bassim, R. W. Rendell, M. Feygelson, M. Ukaegbu, R. Kasica, L. Shirey, C. Hosten, *ACS Nano* **2011**, *5*, 4046 – 4055.
[20] W. J. Cho, Y. Kim, J. K. Kim, *ACS Nano* **2012**, *6*, 249 – 255.
[21] J. Li, A. Salandrino, N. Engheta, *Phys. Rev. B* **2007**, *76*, 245403.
[22] F. Kretschmer, U. Mansfeld, S. Hoeppener, M. D. Hager, U. S. Schubert, *Chem. Commun.* **2014**, *50*, 88 – 90.

Manuscript received: February 19, 2016
Revised: March 24, 2016
Final Article published: ■■ ■■, 0000

COMMUNICATION

SERS Substrates

He Liu, Almut M. Schwenke, Florian Kretschmer, Stephanie Hoeppener, Ulrich S. Schubert*

■■ – ■■

Gold Nanoparticle Cluster Arrays for High-Performance SERS Substrates Fabricated by Electro-oxidative Lithography

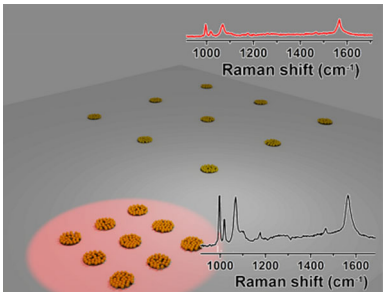

A high-performance SERS substrate was fabricated by combining electro-oxidative lithography and self-assembly procedures. High SERS enhancement factors of 5×10^6 with good reproducibility were achieved by the interparticle and the intercluster plasmon coupling of the Au nanoparticle cluster arrays.

CHEMNANOMAT
CHEMISTRY OF NANOMATERIALS FOR ENERGY, BIOLOGY AND MORE

Supporting Information

Gold Nanoparticle Cluster Arrays for High-Performance SERS Substrates Fabricated by Electro-oxidative Lithography

He Liu,[a, b] Almut M. Schwenke,[a, b] Florian Kretschmer,[a, b] Stephanie Hoeppener,*[a, b] and Ulrich S. Schubert[a, b]

cnma_201600063_sm_miscellaneous_information.pdf

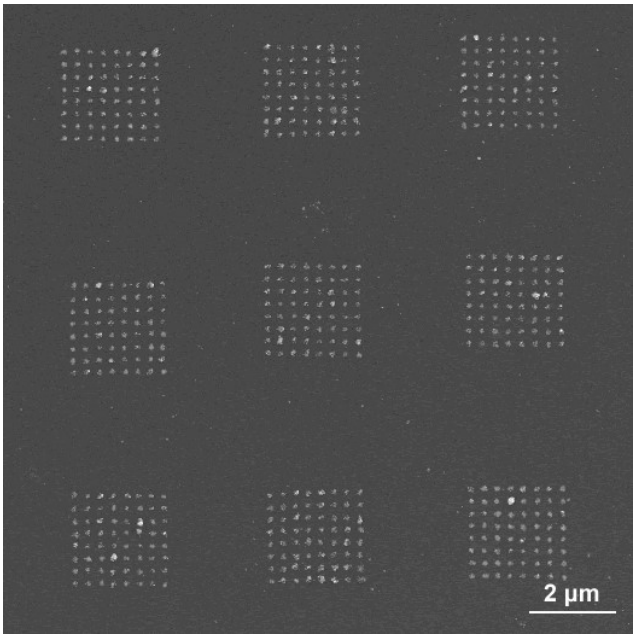

Figure S1. A SEM image of a SERS substrate with nine cluster arrays patterns (gap distance: 150 nm). In this study similar arrays were fabricated for all intercluster spacings to investigate the reproducibility of the fabrication process.

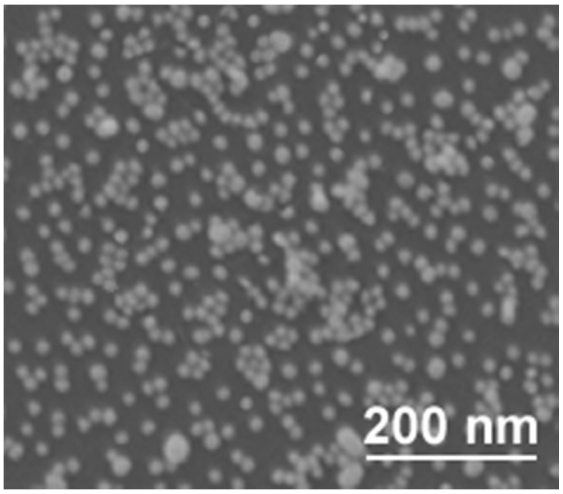

Figure S2. A SEM image of a non-patterned Au nanoparticle substrate.

Calculations of SERS enhancement factors (EF)

The SERS enhancement factor (EF) is calculated as $EF = (I_{substrate}/I_{reference}) \times (N_{reference}/N_{substrate})$, where $I_{substrate}$ and $I_{reference}$ are the SERS intensities of the peak at 1565 cm^{-1} from the SERS substrate and the liquid neat benzenethiol (BT), respectively. $N_{reference}$ and $N_{substrate}$ are the numbers of BT molecules in the focal region of illumination and on the SERS substrate within

the laser spot, respectively. $N_{reference}$ is calculated assuming an confocal depth of ~20 μm, a laser spot size of ~2.5 μm, and a density of 1.073 g/cm^3 for BT. $N_{substrate}$ is estimated by multiplying the active areas of Au nanoparticles within the laser spot by the packing density of BT molecules (4.2×10^{14} molecules/cm^2).[1]

References

[1] L.-J. Wan, M. Terashima, H. Noda, M. Osawa, *J. Phys. Chem. B* **2000**, *104*, 3563.

Publication P4

Reversible nanopatterning on polypyrrole films by atomic force microscope electrochemical lithography

H. Liu, S. Hoeppener, U. S. Schubert

Adv. Funct. Mater. **2016***, 26,* 614–619.

Reversible Nanopatterning on Polypyrrole Films by Atomic Force Microscope Electrochemical Lithography

He Liu, Stephanie Hoeppener, and Ulrich S. Schubert*

A reversible, erasable, and rewritable pattern at the nanoscale is inscribed on polypyrrole films doped with sodium dodecylbenzenesulfonate (PPy(DBS)) utilizing atomic force microscopy based electrochemical lithography. Nanopatterns are formed by applying a bias voltage between a conductive tip and the substrate. Afterward, the generated nanopatterns can be erased completely, followed by rewriting at the same location of the polymer film. Moreover, the alterations of PPy(DBS) during the lithography process are investigated by comparing the changes of the current intensity and surface potential depending on the lithography time.

1. Introduction

Polypyrrole (PPy) is a representative of conducting polymers and has attracted considerable attention since it was discovered by Shirakawa, MacDiarmid, and Heeger in 1976.[1–3] It has unique metal–insulator transitions induced by doping–dedoping processes, while retaining the mechanical properties and processibility of polymers. Many different functional devices have been developed utilizing polypyrrole including, up to now, organic light-emitting diodes,[4] field-effect transistors,[5,6] batteries,[7] and sensors.[8] In analogy with other conducting polymers, the volume of polypyrrole can be controlled by applying a bias voltage.[9,10] The expansion and contraction are thought to be induced primarily by the insertion and expulsion of ions and their associated solvation shells during the oxidation and reduction processes. The electrochemical redox reactions can be expressed by Equations (1) and (2)

$$P^+(A^-) + C^+ + e^- \leftrightarrow P^o(AC) \quad (1)$$

$$P^+(A^-) + C^+ + e^- \leftrightarrow P^o + A^- + C^+ \quad (2)$$

In these equations, P^+ and P^o are refering to the doped (oxidized) and undoped (reduced) states of PPy, respectively. $P^+(A^-)$ represents the anion A^- incorporated in the PPy as a dopant. If the dopant is a large mobile anion, the cation C^+ will be incorporated into the PPy matrix to maintain charge neutrality during the reduction process. That effectively means that the polymer will expand, which is described by Equation (1). Conversely, as shown in Equation (2), if the PPy is doped with a small anion the anions will leave the polymer matrix after the reduction and, thus, the polymer will contract. In addition, both Equations (1) and (2) describe reversible reactions.

Up to now, the reversible volume change of PPy is mainly used in the field of actuation, such as, artificial muscles, implants, and robotic parts,[11–13] which are mostly addressing device dimensions in the macro or microscale. Few studies have been focused on utilizing this reversible expansion at the nanoscale. For instance, Lee et al. demonstrated the actuation behavior of individual polypyrrole nanowires with a diameter below 100 nm, which were embedded in polycarbonate membranes.[14] Jeon et al. reported the fabrication of electrically responsive nanoporous membranes by electropolymerization of PPy doped with sodium dodecylbenzenesulfonate (NaDBS) on the upper part of an anodized aluminum oxide membrane.[15] During the last decades, many efforts have been devoted to developing fast, nonvolatile, and inexpensive techniques for data storage.[16] Conducting polymers, which are promising alternatives to conventional silicon materials, have been intensively investigated as memory devices due to their mechanical flexibility, good manufacturability, and their low cost.[17–19] In particular, by utilizing these materials at the nanoscale, high density memory devices can be potentially fabricated. Here, we propose a reversible nanopatterning method on PPy doped with NaDBS (PPy(DBS)) films by the application of atomic force microscopy (AFM) initiated electrochemical lithography.[20] AFM lithography is a good approach for generating patterns at the nanometer scale which is used in the field of patterning polymers. For example, Lyuksyutov et al. produced patterns on polymer films utilizing an AFM tip by Joule heating which was induced by a nonuniform electric field.[21] Nam et al. fabricated polypyrrole nanowires by electropolymerization of pyrrole monomers with an AFM tip on gold surfaces.[22] In the present work, a voltage, which is applied between a conductive AFM tip and the substrate, induces the reversible local electrochemical redox reaction of the PPy(DBS) and the generation of nanopatterns with a resolution limit down to ≈80 nm is possible. These patterns can be erased completely by applying the opposite voltage. Additionally, the write–erase process can be repeated

H. Liu, Dr. S. Hoeppener, Prof. U. S. Schubert
Laboratory of Organic and Macromolecular Chemistry (IOMC)
Friedrich Schiller University Jena
Humboldtstr. 10, 07743 Jena, Germany
E-mail: s.hoeppener@uni-jena.de
H. Liu, Dr. S. Hoeppener, Prof. U. S. Schubert
Jena Center for Soft Matter (JCSM)
Friedrich Schiller University Jena
Philosophenweg 7, 07743 Jena, Germany

DOI: 10.1002/adfm.201503834

on the same position of the PPy(DBS) film. With this approach reversible volume change and resistance switching effects can be obtained at the same time on the PPy(DBS) film. This patterning method could open up further possibilities for the fabrication of memory devices at the nanoscale by utilizing PPy.

2. Results and Discussion

An essential factor of the AFM lithography process is the availability of smooth substrates of PPy(DBS). In this study, the time of the electropolymerization was set to 1 min. Under this condition, a smooth surface (**Figure 1**a) was obtained with a root mean square roughness of ≈1.5 nm, as measured by AFM tapping mode investigations (Figure 1c). The thickness of the PPy(DBS) film generated on the Au substrate is in this case about 60 nm (Figure 1b). As shown in Figure 1c, some small protrusions appeared on the PPy(DBS) surface, which increased in size at longer deposition times.[23] As mentioned before, large anions such as dodecylbenzenesulfonate (DBS) are incorporated within the PPy matrix during the electropolymerization process and the anions will be trapped when the polymer is reduced. The Na^+ cations and their associated solvation shells will move to the polymer matrix to compensate for charges, resulting in an expansion of the volume and, thus, a swelling of the PPy occurs. For the AFM electrochemical lithography process, water vapor is adsorbed to the tip and the surface and forms a water bridge between the tip and the substrate, which provides a medium for the electrochemical reactions. In the reported experiments, a negative bias voltage (−5 V) was applied to the Au layer and a conductive AFM tip was scanned along a defined pathway (e.g., a circle) while keeping the contact force constant (**Scheme 1**). After the lithography process, AFM tapping mode imaging of the resulting structures was performed with the same tip. **Figure 2**a shows that a circle grew at the locations where the tip was scanned with the applied bias voltage. This process also alters the electrical properties of the substrate. The current intensity was measured between the tip and each point of the surface and a current intensity map was obtained (Figure 2b). The current intensity in the lithographic area (≈6 nA) was lower compared with the other areas (≈11 nA), which indicates that reduced, less conducting PPy(DBS) was formed during the AFM lithography process. For the current intensity measurements, a relatively small bias voltage (1 V)

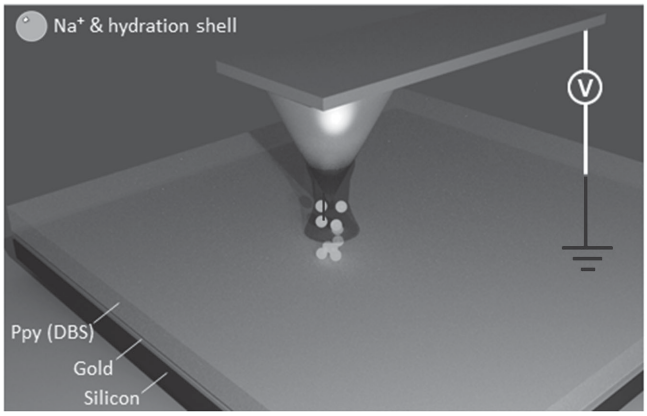

Scheme 1. Schematic illustration of the write–erase process on PPy(DBS) films.

was used to avoid inducing additional changes to the PPy(DBS) films. The patterning of the PPy films was performed at a moderate, constant force. Higher contact forces essentially had no significant influence on the obtainable line width, but it was observed that the tip lifetime rapidly decreased, either due to the loss of the conductive coating or due to the fact that polymer material gradually contaminates the tip, rendering it nonconductive. On the other hand, if only very small contact forces were applied the formation of the required water bridge became unreliable and the patterning was incomplete. In general, it has to be mentioned that the quality of the used AFM tip is important for the obtainable line-width as well as for the number of writing processes that can be performed. By optimizing the applied force to the tip it was possible to achieve ≈100 writing and erasing cycles without significant degradation of the tip performance.

The effect of the applied patterning voltage was also investigated. In general, lowering the patterning voltages requires the increase of the patterning times to obtain comparable results, however, below a voltage of <−3 V at a relative humidity of 50% no pattern formation was observed, even at very long contact times. The AFM software permits to apply different numbers of bias voltage pulses onto the same point on the patterns. This increases the duration of the overall voltage pulse in an intermitted fashion. No significant differences between the continuous voltage application and the intermitted application

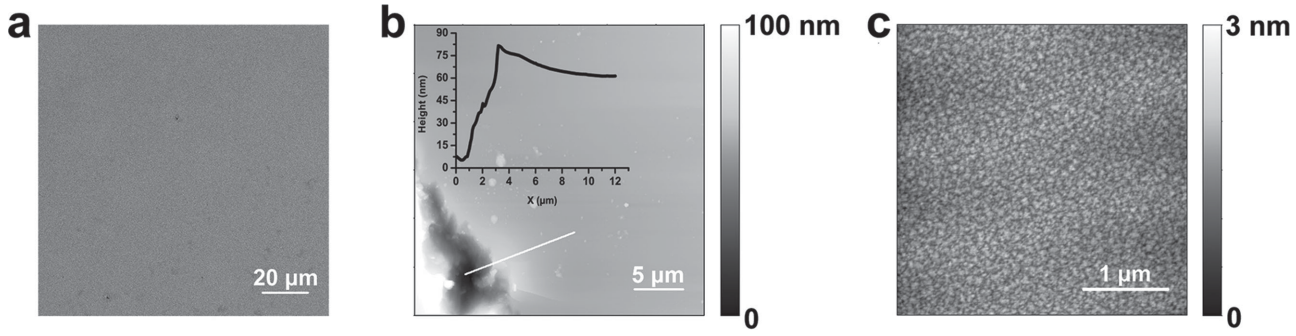

Figure 1. a) SEM and b) AFM topography images of the electrodeposited PPy(DBS) films and cross section of the topography measured along the white line. c) Zoomed view of (b).

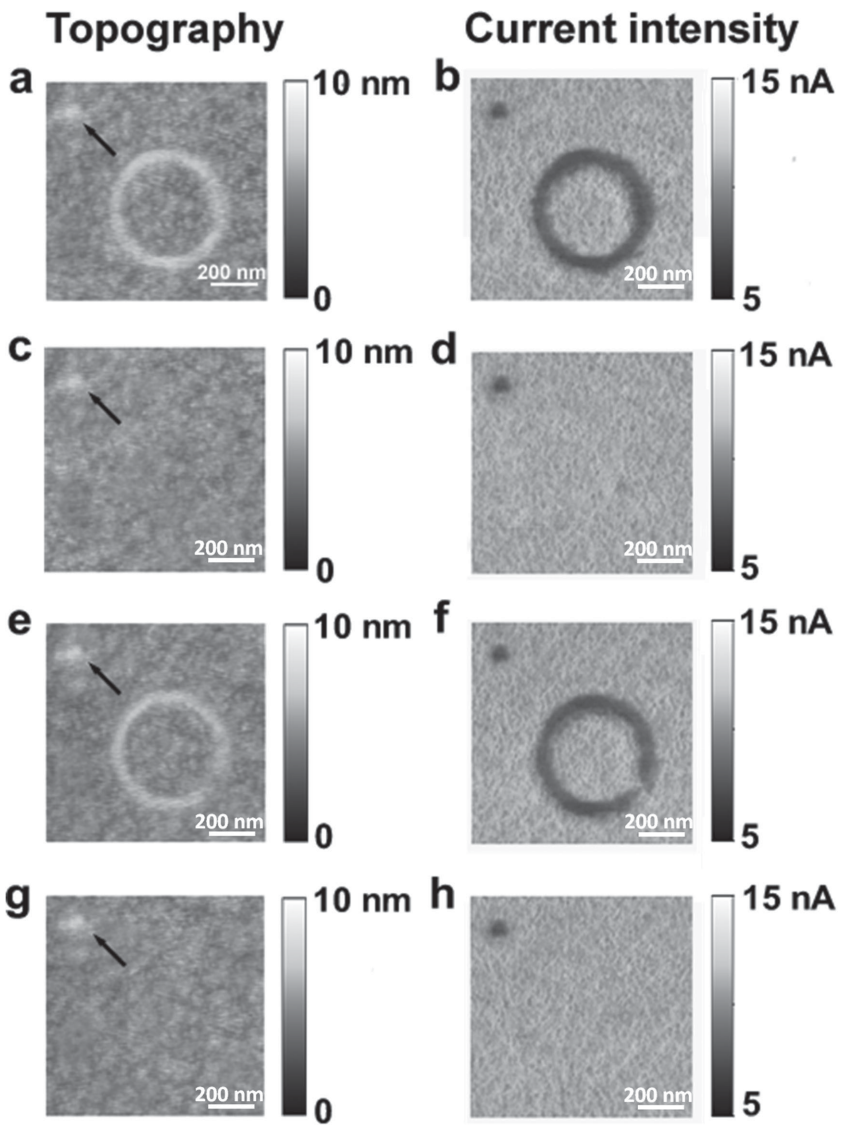

Figure 2. a) Topography and b) current intensity images of a circle written by conductive contact mode AFM on PPy(DBS) films (writing time: 5 ms); c,d) after erasing the circle (erasing time: 5 ms); e,f) rewriting a circle in the same area (writing time: 5 ms); g,h) after re-erasing the circle (erasing time: 5 ms). For orientation, a marker was inscribed in the upper-left corner of the images (indicated by an arrow). The size of each image is 1 μm × 1 μm.

of shorter pulses were observed. Repeated scanning of the AFM tip in the patterned area did not degrade or affect the topographic features. The pattern stability was tested after three weeks of inscription and no differences in the patterns were found. However, long term stability tests were not yet performed.

After demonstrating the successful electrochemical modification of the substrates their potential utilization as storage devices was tested. The ability of erasing the created structures is mandatory for this target. Figure 2c displays that the circle, generated in the first writing step, can be erased completely when the tip is scanned in the circle area with an opposite voltage (5 V) by applying the same inscription time (5 ms). In addition, the lithographic pattern also disappeared in the current intensity image (Figure 2d), which indicates that the reduced PPy(DBS) was oxidized again in the erasing process and returned to the conducting state. For the rewriting ability, it is important to ensure that the lithography process was performed in the same area where the structure was written at the first time. For this reason, a dot mark was additionally placed as an identifiable label in the upper left corner of each image during the first writing step (see arrows in Figure 2). Another circle was generated at the same location of the PPy(DBS) film utilizing the same writing procedure. Afterwards, the structure could be erased again by applying the opposite voltage. Write–erase cycles performed at the same position could be successfully repeated for 17 times with no observable memory effect of the previous writing process.

Additionally, scanning Kelvin probe microscopy (SKPM) was used for analyzing the chameical changes induced by the AFM electrochemical lithography process. The surface potential is mainly influenced by the chemical changes of the surface.[24] **Figure 3**a shows a surface potential map of a PPy(DBS) film after inscribing a circle. For the patterned area, the surface potential decreased from ≈70 to ≈40 mV. Afterwards, this value returned back to the original value after the erasing process (Figure 3c). The reversible changes also indicate that the PPy(DBS) film underwent reduction and reoxidation processes which are corresponding to the writing and erasing processes, respectively. As reported in literature, in addition to the reversible expansion, irreversible expansion may also occur in the redox reaction of PPy(DBS), which is thought to be caused by the irreversible insertion of ions and the swelling by the solvent.[25] In order to obtain a deeper insight into the change of the PPy(DBS) during the reversible structuring, lithography processes at different writing times were performed. As depicted in Figure 3d,e, the surface potential decreased more strongly at longer writing times (8 ms) and the surface potential value decreased from ≈70 to ≈25 mV. After erasing, the potential of the pattern area did not recover completely, which is thought to be caused by the irreversible insertion of Na^+ ions (Figure 3f). For this reason, the limitations of the write–erase process were studied in detail. **Figure 4** summarizes the topography and current intensity images of the generated circles utilizing different lithography times. For the writing processes, the expansion of volume increased with the writing time. Thus, the height of circles increased from ≈2 to ≈8 nm and the line width of the structures increased from ≈80 to ≈200 nm when the lithography times changed from 2 to 10 ms (Figure S1, Supporting Information). The

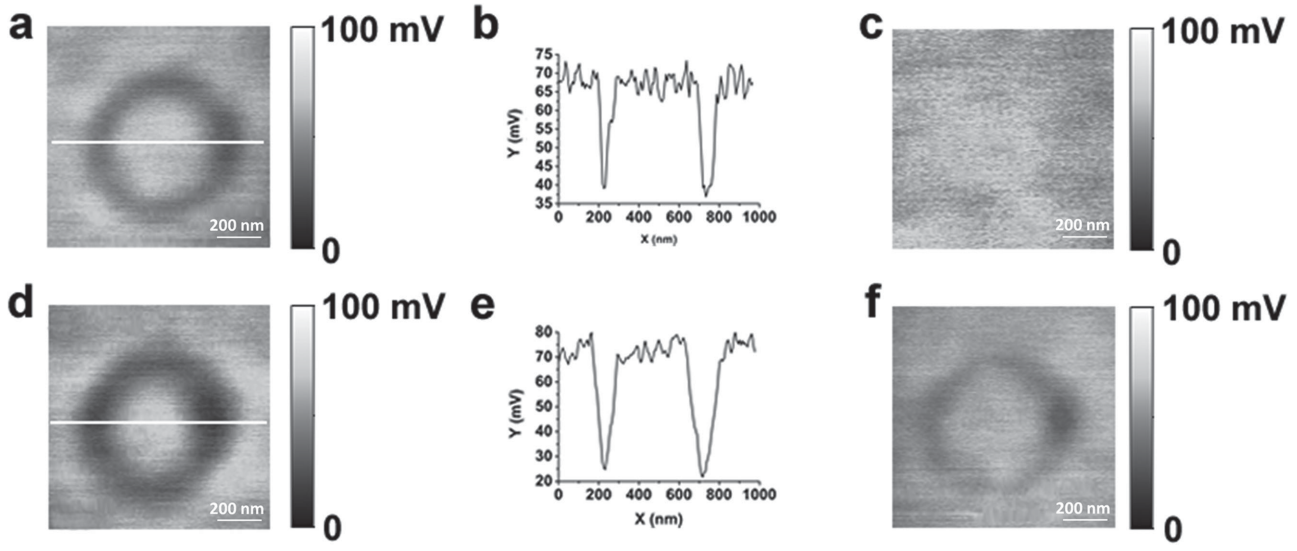

Figure 3. a,c) Surface potential images after writing and erasing a circle (writing time: 5 ms and erasing time: 5 ms). b) Cross section of the white line in (a). d,f) Surface potential images after writing and erasing a circle using longer times (writing time: 8 ms and erasing time: 8 ms). e) Cross section of the white line in (d). The size of each image is 1 μm × 1 μm.

current decrease of circles displayed a similar trend and changed from ≈2 to ≈9 mA (Figure S2, Supporting Information). These results can be explained by the fact that more PPy(DBS) was reduced during the electrochemical reaction at longer lithography times. As a result, a stronger increment of the volume and a stronger decrement of the conductivity took place. However, as shown in Figure 4, the circles can still be erased completely if the writing time is 2 ms or even 5 ms. However, when the writing time increased to 8 ms, only a part of the pattern could be erased. With further increased writing time (10 ms), the inerasable parts became larger, even when utilizing longer erasing times. For instance, in the case of the pattern when utilizing a writing time of 10 ms, the inerasable parts were nearly the same by applying an erasing time of 10 ms or even 15 ms. For a writing time of 8 ms, the height increase and current decrease of the inerasable parts were found to be ≈2 nm and ≈1.5 mV, respectively (Figure S3a,c, Supporting Information). For a longer writing time (10 ms), these values increased to ≈3.25 nm and ≈5 mV (Figure S3b,d,e, Supporting Information), respectively. Thus, we suggest that the reversible write–erase process can be accomplished only at a short lithography time, while longer times will cause an irreversible expansion which occurs due to the fact that the reversible expansion of PPy(DBS) occurs quickly, while most irreversible expansion takes much longer to stabilize.[25] Additionally, it was found that short writing times are also beneficial in terms of obtainable line and point resolution of the introduced method.

Also, repeated writing and erasing might result in the formation of irreversible structures. After 17 writing and erasing cycles the first irreversible parts of the pattern started to appear. It was, moreover, observed that patterning voltages <–9 V inevitably result in nonerasable features, which is attributed to an irreversible reaction of the PPy and/or excessive Joule heating which might result in an irreversible mass transport. These points have to be addressed in subsequent studies, as SKPM, due to its surface sensitivity, does not provide a clear picture to unambiguously answer this question at this point.

3. Conclusions

In summary, a reversible, erasable, and rewritable nanopattern with a routinely achieved resolution limit of ≈80 nm was fabricated on the PPy(DBS) films utilizing AFM electrochemical lithography. A distinct height increase was generated due to the incorporation of Na^+ ions and their solvation shells into the PPy matrix during the writing process. Afterward, the writing pattern can be erased completely by application of an opposite voltage. The changes of current intensity and surface potential indicate that PPy(DBS) underwent reduction and reoxidation processes, which were interpreted as writing and erasing processes, respectively. However, some inerasable parts of the pattern were also observed at increasing lithography times and high writing voltages, owing to an irreversible expansion of PPy(DBS). After erasing, the pattern can be rewritten at the same location of the film, which can be followed by additional erasing steps. Overall, the reversible volume change and resistance switching effects provide a possibility for the fabrication of memory nanodevices based on conductive polymers. In addition, the fabrication of memory devices at the micrometer scale can be realized as well utilizing parallel electrochemical lithography approaches which are by the application of stamps instead of AFM tips.[26,27]

4. Experimental Section

Sample Preparation: Silicon wafers (Siegert Wafer) were coated by thermal evaporation (QUORUM, Q150T) with a thin (60 Å) adhesion layer of titanium followed by a layer of gold (2000 Å). The pyrrole monomers (Aldrich) were distilled before use. PPy(DBS) was deposited

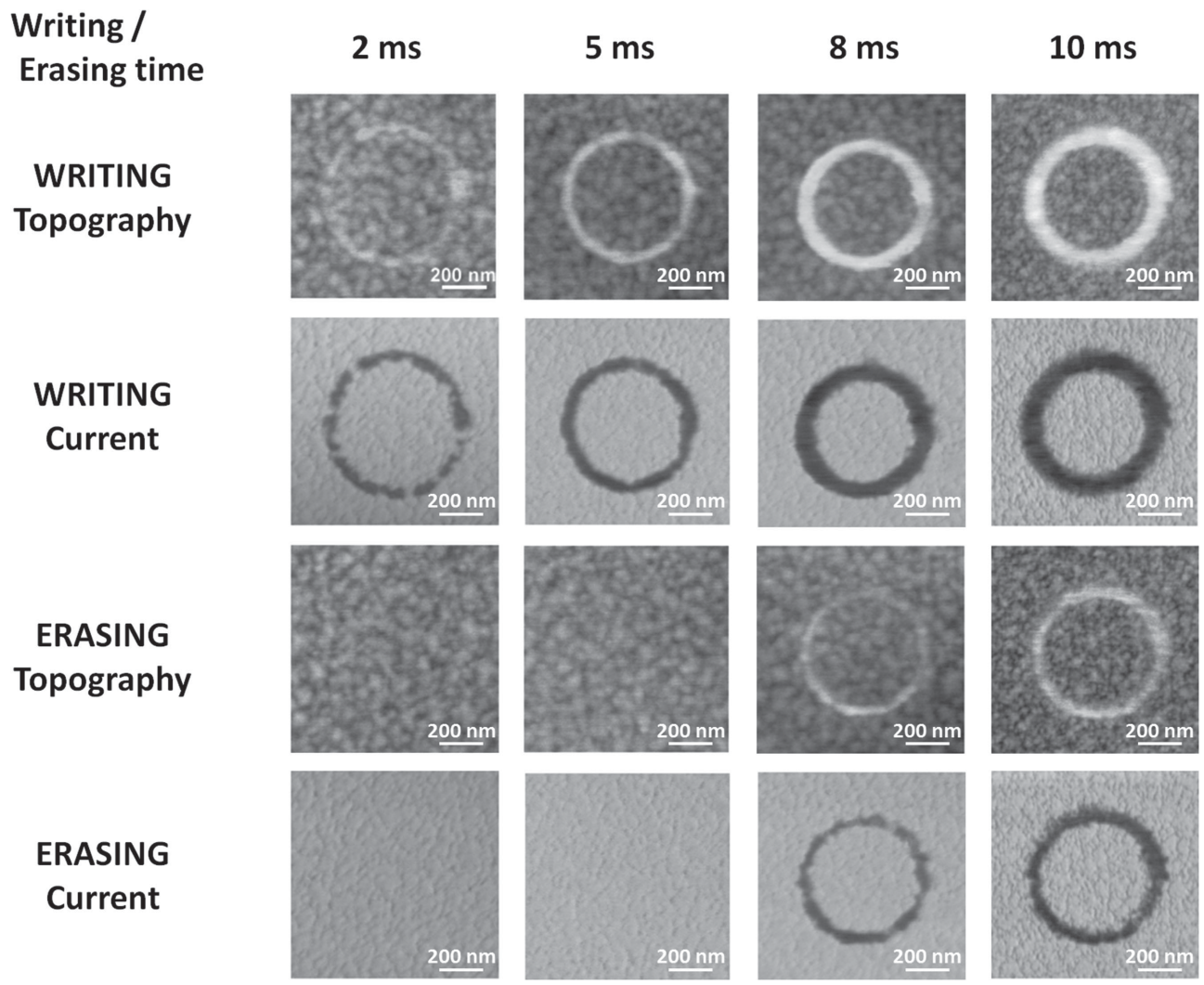

Figure 4. Comparison of the writing and erasing processes using different operation times. The size of each image is 1 μm × 1 μm.

potentiostatically at 0.55 V (vs Ag/AgCl) in an aqueous solution of 0.1 M pyrrole and 0.1 M NaDBS (Aldrich) in a three-neck glass electrochemical cell (Princeton Applied Research, VersaSTAT MC). A platinum wire was used as a counter electrode. The deposition time was 1 min, afterward, the surface was rinsed in ultrapure water to remove the physically adsorbed, unpolymerized pyrrole and NaDBS. Scanning electric microscopy (SEM) was conducted with a LEO 1530 Gemini (Zeiss) utilizing a SE2 detector.

AFM Electrochemical Lithography: Write–erase processes were performed using an AFM (NT-MDT, NTegra Aura) with a close-loop scanner system placed in a home-built humidity control chamber. Lithography experiments were carried out at room temperature at a controlled humidity (50% rel. humidity) utilizing a Pt coated AFM tip (NT-MDT, NCS36 Ti-Pt). Nanopatterns were created in contact mode, by varying the pulse duration while keeping the contact force constant. During the writing (erasing) process, a negative (positive) bias voltage was applied to the gold layer and the AFM tip was grounded all the time. Afterward, the patterns were imaged in tapping mode AFM (using the same tip).[28]

Current Intensity and Scanning Kelvin Probe Measurements: Current measurements were conducted by AFM in contact mode and a bias voltage of 1 V was applied between the tip (NT-MDT, NCS36 Ti-Pt) and the sample. Surface potential distributions were investigated by SKPM. The AFM/SKPM instrument was operated in tapping mode while a 1.5 V peak-to-peak AC voltage (at the resonance frequency of the cantilever) was applied between the tip and the sample. All measurements were performed at a relative humidity of 30%–50%.

Supporting Information

Supporting Information is available from the Wiley Online Library or from the author.

Acknowledgements

H.L. is grateful to the China Scholarship Council (CSC) for a fellowship grant. The work was conducted in the framework of the "Photonic Nanostructures" (PhoNa) project funded by the German Ministry of Education and Research (BMBF) in the program "Spitzenforschung und Innovation in den Neuen Ländern." The authors thank Prof. Anna Ignaszak and Kun Cong for the preparation of the PPy(DBS) films.

Received: September 10, 2015
Revised: October 16, 2015
Published online: December 15, 2015

[1] H. Shirakawa, *Angew. Chem. Int. Ed.* **2001**, *40*, 2574.
[2] A. G. Macdiarmid, *Angew. Chem. Int. Ed.* **2001**, *40*, 2581.
[3] A. J. Heeger, *Angew. Chem. Int. Ed.* **2001**, *40*, 2591.
[4] J. Gao, A. J. Heeger, J. Y. Lee, C. Y. Kim, *Synth. Met.* **1996**, *82*, 221.
[5] H. Yoon, S. Ko, J. Jang, *J. Phys. Chem. B* **2008**, *112*, 9992.
[6] C. C. Bof Bufon, T. Heinzel, *Appl. Phys. Lett.* **2006**, *89*, 012104.
[7] S. Li, K. Shu, C. Zhao, C. Wang, Z. Guo, G. Wallace, H. K. Liu, *ACS Appl. Mater. Interfaces* **2014**, *6*, 16679.
[8] N. Chartuprayoon, C. M. Hangarter, Y. Rheem, H. Jung, N. V. Myung, *J. Phys. Chem. C* **2010**, *114*, 11103.
[9] J. M. Sansiñena, V. Olazábal, T. F. Otero, C. N. Polo da Fonseca, M.-A. De Paoli, *Chem. Commun.* **1997**, 2217.
[10] R. H. Baughman, *Synth. Met.* **1996**, *78*, 339.
[11] H. Okuzaki, T. Kuwabara, K. Funasaka, T. Saido, *Adv. Funct. Mater.* **2013**, *23*, 4400.
[12] C. Immerstrand, K. Magnusson, E. Jager, M. Krogh, M. Skoglund, A. Selbing, O. Inganäs, *MRS Bull.* **2002**, *27*, 461.
[13] E. W. H. Jager, O. Inganäs, I. Lundström, *Science* **2000**, *288*, 2335.
[14] A. S. Lee, S. F. Peteu, J. V Ly, A. A. G. Requicha, M. E. Thompson, C. Zhou, *Nanotechnology* **2008**, *19*, 165501.
[15] G. Jeon, S. Y. Yang, J. Byun, J. K. Kim, *Nano Lett.* **2011**, *11*, 1284.
[16] J. C. Scott, *Science* **2004**, *304*, 62.
[17] Z. Xu, M. Gao, L. Yu, L. Lu, X. Xu, Y. Jiang, *ACS Appl. Mater. Interfaces* **2014**, *6*, 17823.
[18] A. A. Golriz, T. Kaule, J. Heller, M. B. Untch, P. Schattling, P. Theato, M. Toda, S. Yoshida, T. Ono, H.-J. Butt, J. S. Gutmann, R. Berger, *Nanoscale* **2011**, *3*, 5049.
[19] G. Jiang, A. Baba, R. Advincula, *Langmuir* **2007**, *23*, 817.
[20] R. Garcia, A. W. Knoll, E. Riedo, *Nat. Nanotechnol.* **2014**, *9*, 577.
[21] S. F. Lyuksyutov, R. A. Vaia, P. B. Paramonov, S. Juhl, L. Waterhouse, R. M. Ralich, G. Sigalov, E. Sancaktar, *Nat. Mater.* **2003**, *2*, 468.
[22] K. Nam, G. Lee, H. Jung, J. Park, C. H. Kim, J. Seo, D. S. Yoon, S. W. Lee, T. Kwon, *Nanotechnology* **2011**, *22*, 225303.
[23] T. Silk, Q. Hong, J. Tamm, R. G. Compton, *Synth. Met.* **2000**, *93*, 59.
[24] D. Meroni, S. Ardizzone, U. S. Schubert, S. Hoeppener, *Adv. Funct. Mater.* **2012**, *22*, 4376.
[25] D. Melling, S. Wilson, E. W. H. Jager, *Smart Mater. Struct.* **2013**, *22*, 104021.
[26] F. C. Simeone, C. Albonetti, M. Cavallini, *J. Phys. Chem. C* **2009**, *113*, 18987.
[27] M. Cavallini, Z. Hemmatian, A. Riminucci, M. Prezioso, V. Morandi, M. Murgia, *Adv. Mater.* **2012**, *24*, 1197.
[28] R. García, A. S. Paulo, *Phys. Rev. B* **1999**, *60*, 4961.

ADVANCED FUNCTIONAL MATERIALS

Supporting Information

for *Adv. Funct. Mater.,* DOI: 10.1002/adfm.201503834

Reversible Nanopatterning on Polypyrrole Films by Atomic Force Microscope Electrochemical Lithography

He Liu, Stephanie Hoeppener, and Ulrich S. Schubert*

Supporting information

Reversible Nanopatterning on Polypyrrole Films by Atomic Force Microscope Electrochemical Lithography

He Liu,[1,2] Stephanie Hoeppener,[1,2]* and Ulrich S. Schubert[1,2]

1. Laboratory of Organic and Macromolecular Chemistry (IOMC), Friedrich Schiller University Jena, Humboldtstr. 10, 07743 Jena, Germany
2. Jena Center for Soft Matter (JCSM), Friedrich Schiller University Jena, Philosophenweg 7, 07743 Jena, Germany

Corresponding author: Dr. Stephanie Hoeppener

Tel: +49 (0)3641 948596

Fax: +49 (0)3641 948202

E-mail: s.hoeppener@uni-jena.de

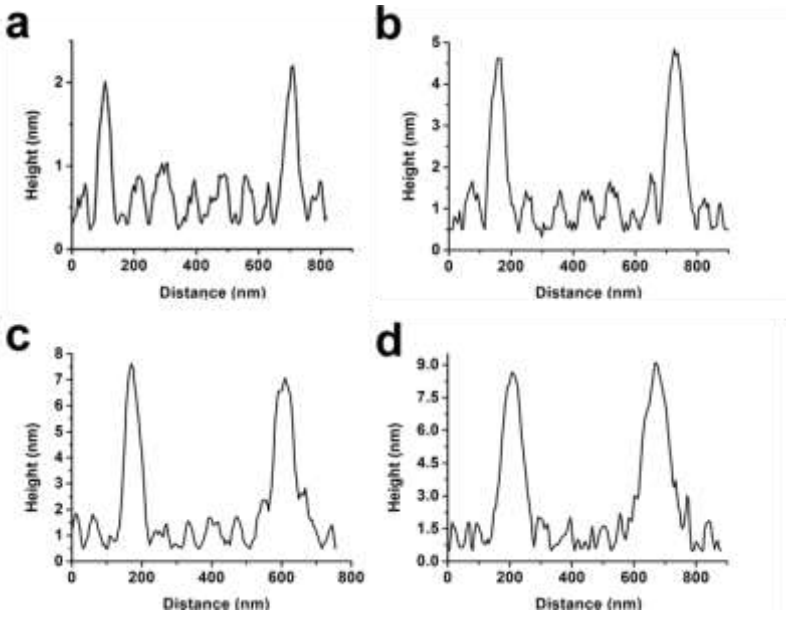

Figure S1. Distance-height profiles corresponding to the topography images of the written circles at different writing times in Fig. 4 (a: 2 ms, b: 5 ms, c: 8 ms, d: 10 ms).

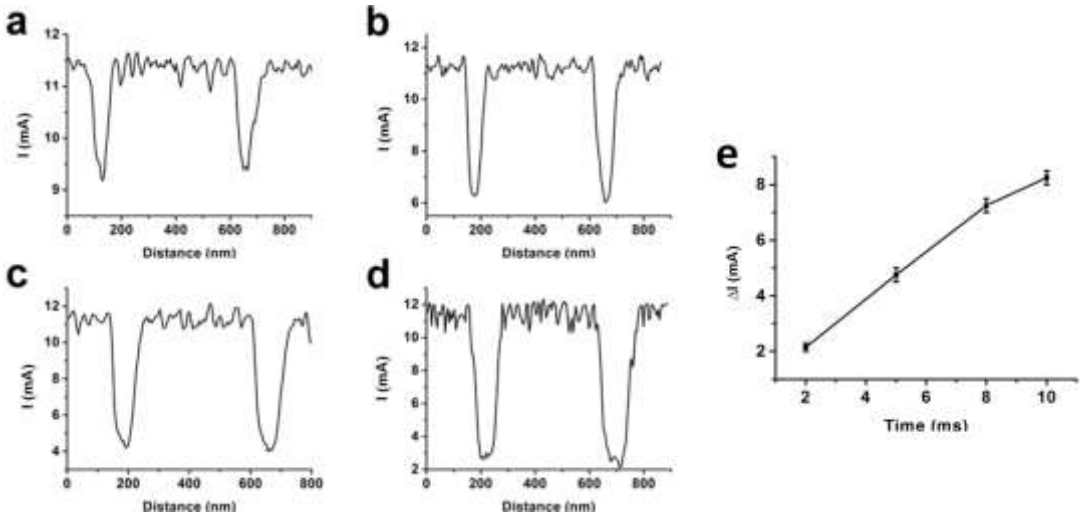

Figure S2. Distance-current profiles corresponding to the current images of the circles inscribed at different writing times in Fig. 4 (a: 2 ms, b: 5 ms, c: 8 ms, d: 10 ms). e) Plot of the differences in the conductivity obtained after different writing times.

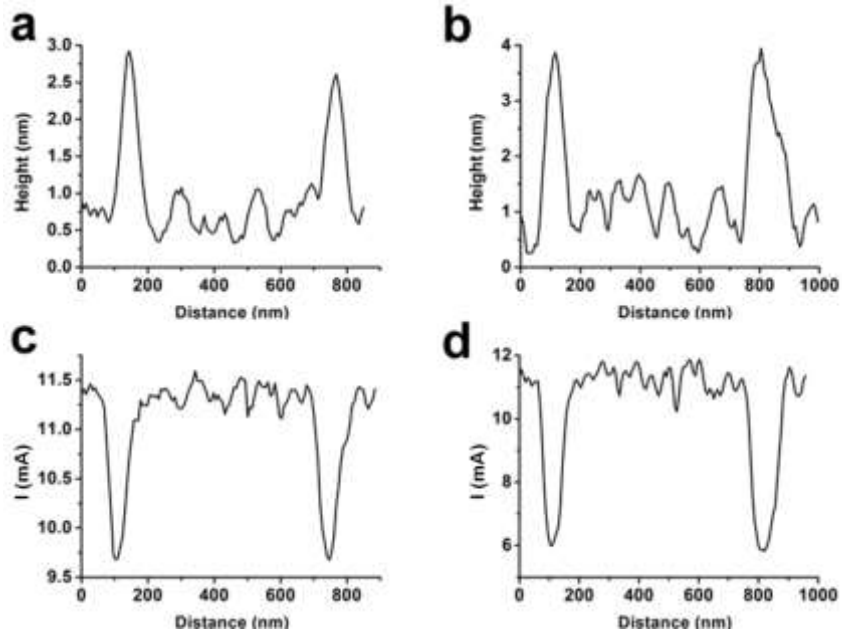

Figure S3. Distance-height (a, b) and distance-current (c, d) profiles corresponding to the topography and current images of the circles after erasing processes in Fig. 4 (a, c: 8 ms; b, d: 10 ms).

Publication P5

Site-specific surface functionalization of graphene via electro-oxidative lithography for bio-sensing applications

H. Liu, S. Hoeppener, U. S. Schubert

ChemPhysChem **2016**, DOI: 10.1002/cphc.201600490.

ChemPubSoc Europe

DOI: 10.1002/cphc.201600490

CHEMPHYSCHEM Articles

Site-Specific Chemical Surface Functionalization and Electronic Patterning of Graphene by Electrooxidative Lithography

He Liu,[a, b] Stephanie Hoeppener,*[a, b] and Ulrich S. Schubert[a, b]

The combination of different properties being manipulated on nanomaterials is one of the challenges in nanotechnology research. In particular, the possibility to tailor the electronic and chemical properties offers promising possibilities for the design of functional nanostructures. Herein, we report an approach that permits control of these properties on the basis of electrooxidative lithography to structure reduced graphene oxide functionalized with a self-assembled monolayer of *n*-octadecyltrichlorosilane. The electrochemical oxidation process first induces the formation of polar acid groups on the monolayer, which can be used to covalently bind nanoparticles and molecules and, secondly, also allows the reoxidation of the underlying reduced graphene oxide. As such, the chemical signature as well as the electronic properties of the substrate can be tailored on the micro- and nanometer scale. Details on the oxidation of the monolayer as well as thorough characterization of the electronic properties will be presented. Finally, the approach is used to demonstrate the fabrication of a sensitive glucose sensor device.

1. Introduction

During the last decades, a large variety of nanomaterials have been developed featuring superior properties, that is, high surface-to-volume ratio, high catalytic activity, localized plasmon resonances, stability at high current densities, an so on. However, the combination of nanomaterials into complex frameworks so far remains a challenge. On the route towards a feasible nanopatterning strategy to combine different materials as well as to combine different functionalities, lithographic strategies are frequently discussed. In particular, graphene has been explored as a potential building block for various electronic device applications, owing to its exceptionally high conductivity and carrier mobility.[1–5] Similar to silicon-based materials in microelectronic processing, lithographic patterning of graphene represents an essential step for the fabrication of graphene devices.[6] Existing approaches of patterning graphene include template transfer,[7,8] mask etching,[9,10] and direct-write processes.[11–13] Among these approaches, direct-write methods have gained significant attention, because they enable resist-free structuring and avoid contamination of the graphene with resist used in conventional e-beam and photolithographic approaches. Zhou et al. developed a focused laser beam technique to fabricate an extended area of micropatterned graphene oxide (GO) and reduced GO (RGO) multilayers on quartz substrates.[11] Lemme and co-workers reported the etching of graphene devices with a helium ion beam including in situ electrical measurements during the lithographic process.[14] Compared to optical and electron beam lithography, scanning probe induced direct-write processes are cost effective and can be applied under ambient processing conditions.[15] For example, Wei et al. obtained RGO patterns with nanoscale resolution by the local thermal reduction of GO with a heated atomic force microscope tip.[16] Up to now, studies on direct-write methods utilizing a probe have been mainly focused on tailoring the electrical structure on the graphene surface (i.e. tip-induced conversion between graphene and graphene oxide). Only a few approaches report the generation of a chemical structure on graphene films. For instance, Hirtz et al. introduced phospholipid membranes as a route for the noncovalent immobilization of various functional groups on graphene by using dip-pen lithography.[17] A recent review about scanning probe lithographic approaches to structure graphene and graphene oxides is provided by Kulkarni et al.[18]

Herein, we report the development of a new direct-write method utilizing electrooxidative lithography[19] of self-assembled monolayers (SAMs) deposited onto graphene layers that can simultaneously address tailoring of both the chemical and electrical properties of graphene. These monolayers can be utilized in a range of electrical devices and can manipulate the electron transfer, either within the molecular network or by utilizing the covalent siloxane bond between the molecule and the substrate.[20–23] In the present study, *n*-octadecyltrichlorosilane (OTS) SAMs were used to functionalize graphene oxide and to generate a chemically active surface pattern by electro-

[a] H. Liu, Dr. S. Hoeppener, Prof. U. S. Schubert
Laboratory of Organic and Macromolecular Chemistry (IOMC)
Friedrich Schiller University Jena
Humboldtstr. 10, 07743 Jena (Germany)

[b] H. Liu, Dr. S. Hoeppener, Prof. U. S. Schubert
Jena Center for Soft Matter (JCSM)
Friedrich Schiller University Jena
Philosophenweg 7 07743 Jena (Germany)
E-mail: s.hoeppener@uni-jena.de

Supporting Information for this article can be found under: http://dx.doi.org/10.1002/cphc.201600490.

oxidative lithography. Electrooxidative lithography has been used to chemically pattern self-assembled monolayers with nanometer resolution.[24–26] Surface modification can be followed by the assembly of functional molecules, complexes, and particles, which also enables the targeted, sequential construction of functional device features. According to this approach, we can directly obtain an addressable, chemically functional pattern on the surface of graphene and, additionally, manipulate the electronic properties of the underlying graphene layers. The details of the oxidation process were analyzed by height and current atomic force microscopy (AFM) measurements of written dot patterns fabricated at different oxidation times. Moreover, silver nanoparticles were utilized to confirm the chemical functionalization of the site-selectively oxidized areas and the generated functional groups formed during the lithographic oxidation. To demonstrate the applicability of the introduced approach, a glucose sensor was fabricated.

Glucose biosensors based on nanomaterials, such as carbon nanotubes and metal nanoparticles, have recently been extensively studied.[27–29] In comparison with conventional nanomaterials, graphene-based biosensors are advantageous because of the possibility to obtain large detection areas, to utilize new sensing mechanisms, and the easy functionalization.[30–32] On the basis of the introduced electrooxidative lithography approach, a sensor device was fabricated that allowed the detection of glucose by monitoring current changes in the graphene device. A detection limit of 0.01 mM was achieved and demonstrated the capabilities of the site-selective manipulation of the chemical and electronic properties of graphene by electrooxidative lithography.

2. Results and Discussion

2.1. Preparation and Characterization of OTS-RGO Films

One of the aims of the present study was the functionalization of graphene and the local fabrication of chemically active surface patterns. These patterns combine unique electronic properties with chemical addressability. This combination is a strong feature of the introduced lithographic process, which provides interesting possibilities for nanofabrication. The outline of the performed functionalization sequence is illustrated in Scheme 1.

First, an (aminopropyl)trimethoxysilane (APTMS) monolayer was formed on a cleaned silicon wafer. This layer served as an adhesion promotor for the self-assembly of graphene oxide (GO) (Scheme 1 a). Due to the presence of abundant polar oxygen-containing groups, GO can be well dispersed in aqueous solutions and can be utilized for further modification of the GO by chemical reaction and the self-assembly of molecules.[33,34] In particular, *n*-octadecyltrichlorosilane (OTS) is an attractive molecule to be self-assembled onto GO, as OTS forms a laterally polymerized network that can anchor to the polar surface groups of GO [Scheme 1 b, c (left)]. Stable films of OTS can be formed that withstand, for example, subsequent thermal treatment, which can change the electronic properties of GO and forms reduced graphene oxide (RGO) [Scheme 1 c

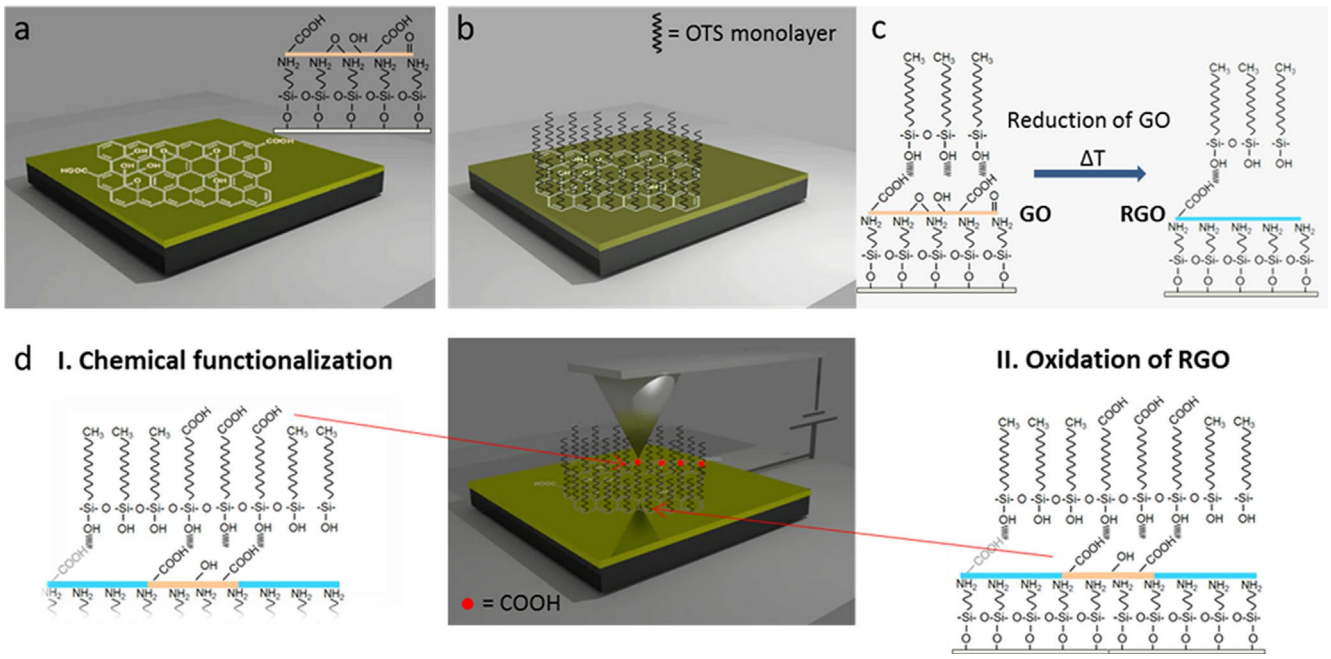

Scheme 1. Schematic representation of the oxidation process. a) Graphene oxide (GO) immobilized on an APTMS self-assembled monolayer. b) Self-assembly of an OTS monolayer onto the graphene oxide flake. c) Thermal reduction of GO into reduced GO (RGO). The OTS monolayer remains structurally intact because of good lateral cross-linking of the OTS monolayer and anchorage to residual oxide groups on RGO. d) Electrooxidative lithography is performed on the OTS monolayer by means of an electrically biased AFM tip (middle). During this process, first the top functional groups of the OTS monolayer are chemically oxidized in close vicinity of the tip and polar groups are formed (left). Simultaneously, the RGO is oxidized again in these areas.

(right)]. These substrates can be used as suitable substrates for electronic and chemical patterning by means of electrooxidative lithography (Scheme 1 d, right).

The individual functionalization steps were followed by means of water contact angle (WCA) measurements, FTIR and Raman spectroscopy, as well as by morphological studies conducted by AFM. Whereas the cleaned silicon wafer exhibited a typical water contact angle of $<5^\circ$, the water contact angle increased to $(58\pm3)^\circ$ after the APTMS assembly, which indicated the successful functionalization of the silicon surface. The observed water contact angle slightly decreased to $(45\pm4)^\circ$ after the self-assembly of GO (GO-APTMS) due to the presence of the polar surface groups of GO. A discontinuous film of individual GO sheets with a thickness of about 1 nm was attached onto the APTMS-covered surface, as observed by AFM investigations (Figure 1 b). After the self-assembly of the OTS monolayer onto GO (OTS-GO), the contact angle strongly increased to approximately $(98\pm3)^\circ$. This value is much higher than that of GO-APTMS but is still lower than that on a compact OTS monolayer [$(110\pm3)^\circ$],[35] and this was mainly attributed to the formation of only an incomplete layer of GO sheets on the surface, as observed by AFM investigations (Figure 1 b).

These observations were supplemented by FTIR spectroscopy, in particular, by the analysis of the $-CH_2$ stretching vibrations. These bands are not observable for the APTMS-GO substrates, as the signal intensities arising from the propyl units of the APTMS monolayer are too weak. However, after the self-assembly of the OTS monolayer, the $-CH_2$ vibrations are clearly observable and are located at $\tilde{\nu}=2918$ and 2850 cm^{-1} (Figure 2 a). The positions of these bands indicate the formation of a well-organized OTS monolayer on the graphene oxide sheets. Additionally, as shown in Figure 1 c, the AFM investigations confirm the formation of a smooth OTS film morphology with a root mean square (RMS) roughness of 0.77 nm.

At this stage, the insulating electronic properties of GO were modified by an additional reduction step [Scheme 1 c (right)]. For large-scale substrates, heating to 200 °C under a protective N_2 atmosphere for 2 h results in the reduction of GO (OTS-RGO).[36,37] Despite the elevated temperatures, the WCA of the OTS-RGO did not significantly change during the reduction step [$(97\pm3)^\circ$], which indicated that the OTS monolayer was preserved during the thermal reduction of GO. During the reduction step, the polar surface groups of the GO are also supposed to be reduced. As a consequence, one would expect the monolayer to significantly degrade. However, due to the fact that OTS forms a laterally polymerized network, a higher film stability was obtained relative to that of other self-assembly molecules (i.e. thiols), and the film was preserved even if the number of direct anchoring points was reduced due to reduction of the oxygen-containing surface groups of GO. This was further confirmed by FTIR spectroscopy analysis of the $-CH_2$ stretching vibrations (Figure 2 a), which shifted only slightly towards higher wavenumbers. The AFM image (Figure 1 d) revealed a small increase in the surface roughness

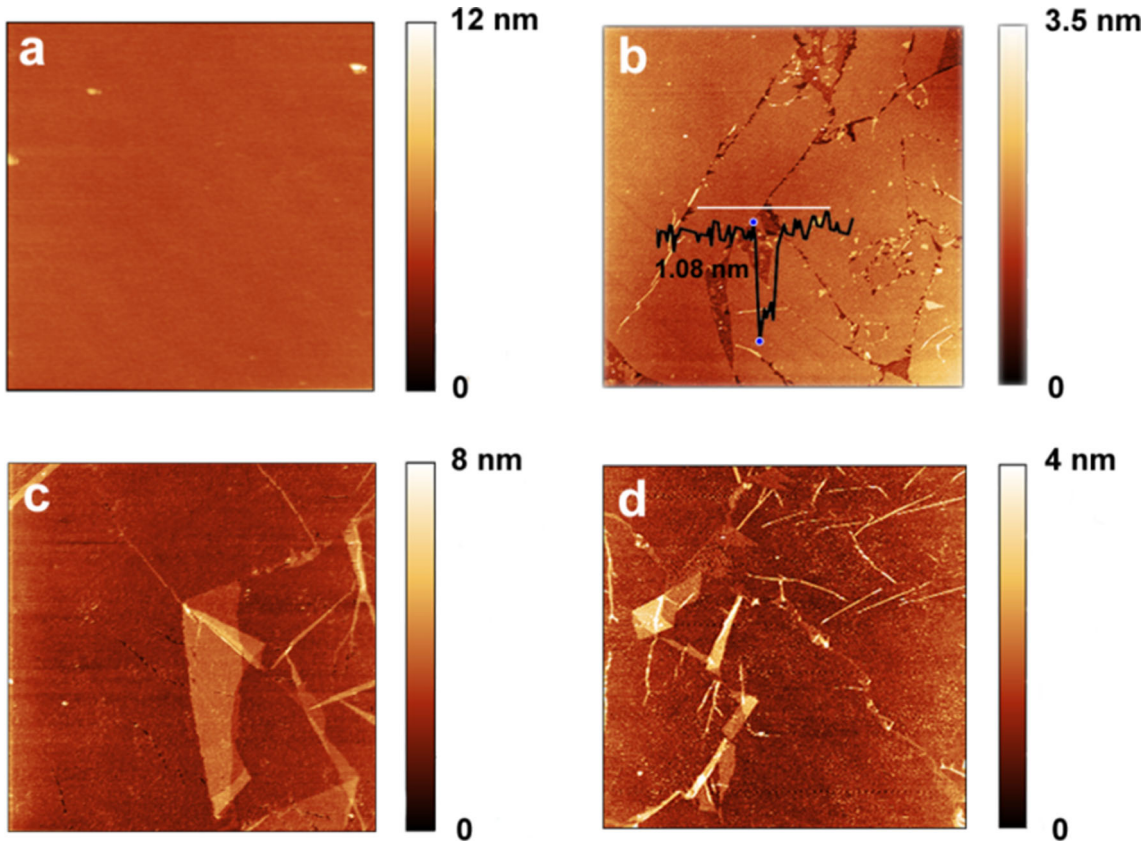

Figure 1. AFM images of a) APTMS, b) GO-APTMS, c) OTS-GO, and d) OTS-RGO. The area for the image is always 5 μm × 5 μm.

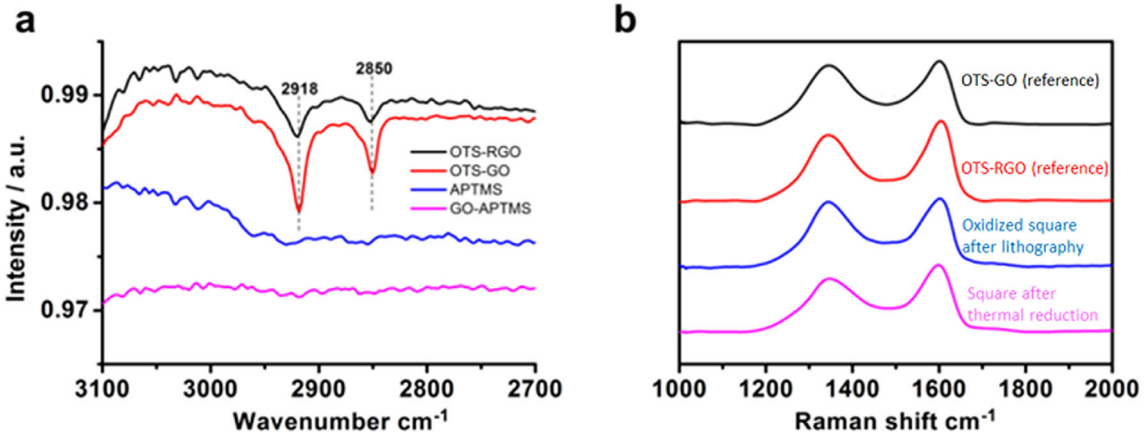

Figure 2. a) FTIR spectra of different samples; b) Raman spectra of OTS-GO, OTS-RGO, lithographic square areas before and after thermal reduction.

(RMS roughness: 1.02 nm); however, the reasonably homogeneous nature and low surface roughness of the films were still preserved after the thermal annealing step. Important in this reduction step was the fact that relatively low heat-treatment temperatures of only 200 °C were chosen to avoid the destruction of the OTS monolayer and, moreover, to prevent the splitting of GO into smaller domains.[37]

Additionally, Raman investigations of OTS-GO and OTS-RGO were performed to confirm the reduction step (Figure 2b). The curves display two prominent bands at shifts of 1346 and 1600 cm^{-1} corresponding to the D and G modes of graphene. The G mode is related to vibration of the sp^2-hybridized carbon atoms, and the D mode corresponds to the sp^3-hybridized carbon atoms.[36,37] Thus, the ratio of the intensities of these bands (I_D/I_G) is related to the electronic structure of GO/RGO. This ratio decreased from 1.50 to 1.16 after thermal reduction, and consequently, a large part of GO was reduced to RGO. Other evidence for the reduction of GO was obtained by sheet resistance measurements, which decreased from (9740 ± 25) to (67 ± 3) Ω sq^{-1} after the heat treatment. These experiments confirmed that conductive RGO layers could be obtained, whereas they were still covered with a reasonably well-ordered monolayer of OTS (Figure 2a). These substrates can be used for the site-selective formation of chemically active, addressable functional surface groups, and additionally, the surface properties of the underlying RGO can be electronically tailored by means of electrooxidative nanolithography (Scheme 1d).

2.2. Electrooxidative Nanolithography on OTS-RGO Substrates

Electrooxidative lithography is a tip or conductive stamp based approach that enables the structuring of OTS monolayers with chemically active functional groups [Scheme 1d (I)].This is achieved by applying a negative bias voltage to a conductive AFM tip or a conductive stamp. Whereas the pattern resolution is in the micrometer scale in the latter approach, a tip-mediated electrooxidation process can yield chemical patterns with dimensions down to 10 nm. The pattern resolution obtained within the tip-mediated process is governed by the oxidation conditions (e.g. relative humidity, applied voltage, and pulse length) as well as the tip dimensions.[38] In the course of the electrooxidation process, the $-CH_3$ surface terminal groups of the SAM are oxidized into polar functional groups, that is, –COOH groups, in the area of tip contact. Only recently was this oxidation process, so far mainly applied on slightly doped silicon wafers functionalized with an OTS monolayer, successfully transferred to other conductive substrates, for example, OTS-coated indium tin oxide (ITO).[39] This development motivated the use of the electrooxidative patterning approach also on OTS-GO covered substrates. Due to the high sheet resistance of OTS-GO films, no successful functionalization could be achieved. Only if reduced GO films (OTS-RGO) were utilized chemical patterning of the substrates was possible. The oxidation process of the self-assembled monolayers was directly observable by contact mode AFM investigations. An oxidized ring structure fabricated by applying a bias voltage of −10 V at a relative humidity (RH) of 50% and a pulse duration of 3 ms is depicted in Figure 3.

The oxidation process resulted in a drastic change in the surface properties of the OTS-covered substrates in the oxidized areas. In fact, the hydrophilic properties of the –COOH groups, formed during the electrooxidation process, could be visualized by means of lateral force AFM investigations (Figure 3b). Due to preferred absorption of water vapor from ambient air, the oxidized areas showed a pronounced increase in the lateral friction exerted onto the AFM tip relative to that of the unmodified, hydrophobic OTS monolayer. To further confirm the chemical functionalization introduced by the electrooxidation process, scanning Kelvin probe microscopy (SKPM) was utilized, as the surface potential is influenced by the chemical changes on the surface. Figure 4a shows the surface potential map of an oxidized circle (bias voltage: −10 V, RH: 50%, pulse duration: 2.5 ms). The surface potential increased by about 25 mV in the lithographic area (Figure 4b) with respect to the surrounding, nonoxidized OTS monolayer. This increase is in agreement with investigations performed on electrooxidized OTS-Si samples, for which higher surface potential values were also found in the oxidized areas.[36] Tapping mode AFM investi-

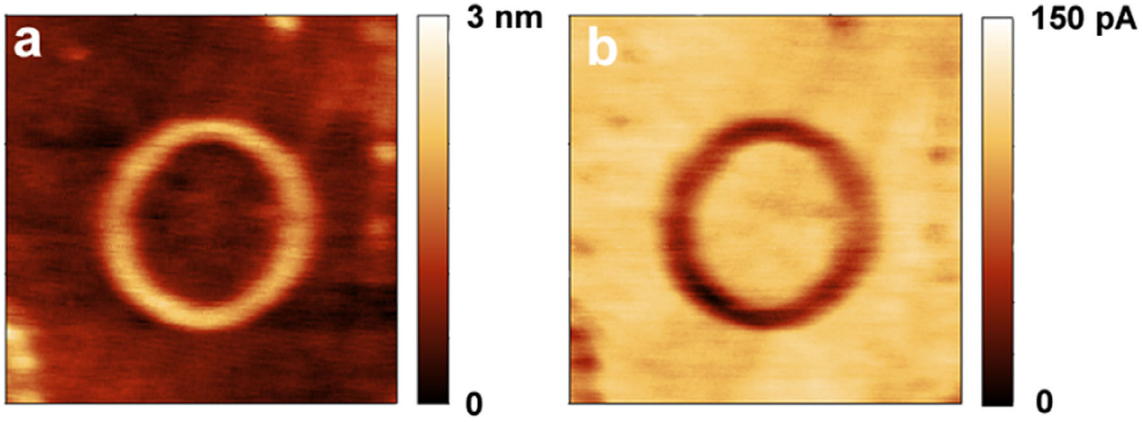

Figure 3. Height (tapping mode) and lateral force (contact mode) images for electrooxidative lithography on the OTS-RGO substrate. Lateral forces appear with reversed contrast upon changing the scan direction. The area for the image is always 3 μm×3 μm.

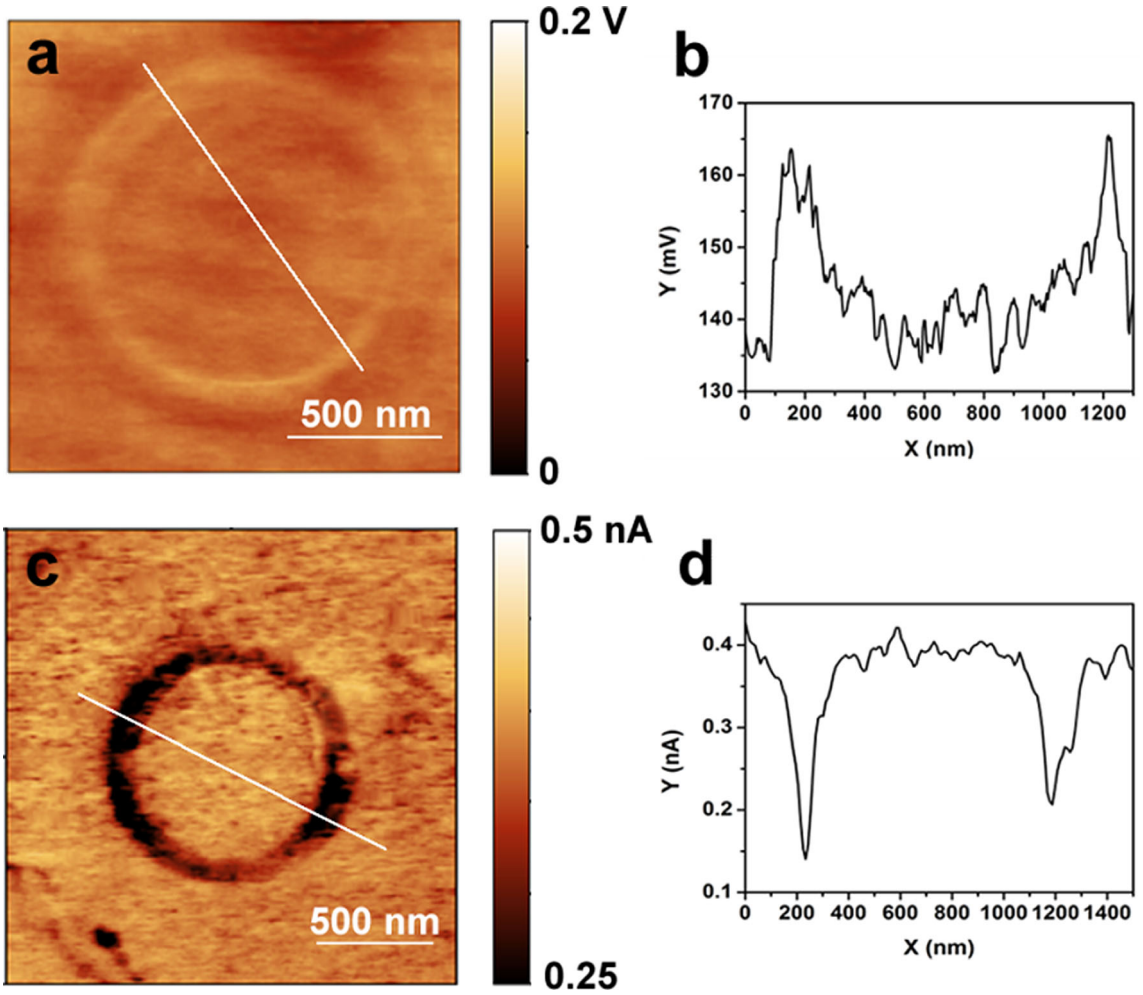

Figure 4. a, c) Surface potential and current images and b, d) their corresponding section analyses for electrooxidative lithography conducted on the OTS-RGO surface.

gations, moreover, revealed a height increase of around 1.5 nm in the oxidized ring area (Figure 3a). Possible reasons for this increase in height are the oxidation of RGO or even the oxidation of the silicon substrate itself. To investigate this issue in more detail, micro-Raman investigations (Figure 2b) of a square area generated by electrooxidative lithography (bias voltage: −10 V, RH: 50%, pulse duration: 3 ms, 8 μm×8 μm) (Figure S1, Supporting Information) were conducted, and it was found that the characteristic ratio of the intensities of the D and G bands (I_D/I_G) was 1.46, which is almost the same value

as that observed for GO before thermal reduction ($I_D/I_G = 1.50$) (Figure 2b). These findings strongly suggest that not only electrochemical oxidation of the OTS monolayer occurred but that, additionally, oxidation of RGO took place. This process is reversible, and the substrate can be thermally reduced again with the same method as mentioned above. The reduction was, moreover, confirmed by micro-Raman investigations. As shown in Figure 2b, the I_D/I_G ratio decreased to 1.19, which is close to that of OTS-RGO before lithographic oxidation ($I_D/I_G = 1.16$) (Figure 2b).

The conversion of RGO into GO by reoxidation also had a strong influence on the electronic properties of the substrate. A powerful means to investigate this aspect is the possibility to measure current maps by means of contact mode AFM imaging with an applied voltage between the conductive tip and the sample. Figure 4c illustrates a current mapping of the oxidized ring structure. The detectable current decreased in the oxidized areas, which indicated reoxidation of RGO in the electrooxidized areas. However, to exclude the possibility that the drop in conductivity could also be related to the growth of silicon oxide at the monolayer–Si interface, detailed investigations of the oxidation process were performed by fabricating a set of dot patterns with different oxidation times (bias voltage: −10 V, RH: 50 to 55%) by utilizing the same tip for oxidation and analysis of all structures to make sure that the tip parameters were not influencing the results. These experiments were conducted on bare silicon wafers, RGO assembled on an APTMS-modified silicon wafer, and finally on the OTS-RGO substrates for comparison (Figure 5). The changes in the height and conductivity were analyzed for the individual structures (Figures S2–S7). Figure 5a summarizes the respective height increases observed during the oxidation process. For the reference measurements on silicon, a self-limiting growth of the oxide patterns was observed.[40] In the cases of RGO-APTMS and OTS-RGO, different oxidation profiles were obtained. At short oxidation times between 0 and 1.4 ms, a relatively slow height increase was observed until a structure height of approximately 0.5 nm was reached. After that, the height increase accelerated until a structure height of 2.5 nm was obtained. After 8 ms, the height increase stopped at a structure height of 3 nm. No significant differences could be observed between RGO and the OTS-RGO-modified samples. Thus, clearly, the oxidation of the OTS monolayer did not significantly contribute to the observed height increases. We suggest that in the first stage the height increase was mainly induced by the conversion of graphene into graphene oxide and then the oxidation of Si occurred during the second and third stages. This conclusion is consistent with the reports of Chuang and co-workers.[41] Moreover, for the first stage of OTS-RGO oxidation, the value of the height increase (≈0.5 nm) is consistent with the height increase expected from graphene to graphene oxide.[42]

Additionally, the current decrease on the oxidized dot patterns was analyzed (Figure 5b). Gradually decreasing current differences between the oxidized structures and the surrounding, unmodified substrates were observed for all curves. Also, it was found that the influence of the monolayer was small. Effectively, the final difference between OTS-RGO and the bare silicon characteristics (−4 pA) reflects the changes in the conductivity of RGO.

Whereas the influence of the OTS monolayers on the electronic properties of RGO was found to be negligible, the electrooxidative lithography process of the surface terminal groups adds an additional feature that enables the site-selective functionalization of RGO in the oxidized areas. Due to the fact that polar functional groups, that is, –COOH groups, are generated by the oxidation of the monolayer, these areas can be utilized to selectively bind Au ions onto the carboxyl groups, which can be reduced subsequently by H_2O_2. These nanoparticles can be further enlarged by an electroless silver-plating method to obtain larger nanoparticles, which can be easily detected by means of tapping mode AFM imaging (Figure S8a). The Ag nanoparticles exhibited remarkable stability, as they were stable even against adhesion tape, which was used to clean the substrate from contaminants derived from the wet-chemical metalization procedure. This stability, moreover, enabled subsequent reduction of GO in the electrooxidatively modified areas by thermal treatment. After the formation of the Ag nanoparticles, the substrate was thermally reduced again by using the same method of thermal reduction. It was clearly ob-

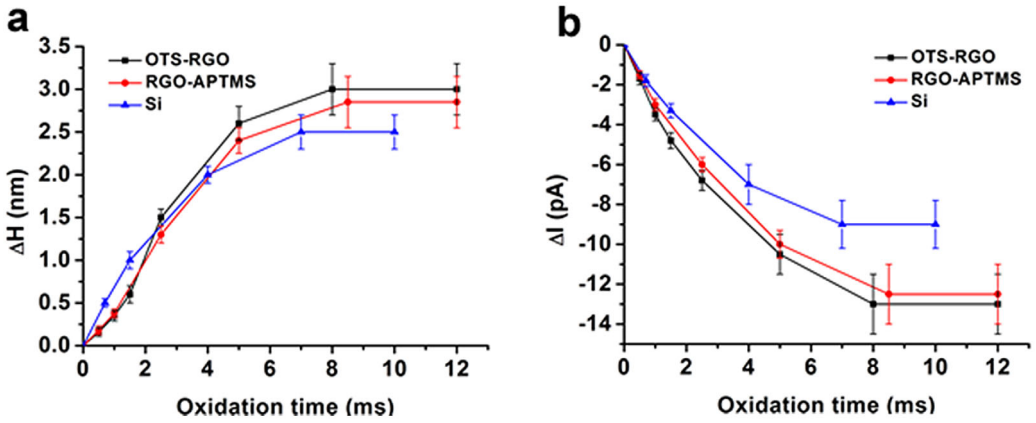

Figure 5. Analysis of the a) height increase (ΔH) and b) current decrease (ΔI) of dot patterns fabricated by means of electrooxidation lithography at different oxidation times.

served that the particles remained on the oxidized structure during the thermal reduction process (Figure S8b). These experiments highlight the versatile possibilities to combine tip-based lithography with OTS monolayer functionalized GO and offers attractive possibilities to combine the chemical and electronic features of the oxidation process to create functional nanostructures.

2.3. Glucose Detection on the Basis of Electrooxidative Lithography

Next to the site-selective assembly of nanoparticles, functional molecules can also be covalently assembled onto oxidized structures. Graphene offers promising prospects for the fabrication of biosensors due to its unique properties, such as its fast electron transport, its large detecting area, and the diversity of its possible functionalizations. Here, we demonstrate the fabrication of a glucose sensor on the basis of an OTS-RGO micropattern. The micropattern was prepared by using the method that was reported in previous work, and we transferred the approach of electrooxidative lithography to the micrometer scale by utilizing a conductive stamp instead of a conducting AFM tip.[43] After applying a suitable electrical bias voltage between a transmission electron microscopy (TEM) copper grid with a diameter of 3.05 mm and the OTS-RGO, the $-CH_3$ groups of OTS were converted into –COOH groups, which occurred in a manner similar to electrooxidative lithography based on an AFM tip. Figure 6a shows an optical micrograph of water vapor condensation on the micropattern of the oxidized structure. After thermal reduction, this micropattern facilitated with –COOH groups was used to bind glucose oxidase (GOD) through amide bonding after activation with *N*-hydroxysuccinimide (NHS)/1-ethyl-3-(3-dimethylaminopropyl)carbodiimide hydrochloride (EDC). As shown in Figure 6b,c, the enzymes were selectively immobilized on the lithographic stripe areas with good coverage. GOD catalyzes the oxidation of glucose in the following reaction [Eq. (1)]:

$$\text{D-glucose} + O_2 + H_2O \rightarrow \text{D-gluconic acid} + H_2O_2 \quad (R1)$$

The reaction product H_2O_2 can increase the conductance of graphene. This current increase is not caused by the direct transfer of electrons, but the reaction product H_2O_2 plays an essential role and is responsible for a small p-doping effect.[31] Only a minute amount of H_2O_2 will cause a detectable enhancement in the current, because of the small size of the device at the micrometer scale. Consequently, a very low detection limit of glucose can be achieved. Figure 6d illustrates the current values corresponding to different concentrations of glucose. At low glucose concentrations, the current shows an almost linear increase with concentration. The percentage increase in the current value in response to 0.01 mM glucose was about 14%. Afterwards, the current growth slowed down when the concentration was higher than 0.1 mM due to a limit-

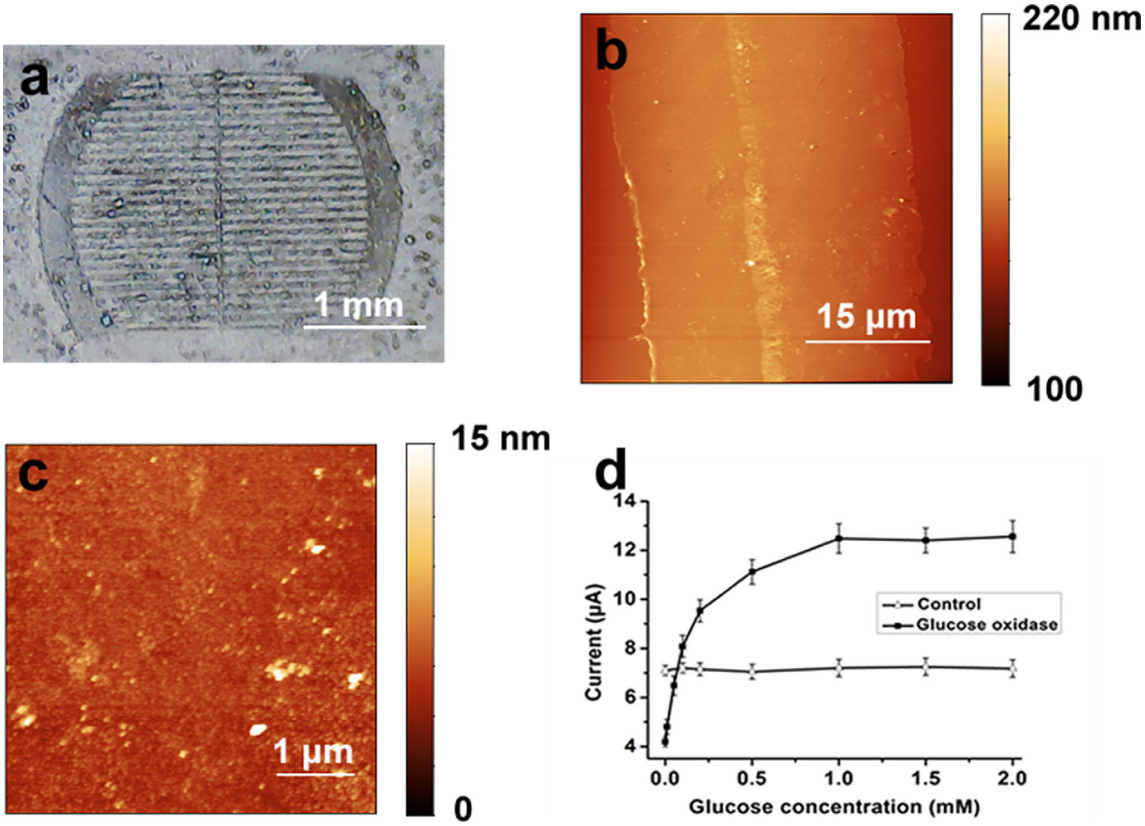

Figure 6. a) An optical micrograph of water condensation grid patterns on OTS-RGO, b,c) AFM images of GOD on the oxidized areas, and d) current responses of glucose at different concentrations.

ed number of active sites of GOD on the pattern. The final saturated detection concentration was 1 mM. In a control experiment (Figure 6d) on an unmodified stripe micropattern, the current did not scale with an increase in the concentration of glucose, which proved that the oxidation caused by GOD played a key role in this sensing process.

3. Conclusions

In conclusion, we demonstrated a direct-write method by electrooxidative lithography of self-assembled OTS monolayers deposited onto graphene layers. This approach permitted tailoring of the chemical and electronic properties of the substrates in a versatile fashion and opened up new possibilities for the fabrication of complex devices, potentially also including different nanomaterials with specialized functionalities.

We investigated the characteristics of the electrochemical oxidation steps and elucidated the mechanism of the oxidation and reoxidation reactions by means of scanning Kelvin probe microscopy and current measurements and by (micro)spectroscopic methods.

Finally, the utilization of the created patterns for the site-selective assembly of nanoparticles and functional glucose oxidase molecules was demonstrated, and the latter resulted in the fabrication of a sensitive glucose sensor system.

Experimental Section

Materials

Toluene, *n*-octadecyltrichlorosilane (OTS), (3-aminopropyl)trimethoxysilane (APTMS), biscyclohexane (BCH), glucose oxidase (GOD), and *N*-hydroxysuccinimide (NHS) were obtained from Aldrich. 1-Ethyl-3-(3-dimethylaminopropyl)carbodiimide hydrochloride (EDC) and D-glucose were obtained from Alfa Aesar and Carl Roth, respectively. Dry BCH was obtained by distillation over sodium and was used for the self-assembly reactions of OTS. All other reagents were used without further purification. Double-sided polished p-type silicon wafers (100) were purchased from Siegert Wafer (resistivity: 10 to 20 Ω cm). The Si substrates were cleaned by Ar plasma (2 min) before use.

Fabrication of Multilayer Films

GO was synthesized from natural graphite powder by a modified Hummer's protocol.[44] Self-assembled monolayers of OTS on the surface of graphene were prepared by utilizing the following procedure:[37,45] First, a Si wafer was immersed in an APTMS saturated vapor for 30 min. Subsequently, the wafer was taken out and sonicated in ultrapure water, which was followed by thermal annealing in air for 2 h. Afterwards, the APTMS-modified Si substrate was kept in the prepared GO aqueous solution (1 mg mL^{-1}) for 12 h and was then ultrasonically cleaned in ultrapure water and blown dry with N_2. GO sheets were grafted onto the surface by electrostatic interactions, and the obtained sample was defined as GO-APTMS. Afterwards, GO-APTMS was incubated in a solution of OTS (10 μL) in BCH (2 mL) for 1 min and was subsequently cleaned by sonication in toluene and drying in N_2 to remove nonspecifically adsorbed OTS molecules. The as-prepared sample was defined as OTS-GO. At last, OTS-GO was thermally reduced at 200 °C for 2 h under an N_2 atmosphere. The obtained sample was defined as OTS-RGO. For comparison, the reduced GO substrate without OTS modification was also prepared (RGO-APTMS) under the same thermal reduction conditions. The water contact angles (WCA) on different substrates were tested by a Krüss DSA10 contact angle goniometer. The monolayers were analyzed by atomic force microscopy (AFM, NT-MDT, NTegra Aura) by using tapping mode tips (NT-MDT, NCS35/AIBS) and by Fourier-transform infrared spectroscopy in transmission mode (FTIR, Bruker Hyperion spectrometer). The resistances of the samples were obtained by LUCAS LABS PRO4-6400. Raman spectra (Lab RAMHR800, Horiba, Hobin Yvon, France, 532 nm laser excitation) were employed to characterize the microstructure of the samples. All tests were analyzed in triplicate.

Electrooxidative Lithography

Electrooxidation lithography was performed in contact mode by utilizing a Pt-coated AFM tip (NT-MDT Ti-Pt) by operating the microscope (NT-MDT, NTegra Aura) in a home-built chamber that permitted control of the relative humidity. Experiments were performed at room temperature. Oxidation parameters were varied by adjusting the bias voltage, pulse duration, and relative humidity in the chamber. All measurements were performed at a constant force to exclude influences arising from this parameter. The microlithography was achieved by a TEM grid, which was cut partially on the edges (Agar Grids 300 Parallel Bar, Copper, 3.05 mm). Oxidation was performed at an applied voltage of −30 V for a few seconds.

Scanning Kelvin Probe and Current Images Measurements

The surface potential was assessed by means of scanning Kelvin probe microscopy (SKPM) performed with a Pt-coated AFM tip (NT-MDT, NCS36 Ti-Pt). The microscope was therefore operated in SKPM mode. In a first scan, the topography of the sample was determined by tapping mode investigation. The same scan line was than scanned again in lift mode with an additional 3 V peak-to-peak AC voltage at the resonance frequency of the cantilever applied between the tip and the sample. In the case of current image measurements, the instrument was operated in contact mode and a bias voltage of 3.5 V was used between the tip and the substrate. All measurements were performed at ambient humidity (30 to 40% RH).

Selective Nanoparticles Growth

In a first step, the substrates bearing the electrooxidized patterns were incubated in an aqueous solution of gold(III) chloride trihydrate (10 min). The samples were subsequently rinsed with deionized water and dried in a stream of N_2. The reduction of the bound Au ions was performed by applying H_2O_2 vapor in a closed vial for 2 h. After the reduction process, only small particles were found in the patterned areas. Their size was enlarged by applying a commercial Ag enhancer solution used, for example, in electron microscopy (Sigma–Aldrich). During this wet-chemical process, contamination with precipitating precursors might have occurred. Scotch tape (3M) was attached to the substrates and was finally removed. This process resulted in efficient removal of nonspecifically attached particles.

After preparing the Ag nanoparticles on the oxidized pattern, the substrate was thermally reduced again at 200 °C for 2 h under a N_2 atmosphere.

Detection of Glucose

The substrate patterned by a TEM grid was first thermally reduced under the same conditions as those stated before. Afterwards, the substrate was incubated in EDC (10 mg mL^{-1}) and NHS (1 mg mL^{-1}) mixed solution for 1 h. The NHS-functionalized graphene was then immersed into 2 mg mL^{-1} glucose oxidase (GOD) in Na_2CO_3/$NaHCO_3$ buffer solution (pH 9.0) overnight at 4 °C followed by rinsing with deionized water and phosphate-buffered saline solution (PBS). Silver conducting paint was used to prepare electrodes on both sides of the pattern array. Then, nail polish was utilized to insulate the electrodes and to define a chamber for glucose in PBS solution (Figure S9). All electrical measurements were performed by using a source meter (Keithley 2400). Each sample was tested three times. After each test, the chamber was washed with plenty of PBS solution. As a reference, a patterned substrate without functionalization of GOD was used for the detection of glucose.

Acknowledgements

H.L. is grateful to the China Scholarship Council (CSC) for a fellowship grant. The work was conducted in the framework of the "Photonic Nanostructures" (PhoNa) project funded by the German Ministry of Education and Research (BMBF) in the program "Spitzenforschung und Innovation in den Neuen Ländern".

Keywords: graphene · lithography · monolayers · nanostructures · sensors

[1] A. K. Geim, K. S. Novoselov, *Nat. Mater.* **2007**, *6*, 183 – 191.
[2] Y. Zhang, T.-T. Tang, C. Girit, Z. Hao, M. C. Martin, A. Zettl, M. F. Crommie, Y. R. Shen, F. Wang, *Nature* **2009**, *459*, 820 – 823.
[3] T. Kurkina, S. Sundaram, R. S. Sundaram, F. Re, M. Masserini, K. Kern, K. Balasubramanian, *ACS Nano* **2012**, *6*, 5514 – 5520.
[4] A. W. Cummings, D. L. Duong, V. L. Nguyen, D. Van Tuan, J. Kotakoski, J. E. Barrios Vargas, Y. H. Lee, S. Roche, *Adv. Mater.* **2014**, *26*, 5079 – 5094.
[5] Y. Kim, J. Park, J. Kang, J. M. Yoo, K. Choi, E. S. Kim, J.-B. Choi, C. Hwang, K. S. Novoselov, B. H. Hong, *Nanoscale* **2014**, *6*, 9545 – 9549.
[6] Y. Zhou, K. P. Loh, *Adv. Mater.* **2010**, *22*, 3615 – 3620.
[7] S. W. Kwon, T. Y. Kim, Y. Kim, M. Byun, Z. Lin, K. S. Suh, D. H. Yoon, W. S. Yang, *Soft Matter* **2011**, *7*, 6811 – 6815.
[8] C. Wu, Q. Cheng, S. Sun, B. Han, *Carbon* **2012**, *50*, 1083 – 1089.
[9] C. X. Cong, T. Yu, Z. H. Ni, L. Liu, Z. X. Shen, W. Huang, *J. Phys. Chem. C* **2009**, *113*, 6529 – 6532.
[10] Y. Cao, S. Liu, Q. Shen, K. Yan, P. Li, J. Xu, D. Yu, M. L. Steigerwald, C. Nuckolls, Z. Liu, X. Guo, *Adv. Funct. Mater.* **2009**, *19*, 2743 – 2748.
[11] Y. Zhou, Q. Bao, B. Varghese, L. A. L. Tang, C. K. Tan, C.-H. Sow, K. P. Loh, *Adv. Mater.* **2010**, *22*, 67 – 71.
[12] D. C. Bell, M. C. Lemme, L. A. Stern, J. R. Williams, C. M. Marcus, *Nanotechnology* **2009**, *20*, 455301.
[13] K. Zhang, Q. Fu, N. Pan, X. Yu, J. Liu, Y. Luo, X. Wang, J. Yang, J. Hou, *Nat. Commun.* **2012**, *3*, 1194.
[14] M. C. Lemme, D. C. Bell, J. R. Williams, L. A. Stern, B. W. H. Baugher, P. Jarillo-Herrero, C. M. Marcus, *ACS Nano* **2009**, *3*, 2674 – 2676.
[15] R. Garcia, A. W. Knoll, E. Riedo, *Nat. Nanotechnol.* **2014**, *9*, 577 – 587.
[16] Z. Wei, D. Wang, S. Kim, S.-Y. Kim, Y. Hu, M. K. Yakes, A. R. Laracuente, Z. Dai, S. R. Marder, C. Berger, W. P. King, W. A. de Heer, P. E. Sheehan, E. Riedo, *Science* **2010**, *328*, 1373 – 1376.
[17] M. Hirtz, A. Oikonomou, T. Georgiou, H. Fuchs, A. Vijayaraghavan, *Nat. Commun.* **2013**, *4*, 2591.
[18] N. Kurra, R. G. Reifenberger, G. U. Kulkarni, *ACS Appl. Mater. Interfaces* **2014**, *6*, 6147 – 6163.
[19] R. Maoz, E. Frydman, S. R. Cohen, J. Sagiv, *Adv. Mater.* **2000**, *12*, 725 – 731.
[20] P. Ardalan, T. P. Brennan, H. Lee, J. R. Bakke, I. Ding, M. D. McGehee, S. F. Bent, *ACS Nano* **2011**, *5*, 1495 – 1504.
[21] C. A. Richter, C. A. Hacker, L. J. Richter, *J. Phys. Chem. B* **2005**, *109*, 21836 – 21841.
[22] D.-J. Yun, S. Lee, K. Yong, S.-W. Rhee, *ACS Appl. Mater. Interfaces* **2012**, *4*, 2025 – 2032.
[23] R. Schmidt, J. H. Oh, Y.-S. Sun, M. Deppisch, A.-M. Krause, K. Radacki, H. Braunschweig, M. Könemann, P. Erk, Z. Bao, F. Würthner, *J. Am. Chem. Soc.* **2009**, *131*, 6215 – 6228.
[24] S. Hoeppener, U. S. Schubert, *Small* **2005**, *1*, 628 – 632.
[25] T. Druzhinina, S. Hoeppener, N. Herzer, U. S. Schubert, *J. Mater. Chem.* **2011**, *21*, 8532 – 8536.
[26] T. S. Druzhinina, C. Höppener, S. Hoeppener, U. S. Schubert, *Langmuir* **2013**, *29*, 7515 – 7520.
[27] A. Heller, B. Feldman, *Chem. Rev.* **2008**, *108*, 2482 – 2505.
[28] Y. Du, X.-L. Luo, J.-J. Xu, H.-Y. Chen, *Bioelectrochemistry* **2007**, *70*, 342 – 347.
[29] L. Li, Q. Sheng, J. Zheng, H. Zhang, *Bioelectrochemistry* **2008**, *74*, 170 – 175.
[30] C. Shan, H. Yang, J. Song, D. Han, A. Ivaska, L. Niu, *Anal. Chem.* **2009**, *81*, 2378 – 2382.
[31] Y. Huang, X. Dong, Y. Shi, C. M. Li, L.-J. Li, P. Chen, *Nanoscale* **2010**, *2*, 1485 – 1488.
[32] S. Alwarappan, C. Liu, A. Kumar, C.-Z. Li, *J. Phys. Chem. C* **2010**, *114*, 12920 – 12924.
[33] A. B. Bourlinos, D. Gournis, D. Petridis, T. Szabó, A. Szeri, I. Dékány, *Langmuir* **2003**, *19*, 6050 – 6055.
[34] B. Lee, Y. Chen, F. Duerr, D. Mastrogiovanni, E. Garfunkel, E. Y. Andrei, V. Podzorov, *Nano Lett.* **2010**, *10*, 2427 – 2432.
[35] D. L. Angst, G. W. Simmons, *Langmuir* **1991**, *7*, 2236 – 2242.
[36] H. Kang, A. Kulkarni, S. Stankovich, R. S. Ruoff, S. Baik, *Carbon* **2009**, *47*, 1520 – 1525.
[37] J. Ou, J. Wang, S. Liu, B. Mu, J. Ren, H. Wang, S. Yang, *Langmuir* **2010**, *26*, 15830 – 15836.
[38] D. Wouters, R. Willems, S. Hoeppener, C. F. J. Flipse, U. S. Schubert, *Adv. Funct. Mater.* **2005**, *15*, 938 – 944.
[39] D. Meroni, S. Ardizzone, U. S. Schubert, S. Hoeppener, *Adv. Funct. Mater.* **2012**, *22*, 4376 – 4382.
[40] P. Avouris, T. Hertel, R. Martel, *Appl. Phys. Lett.* **1997**, *71*, 285 – 287.
[41] M.-C. Chuang, H.-M. Chien, Y.-H. Chain, G.-C. Chi, S.-W. Lee, W. Y. Woon, *Carbon* **2013**, *54*, 336 – 342.
[42] H. C. Schniepp, J.-L. Li, M. J. McAllister, H. Sai, M. Herrera-Alonso, D. H. Adamson, R. K. Prud'homme, R. Car, D. A. Saville, I. A. Aksay, *J. Phys. Chem. B* **2006**, *110*, 8535 – 8539.
[43] S. Hoeppener, R. Maoz, J. Sagiv, *Nano Lett.* **2003**, *3*, 761 – 767.
[44] Y. Xu, H. Bai, G. Lu, C. Li, G. Shi, *J. Am. Chem. Soc.* **2008**, *130*, 5856 – 5857.
[45] J. Ou, Y. Wang, J. Wang, S. Liu, Z. Li, S. Yang, *J. Phys. Chem. C* **2011**, *115*, 10080 – 10086.

Manuscript received: May 18, 2016
Final Article published: ■■ ■■, 2016

ARTICLES

H. Liu, S. Hoeppener, U. S. Schubert*

■■ – ■■

Site-Specific Chemical Surface Functionalization and Electronic Patterning of Graphene by Electrooxidative Lithography

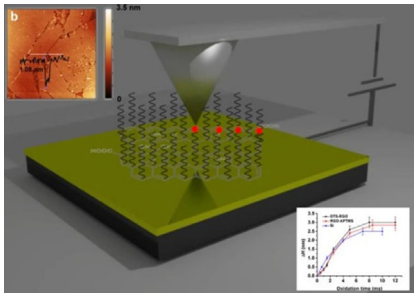

The write way: A new direct-write method to tailor the chemical and electronic properties of reduced graphene oxide on the basis of electrooxidative lithography is introduced. This significantly extends the possibilities to form functional micro- and nanostructures and to combine properties of different nanomaterials in a versatile fashion.

Publication P6

Extending the range of possible substrates for the electro-oxidation of *n*-Octadecyltrichlorosilane (OTS) self-assembled monolayers

D. Meroni,* H. Liu,* S. Ardizzone, U. S. Schubert, S. Hoeppener (*equal contribution)

Submitted to *Nanotechnology.*

Extending the Range of Substrates for the Electrooxidation of Octadecyltrichlorosilane (OTS) Self-assembled Monolayers

Daniela Meroni,[a,b#,*] He Liu,[c#] Ulrich S. Schubert[c,d,e] and Stephanie Hoeppener[c,d,e*]

[a] Dipartimento di Chimica, Università degli Studi di Milano, Via Golgi 19, 20133 Milano, Italy

[b] Consorzio Interuniversitario Nazionale per la Scienza e la Tecnologia dei Materiali (INSTM), Via Giusti 9, 50121 Firenze, Italy

[c] Laboratory of Organic and Macromolecular Chemistry (IOMC), Friedrich Schiller University Jena, Center of Applied Sciences, Philosophenweg 7, 07743 Jena, Germany

[d] Jena Center for Soft Matter (JCSM), Friedrich-Schiller-University Jena, Philosophenweg 7, 07743 Jena, Germany

[e] Center for NanoScience (CeNS), Ludwig-Maximilians-Universität, Schellingstraße 4, 80799 Munich, Germany

* *Corresponding authors:* e-mail: s.hoeppener@uni-jena.de, meroni.daniela@unimi.it

# These authors contributed equally.

Abstract

Surface functionalization of oxides plays a fundamental role in nanotechnology, from microelectronics to photovoltaics. Local oxidation by scanning probe is a powerful tool to

fabricate chemical patterns at the nanometer scale, enabling the hierarchical assembly of complex structures. Notwithstanding the paramount interest in the tailored functionalization of various kinds of oxide materials, most of the literature about probe-based electrooxidation lithography has so far focused on Si wafer substrates. The potential of titanium dioxide (TiO_2) and surface-passivated aluminum (Al/AlO_x) to serve as substrates for electrooxidative nanolithography is here demonstrated. The results obtained on TiO_2 and Al/AlO_x are compared with reference commercial substrates, such as surface-passivated silicon (Si/SiO_x) and indium tin oxide (ITO). The conditions for the functionalization of the different substrate materials with *n*-octadecyltrichlorosilane (OTS) monolayers are reported. Next to the structural study of the formed monolayers by contact angle goniometry, Fourier Transform Infrared (FTIR) spectroscopy and Scanning Force Microscopy (SFM), the different oxidation processes on bare and OTS-functionalized substrates were studied by lateral force imaging and scanning Kelvin probe microscopy. Chemical activation was also confirmed by metallization processes.

Keywords

Titanium dioxide; aluminium oxide; patterning; surface functionalization; alkylsilane; self-assembly

Introduction

The functionalization of silicon and glass by self-assembled monolayers (SAMs) consisting of silane molecules is frequently used as a fabrication step in nanotechnology and surface chemistry [1]. In general this class of molecules can serve as a versatile precursor to introduce surface functionality, to modify the surface energy and wetting properties, to induce bioaffinity and adhesion or to promote the formation of protective layers, etc.. Compared to thiolated precursors, which represent the other class of frequently utilized precursors that can self-assemble onto gold or silver substrates, silane molecules can be used to functionalize hydroxylated surfaces, *i.e.*, glass, silicon and metal oxides. However, the self-assembly process is in general more difficult to control for silanes compared to their thiolated counterparts. While the self-assembly of silanes onto silicon/silicon oxide (Si/SiO_x) and glass substrates is well documented in the literature, the number of contributions focusing on the functionalization of other substrates is comparably small – even though during the last years the interest in functionalizing oxide materials is strongly increasing because of their tremendous technological relevance [2-7], both for the functionalization of large surface areas as well as for the utilization of SAMs for micro- and nanolithography [7-9]. Octadecyltrichlorosilane (OTS) functionalized substrates can serve as a base monolayer for a variety of patterning approaches in particular for electrooxidative lithography. Electrooxidative nano- and microlithography have been developed during the last years into a powerful tool for the structuring of SAMs consisting of OTS. Different concepts have been developed to fabricate a large diversity of nanostructures [10]. However, only recently we succeeded to expand the methodology to other substrates than Si/SiO_x. We could demonstrate that ITO can also serve as a substrate for the electrooxidation process [11], while very recently we demonstrated the reversible nanopatterning of polypyrrole films [12]. Based on these developments, we screened other potentially interesting substrate materials with the aim of applying electrooxidation to obtain chemically active surface patterns on two additional technologically important substrates. Since the chemistry of the self-assembly of OTS monolayers requires hydroxylated substrates, in particular the modification of titanium dioxide (TiO_2) and surface-passivated aluminum (Al/AlO_x) substrates was targeted.

TiO_2 represents an interesting substrate material which is, *e.g.*, utilized in new generation solar cell layouts. Morris *et al.* introduced alkylsilane-TiO_2 hybrid films as active layers in dye sensitized solar cells to decrease dark currents and to increase the open circuit photovoltage [13]. The authors ascribed the higher efficiencies of these solar cells to the covalent bonds formed between the chromophores and the titania network, which can enhance

the electron transfer within the network as well as between the network and the conducting substrate. This effect prevents recombination processes and improves the overall efficiency of light electricity conversion [13-14]. Zamborini *et al.* reported the use of aminosilane linkers to covalently attach dyes to the TiO_2 photoanodes in dye-sensitized solar cells, resulting in an increased stability toward water, heat, and UV light compared to traditionally prepared photoanodes [15]. Very recently, silane functionalized TiO_2 was reported to increase the performance of perovskite solar cells by tuning the interface electronic structure and passivating the recombination process [16].

Additionally, TiO_2 shows attractive photocatalytic properties which can be used in self-cleaning surfaces, air and water purification and photoelectrochemical conversion. A patterning method called photocatalytic lithography utilizes the photocatalytic activity of TiO_2 under UV irradiation for the site-selective degradation of a alkylsilane monolayer [17]. In this way patterned surfaces can be created with localized superhydrophobic/superhydrophilic features, which can be used for water collection from the gas phase, liquid transportation and separation, off-set printing and smart microfluidic devices [18, 19]. Despite the great applicative interest, SAMs on TiO_2 have been by far less extensively studied than the modification possibilities on silicon [20].

Also aluminum is regarded as a technologically important substrate widely exploited in electrode applications, in OLED devices and others. Very recently, the application of patterned Al films in nanophotonic devices and biosensors has been proposed due to their plasmonic properties [21,22]. Aluminum surfaces under atmospheric conditions are covered by a thin pseudo-boehmite native layer (in the following called AlO_x), that consists of two main phases: γ-Al_2O_3 and γ-Al(O)OH [23]. In recent years, molecular coatings based on silanes, thanks to their ability to form durable bonds with the passive oxide layer, have been investigated as alternative to chromium-based protective coatings for aluminum substrates [24-25].

In this work, we conducted a comparative study which highlights the differences in the preparation of OTS SAMs onto four highly different substrates (Si/SiO_x, ITO, TiO_2, Al/AlO_x) and their utilization in electrooxidation lithography. The functionalization and electrooxidation lithography of Si/SiO_x and ITO substrates, which have been previously reported in detail [11], will serve as a reference for the comparison in this contribution.

Methods

Reagents were purchased from different suppliers. Bicyclohexyl (BCH) was distilled over sodium before use, while all other reagents were used without further purification.

Double side polished p-doped silicon wafers with a resistivity of 1 to 10 Ωcm (according to the data sheet) were purchased from University Wafer. ITO layers on float glass supports were obtained from PGO (surface resistivity: 80 Ω/sq) and from Sigma-Aldrich (surface resistivity: 15-25 and 70-100 Ω/sq).

TiO_2 films were prepared starting from a titania stable and homogeneous sol, synthesized according to the following procedure. N-Butanol (5.3 mL) and acetylacetone (0.4 mL) were mixed in a test tube. Then, 4.2 mL titanium(IV) butoxide was added to the solution, which was subsequently stirred for 30 min at room temperature. Glacial acetic acid (0.3 mL) was added dropwise to the solution under stirring. The resulting sol (yellowish and transparent) was stable for several weeks. The titania films were deposited by spin coating the obtained sol on ITO layers (2000 rpm, 20 s). The resulting films were immediately calcined at 400 °C under O_2 flux (1 L h^{-1}) for 1.5 h.

Thick Al films (>100 nm) were thermally evaporated onto freshly cleaved mica substrates (Plano). The films were carefully removed and the interface site between the Al film and the mica substrate was used for the self-assembly of OTS. To improve the stability, the Al films were backed with a silicon support.

Prior to the self-assembly all samples were cleaned by oxygen plasma (Diener Electronics) until a complete wetting by water was achieved (2 min for the silicon wafer, ITO and Al/AlO_x, 15 min for TiO_2). Dry BCH was used as a solvent for the n-OTS (1 mL dry BCH, 5 µL OTS). The samples were immersed into the solution until dewetting of the substrate was observed when pulling out the substrates from the self-assembly solution. Samples were blow dried in a stream of N_2 and subsequently sonicated in toluene for 30 s. Samples were carefully dried again in a stream of N_2.

Contact angle measurements were performed on a CA10 goniometer (Data Physics Instruments). Fourier transform infrared (FTIR) investigations were performed in reflectance mode utilizing a Bruker Hyperion FTIR microscope. Scanning force microscopy (SFM) and Scanning Kelvin Probe Microscopy (SKPM) investigations were conducted on a NTegra Aura system (NT-MDT). Commercially available SFM tips from µMash were used (NSC35 for tapping mode investigations, Pt or Pt-Ti coated NSC36 for electrooxidation and surface potential measurements). For SKPM measurements, a scan frequency of 1.0 Hz and a 2.5 V peak-to-peak AC voltage at the resonance frequency of the cantilever between the probe tip and the sample were applied. Measurements were carried out at ambient humidity (relative

humidity, R_H: 30-50%). Electrooxidation was performed in contact mode utilizing the vector (Si/SiO_x, ITO, Al/AlO_x) or spectroscopy mode (for TiO_2 showing the most demanding oxidation times) of the SFM software. The humidity was controlled by means of a humidifier. Pulse voltages, pulse duration and R_H values are listed in figures.

The site-selective growth of noble metal nanoparticles was carried out by immersing the patterned substrate in an aqueous Ag(II) acetate solution. The substrate was then rinsed with deionized water, dried in a N_2 stream and treated with hydrazine or hydrogen peroxide in the vapor phase. Finally, the substrate was treated with a commercial Ag enhancer solution (Aldrich).

Results and discussion

Essential for the comparability of the electrooxidation process is the availability of smooth substrates. The characterization of the formed nanostructures is restricted mainly to probe based analysis techniques, as spectroscopic techniques frequently provide neither the lateral resolution nor the required sensitivity. In this study, lateral force imaging and Scanning Kelvin Probe Microscopy (SKPM) were used as a powerful investigation tool; smooth substrates were thus required as lateral force and SKPM signals might be convoluted by topographical features on rough substrates. While Si wafers and ITO (23 nm-thick layer on float glass) (**Figure 1a**) substrates are commercially available in a sufficient quality, TiO_2 and Al/AlO_x had to be custom-made. Simple preparation procedures, requiring widely available laboratory equipment, were selected. TiO_2 layers were prepared on either glass or commercial ITO substrates by calcination of thin, spin coated films obtained from a stable titania sol. SFM thickness investigations on partially removed films revealed a TiO_2 thickness of 170 nm. The film structure of the TiO_2 layers shows a homogeneous surface with a sufficiently small surface roughness (**Figure 1b**).

	ITO	TiO_2	Al/AlO_x
RMS amplitude (5 µm x 5 µm)	0.4 nm	0.8 nm	2.0 nm
Tapping mode topography	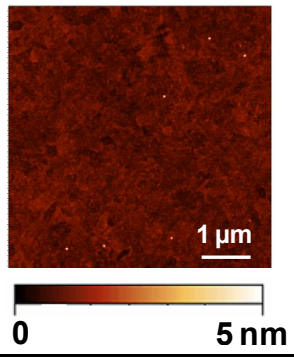	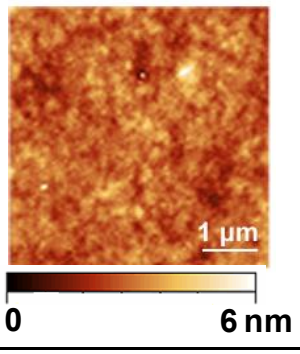	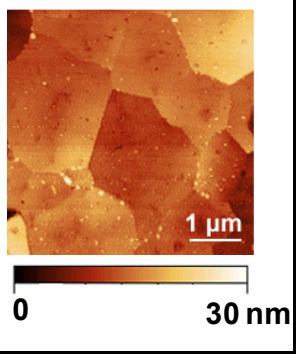

Figure 1: Tapping mode SFM images of the respective surfaces. a) ITO on float glass, b) TiO_2 on smooth ITO layer and c) Inverted Al/AlO_x layers after oxidation at ambient conditions.

Smooth Al/AlO_x samples were prepared by the following procedure: A several hundred nanometers thick film of Al was thermally evaporated onto a freshly cleaved mica substrate. The film was afterwards removed from the mica and a surface featuring micrometer large and smooth Al domains was obtained (**Figure 1c**) at the interface previously facing the mica substrate. The formation of a native oxide layer was achieved by exposure to air and by O_2 plasma treatment [26]. Literature studies report oxide layers on Al surfaces of thicknesses in the range of 3-5 nm [27, 28], quite comparable with the thickness of the native layer on Si wafers. To enable convenient handling of the rather flexible films, a silicon support was used to stabilize them.

OTS monolayer films could be obtained for all substrates by dip coating in an OTS-BCH solution. Adaptations of the self-assembly procedure had to be made on the different substrates in particular concerning the immersion time, which is rather different for the individual substrate materials. The typical required immersion times are listed in **Figure 2**, together with the characteristic properties of the obtained monolayers.

	Si/SiO_x	ITO	TiO_2	Al/AlO_x
Immersion time (min)	< 1	5 - 10	10 - 60	5
Water contact angle (°)	107 ± 1	108 ± 1	105 ± 2	104 ± 2
FTIR υCH_2 (cm^{-1})	2918 / 2850	2922 / 2852	2919 / 2850	2916 / 2849
Tapping mode topography	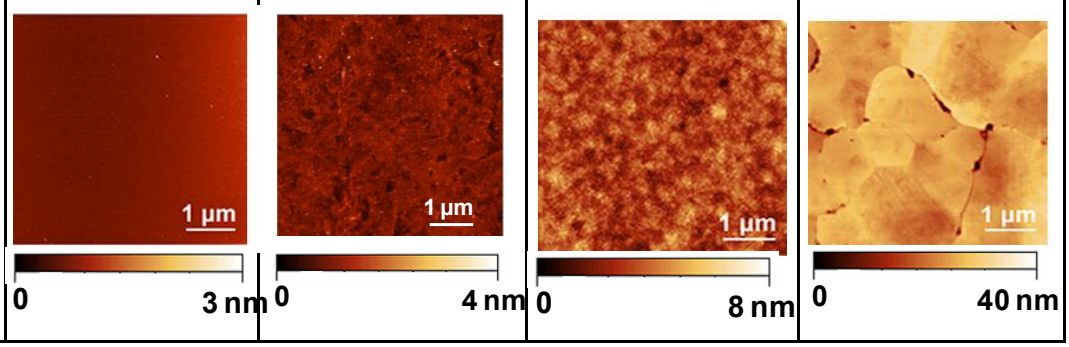			

Figure 2: Summary of the parameters and characteristic properties OTS monolayers prepared on different substrates. FTIR spectra of the samples can be found in the Supplementary data (**Figure S1**).

The rate of functionalization of the substrates is rather different. Si/SiO_x shows the fastest functionalization characteristics, whereas ITO, Al/AlO_x and TiO_2 require long assembly times to obtain a reasonable OTS functionalization. In general, the water content of the utilized BCH solutions is very critical for all substrates [29] and this parameter is more crucial for the substrates requiring long immersion times.

Based on water contact angle measurements alone the quality of the monolayers is hardly accessible, as, *e.g.*, the surface roughness has a considerable influence. Hence, the layers were additionally evaluated by means of FTIR and SFM investigations (**Figure 2**).

Al/AlO_x shows the best monolayer formation as reflected in the peak position of the CH stretching vibrations [30], indicating the formation of a densely packed OTS monolayer. The peak position of the CH stretching vibrations in OTS-functionalized TiO_2 and ITO are instead at higher wavenumbers, suggesting a noticeable difference in the grafting density of the SAM.

In the case of ITO, this conclusion is also supported by the observation of dendritic structures in the SFM phase images (**Figure S2**) that previous studies attributed to areas of more compact monolayer surrounded by areas where the silane molecules are less ordered and compactly arranged [11].

Several aspects may influence on one side the rate of reactivity and on the other side the compactness of the monolayer, including the polarity of the M–O bond, the point of zero charge of the oxide, and the density of surface hydroxyls. For instance, Kim *et al.* observed a lower density of adsorption of a alkylsilane-mediated protein onto TiO_2 with respect to SiO_2 and attributed it to the difference in ionic character between the two oxides [31]. Matching results were obtained in our laboratory comparing the alkylsilane adsorbed amounts on functionalized TiO_2 and SiO_2 nanoparticles of comparable surface area by solid state NMR [32]. Consistently, literature data referring to both nanoparticles and film surfaces indicate a systematic larger density of surface hydroxyl groups in AlO_x with respect to SiO_x [27]. AlO_x surfaces are known at the same time to be populated by several kinds of –OH groups arising from different terminations [33, 34], while in the case of SiO_2, silanol bonds (Si–OH) are predominant. In the case of TiO_2 instead chemisorbed water is the prevailing source of hydroxyl groups [32].

The fabricated OTS functionalized oxide layers can serve as substrates for electrooxidation nanolithography. OTS-functionalized Si/SiO_x, ITO, TiO_2 and Al/AlO_x substrates were investigated regarding their ability to be structured by means of probe-based electrooxidative lithography. Negative tip bias voltage pulses were applied in the vector lithography or the spectroscopy mode of the SFM facility. These voltage pulses initiate an electrochemical oxidation process of the SAM and generate polar functional groups by converting the surface exposed $–CH_3$ groups of the SAM [10]. Detailed studies have up to now only be reported on OTS monolayers on Si/SiO_x and ITO [10, 11, 35]. Therefore, a comparative study was performed to investigate and correlate the oxidation process also on the other substrates to elucidate important differences in the oxidation characteristics.

	Si/SiO_x	ITO	TiO_2	Al/AlO_x
Oxidation conditions	-10 V; R_H = 60% 5-10 ms	-12 V; R_H = 75% 10-25 ms	-15 V; R_H = 55% 70-90 ms	-10 V; R_H = 45% 10-60 ms
Tapping mode height image	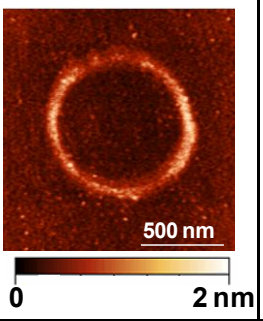	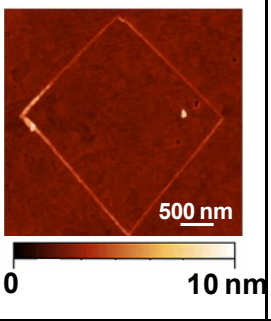	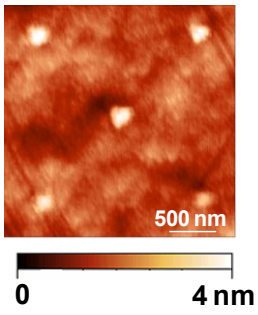	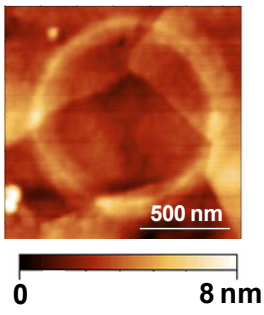
Lateral force image	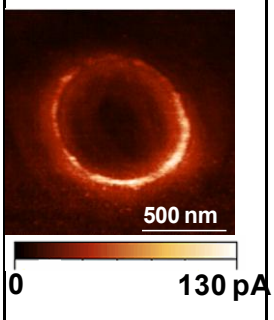	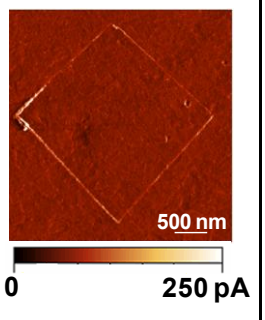	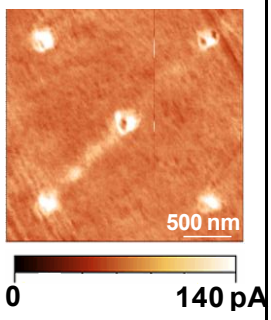	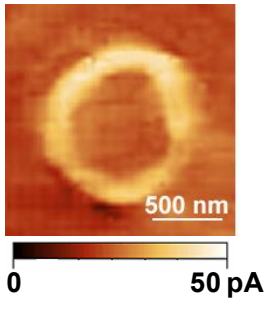
Surface potential images	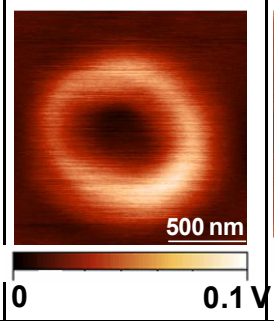	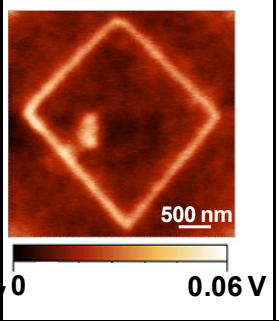	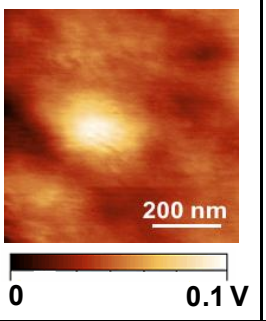	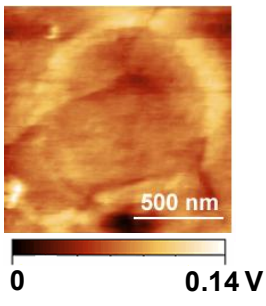
Surface potential difference	+ 80 mV (oxidation time: 10 ms)	+ 60 mV (oxidation time: 25 ms)	+ 70 mV (oxidation time: 80 ms)	+ 40 mV (oxidation time: 30 ms)

Figure 3: Comparison of the electrooxidation process on different OTS modified substrates.

The required oxidation conditions to obtain surface patterns on the different OTS functionalized substrates are summarized in **Figure 3**. The reported voltage and relative humidity conditions indicate the lowest values required for the oxidation to proceed. A range of oxidation times is reported for each substrate. Such a range of oxidation conditions define a plateau region where the oxidation results (line-width, current injection, etc.) stay more or less constant, as previously reported in the literature for OTS-Si systems [35]. For all samples

except TiO_2, the electrooxidations were carried out in vector mode, *i.e.* by rastering the tip across the substrate in a pre-determined geometry to obtain a specific shape (several kinds of geometries are reported as an example).

Figure 3 clearly shows that the different OTS-functionalized surfaces require also different oxidation conditions. In particular the oxidation time and required oxidation voltages show strong variations. While oxidation times for Si/SiO_x substrates are very short (5-10 ms), ITO and Al/AlO_x request longer oxidation times (10-60 ms). The most demanding substrate in this respect was TiO_2 which requires oxidation times as long as 90 ms to obtain the electrooxidized features. In particular the long oxidation times made it impossible to use the vector mode of the SFM software to carry out the lithography on TiO_2. For this substrate, results could be obtained exclusively in the spectroscopy mode, which has the main limitation of producing only arrays of dots instead of complex patterns.

Similar to the case of ITO, which requires the insertion of a silicon spacer into the setup, also for Al/AlO_x a Si spacer, acting as a resistor in series with the tip/sample [11], was inserted to tune the electron injection. On the other hand, oxidations on Si/SiO_x as well as on TiO_2, were performed without additional resistors.

It is well known that the relative humidity plays a relevant role in the electrooxidation process [10]. In the case of ITO, lithography could be successfully carried out by limiting the electron exchange and by working at high relative humidity conditions. The situation is different for OTS-TiO_2 and OTS-Al/AlO_x samples, where the relative humidity represents a less crucial parameter, as electrooxidative lithography could be carried out at relative mild air humidity conditions (45-55%). In the case of TiO_2, demanding oxidation conditions were required even at higher humidity contents. The latter observation is in agreement with previous studies reporting that humidity mainly influences the reliability of the oxidation process and the line-thickness of the oxidized features [36]. Long oxidation times and high humidity requirements have also an influence on the obtainable lateral resolution of the inscribed patterns. In general the line width of oxidized features depends on the size of the formed water meniscus [37]. Longer oxidation times result in a gradual spreading of the water meniscus' contact line which enlarges the area of oxidation. High humidity conditions feature the same effect. As such the obtained line width is best in case of OTS monolayers self-assembed on Si/SiOx substrates and is largest for TiO_2 which in particular requires a long oxidation time.

The nature of the formed structures can be efficiently investigated by the Scanning Kelvin Probe Microscopy (SKPM) mode of SFM, which provides access to the local surface potential of the formed patterns. The detected differences in the surface potential are directly

related to the chemical nature of the formed groups. For all substrates, a significant positive surface potential difference was detected between patterned and un-modified areas, strongly suggesting a comparable functionalization of the patterned areas. The overall values are only slightly different and range between +60 to +80 mV, only for Al/AlO_x a smaller surface potential change of +40 mV was observed.

In order to ensure that the formed structures are unambiguously related to the functionalization of the OTS monolayer and are not a result of a degradation process of the monolayer and/or an associated phase transition related phenomena of the underlying substrates, oxidations were also performed on the bare substrates. For Si/SiO_x layers the well-known anodization reactions were observed [38, 39], which result in the formation of elevated structures consisting of silicon oxide as observed by tapping mode SFM (**Figure S3**). Consequently, in this case no obvious differences in the surface potential could be observed, as reported previously [11], because the substrate as well as the anodized features consist of the same material. Similar results were obtained for bare Al/AlO_x (**Figure S4**) as well as for ITO (**Figure S3**). While for Al/AlO_x the observed increase in height can be attributed to anodization reactions similar to the case of SiO_x, in the case of ITO the attribution is less straightforward. Previous studies suggested the occurrence of over-oxidation of the oxide, resulting in crystal growth or phase change [11], although the nanometric scale of the features made it impossible to probe the oxidized features with conventional techniques such as XPS. The situation is different for TiO_2. On this substrate no elevated topographical structures could be observed in tapping mode SFM after the oxidation experiments (**Figure S4**). This can be explained considering that the TiO_2 substrate is a bulk oxide phase formed by a sol-gel process, whereas the other substrates are just covered by a thin native oxide layer. Surface potential images do not present marked differences between oxidized structures and unpatterned areas (**Figure S4**), in agreement with previous reports about unfunctionalized Si and ITO [11].

As a final indirect proof for the functionalization of the OTS monolayer during the electrooxidation process, the growth of noble metal nanoparticles on the structures was tested using a procedure previously reported for patterned OTS-Si surfaces [11]. The chemical activation of the SAM by electrooxidation lithography generates surface functional groups on the monolayers which can be efficiently loaded with metal ions (*e.g.,* silver ions) from aqueous solutions. Subsequent reduction of the metal ions by hydrazine or hydrogen peroxide vapor resulted in the template guided formation of silver nanoparticles which can subsequently be enhanced by a deposition process from a commercial silver enhancer solution

[35]. **Figure 4** depicts the results of this metal deposition on ITO, TiO_2 and Al/AlO_x substrates demonstrating indirectly the presence of functional groups.

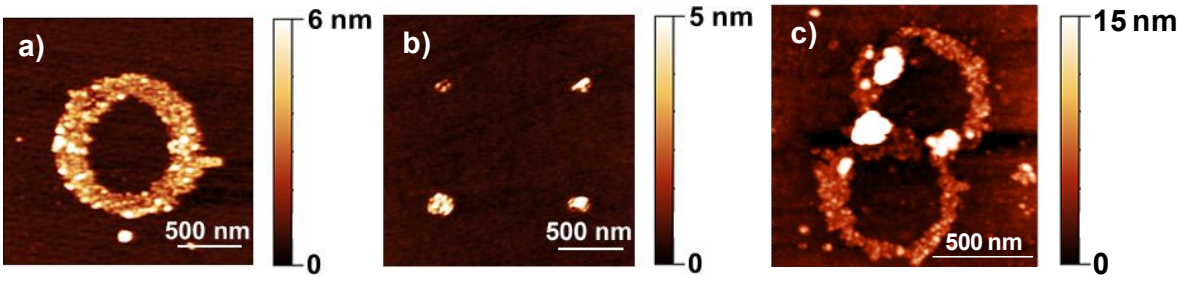

Figure 4: Tapping mode height images of the metallization of the patterned areas after *in-situ* formation of noble metal nanoparticles on a) Al/AlO_x and b) TiO_2 and c) ITO.

Conclusions

We demonstrate the ability of a number of technologically important substrates to form high quality OTS monolayers. Next to the well-established functionalization of Si/SiO_x substrates, the experimental conditions for the reliable formation of OTS monolayers on ITO, TiO_2 and Al/AlO_x substrates are reported. Interestingly, despite of the relevant differences concerning both the surface properties, good quality OTS monolayers were obtained for all substrates by a careful adaptation of the deposition parameters. These monolayers could be furthermore structured by means of electrooxidative nanolithography to create chemically active nanometric surface patterns. Significant differences in the oxidation parameters required for OTS structuring were found, depending on film thickness and conductivity of the tested oxides. Nevertheless, all substrates were suitable to form functional groups, which were used to site-selectively generate metal nanostructures on the oxidized areas. Additionally, surface potential measurements were employed to further investigate the chemical nature of the oxidized areas, revealing a similarity of the oxidation processes occurring on the OTS-functionalized individual substrates. In contrast to Si/SiO_x, ITO and Al/AlO_x, no anodization reaction of the underlying TiO_2 was observed.

The obtained results bear significance in a number of research areas where the formation of layers showing uniform properties, such as adhesion or corrosion, is desired irrespectively of the support features, as in the case of multi-component metal alloys.

Acknowledgments

H. Liu gratefully acknowledges a CSC fellowship. Dr. C. Höppener is kindly acknowledged for providing the evaporated aluminum layers. This work was financially supported by the

BMBF project ‘Photonic Nanomaterials’ of the Excellence Initiative ‘Spitzenforschung in den Neuen Ländern’.

References

[1] Onclin, S.; Ravoo, B. J.; Reinhoudt, D. N. Engineering Silicon Oxide Surfaces Using Self-Assembled Monolayers. *Angew. Chem. Int. Ed.* **2005**, *44*, 6282-6304.

[2] Wang, D.; Liu, Y.; Liu, X.; Zhou, F.; Liu, W.; Xue, Q. Towards a Tunable and Switchable Water Adhesion on a TiO_2 Nanotube Film with Patterned Wettability. *Chem. Commun.* **2009**, 7018-7020.

[3] Zhang, Q.; Hu, Z.; Liu, Z.; Zhai, J.; Jiang, L. Light-Gating Titania/Alumina Heterogeneous Nanochannels with Regulatable Ion Rectification Characteristic. *Adv. Funct. Mater.* **2014**, *24*, 424-431.

[4] Manoudis, P. N.; Karapanagiotis, I.; Tsakalof, A.; Zuburtikudis, I.; Kolinkeová, B.; Panayiotou, C. Superhydrophobic films for the protection of outdoor cultural heritage assets. *Appl. Phys. A* **2009**, *97*, 351-360.

[5] Li,. J.F.; Marks, T.J. Air-Stable, Cross-Linkable, Hole-Injecting/Transporting Interlayers for Improved Charge Injection in Organic Light-Emitting Diodes. *Chem. Mater.* **2008**, 20, 4873-4882

[6] Song, Y.-Y.; Hildebrand, H.; Schmuki, P. Photoinduced Release of Active Proteins from TiO_2 Surfaces. *Electrochem. Commun.* **2009**, *11*, 1429-1433.

[7] Soliveri, G.; Annunziata, R.; Ardizzone, S.; Cappelletti, G.; Meroni, D. Multiscale Rough Titania Films with Patterned Hydrophobic/Oleophobic Features. *J. Phys. Chem. C* **2012**, *116*, 26405-26413.

[8] Herzer, N.; Hoeppener, S.; Schubert, U. S. Fabrication of patterned silane based self-assembled monolayers by photolithography and surface reactions on silicon-oxide substrates. *Chem. Commun.* **2010**, *46*, 5634-5652.

[9] Claridge, S. A.; Liao, W.-S.; Thomas, J. C.; Zhao, Y.; Cao, H. H.; Cheunkar, S.; Serino, A. C.; Andrews, A. M.; Weiss, P. S. From the Bottom Up: Dimensional Control and Characterization in Molecular Monolayers. *Chem. Soc. Rev.* **2013**, *42*, 2725-2745.

[10] Wouters, D.; Hoeppener, S.; Schubert, U. S. Local Probe Oxidation of Self-Assembled Monolayers: Templates for the Assembly of Functional Nanostructures. *Angew. Chem. Int. Ed.* **2009**, *48*, 1732-1739.

[11] Meroni, D.; Ardizzone, S.; Schubert, U. S.; Hoeppener, S. Probe-Based Electro-Oxidative Lithography of OTS SAMs Deposited onto Transparent ITO Substrates. *Adv. Funct. Mater.* **2012**, *22*, 4376-4382.

[12] Liu, H.; Hoeppener, S.; Schubert, U.S. Reversible Nanopatterning on Polypyrrole Films by Atomic Force Microscope Electrochemical Lithography. *Adv. Funct. Mater.* **2015**, DOI: 10.1002/adfm.201503834.

[13] Morris, A. J.; Meyer, G. J. TiO_2 Surface Functionalization to Control the Density of States. *J. Phys. Chem. C* **2008**, *112*, 18224-18231.

[14] Lin, C.-L.; Yeh, M.-Y.; Chen, C.-H.; Sudhakar, S.; Luo, S.-J.; Hsu, Y.-C.; Huang, C.-Y.; Ho, K.-C.; Luh, T.-Y. Silica−Titania-Based Organic−Inorganic Hybrid Materials for Photovoltaic Applications. *Chem. Mater.* **2006**, *18*, 4157-4162.

[15] Luitel, T.; Zamborini, F. P. Covalent modification of photoanodes for stable dye-sensitized solar cells. *Langmuir* **2013**, *29*, 13582-13594.

[16] Liu, L.; Mei, A.; Liu, T.; Jiang, P.; Sheng, Y.; Zhang, L.; Han, H. Fully Printable Mesoscopic Perovskite Solar Cells with Organic Silane Self-Assembled Monolayer. *J. Am. Chem. Soc.* **2015**, *137*, 1790- 1793.

[17] Nakata, K.; Fujishima, A. TiO_2 photocatalysis: Design and applications. *J. Photochem. Photobiol. C* **2012**, *13*, 169-189.

[18] Yao, X.; Song, Y.; Jiang, L. Applications of Bio-Inspired Special Wettable Surfaces. *Adv. Mater.* **2011**, *23*, 719-734.

[19] Liu, K.; Cao, M.; Fujishima, A.; Jiang, L. Bio-Inspired Titanium Dioxide Materials with Special Wettability and Their Applications. *Chem. Rev.* **2014**, *114*, 10044–10094.

[20] Paz, Y. Self-assembled monolayers and titanium dioxide: From surface patterning to potential applications. *Beilstein J. Nanotechnol.* **2011**, *2*, 845-61.

[21] Canalejas-Tejero, V.; Barrios, C.A. Compact discs as versatile cost-effective substrates for releasable nanopatterned aluminium films. *Nanoscale* **2015**, *7*, 3435–3439.

[22] Canalejas-Tejero, V.; Herranz, S.; Bellingham, A.; Moreno-Bondi, M.C.; Barrios, C.A. Passivated Aluminum Nanohole Arrays for Label-Free Biosensing Applications. *ACS Appl. Mater. Interfaces* **2014**, *6*, 1005–1010.

[23] Giza, M.; Thissen, P.; Grundmeier, G. Adsorption kinetics of organophosphonic acids on plasma-modified oxide-covered aluminum surfaces. *Langmuir* **2008**, *24*, 8688-8694.

[24] Frignani, A.; Zucchi, F.; Trabanelli, G.; Grassi, V. Protective Action Towards Aluminium Corrosion by Silanes with a Long Aliphatic Chain. *Corr. Sci.* **2006**, *48*, 2258-2273.

[25] Hintze, P. E.; Calle, L. M. Electrochemical Properties and Corrosion Protection of Organosilane Self-Assembled Monolayers on Aluminum 2024-T3. *Electrochim. Acta* **2006**, *51*, 1761-1766.

[26] Strohmeier, B. R. The effects of O_2 plasma treatments on the surface composition and wettability of cold-rolled aluminum foil. *J. Vac. Sci. Technol. A* **1989**, *7*, 3238-3245.

[27] McCafferty, E.; Wightman, J. P. Determination of the concentration of surface hydroxyl groups on metal oxide films by a quantitative XPS method. *Surf. Interf. Anal.* **1998**, *26*, 549-564.

[28] Matsuo, P. J.; Standaert, T. E. F. M.; Allen, S. D.; Oehrlein, G. S.; Dalton, T. J. Characterization of Al, Cu, and TiN surface cleaning following a low-K dielectric etch. *J. Vac. Sci. Technol. B* **1999**, *17*, 1435-1447.

[29] Ulman, A. Formation and Structure of Self-Assembled Monolayers. *Chem. Rev.* **1996**, *96*, 1533-1554.

[30] Vallant, T.; Kattner, J.; Brunner, H.; Mayer, U.; Hoffmann, H. Investigation of the formation and structure of self-assembled alkylsiloxane monolayers on silicon using in situ attenuated total reflection infraredspectroscopy. *Langmuir* **1999**, *15*, 5339 –5346.

[31] Kim, H.; Noh, K.; Choi, C.; Khamwannah, J.; Villwock, D.; Jin, S. Extreme Superomniphobicity of Multiwalled 8 nm TiO_2 Nanotubes. *Langmuir* **2011**, *27*, 10191-10196.

[32] Soliveri, G.; Meroni, D.; Cappelletti, G.; Annunziata, R.; Aina, V.; Cerrato, G.; Ardizzone, S. Engineered organic/inorganic hybrids for superhydrophobic coatings by wet and vapour procedures. *J. Mater. Sci.* **2014**, *49*, 2734-2744.

[33] Peri, J. B. A Model for the Surface of γ-Alumina. *J. Phys. Chem.* **1965**, *69*, 220-230.

[34] Morterra, C.; Magnacca, G. A case study: surface chemistry and surface structure of catalytic aluminas, as studied by vibrational spectroscopy of adsorbed species. *Catal. Today* **1996**, *27*, 497-532.

[35] Druzhinina, T. S.; Hoeppener, S.; Schubert, U. S. New Design Concepts for the Fabrication of Nanometric Gap Structures: Electrochemical Oxidation of OTS Mono- and Bilayer Structures. *Small* **2012**, *8*, 852-857.

[36] Hoeppener, S.; Maoz, R.; Sagiv, J. Contact Electrochemical Replication of Electrochemically Printed Monolayer Patterns. *Adv. Mater.* **2006**, *18*, 1286-1290.

[37] Druzhinina, T.; Hoeppener, S.; Herzer, N.; Schubert, U.S. Fabrication of ring structures by anodization lithography on self-assembled OTS monolayers. *J. Mater. Chem.* **2011**, *21*, 8532-8536.

[38] Sugimura, H.; Nakagiri, N. Chemical Approach to Nanofabrication: Modifications of Silicon Surfaces Patterned by Scanning Probe Anodization. *Jap. J. Appl. Phys.* **1995**, *34*, 3406-3411.

[39] Gordon, A. E.; Fayfield, R. T.; Litfin, D. D.; Higman, T. K. Mechanisms of surface anodization produced by scanning probe microscopes. *J. Vac. Sci. Technol. B.* **1995**, *13*, 2805-2808.

Supplementary data

Extending the Range of Substrates for the Electro-oxidation of *n*-Octadecyltrichlorosilane (OTS) Self-assembled Monolayers

Daniela Meroni,[a,b#,*] He Liu,[c#] Ulrich S. Schubert[c,d,e] and Stephanie Hoeppener[c,d,e*]

[a] Dipartimento di Chimica, Università degli Studi di Milano, Via Golgi 19, 20133 Milano, Italy

[b] Consorzio Interuniversitario Nazionale per la Scienza e la Tecnologia dei Materiali (INSTM), Via Giusti 9, 50121 Firenze, Italy

[c] Laboratory of Organic and Macromolecular Chemistry (IOMC), Friedrich Schiller University Jena, Center of Applied Sciences, Philosophenweg 7, 07743 Jena, Germany

[d] Jena Center for Soft Matter (JCSM), Friedrich-Schiller-University Jena, Philosophenweg 7, 07743 Jena, Germany

[e] Center for NanoScience (CeNS), Ludwig-Maximilians-Universität, Schellingstraße 4, 80799 Munich, Germany

# These authors contributed equally.

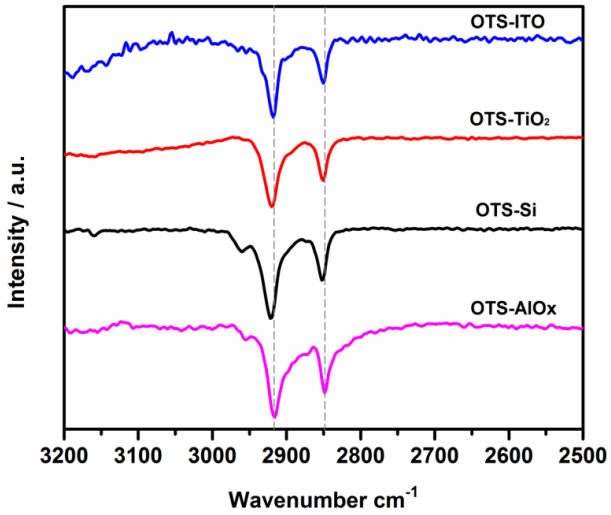

Figure S1: FT-IR spectra of OTS monolayers self-assembled on different substrates.

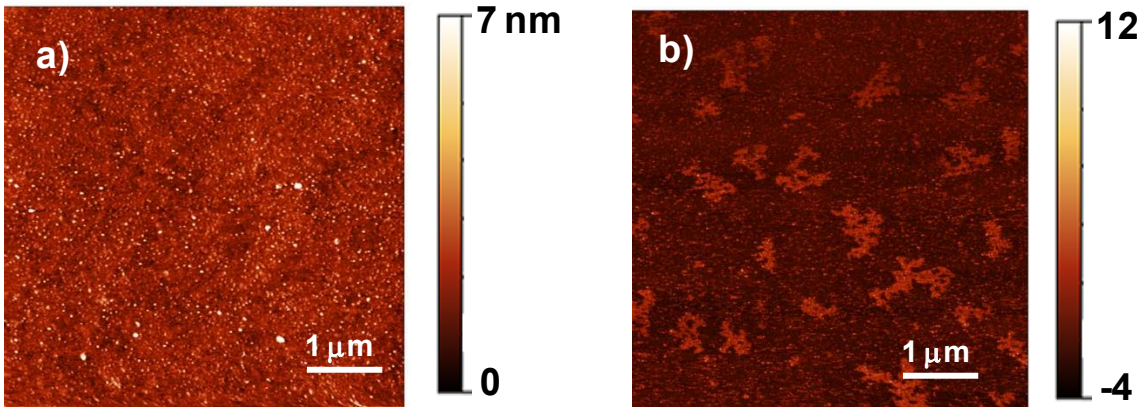

Figure S2: Dendritic island structure formed within the OTS films on ITO. a) Tapping mode height image of the surface. b) Corresponding phase image which reveals the presence of islands.

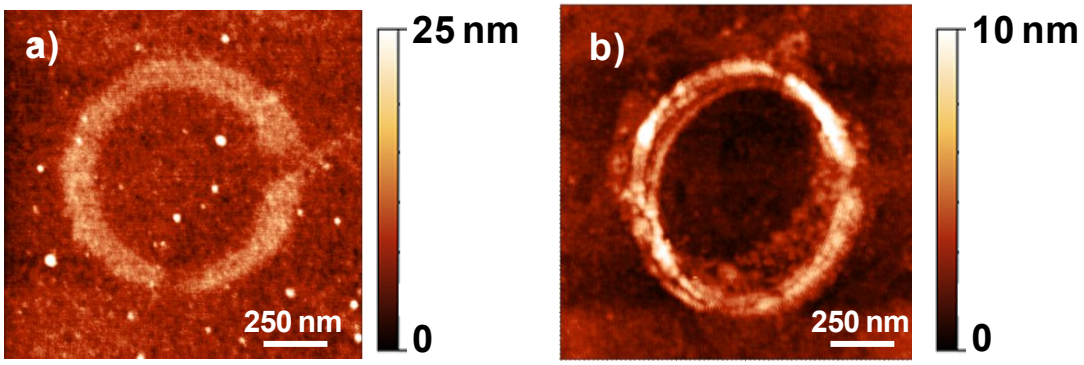

Figure S3: Height images measured in tapping mode of a) bare Si and b) bare ITO.

	TiO_2	AlO_x
Oxidation conditions	–15 V, R_H = 55% 70 ms	–10 V, R_H= 45% 30 ms
SFM lateral force images	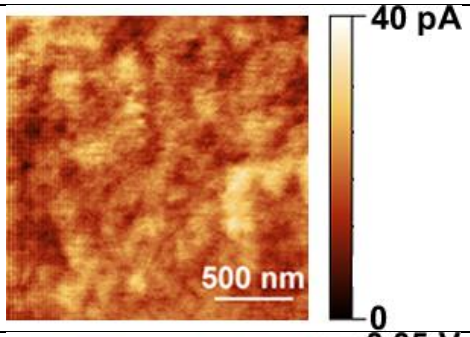	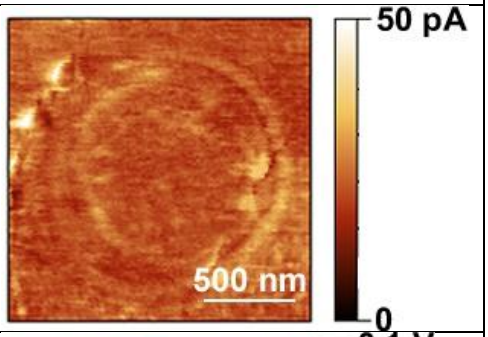
Surface potential images	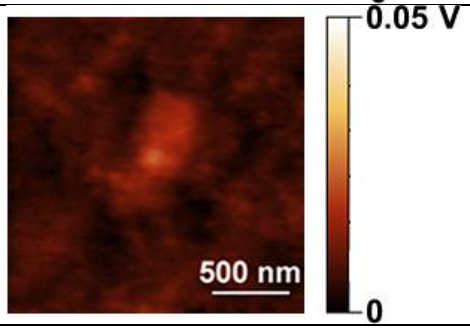	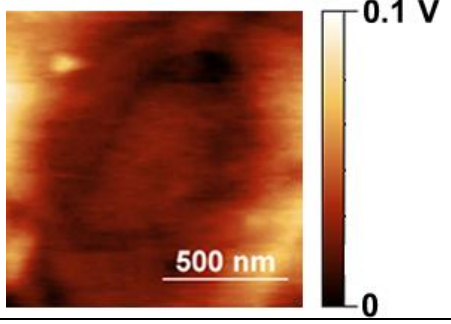

Figure S4: Comparison of the lateral force and surface potential images relative to electrooxidation process on TiO_2 and AlO_x. Results for OTS/Si and OTS/ITO can be found in [1].

[1] Meroni, D.; Ardizzone, S.; Schubert, U. S.; Hoeppener, S. *Adv. Funct. Mater.* **2012**, *22*, 4376–4382.